ÉCOLE DE TECHNOLOGIE SUPÉRIEURE
UNIVERSITÉ DU QUÉBEC

MANUSCRIPT-BASED THESIS PRESENTED TO
ÉCOLE DE TECHNOLOGIE SUPÉRIEURE

IN PARTIAL FULFILLMENT OF THE REQUIREMENTS
FOR THE DEGREE OF DOCTOR OF PHILOSOPHY
Ph.D.

BY
Oliviu ŞUGAR GABOR

VALIDATION OF MORPHING WING METHODOLOGIES ON AN UNMANNED AERIAL SYSTEM AND A WIND TUNNEL TECHNOLOGY DEMONSTRATOR

MONTREAL, 18TH OF DECEMBER 2015

BOARD OF EXAMINERS

THIS THESIS HAS BEEN EVALUATED

BY THE FOLLOWING BOARD OF EXAMINERS

Dr. Ruxandra Mihaela Botez, Thesis Supervisor
Department of Automated Production Engineering at École de Technologie Supérieure

Dr. Philippe Bocher, Chair, Board of Examiners
Department of Mechanical Engineering at École de Technologie Supérieure

Dr. Guy Gauthier, Member of the Jury
Department of Automated Production Engineering at École de Technologie Supérieure

Dr. Marius Paraschivoiu, External Evaluator
Department of Mechanical and Industrial Engineering, Concordia University

THIS THESIS WAS PRENSENTED AND DEFENDED

IN THE PRESENCE OF A BOARD OF EXAMINERS AND THE PUBLIC

ON THE 15TH OF DECEMBER 2015

AT ÉCOLE DE TECHNOLOGIE SUPÉRIEURE

ACKNOWLEDGMENTS

First and foremost, I would like to express my gratitude to my thesis advisor, Prof. Ruxandra Mihaela Botez for her continuous guidance and support throughout the duration of the project, for her constant encouragement, for the motivation to participate at conferences and for presenting me the great opportunity of performing this research.

Thank you to the Hydra Technologies Team in Mexico for their continuous support, and especially Mr. Carlos Ruiz, Mr. Eduardo Yakin and Mr. Alvaro Gutierrez Prado.

I would like to thank the industrial and academic partners of the CRIAQ MDO 505 project, Bombardier Aerospace, Thales Canada and École Polytechnique for their support and expertise, and especially Mr. Patrick Germain and Mr. Fassi Kafyeke from Bombardier Aerospace, Mr. Philippe Molaret from Thales Canada and Mr. Eric Laurendeau from École Polytechnique.

Thanks are due to all past and present members of LARCASE who participated and contributed to the realization of this project, Fabien, Yvan, Jeremie, and especially Antoine and Tristan, for their suggestions, dedication and hard work.

A great thank you to my family in Romania, for their constant love, encouragement and support, for the understanding they showed when I decided to continue my studies eight thousand kilometers away and for always helping me follow my dreams, wherever they may take me.

To Andreea, a huge thank you for everything, without her I would not be where I am today, nor would I be the person that I am today.

VALIDATION OF MORPHING WING METHODOLOGIES ON AN UNMANNED AERIAL SYSTEM AND A WIND TUNNEL TECHNOLOGY DEMONSTRATOR

Oliviu ŞUGAR GABOR

ABSTRACT

To increase the aerodynamic efficiency of aircraft, in order to reduce the fuel consumption, a novel morphing wing concept has been developed. It consists in replacing a part of the wing upper and lower surfaces with a flexible skin whose shape can be modified using an actuation system placed inside the wing structure. Numerical studies in two and three dimensions were performed in order to determine the gains the morphing system achieves for the case of an Unmanned Aerial System and for a morphing technology demonstrator based on the wing tip of a transport aircraft.

To obtain the optimal wing skin shapes in function of the flight condition, different global optimization algorithms were implemented, such as the Genetic Algorithm and the Artificial Bee Colony Algorithm. To reduce calculation times, a hybrid method was created by coupling the population-based algorithm with a fast, gradient-based local search method. Validations were performed with commercial state-of-the-art optimization tools and demonstrated the efficiency of the proposed methods.

For accurately determining the aerodynamic characteristics of the morphing wing, two new methods were developed, a nonlinear lifting line method and a nonlinear vortex lattice method. Both use strip analysis of the span-wise wing section to account for the airfoil shape modifications induced by the flexible skin, and can provide accurate results for the wing drag coefficient. The methods do not require the generation of a complex mesh around the wing and are suitable for coupling with optimization algorithms due to the computational time several orders of magnitude smaller than traditional three-dimensional Computational Fluid Dynamics methods.

Two-dimensional and three-dimensional optimizations of the Unmanned Aerial System wing equipped with the morphing skin were performed, with the objective of improving its performances for an extended range of flight conditions. The chordwise positions of the internal actuators, the spanwise number of actuation stations as well as the displacement limits were established. The performance improvements obtained and the limitations of the morphing wing concept were studied. To verify the optimization results, high-fidelity Computational Fluid Dynamics simulations were also performed, giving very accurate indications of the obtained gains.

For the morphing model based on an aircraft wing tip, the skin shapes were optimized in order to control laminar flow on the upper surface. An automated structured mesh generation procedure was developed and implemented. To accurately capture the shape of the skin, a precision scanning procedure was done and its results were included in the numerical model.

High-fidelity simulations were performed to determine the upper surface transition region and the numerical results were validated using experimental wind tunnel data.

Keywords: morphing wing, aerodynamic optimization, non-linear lifting line, non-linear vortex lattice, computational fluid dynamics, experimental validation, unmanned aerial system

VALIDATION DES MÉTHODOLOGIES POUR LES AILES DÉFORMABLES SUR UN SYSTÈME AUTONOME DE VOL ET SUR UN DÉMONSTRATEUR TECHNOLOGIQUE PUR DES ESSAIS EN SOUFFLERIE

Oliviu ŞUGAR GABOR

RÉSUMÉ

Dans le but d'augmenter l'efficacité aérodynamique des avions, afin de réduire la consommation de carburant, un nouveau concept d'aile déformable a été développé. Le système remplace une partie des surfaces supérieures et inférieures de l'aile avec une peau flexible dont sa forme peut être modifiée en utilisant un système d'actionnement placé à l'intérieur de la structure de l'aile. Des études numériques en deux et trois dimensions ont été effectuées afin de déterminer les gains du système de déformation pour un système autonome de vol, et pour un modèle déformable basé sur le bout de l'aile d'un avion de transport.

Dans le but d'obtenir les formes optimales de la peau de l'aile en fonction des conditions de vol, différents algorithmes d'optimisation globale ont été mises en œuvre, telles que l'Algorithme Génétique et la Algorithme de la Colonie des Abeilles Artificielles. Pour réduire les temps de calcul, une méthode hybride a été créée en couplant l'algorithme basé sur la population avec une méthode de recherche locale basée sur l'évaluation du gradient. Les validations des résultats obtenus numériquement ont été effectuées avec des outils commerciaux d'optimisation et ont démontré l'efficacité des méthodes proposées.

Pour déterminer avec précision les caractéristiques aérodynamiques de l'aile déformable, deux nouvelles méthodes ont été élaborées, une méthode non-linéaire de ligne portante et une méthode non-linéaire de réseaux des tourbillons. Les deux utilisent l'analyse des sections dans l'envergure de l'aile pour tenir compte des modifications de formes aérodynamiques induites par la peau flexible, et peuvent fournir des résultats précis pour le coefficient de traînée de l'aile. Ces méthodes ne nécessitent pas la génération d'un maillage complexe autour de l'aile et sont adaptées pour leur couplage avec des algorithmes d'optimisation en raison du temps de calcul qui est beaucoup plus petit que le temps de calculs des méthodes traditionnelles de la dynamique computationnelle des fluides.

Des optimisations en deux et en trois dimensions de l'aile du système autonome de vol équipé avec la peau déformable ont été réalisées, avec l'objectif d'améliorer ses performances aérodynamiques pour une gamme large de ses conditions de vol. Les positions dans le sens de la corde des actionneurs internes, le nombre de stations d'actionnement dans le sens de l'envergure ainsi que les limites de déplacement de ces actionneurs ont été établies. Les améliorations de performances obtenues et les limites du concept de l'aile de déformable ont été étudiées. Pour vérifier les résultats de l'optimisation, de simulations de haute-fidélité en utilisant des logiciels connus en dynamique computationnelle des fluides ont également été réalisées, donnant des indications très précises sur les gains obtenus.

Pour le modèle déformable basé sur le bout de l'aile d'un avion de transport, les formes de la peau ont été optimisées afin de contrôler l'écoulement laminaire sur sa surface supérieure. Une procédure automatisée de génération de maillage structuré a été développé et mise en œuvre. Pour déterminer avec précision la forme de la peau, une procédure de scanning de précision a été faite et ses résultats ont été inclus dans le modèle numérique. Des simulations haute-fidélité ont été effectuées afin de déterminer la région de transition sur la surface supérieure et ensuite les résultats numériques ont été validés en utilisant des données expérimentales obtenues en soufflerie.

Mots clé : aile déformable, optimisation aérodynamique, ligne portante non-linéaire, réseaux des tourbillons non-linéaire, dynamique computationnelle des fluides, validation expérimentale, système autonome de vol

TABLE OF CONTENTS

Page

LIST OF TABLES

Page

LIST OF FIGURES

Page

LIST OF ABREVIATIONS

ABC	Artificial Bee Colony optimization algorithm
ALM	Augmented Lagrangian Method
ATAG	Air Transport Action Group
BFGS	Broyden-Fletcher-Goldfarb-Shanno optimization algorithm
CFD	Computational Fluid Dynamics
CIRA	Italian Aerospace Research Center (Centro Italiano Ricerche Aerospaziali)
CNRC	Canada National Research Council
DLM	Doublet Lattice Method
DLR	German Aerospace Research Center (Deutsches Zentrum fur Luft und Raumfahrt)
EADS	European Aeronautic Defence and Space Company
ETS	École de Technologie Supérieure
GA	Genetic Algorithm
IAR-CNRC	Institute for Aerospace Research – Canadian National Research Center
ICAO	International Civil Aviation Organization
LARCASE	Laboratory of Applied Research in Active Control, Avionics and Aeroservoelasticity
LLM	Lifting Line Method
MAC	Mean Aerodynamic Chord
MDO	Multi-Disciplinary Optimization
NACA	National Advisory Committee for Aeronautics
NASA	National Aeronautics and Space Administration
NURBS	Non-uniform Rational B-Splines

SMA	Shape Memory Alloy
SST	Shear Stress Transport
UAS	Unmanned Aerial System
UAV	Unmanned Aerial Vehicle
VLM	Vortex Lattice Method

LIST OF SYMBOLS AND UNITS OF MEASUREMENTS

a_{ij}	Aerodynamic influence coefficients for the VLM
A_i	Surface of a wing panel/strip
b	Wing span
b_i	Elements of the linear system right hand side for the VLM
B	Wing half-span
$\mathbf{B}$	Approximate Hessian matrix
c_i	Chord of a wing strip
$\mathbf{c}_i$	Unit vector in the direction of the local chord for a wing strip
C	Airfoil chord
C_{d_i}	Drag coefficient of a wing strip airfoil
C_{l_i}	Lift coefficient of a wing strip airfoil
C_D	Wing drag coefficient
C_{D_0}	Wing profile drag coefficient
C_{D_I}	Wing induced drag coefficient
C_F	Skin friction coefficient
C_L	Wing lift coefficient
C_{L_α}	Derivative of lift coefficient with the angle of attack
C_m	Wing pitching moment coefficient
C_{m_α}	Derivative of pitching moment coefficient with the angle of attack
ΔCP	Pressure coefficient variation between wing upper and lower surfaces
C_P	Pressure coefficient

$\mathbf{C}(u)$	Point on a NURBS curve
D	Wing drag
f	Objective function to be minimized
$\mathbf{dF}_i$	Force vector acting on the bound segment of a horseshoe vortex
$\mathbf{F}$	Aerodynamic force generated by the wing
$\mathbf{F}_i$	Aerodynamic force acting on a panel/strip of the wing surface
g_i	Equality constraints
h	Static enthalpy
h_i	Inequality constraints
H	Total enthalpy
$\bar{I}$	Unit tensor
$\mathbf{J}$	Jacobian matrix
k	Turbulent kinetic energy
K	Number of NURBS control points
l	Length of the flexible skin
$\mathbf{dl}_i$	Vector along the bound segment of a horseshoe vortex
L	Wing lift
M	Mach number
$\mathbf{dM}_i$	Quarter chord moment of a wing strip
$\mathbf{M}$	Aerodynamic moment about the root chord quarter chord point generated by the wing
n	Order of the NURBS curve
$\mathbf{n}_i$	Unit vector normal to the wing surface for a wing panel/strip

N	Number of horseshoe/ring vortices and panels on the wing surface
N_X	Chordwise number of panel on the wing surface
N_Y	Spanwise number of panel on the wing surface
$N_{i,n}$	NURBS curve basis functions
p	Static pressure
p_0	Reference pressure
$\mathbf{p}_k$	BFGS method search direction
Pr_t	Turbulent Prandtl number
$\mathbf{P}_i$	Control point of a NURBS curve
Q_∞	Freestream dynamic pressure
$\mathbf{r}_0$	Vector along a vortex segment
$\mathbf{r}_1$	Vector from the beginning of a vortex segment to an arbitrary point in space
$\mathbf{r}_2$	Vector from the end of a vortex segment to an arbitrary point in space
$\mathbf{r}_i$	Position vector of wing strip quarter chord and panel collocation point with reference to root chord quarter chord point
$\mathbf{R}$	Nonlinear system of equations
Re	Reynolds number
$Re_{\theta c}$	Critical Reynolds number
$Re_{\theta t}$	Momentum thickness transition Reynolds number
S	Wing area
t_i	NURBS curve knot
T	Air temperature
u	NURBS curve parameter

U_i	Component of the fluid velocity field
$\mathbf{v}_\infty$	Unit vector in the direction of the freestream flow
$\mathbf{v}_{ij}$	Velocity induced by horseshoe/ring vortex j, considered to be of unit intensity, at the control point of horseshoe/ring vortex i
V_i^T	Modulus of surface transpiration velocity
$\mathbf{V}$	Velocity vector
$\mathbf{V}_\infty$	Freestream velocity vector
$\mathbf{V}_i$	Local velocity at the bound segment of a horseshoe vortex and at the collocation point of a ring vortex
$\mathbf{V}_i^T$	Surface transpiration velocity vector
w_i	NURBS curve weight
$\mathbf{x}$	Optimization problem solution
X	Chordwise coordinate
X_{TR}	Upper surface transition point location
$\mathbf{X}$	Solution vector for the nonlinear system of equations
Δy_i	Span of a wing strip
$\mathbf{y}_k$	Difference between two successive estimations of the gradient
Y	Spanwise coordinate
α_g	Geometric angle of attack of the wing
α_i	Local angle of attack for a wing strip
α_k	BFGS method advancement step
β	Penalty coefficient control parameter
γ	Intermittency

γ_{ij}	Geometric vector along the ij edge of a vortex ring
Γ	Vortex intensity
$\Delta\Gamma$	Vortex intensity correction
δ	Displacement of a NURBS control point
δ_{ij}	Kronecker delta function
δ_{max}	Upper limit for NURBS control point movement
δ_{min}	Lower limit for NURBS control point movement
λ	Thermal conductivity
λ_i	Lagrangian multipliers
μ	Air dynamic viscosity
μ_{eff}	Effective viscosity
μ_t	Turbulent viscosity
ρ	Air density
$\bar{\tau}$	Fluid stress tensor
φ	Perturbation potential
Φ	Modified objective function
Φ_∞	Freestream potential
ω	Specific dissipation rate
Ω	Under-relaxation factor

INTRODUCTION

The air transportation industry is one of the key areas that contribute to the economic development around the world. Although only 0.5 % of the total volume of international trading is done by air, this small volume accounts for almost 35% of the total trade value (ATAG, 2014), aircrafts being used especially for high value, time sensitive merchandise. Since the beginning of civil aviation, there has also been a steady increase in the number of people using airplanes as a fast and safe transportation method, airlines carrying almost 3 billion passengers in 2014 alone. This high level of development that has been achieved by the industry has also transformed it into a major source of pollution. It is estimated that in 2014, over 2% of the worldwide carbon dioxide emissions were caused by the commercial airline companies (ATAG, 2014).

The high growth rate of aviation traffic experienced up to present day will accelerate over the next decades. The International Civil Aviation Organization (ICAO) estimates that the number of flights will triple by the year 2050 (ICAO, 2010). This high growth rate, together with growing global concern for the preservation of the environment and the reduction of greenhouse gas emissions obliges the aerospace industry to search for solutions to improve the efficiency of aircraft. According to the 2014 United Nation Climate Summit, in order to promote sustainable development and to minimize the impact on future climate changes, the aviation industry should improve its fuel efficiency by 1.5% per year, and by 2050 achieve net carbon dioxide emission that will be half of what they were in 2005, despite the predicted increase in the number of flights (ATAG, 2014). Figure 0.1 presents the estimated net emission of carbon dioxide of the air transport industry up to 2050, depending on the number of solutions adopted in order to provide the required efficiency increase.

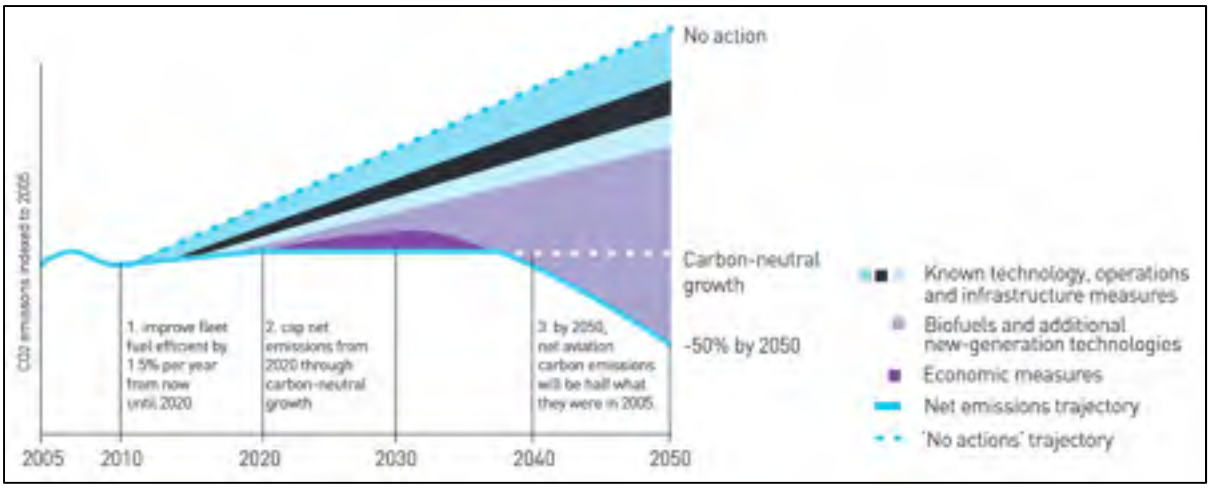

Figure 0.1 Estimation of carbon dioxide emission for the aviation sector, in function of the number of actions taken to increase efficiency.
Taken from ATAG (2014)

One possibility of achieving this desired efficiency is the new-generation technology of wing morphing, the active and controlled modification of one or several wing characteristics during flight. Today's aircraft are designed during a multi-point optimization process, meaning that they perform well over a range of different flight conditions, but the performance is sub-optimal for each flight condition. In theory, a morphing wing could allow the aircraft to fly at optimal lift to drag ratios for each condition encountered during a flight, by changing its wing's characteristics and controlling them according to the flow conditions. The approach represents, in essence, a single-point optimization of the wing geometry, performed for each different flight condition, thus eliminating the compromises associated with today's multi-point optimization approach.

In Figure 0.2, a performance plot is presented for the BMQ-34 Firebee unmanned target drone, for different flight conditions (take-off, climbing, cruise, loitering and manoeuvring), at various altitudes (sea level, 30,000 feet and 60,000 feet). The performance plot, created through the research of Joshi et al. (2004), shows the performance of the drone for the chosen conditions, as well as the theoretical performance that could be achieved by equipping the drone with a morphing wing capable of airfoil changes and a morphing wing capable of

geometry changes. It can be seen that the use of the morphing wing can substantially increase the flight performance of the unmanned drone, for nearly all of the analysed cases.

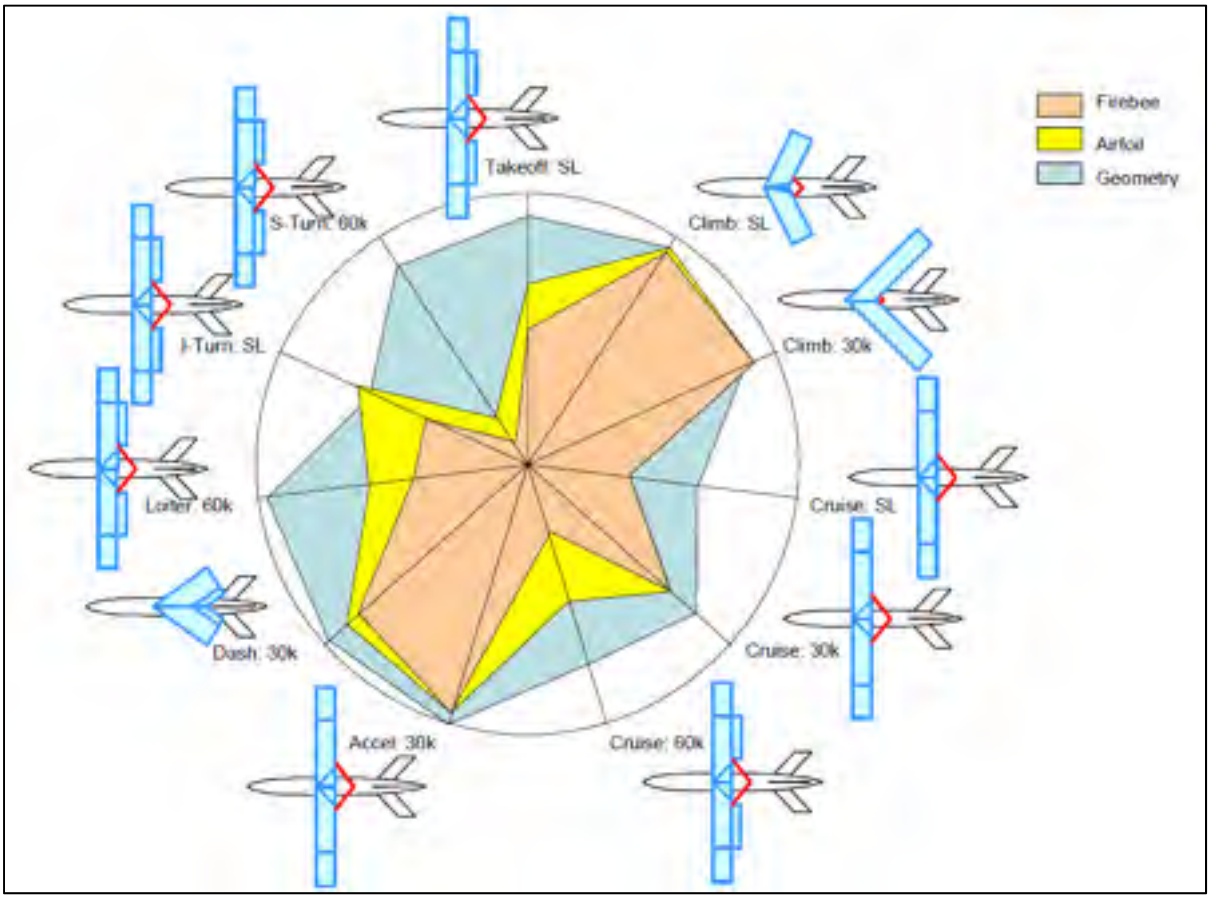

Figure 0.2 Performance increase achieved for various flight conditions by using a morphing wing technology.
Taken from Joshi et al. (2004)

Researchers have proposed different technological solutions for obtaining the desired wing adaptability, and some concepts achieved important theoretical performance improvements compared to the baseline design. However, the technology being only in its first phases of development, its technological readiness level is still very low, and only a few concepts have been sufficiently progressed to reach wind tunnel testing, and even fewer have actually been flight tested (Barbarino et al., 2011).

Morphing architectures are a promising solution for the development of the next generation of green aircraft, and many large industry companies are investigating the benefits of this technological approach. However, there is still a lack of sufficient applied research projects that clearly present the possible advantages, due to the high costs involved in developing functional wind tunnel or flight-worthy morphing models. Under these conditions, Unmanned Aerial Vehicles (UAVs) have become the system of choice for the investigation of morphing aircraft solutions, due to much lower costs needed for the development, implementation, and finally flight testing of the morphing system.

0.1 Problem Statement

With the increasing role of Unmanned Aerial Vehicles in surveillance and combat operations, an increase in their operational range, agility and versatility is necessary. A morphing wing system could prove a viable technological solution that would allow the UAV to achieve the desired efficiency. The reasons for developing shape morphing UAVs can be summarized with the following three objectives in mind (Barbarino, 2009):

- adaptability, by making the aircraft more versatile and thus suitable for a wider range of flight conditions;
- multi-objective, by trying to accommodate one aircraft to diverse, even contradictory mission scenarios, and performing all of them as efficiently as possible;
- efficiency, leading to improved, intelligent structures, capable of better efficiency in terms of energy consumption.

Civil aviation could also greatly benefit from the performance gains that a morphing wing system could provide. The ability to increase the extent of laminar flow over the wing surface for all flight conditions that occur during a typical flight, as well as the reduction of the upper surface shock wave intensity during cruise flight could lead to significant reductions in drag, and thus in fuel consumption. The morphing wing approach could eliminate some of the compromises associated with today's aircraft design procedures, allowing the industry to increase the efficiency of their products.

The research presented in this thesis was performed as part of two projects: the Hydra Technologies S4 Éhecatl Unmanned Aerial System (UAS) morphing wing, and the CRIAQ MDO 505 morphing wing, designed based on the wing tip of a typical passenger aircraft.

0.1.1 Hydra Technologies S4 Éhecatl morphing wing

The UAS-S4 Éhecatl was obtained by Prof. Ruxandra Botez from Canada Foundation for Innovation (CFI) and Ministère du Développement Économique, Innovation et Exportation (MDEIE), and was designed and build in Mexico by Hydra Technologies. It was created as an unmanned aerial surveillance system, directed towards providing security and surveillance capabilities for the Armed Forces, as well as civilian protection in hazardous situations. The existence of this aircraft at ÉTS will make possible the design, construction and implementation of the morphing wing system, and thus will provide experimental flight test data in addition to the numerical research presented in this thesis. General information about the characteristics and flight performance of the UAS-S4 Éhecatl is presented in Table 0.1, while the aircraft is shown in Figure 0.3.

Table 0.1 General information about the UAS-S4 Éhecatl

Characteristic	Value
Empty Weight	50 kg
Maximum Take-off Weight	80 kg
Wingspan	4.2 m
Mean Aerodynamic Chord	0.57 m
Wing Area	2.3 m^2
Total Length	2.5 m
Operational Ceiling	15,000 ft
Maximum Airspeed	135 knots
Loitering Airspeed	35 knots
Operational Range	120 km

Figure 0.3 Hydra Technologies UAS-S4 Éhecatl

In order to provide the desired increase in aerodynamic efficiency, the conventional rigid wing of the UAS-S4 is replaced with a morphing wing equipped with a flexible upper surface and leading edge, capable of actively changing the wing's airfoil, depending on the flight condition. In order to implement the wing morphing technique on the UAS, only a limited portion of wing surface can be allowed to change, and the shape modifications introduced must be small enough in order for the concept to remain feasible from a structural point of view.

0.1.2 CRIAQ MDO 505 morphing wing

The CRIAQ MDO 505 Morphing Wing project is an international collaboration between Canadian and Italian industries (Bombardier Aerospace, Thales Canada and Alenia Aeronautica), universities (École de Téchnologie Supérieure, École Polytechnique and University of Naples) and research centers (Canada National Research Council and Italian Aerospace Research Center). The research in this project is focused on demonstrating the structural, aerodynamic and control abilities of a morphing technology demonstrator model,

designed after an aircraft wing tip, equipped with an adaptive upper surface and both rigid and adaptive ailerons during low speed wind tunnel tests.

The full-scale model is an optimized, flexible structure with a 1.5 m span and a 1.5 m root chord and has a taper ratio of 0.72 and a leading edge sweep angle of 8 deg. The wing box and internal structure are manufactured from aluminum, with the composite adaptive upper surface extending from 20% to 65% of the wing chord. The adaptive upper surface was specifically designed and optimised for this project from carbon composite materials. The actuators were also specifically designed and manufactured to the project requirements. Four electric actuators are installed on two actuation lines, fixed to the center ribs and to the composite skin. Each actuator is capable of independent action. On each line the actuators are situated at 32% and 48% of the chord. The aileron (conventional and adaptive) articulation is situated at 72% of the chord. Figure 0.4 presents the concept of the morphing wing and a cross-section view of the model.

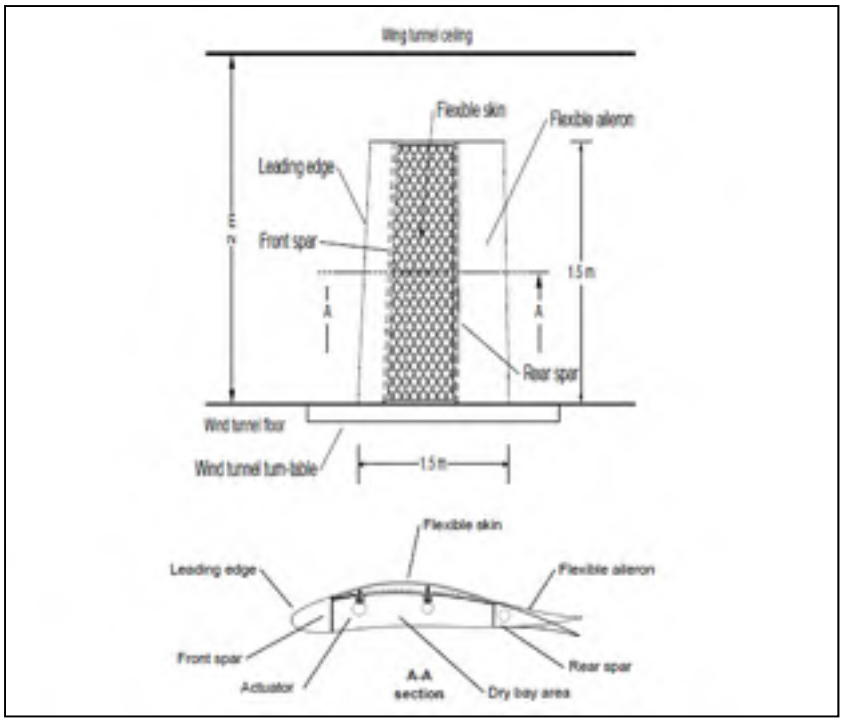

Figure 0.4 CRIAQ MDO 505 Morphing Wing Concept

0.2 Research Objectives

The global objective of the research is to provide an accurate calculation of the performance improvements that could be obtained for both the UAS-S4 and MDO 505 wings by using the flexible skin morphing wing technology, and to determine the wing surface shape changes required to obtain the desired improvements. For the UAS-S4, the analysis is performed for a number of different airspeeds and for a wide range of angles of attack, in order to cover a significant part of the aircraft's flight envelope. For the MDO 505 wing, a number of wind tunnel test cases were established in agreement with all project partners and the analysis is performed for these cases.

To ensure a good progress of the research and to successfully achieve the proposed global objective, the following sub-objectives were established:

1) Conception of geometry parameterization techniques and new optimization algorithms

- The implementation of a Non-Uniform Rational B-Splines (NURBS) methodology for the parameterization of the UAS airfoil and for generating smooth and continuous shapes for the morphed airfoil;
- Further development of the NURBS parameterization methodology in order to allow only a local airfoil shape modification, between some desired chordwise limits;
- The implementation of different constrained global optimization algorithms, such as Genetic Algorithm and Artificial Bee Colony algorithm;
- Further development of the constrained global optimization algorithm in order to accelerate their convergence properties, by performing a hybridisation with a modified version of the gradient-based Broyden-Fletcher-Goldfarb-Shanno optimization algorithm.

2) Application of these methodologies and algorithms for the performance improvement of the UAS-S4 morphing airfoil

- Performing two-dimensional optimizations of the UAS-S4 airfoil with the objective of reducing the airfoil drag coefficient and increasing the region of laminar flow, for a wide range of angles of attack below stall;
- Performing two-dimensional optimizations of the UAS-S4 airfoil with the objective of increasing the maximum lift coefficient and delaying boundary layer separation for angles of attack at stall and immediately after stall.

3) Conception of new aerodynamic methods and solvers

- The development and implementation of a non-linear lifting line method capable of providing an accurate estimation of the UAS-S4 wing aerodynamic coefficients, including a calculation of the viscous drag component;
- The development and implementation of a quasi-three-dimensional non-linear vortex lattice method, capable of providing accurate viscous calculations of the aerodynamic coefficients for wing of various geometric shapes.

4) Application of the new solvers and algorithms for the performance improvement of the UAS-S4 morphing wing

- Further development of the NURBS parameterization methodology in order to allow the reconstruction of the entire three-dimensional morphed wing surface, by performing cubic splines interpolations in the span direction;
- Performing three-dimensional optimizations of the UAS-S4 wing with the objective of increasing the lift-to-drag ratio for a wide range of angles of attack below stall, and analysing the impact of different configurations of the morphing wing approach on the performance gains;
- Performing three-dimensional viscous redesign and optimization of the UAS-S4 morphing wing, with the objective of increasing the lift-to-drag ration, but also an optimization of the low aspect ratio MDO 505 morphing wing, with the goal of reducing the profile drag coefficient.

5) Application of high-fidelity solvers for the performance improvement of the MDO 505 morphing wing and results validation with experimental data

- The adaptation of the three-dimensional surface reconstruction algorithms for generating the MDO 505 morphing skin shapes in function of the actuator displacements;
- The development of an automated procedure for the generation of high-quality structured meshes around the MDO 505 wing, capable of working with the entire range of flexible skin actuators' displacements and aileron deflection angles;
- Performing three-dimensional analysis of the MDO 505 morphing wing with the objective of accurately determining the laminar-to-turbulent transition region and increasing the region of laminar flow;
- Validation of the numerical results using experimental data obtained in the CNRC subsonic wind tunnel during the MDO 505 project testing phase.

0.3 Research Methodology and Models

In order to perform the numerical analysis of a morphing wing system, several different algorithms and codes, both originally developed and commercially available, were coupled and used:

- the NURBS and cubic splines interpolations for generating the morphed airfoil and wing geometries;
- the Genetic and the hybrid Artificial Bee Colony - Broyden-Fletcher-Goldfarb-Shanno algorithms for determining the optimum wing shapes in function of the flight conditions;
- the XFOIL solver for performing the two-dimensional aerodynamic calculations;
- the novel non-linear lifting line method and the original non-linear vortex lattice method for performing the fast three-dimensional aerodynamic calculations and optimizations;
- the ICEM-CFD code for generating the high-quality meshes around the morphing wings;
- the FLUENT solver for performing high-fidelity three-dimensional aerodynamic calculations.

Each one of these models will be briefly presented and explained. All the algorithms developed during the research were programmed using FORTRAN and C, saved and compiled as self-contained 32-bit applications, without requiring any additional libraries. They can be run on any computer using the Windows XP, Vista, Seven, Eight or Ten operating systems, both 32-bit and 64-bit versions. The desired configuration and setup is performed using input files of simple formatting (TXT or DAT files, modifiable by any text editor), and the output is presented in the same way, and can be further post-processed.

0.3.1 Non-Uniform Rational B-Splines

From a numerical point of view, the airfoil was parameterized using Non-Uniform Rational B-Splines (NURBS) (Piegl and Tiller, 1997). The NURBS are a generalization of B-Splines and Bézier curves, offering high flexibility and precision in representing and manipulating analytical curves. From a mathematical point of view, its order, a polygon of weighted control points, and a knot vector define a NURBS curve:

$$\mathbf{C}(u) = \sum_{i=1}^{k} \frac{N_{i,n} w_i}{\sum_{j=1}^{k} N_{j,n} w_j} \mathbf{P}_i \tag{0.1}$$

In the above Equation (0.1), u is the curve parameter, ranging from 0 (the start of the curve) to 1 (the end of the curve), n is the number of control points, $N_{i,n}$ is the i^{th} basis function, of order n, w_i is the weight associated with the i^{th} control point, and $\mathbf{P}_i = [x_i, y_i]$ is the control point. The basis functions are determined using the De Boor recursive formula (De Boor, 1978):

$$\begin{aligned} N_{i,1} &= \begin{cases} 1 \text{ , if } t_i \le u \le t_{i+1} \\ 0 \text{ , otherwise} \end{cases} \\ N_{i,n} &= \frac{u - t_i}{t_{i+n} - t_i} N_{i,n-1} + \frac{t_{i+n+1} - u}{t_{i+n+1} - t_{i+1}} N_{i+1,n-1} \end{aligned} \tag{0.2}$$

where u is again the curve parameter, n is the order of the basis function, while t_i represents the i^{th} knot of the curve knot vector.

When an airfoil curve is given as input, the positions of the control points and the distribution of knots along the curve length are determined through an iterative least-squares curve fitting process (Piegl and Tiller, 1997). As an example, the NACA 4409 airfoil is presented in Figure 0.5, together with the NURBS control polygon associated with it, as resulted from the curve fitting procedure. The vertical coordinate was significantly expanded in order to provide better visualization.

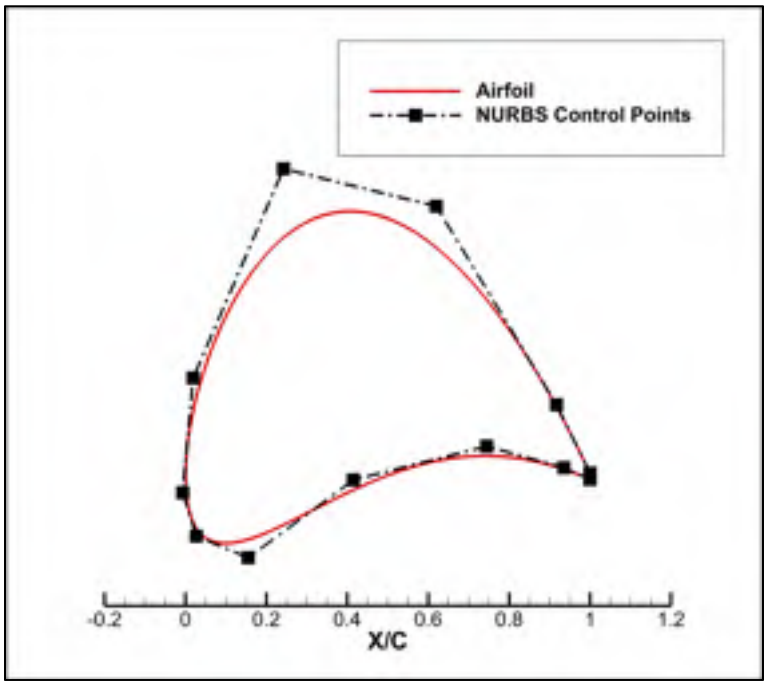

Figure 0.5 Example airfoil and the associated NURBS control points

For the parameterization of the airfoil curves, a 3rd degree NURBS curve has been used, which grants smoothness up to the second derivative. The number of control points associated with a given airfoil depends on the tolerance imposed during the curve fitting process. In general, a number of 12 to 15 NURBS control points is enough to accurately construct an approximation of an airfoil. If more NURBS control points are desired, to

provide better control of the local shape during the airfoil optimization process, the extra control points can be added on the initial control polygon, between the initial points, without affecting the quality of the obtained initial fitting.

To allow the realization of a local modification of the airfoil shape, between some desired points along the airfoil curve length, extra knots were inserted in the NURBS knot vector, in order to clearly mark the limits of the region that changes during the optimization. The control points that correspond to this marked region were then redistributed using a second least-squares curve fitting process, thus providing the desired accuracy, number and distribution of control points needed to control the airfoil local shape change. During the numerical optimization procedure, the morphing of the airfoil curve shape was achieved by changing the coordinates of the NURBS control points.

0.3.2 Cubic splines

The NURBS method is used to parameterize and morph the shape of the airfoil, for the two-dimensional optimization process, and the wing morphing control airfoil sections, placed at several positions along the span, for the three-dimensional optimization process. These airfoil sections correspond to the span-wise positions of the mechanical actuation system lines used to generate the wing surface shape change, and thus only a small number (between 2 and 5) of such wing sections are present on each semi-span. In order to accurately reconstruct the morphed wing surface, this small number of the actuation system sections is not sufficient and more wing airfoil sections must be generated. To achieve this, cubic splines are used to perform interpolations between any two consecutive actuation system sections, and thus generate the required number of wing sections.

Figure 0.6 presents an example of wing geometry created with several airfoil sections along the span direction. Out of these sections, 4 were parameterized using NURBS and then modified (thus simulating the actuation of the wing morphing system), while the other sections were reconstructed with cubic splines interpolations, based on the four main control

sections. Using this procedure, there are enough wing sections along the span to accurately generate the complete morphing wing geometry.

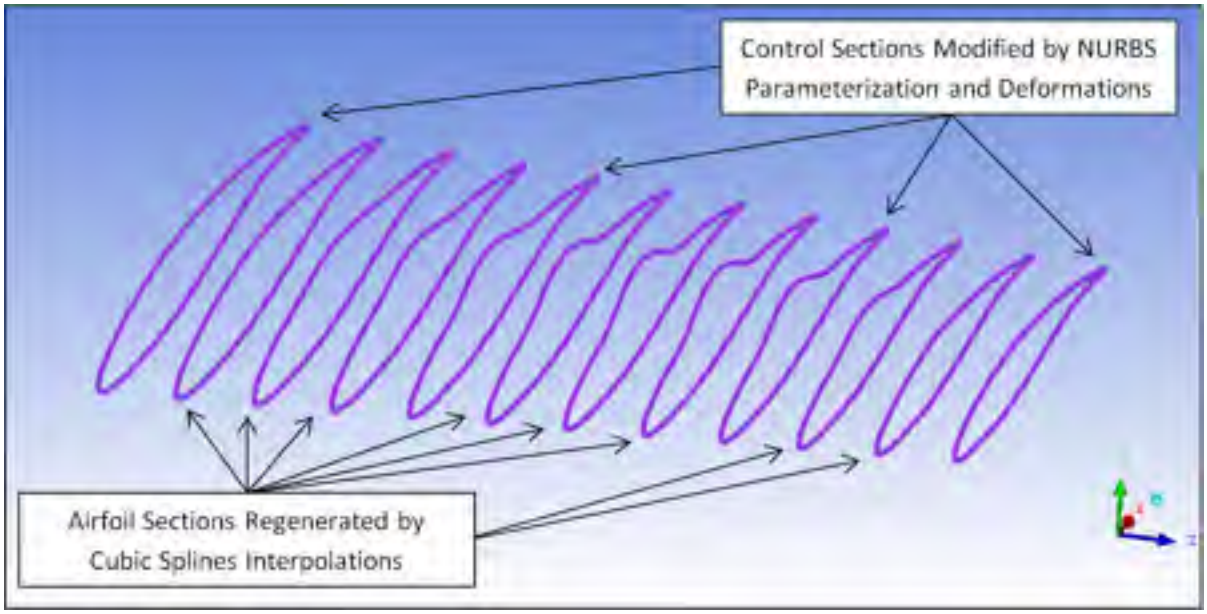

Figure 0.6 Example wing geometry created with several airfoil sections along the span direction

Cubic splines were chosen for the interpolation because of their similarity with the theoretical behaviour of a beam that is bending under uniform loading, and because of their ability to provide very good tangency conditions between two consecutive spline curves, by ensuring smoothness up to the second derivative (Berbente, 1998).

0.3.3 The Genetic Algorithm optimizer

Genetic algorithms are numerical optimization algorithms inspired by natural selection and genetics of living organisms. The algorithms are initialized with a population of guessed individuals, and use three operators namely selection, crossover and mutation to direct the population towards its convergence to the global optimum, over a series of generations (Coley, 1999).

In order to evaluate all individuals in the population, an objective function, called the fitness function, must be defined. This fitness function is calculated for all individuals of a given generation. The higher the values of the fitness function, the higher are the chances of the individual to be selected for the creation of the next generation.

The general outline of the method and all the steps of the genetic algorithm are presented in Figure 0.7. The process of evaluation of the fitness function, selection of the best individuals to become parents, crossover and mutation of the new individuals continues in an iterative way, until the maximum number of generations is reached. Tournament selection, simulated binary crossover (Herrera, 1998) and polynomial mutation (Herrera, 1998) were used. The termination criterion used was the achievement of the maximum number of generations.

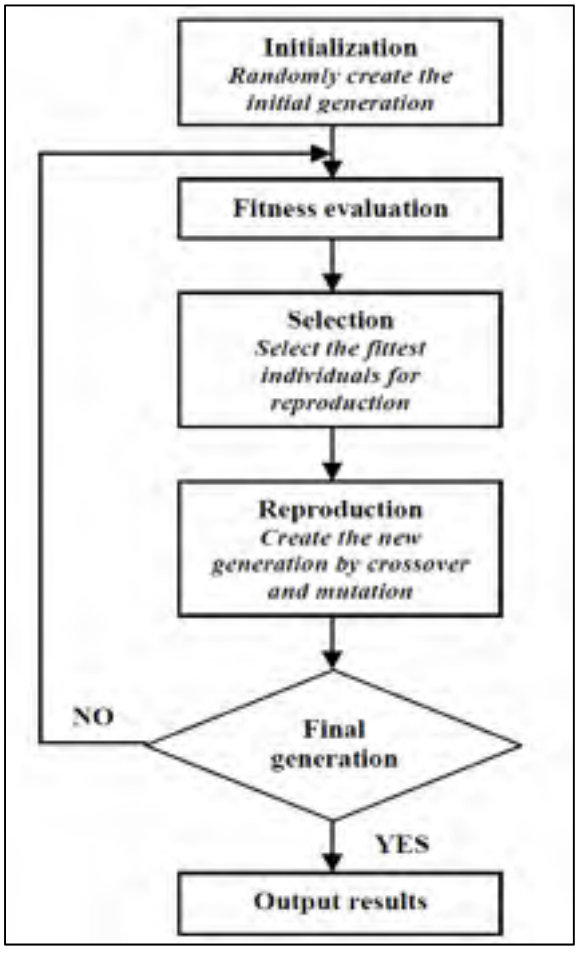

Figure 0.7 Outline of the genetic algorithm

0.3.4 Artificial Bee Colony optimizer

The ABC algorithm is an optimization algorithm based on the intelligent behaviour of a honeybee swarm. Karaboga and Basturk conceived the original algorithm in 2007 (Karaboga and Basturk, 2007), that was applicable only to the unconstrained optimization of linear and nonlinear problems. Other authors have proposed methods for enhancing the algorithm's capabilities, such as the handling of constrained optimization problems (Karaboga and Basturk, 2007) or the significant improvement of its convergence properties (Zhu and Kwong, 2010). Because of the fact that the ABC algorithm simultaneously performs a global search throughout the entire definition domain of the objective function and a local search around the more promising solutions already found, it can efficiently avoid converging towards a local minimum point of the objective function, and thus is able to approximate the global optimum point.

It was discovered that for some problems, after the region of the global optimum was found, the ABC algorithm's rate of convergence significantly decreased. To improve convergence, the ABC method's search routine was substituted by the Broyden-Fletcher-Goldfarb-Shanno (BFGS) algorithm (Bonnans et al., 2006), a type of quasi-Newton iterative method used for nonlinear optimization problems. Since the BFGS method can only be applied to unconstrained optimization, it was coupled with the Augmented Lagrangian Method (ALM) (Powell, 1967) in order to introduce the desired optimization constraints. The use of the ALM-BFGS approach allows obtaining a significantly faster determination of the global optimum position, thus accelerating the convergence rate of the final steps of the optimization procedure. The details of the hybrid ABC and BFGS algorithms, the coupling between them, as well as the general configuration of the morphing wing optimization procedure are presented in Figure 0.8.

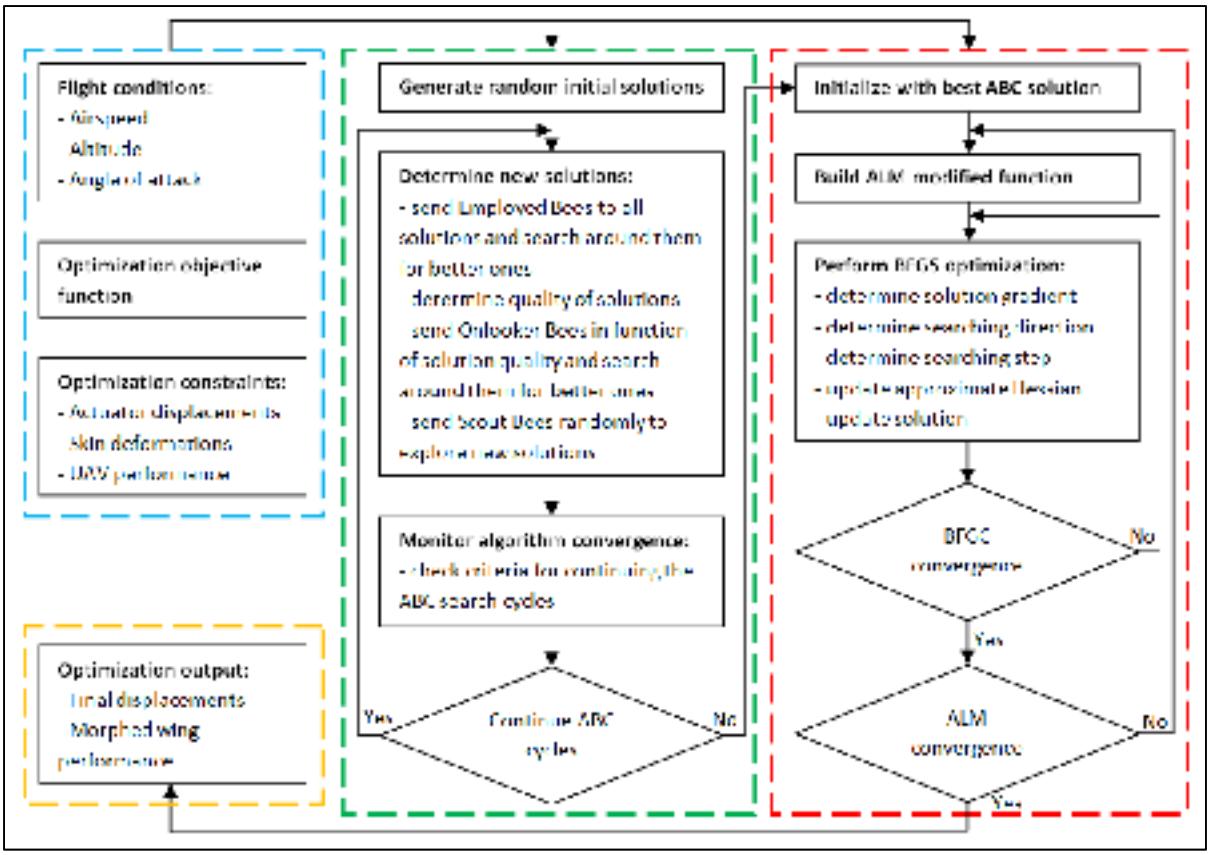

Figure 0.8 Artificial Bee Colony algorithm coupled with the ALM-BFGS algorithm

0.3.5 Two-dimensional flow solver

The code that was used for the calculation of the two-dimensional aerodynamic characteristics of the airfoil is XFOIL, version 6.96, developed by Drela and Youngren (2001). The XFOIL code was chosen because it has proven its precision and effectiveness over time, and because it reaches a converged solution very fast (the order of a few seconds). The inviscid calculations in XFOIL are performed using a linear vorticity stream function panel method (Drela, 1989). A Karman-Tsien compressibility correction is included, allowing good predictions for subsonic, incompressible and compressible flows. For the viscous calculations, XFOIL uses a two-equation lagged dissipation integral boundary layer formulation (Drela, 1989), and incorporates the e^N transition criterion (Drela, 2003). The flow in the boundary layer and in the wake interacts with the inviscid potential flow by use of

the surface transpiration model. The nonlinear system of equations formed by the inviscid flow equations and the boundary layer model equations is solved using Newton's method.

The e^N transition criterion models the growth of Tollmien-Schlichting (TS) waves in the laminar boundary layer, and it permits tracking the true critical frequency by using the amplification rates of the TS waves that are obtained from solutions of the Orr-Sommerfeld equation. Laminar-to-turbulent transition onset depends on the turbulence intensity level of the incoming airflow. In the e^N method, this dependence is accounted for by adjusting the critical amplification factor N to values that are representative for the analysed flow conditions. For the research presented here, N values of 9 and 10 were used, corresponding to calm atmospheric conditions. Because the morphing skin concept is effective at delaying laminar-to-turbulent transition, its performance is directly influenced by the turbulence intensity level of the airflow. A morphed geometry that outperforms the baseline design at a given flight condition (expressed in terms of airspeed, angle of attack, Reynolds number and turbulence intensity) may decrease (or increase) its efficiency for other critical amplification factor values. A detailed sensitivity analysis of the performance improvements obtained with the morphing skin concept, as function of various turbulence intensity levels must be performed. The study will provide a better understanding of the morphing skin behaviour in airflow conditions other than the calm, standard atmosphere model.

0.3.6 Nonlinear lifting line method

Prandtl's classical lifting line theory, first published in 1918, represented the first analytical model capable of accurately predicting the lift and induced drag of a finite span lifting surface. The aerodynamic characteristics predicted by the theory were repeatedly proven to be in close agreement with experimental results, for straight wings with moderate to high aspect ratio. The theory was based on the hypothesis that a finite span wing could be replaced by a continuous distribution of vorticity bound to the wing surface, and a continuous distribution of shed vorticity that trails behind the wing, in straight lines in the direction of the free stream velocity. The intensity of these trailing vortices is proportional to rate of

change of the lift distribution along the wing span direction. The trailing vortices induce a velocity, known as downwash, normal to the direction of the free stream velocity, at every point along the span. Because of the downwash, the effective angle of attack at each section in the spanwise direction is different from the geometric angle of attack of the wing, the difference being called the induced angle of attack. Using the effective angle of attack, the downwash produced by the trailing vortices and the two-dimensional Kutta-Joukowski vortex lifting law, Prandtl developed an integral equation that allowed the calculation of the continuous bound vorticity intensity, and thus the calculation of the wing's lift and induced drag.

The nonlinear method uses a general horseshoe vortex distribution and a fully three-dimensional vortex lifting law (Sugar Gabor, 2013). Because of these characteristics, the method has a wider applicability range compared to the original theory, as it can analyse multiple lifting surfaces placed in the same flow field and the wings that have arbitrary camber, sweep angle and dihedral angle. Also, the method is not based on the assumption of a linear relationship between the lift coefficient and the local angle of attack, thus it can be applied for high geometric angles of attack, to take into consideration the effects of stall. The constraint of medium to high aspect ratio lifting surface that applies to Prandtl's original theory also applies to the nonlinear method.

Using the three-dimensional vortex lifting law, the force acting on any of the horseshoe vortices placed on the wing surface can be written as follows:

$$\mathbf{dF}_i = \rho \Gamma_i \mathbf{V}_i \times \mathbf{dl}_i \tag{0.3}$$

In the above equation, ρ is the air density, Γ_i is the unknown intensity of the horseshoe vortex, $\mathbf{V}_i$ is the local airflow velocity and $\mathbf{dl}_i$ is a spatial vector along the bound segment of the horseshoe vortex, aligned in the direction of the local circulation. The local airfoil velocity is equal to:

$$\mathbf{V}_i = \mathbf{V}_\infty + \sum_{j=1}^{N} \Gamma_j \mathbf{v}_{ij} \tag{0.4}$$

where $\mathbf{V}_\infty$ is the free stream velocity, while $\mathbf{v}_{ij}$ represents the velocity induced by the horseshoe vortex j, considered to be of strength equal to unity, at the control point of horseshoe vortex i.

From the wing strip theory, the magnitude of the aerodynamic force acting on a section of the wing located at a given span location on the wing can be written as:

$$\|\mathbf{F}\|_i = \frac{1}{2} \rho V_\infty^2 A_i C_{l_i} \tag{0.5}$$

The lift coefficient C_{l_i} is the coefficient of the local airfoil situated at the wing span section corresponding to control point i and depends on the local effective angle of attack, while A_i is the area of the considered strip.

If the strip lift coefficient can be determined using other means, such as experimentally determined lift curves or using a two-dimensional airfoil calculation solver, then, by replacing the local velocity given by Equation (0.4) into Equation (0.3), and then equating the modulus of the three-dimensional vortex lifting force presented in Equation (0.3) with the expression given in Equation (0.5), the following nonlinear equation is obtained:

$$\left\| \rho \Gamma_i \left(\mathbf{V}_\infty + \sum_{j=1}^{N} \Gamma_j \mathbf{v}_{ij} \right) \times \mathbf{dl}_i \right\| = \frac{1}{2} \rho V_\infty^2 A_i C_{l_i} \tag{0.6}$$

Writing Equation (0.6) for all the horseshoe vortices on the wing surface, a nonlinear system is obtained that can be solved using Newton's method in order to obtain the unknown vortex intensities. The method presented can be used to calculate the profile drag coefficient of the

wing, in addition to the induced drag coefficient, because the vorticity distribution was determined using the viscous aerodynamic properties of the wing strips airfoils.

The method convergence is very fast, achieving total residual values of 10^{-3} within two or three nonlinear iterations. Good quality results for viscous flows can be obtained with only a small computational effort. In Figures 0.9 and 0.10, a comparison is presented between the numerical and experimental results for a wing constructed from NACA 44-series airfoils. The wing has a span of 4.5 m, a mean aerodynamic chord of 0.42 m, an aspect ratio of 12, a taper ratio of 0.285, a leading edge sweep angle of 3 degrees and a linear twisting of -3 degrees (measured at the wing tip). The experimental results were presented in NACA Technical Note 1270 (Neely et al., 1947) and were obtained at an airspeed of 65 m/s and a Reynolds number of 4.0E+06, as calculated with the mean aerodynamic chord.

It must be noted that the two dimensional strip airfoil analyses were performed with the XFOIL solver, instead of using airfoil performance databases, and this 2D solver significantly overestimates the maximum lift coefficient value for the NACA 44-series airfoils, thus affecting the quality of the lifting line solution for the high angles of attack region.

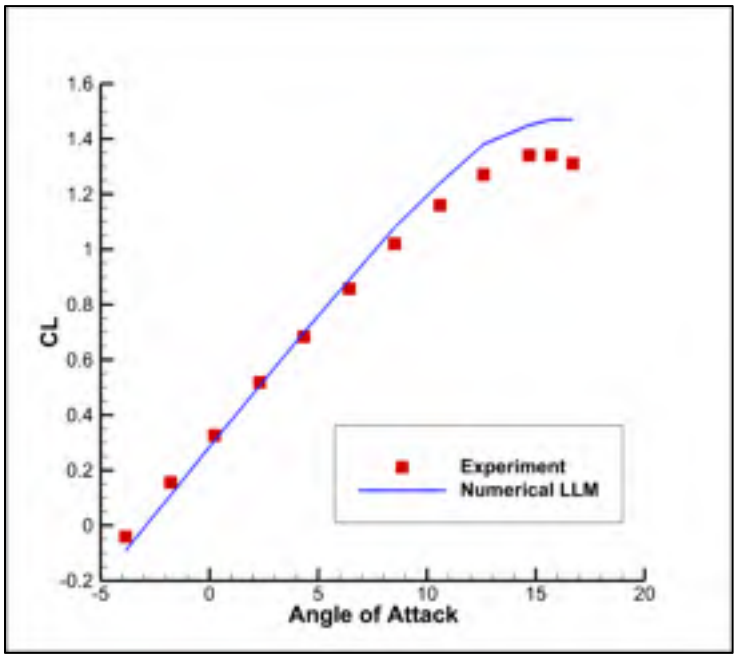

Figure 0.9 Comparison of lift coefficient variation with the angle of attack for the nonlinear lifting line method versus experimental data

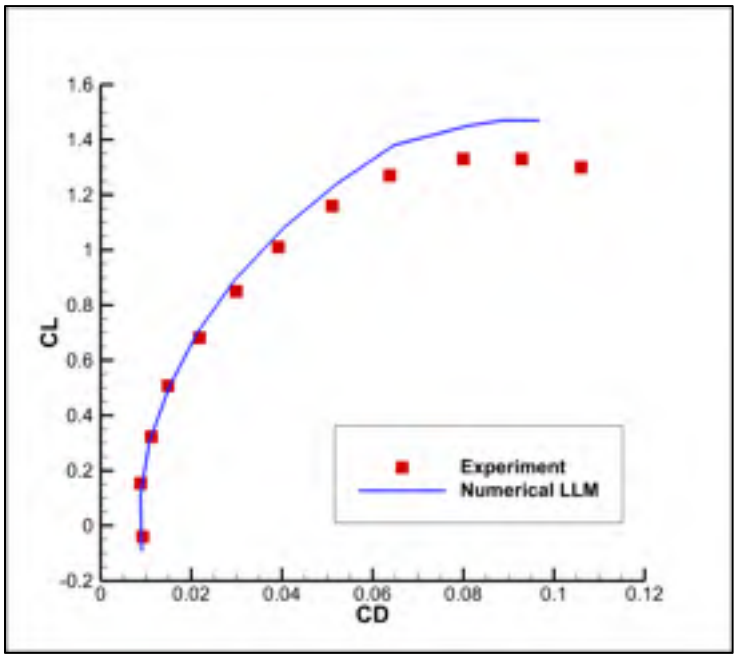

Figure 0.10 Comparison of lift coefficient variation with the drag coefficients for the nonlinear lifting line method versus experimental data

0.3.7 Nonlinear vortex lattice method

Within the framework of the Vortex Lattice Method (VLM) approach (Katz and Plotkin, 1991), the singularity element used is the vortex line solution of the incompressible potential flow equation, while the boundary condition imposed is that of zero flow in the direction normal to the wing's surface. The surface is divided into rectangular panels, and the vortex ring elements are placed on these panels. The leading edge segment of a vortex ring is placed on the quarter chord line of the corresponding panel, while the collocation point is placed at the center of the panel three-quarter chord line.

In the classic VLM approach, the unknown intensities of all the vortex rings distributed over the wing surface are determined by requiring that the zero normal flow boundary condition would be satisfied for all collocation points (Katz and Plotkin, 1991). Knowing that for each collocation point the local velocity is equal to the sum of the freestream velocity and the velocities induced by all the vortex rings over the wing surface and wake, the boundary condition is written as:

$$\left(\mathbf{V}_{\infty} + \sum_{j=1}^{N} \Gamma_j \mathbf{v}_{ij}\right) \cdot \mathbf{n}_i = 0 \tag{0.7}$$

In Equation (0.7) $\mathbf{V}_{\infty}$ is the freestream velocity, N is the total number of vortex rings over the wing surface, $\mathbf{v}_{ij}$ is the velocity induced by the unit strength vortex ring j at the i panel collocation point and $\mathbf{n}_i$ is the surface normal vector calculated at the i panel collocation point.

In the nonlinear VLM approach, the intensities of the vortex rings obtained by solving the linear system presented in Equation (0.7) are adjusted using nonlinear viscous data. For each vortex ring, a correction $\Delta\Gamma$ is defined, so that the final values of the ring vortex intensities become:

$$\Gamma_j \rightarrow \Gamma_j + \Delta\Gamma_j \quad j = 1,2,\dots,N \tag{0.8}$$

Considering that a variation in the intensity of a vortex ring determines a variation in the velocities induced by that vortex ring, the introduction of the $\Delta\Gamma_j$ corrections is followed by the addition of a secondary induced velocity field over the wing surface. Thus, for the nonlinear VLM approach Equation (0.7), becomes:

$$\left(\mathbf{V}_\infty + \sum_{j=1}^{N}\left(\Gamma_j + \Delta\Gamma_j\right)\mathbf{v}_{ij} + \mathbf{V}_i^T\right)\cdot\mathbf{n}_i = 0 \tag{0.9}$$

In order too build the second set of equations needed for the solution of the problem, a nonlinear viscous pressure coefficient distribution is required. This data is obtained by performing a two-dimensional strip analysis of the wing, similar to the analysis performed for the nonlinear lifting line method.

The equations needed to calculate the vortex rings intensity corrections are constructed using the assumption that for all N panels on the wing surface, the pressure coefficient variation obtained from the vortex rings intensities is equal to the nonlinear viscous pressure coefficient variation obtained from the wing strip analysis. For all panels, the following equality is written:

$$\Delta CP_i = \Delta CP_i^{visc} = -\frac{\mathbf{F}_i\cdot\mathbf{n}_i}{A_i Q_\infty} \quad i = 1,2,\dots,N \tag{0.10}$$

In Equation (0.10), $\mathbf{F}_i$ is the aerodynamic force generated by all vortex lines placed on the panel, $\mathbf{n}_i$ is the surface normal vector calculated at the panel collocation point, A_i is the panel area and Q_∞ is the freestream dynamic pressure.

The aerodynamic force acting on a panel of the wing surface is calculated using the three-dimensional vortex lifting law that is also used for the nonlinear lifting line method, and is

presented in Equation (0.3), but this time taking into consideration the vortex lines of all vortex rings that influence the panel. The obtained force will be a nonlinear function of the intensities of all vortex rings strongly interacting on the panel. By coupling the equations resulting from (0.10) with Equation (0.9), a nonlinear system of $2N$ equations is obtained, that allows the calculation of the vortex rings intensities corrections and the correction velocity field, and is presented in Equation (0.11):

$$\mathbf{R} = \begin{Bmatrix} \vdots \\ -\mathbf{F}_i \cdot \mathbf{n}_i + A_i Q_\infty \Delta C P_i^{visc} \\ \vdots \\ - - - - - - - - - - \\ \vdots \\ \sum_{j=1}^{N} \mathbf{v}_{ij} \cdot \mathbf{n}_i \Delta \Gamma_j + V_i^T \\ \vdots \end{Bmatrix} = \mathbf{0} \tag{0.11}$$

The above system is solved using Newton's method. As for the nonlinear lifting line method, because the wing strip analysis was performed as part of the solution procedure, the wing total profile drag can be calculated based on the two-dimensional airfoil drag by direct integration.

The method convergence is very fast, achieving residual values of 10^{-5} within six or seven nonlinear iterations. Thus, good quality results for viscous flows around wings can be obtained with only a small computational effort. In Figures 0.11 and 0.12, a comparison is presented between the numerical and experimental results for the same wing that was earlier used for the nonlinear lifting line versus experimental data comparison (Neely et al., 1947).

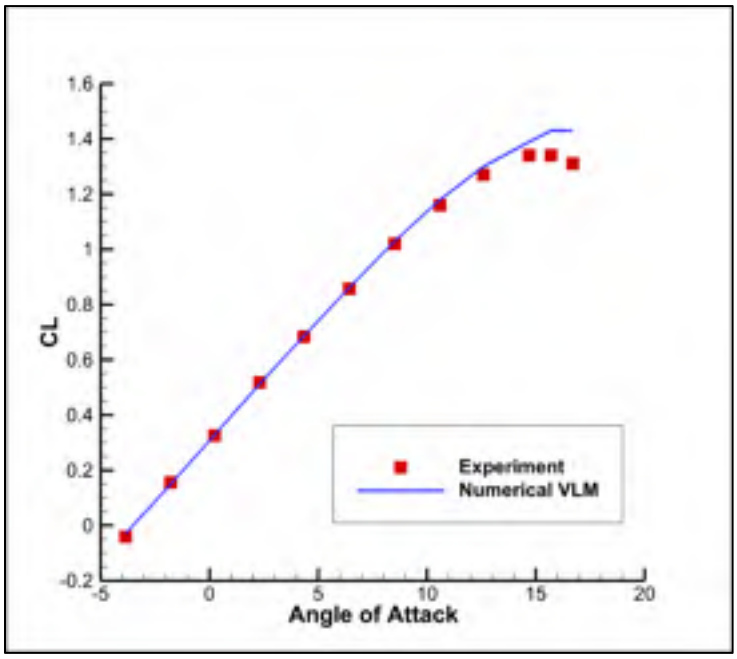

Figure 0.11 Comparison of lift coefficient variation with the angle of attack for the nonlinear vortex lattice method versus experimental data

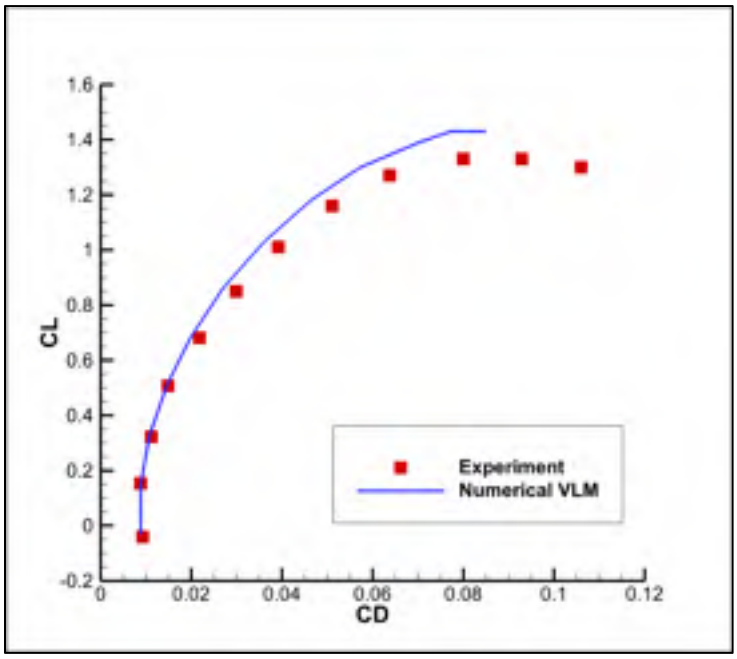

Figure 0.12 Comparison of lift coefficient variation with the drag coefficients for the nonlinear vortex lattice method versus experimental data

0.3.8 Mesh generation code

The high-quality structured meshes used for the numerical simulation were constructed using the ANSYS ICEM-CFD code. In order to ensure that the same meshing parameters were used for all the MDO 505 wing analysis cases an automatic mesh generation procedure was implemented. A script was created for ICEM-CFD, which reads the morphed geometry created by the surface reconstruction algorithm and generates a mesh with the same quality, regardless of the actuators' displacements or aileron deflection angle. The meshes include 400 cells around the wing section (200 on the upper surface and 200 on the lower surface), and 160 cells in the direction of the span (80 on the upper surface and 80 on the lower surface). The wall normal spacing was set to 3E-06 m, a spacing that is refined enough to provide the $y+ < 1$ condition, required for accurate laminar-to-turbulent transition estimation. Figures 0.13 and 0.14 present details on the mesh obtained with the automated procedure for the non-morphed wing without aileron deflection.

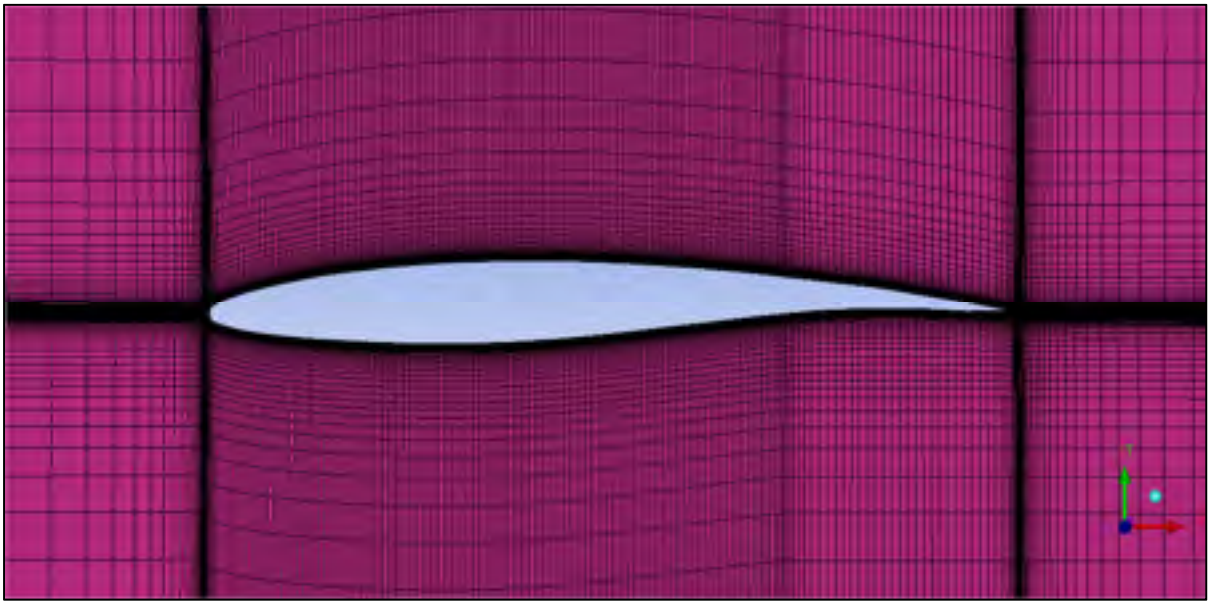

Figure 0.13 View of the MDO 505 mesh on the wing symmetry plane

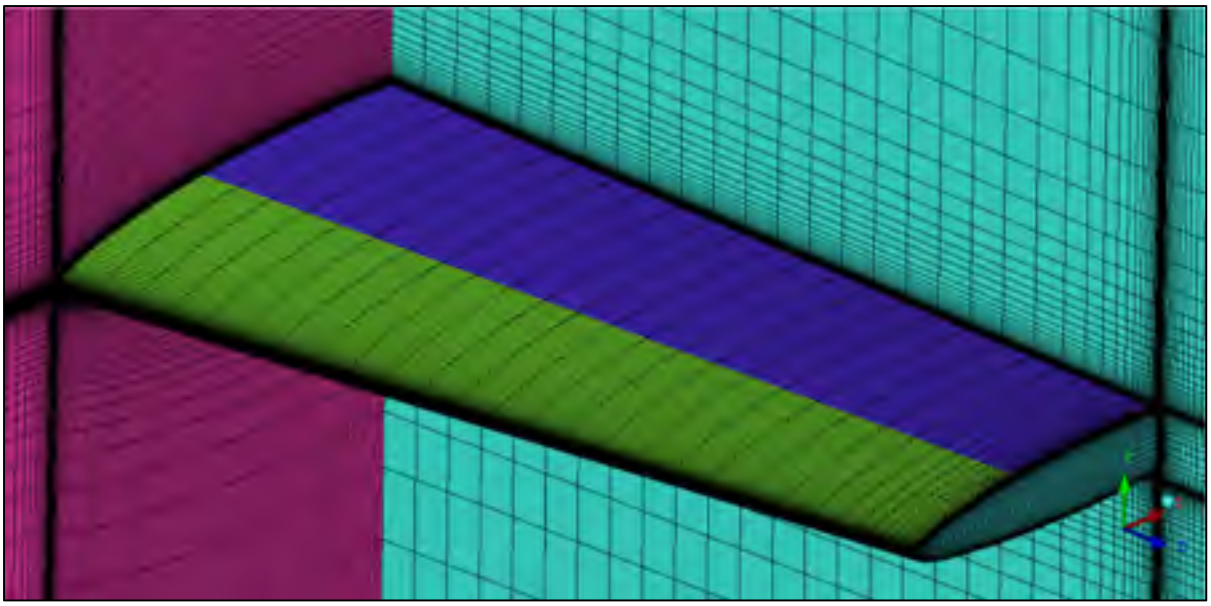

Figure 0.14 The structured mesh around the MDO 505 wing

0.3.9 Three-dimensional flow solver

The high-fidelity three-dimensional numerical simulations were performed with the ANSYS FLUENT solver. The analysis were performed using the $k-\omega$ SST turbulence model (Menter, 2009), coupled with the $\gamma - Re_\theta$ model for predicting the laminar-to-turbulent transition (Menter and Langtry, 2006). The steady-state flow equations were solved using a projection method, achieving the constraint of mass conservation by solving a pressure equation, with the pressure-velocity coupling being done using a high order Rhie-Chow scheme. Cell face values of the pressure were interpolated using a second order central differencing scheme, while for all other variables (turbulence and transition model variables included) a second order upwind scheme was used. Convergence acceleration was achieved with an algebraic multigrid (AMG) approach, using an incomplete lower-upper (ILU) factorization scheme as the linear system smoother.

CHAPTER 1

LITERATURE REVIEW

The prospect of developing wings capable of changing their geometries during flight has interested researchers and designers over the years. Fitting an aircraft with an adaptable wing would reduce the design compromises required to permit its operation in multiple flight conditions (Stanewsky, 2001). No exact definition or clear agreement between researchers exists about the type and the degree of geometrical changes needed to categorize an aircraft as shape morphing. However, there is an agreement that conventional control surfaces, such as flaps, ailerons or slats are not considered as morphing, even if they significantly change the wing camber and its aerodynamic performance. The design of a morphing aircraft represents a truly multidisciplinary problem, requiring the use of new materials and structural layouts, accurate but fast aerodynamic computations and optimizations, accurate and robust actuation mechanisms as well as novel real-time control strategies.

1.1 Morphing Wings and Aircraft

Wing morphing techniques can be classified into three major types: plan-form transformations (sweep angle, span and chord), out-of-plane transformations (twisting, dihedral and spanwise bending) and airfoil transformations (camber and thickness) (Barbarino et al., 2011). Most morphing concepts are focused on changing and controlling only one of the above mentioned geometric parameters, but there were also projects and studies in which combinations of several morphing variables were studied. Unmanned Aerial Vehicles have been the solution chosen by many researchers for the development and implementation of morphing wing concept. This can be explained by the much shorter time-to-delivery, greatly reduced material costs, reduced certification issues and qualification tests, as well as much lower aerodynamic loads that allow the investigation of various morphing concept.

Gamboa et al. (2007) designed a complex mechanical system that allowed both span and chord changes for a morphing wing. The system, consisting of telescopic spars and ribs was also responsible for withstanding the aerodynamic loads, in addition to providing the geometry changes. Numerical analyzes demonstrated that an experimental UAV configuration equipped with the morphing wing achieved drag coefficient reductions between 15% and 23% compared to the baseline design. Lockheed Martin developed the Agile Hunter UAV (Bye and McClure, 2007), (Ivanco et al., 2007), (Love et al., 2007), capable of folding the inner region of the wing over the fuselage, in order to achieve drag reductions during transonic cruise at lower altitudes. A morphing wind tunnel prototype was built and tested up to a Mach number of 0.60. The prototype model demonstrated a successful and accurate actuation under aerodynamic loads, achieving the desired wing shape change in approximately one minute. Several new generation materials were tested and used to manufacture the model, including a shape memory polymer flexible skin.

An important project for the development of morphing wings was the NexGen Aeronautics MFX1 UAV, which included wing sweep and chord changes (Anderson, 2007), (Flanagan et al., 2007). The wing had a morphing truss structure that could be controlled using electrical actuators. A prototype of the UAV was built and successfully flight tested. The morphing wing sustained sweep angle variations of 20 degrees and area changes of 40% under aerodynamic loading, for flight speeds of up to 100 knots. Prabhakar (2015) designed and analysed a UAV equipped with a morphing wing capable of both span and sweep angle changes. The UAV was aerodynamically modelled with the Vortex Lattice Method, and the variation of the longitudinal aerodynamic coefficients was analysed as function of the two parameters. A nonlinear dynamics model was developed and used to simulate the flight behaviour of the UAV, and thus quantified the effect that active wing morphing during flight had on the dynamic response of the aircraft.

A variable wing plan-form UAV was designed and tested by Neal et al. (2004). The system used pneumatic actuators to drive the telescopic and rotating wing, capable of achieving significant wing span and sweep angle changes. Wind tunnel tests were performed and

showed that only three morphing wing configurations were needed to significantly increase the lift-to-drag ratio for the entire flight envelope of the UAV. Supekar (2007) performed an evaluation of the aerodynamic gains that could be obtained by a segmented, telescopic wing mounted on a UAV. In addition to the span changes, the wing could also change the dihedral angle of its outer segment. Vale et al. (2011) also developed a morphing wing capable of span changes through a telescopic system, but in addition achieved conformal changes of the airfoil camber. The two deformation mechanisms could independently to change the wing shape, and were designed for a UAV application, by using a coupled aerodynamic-structural optimization process.

A detailed computational and experimental analysis has been performed by Smith et al. (2014) on the wing of a conventional aircraft that was equipped with two outboard morphing partitions capable of varying the twist and dihedral angles. The morphing system was capable of providing twist variations of up to 3 degrees, and dihedral variations of up to 90 degrees. Computational results were obtained using the high-fidelity TAU computational fluid dynamics code developed at the DLR (German Aerospace Research Center), for both high-speed and low-speed flight conditions, and several angles of attack. An experimental wind tunnel testing was performed on the morphing model, showing variable levels of agreement with of the experimental data with the numerical results. Woods and Friswell (2015) presented a concept for a span changing morphing wing. The mechanism used an internal telescopic structure and a compliant skin to achieve the desired span changes of the morphing wing. Analytical models were used to perform an initial skin design and optimization, based on the expected external aerodynamic loads, while providing the required in-plane and out-of-plane stiffness.

Falcao et al. (2011) proposed a morphing winglet concept for a military class UAV. By changing the winglet cant and toe angles, the system could achieve important performance improvements by effectively controlling the lift distribution at the wingtip region according to different flight conditions. Researchers from NASA Dryden Flight Research Center conducted several flight tests with a UAV equipped with inflatable wings whose span could

be modified by adjusting the pressure input (Murray et al., 2002). The wings were made from several spanwise inflatable tubes, surrounded by sponge and a flexible nylon skin in order to maintain the airfoil shape during flight. The UAV used a high pressure nitrogen inflation system, which could deploy the wings to their full span in less than one second, regardless if the aircraft was on the ground or in flight. Ajaj et al. (2013) presented a morphing wing based on a zigzag wing-box, capable of modifying its span by up to 44%. The wing consisted of a rigid part, housing the fuel tank and transferring the aerodynamic loads to the fuselage, and the morphing partition, housing the deformation mechanism and covered by a flexible skin. This morphing wing concept was used to replace the conventional wing of a medium altitude, long range UAV, to enhance its operational performance and to provide roll control.

Sodja et al. (2015) designed a morphing leading edge concept for a regional transport aircraft. The system demonstrated the capability of at least five degrees leading edge rotation by inducing bending deformations in the wing skin, while matching as close as possible its prescribed aerodynamically optimized shaped. The leading edge was designed using external loads that appear on regional aircraft wings during normal operation, and it successfully transfers these loads on the front spar, while achieving the desired shapes. Daynes (2015) presented a morphing wing concept that was designed to have zero torsional stiffness, in order to minimize actuation force requirements. The concept consisted of carbon-fibre-reinforced plastic strips that were assembled into a grid-like structure including spars and ribs, whose topology was optimized in order to achieve the desired twist stiffness constraint.

Pecora et al. (2011) demonstrated the effectiveness of replacing the conventional segmented flap with a morphing compliant high-lift device, in the case of a regional transport aircraft. Bilgen et al. (2007), (2009) presented a concept of replacing the wing trailing edge devices with a morphing surface, capable of achieving continuous camber variations instead of rigid deflections. The morphing system was designed to replace the ailerons of a UAV, and thus used fast, electrical actuation mechanisms. Both wind tunnel experiments and flight tests were performed, and demonstrated the effectiveness of the concept at providing accurate roll control. Gano and Renaud (2002) presented a concept to increase the aerodynamic efficiency

of a UAV by gradually decreasing the wing thickness as the fuel inside the wing-mounted tank was burned, thus decreasing the drag coefficient.

In the ADIF Adaptive Wing project, carried out by EADS (European Aeronautic Defence and Space Company), Daimler and DLR (German Aerospace Research Center), a compliant structure wing was developed (Monner et al., 1998). It was a structure that was able to redistribute external aerodynamic forces so that it could be morphed in certain predetermined areas, while it remained rigid to deformation in other areas. The trailing edge part of the wing was composed of a flexible structure made of several rigid plate elements connected with a cinematic type mechanism. Each rib was actuated at a single, predetermined point. The desired rotation was transferred to the other plates of the rib via the cinematic mechanism in order to obtain the desired wing shape.

Liu et al. (2015) designed and tested a high aspect ratio wing equipped with a controllable flexible trailing edge, aimed at replacing conventional control surfaces. The experimental wind tunnel testing investigated the influence of the trailing edge flexion timing on the overall performance of the system, for high angles of attack values. It was found that the morphing wing could provide significant improvements over the baseline design if the flexion motion was well synchronized with the leading edge vortex shedding process occurring in the case of leading edge separation. The trailing edge flexing speed did not have an important influence on the results. Pankonien and Inman (2015) presented a concept for morphing ailerons designed to replace the conventional wing control surfaces of a UAV. In this morphing aileron system, active sections of Macro Fibre Composites driving internal compliant mechanism, as well as inactive sections of elastomer honeycomb were combined. The optimal shape configurations were determined using the lifting line theory. The aerodynamic performance of the system was evaluated using wing tunnel testing, performed for fixed values of the lift coefficient at off-design angle of attack values. The measurements were focused on the drag coefficient penalty associated with classic control surface deflections at off-design flight conditions. The morphing trailing edge achieved drag

reductions up to 20% compared to the original design, thus justifying the increased mass and complexity of the system.

Sleesongsom (2013) presented a morphing wing concept obtained through a detailed structural optimization procedure. Several of the traditional steps taken in the design of a composite wing structured were coupled and performed simultaneously, using a constrained population-based multi-objective optimization algorithm. The unconventional structure of the morphing wing was then analysed under various aerodynamic loads, and verified for aeroelastic deformations limits, in order to validate the proposed concept. Previtali (2014) performed a numerical study to investigate the roll control performance of a morphing wing concept. The system used compliant ribs and was aimed to replace the conventional ailerons for a conventional aircraft. The design approach considered the three-dimensional aero-structural behaviour of the morphing wing, and used optimization techniques. Computations showed the possibility of producing sufficient roll control authority up to speeds of 250 km/h, and indicated the weight penalties associated with implementing the compliant rib morphing solution on the aircraft.

Lyu (2014) performed an aerodynamic optimization for a wing equipped with a morphing trailing edge system. The computations were performed with a high-fidelity computational fluid dynamics solver, coupled with an optimization routine. The wing base geometry was designed with a multipoint approach, while the optimal shape of the morphing trailing edge was determined for each different flight condition. Very good results were obtained for cruise flight, with drag reduction of 1% for the on-design conditions, and reductions of over 5% for the off-design conditions, compared to the base multipoint optimized wing.

A comprehensive study on the possible impact of morphing wing configurations on the range performance of a regional airplane powered by turbofan engines was performed by Filippone (2014). Many aspects were taken into consideration, including the structural design of the morphing wing, increases in aerodynamic performance, weight changes, energy consumption and trade-off analysis. The aerodynamic characteristics of the complete aircraft were

estimated using several numerical, analytical and semi-empirical methods. The structural model was constructed using a finite element approximation, while the flight performance and fuel consumption were estimated with an in-house code. The obtained results have shown that the fuel consumption reduction achieved for the regional aircraft is only marginal, unless a redesign of the wing internal structure and plan-form shape were also done. By use of a change in the wing base design, coupled with the introduction of a morphing technology, more significant improvements could be obtained.

The CRIAQ 7.1 project took place between 2006 and 2009 and was realized following a collaboration between teams from École de Technologie Supérieure (ÉTS), École Polytechnique de Montréal, Bombardier Aerospace, Thales Canada and the Institute for Aerospace Research-Canadian National Research Center (IAR-CNRC). The objective of the project was to improve and control the laminarity of the flow past a morphing wing, in order to obtain important drag reductions (Botez, 2007). The two-dimensional wing was designed starting from the WTEA natural laminar airfoil. The morphing wing active structure was composed of three main subsystems: 1) a flexible, composite material upper surface, stretching between 3% and 70% of the airfoil chord; 2) a rigid inner surface; 3) a Shape Memory Alloy (SMA) actuator group located inside the wing box, which could morph the flexible skin at two points, located at 25.3% and 47.6% of the chord (Brailovski et al., 2008). Numerical optimizations were performed on the airfoil prior to model manufacturing (Pages, 2007), and promising results were obtained: the morphing system was able to delay the transition location downstream by up to 30% of the chord, and to reduce the airfoil drag by up to 22%. For each different flight condition, the optimal displacements for the SMA actuators, which were determined through the numerical optimization procedure, were provided using two different control approaches. In the open loop configuration, the desired displacements were directly imposed on the system (Popov et al., 2010) while in the closed loop configuration, the displacements were automatically determined as a function of the pressure readings from the wing upper surface (Popov et al., 2010). The wind tunnel tests were performed in the 2 m by 3 m atmospheric closed circuit subsonic wind tunnel at IAR-

CNRC and validated the numerical wing optimisations (Sainmont et al., 2009) and designed control techniques (Grigorie, 2012).

1.2 The Lifting Line Theory

The lifting line theory, originally developed by Prandtl (1918) and published in 1918, represented the first analytical aerodynamic model capable of calculating the lift and the induced drag of a finite span lifting surface. Experimental results have demonstrated the accuracy of the theory in predicting the linear portion of a wing's lift curve characteristics for straight wings with moderate to high aspect ratio. The traditional closed form solution of Prandtl's equation was first presented by Glauert (1927), and consisted of a truncated sine functions series for the spanwise distribution of bound vorticity, whose coefficients are determined by a collocation method, requiring that the lifting line equation be satisfied at a finite number of stations along the wing span.

Due to its relative simplicity and the accuracy of the predicted results, the lifting line theory was widely used in the years after its initial publication. Researchers such as Tani (1934) and Multhopp (1938) have proposed alternative methods for the solution of Prandtl's equation, increasing the quality of the obtained results, but without proposing any modification of the underlying hypothesis or of the mathematical model. Other authors have proposed modifications of the original theory, which further increased its accuracy, but also extended its range of applicability. Jones (1941) proposed a modification that allowed to include the effects of the wing's chord distribution, while Weissinger (1947) reformulated the theory in order to apply it to wings with small to moderate sweep angles. Sivells and Neely (1947) proposed a correction based on the experimental aerodynamic properties of the airfoil used to construct the wing geometry, thus altering the theory's results as function of the real, viscous behaviour of the airflow. This correction allowed them to calculate the viscous drag, in addition to the induced drag, and extended the theory's applicability range to both pre-stall and post-stall regimes.

With the development of more powerful computers, many researchers have worked on the development of purely numerical approaches for solving Prandtl's lifting line equation. From the 1980's onwards, a significant increase in the interest given to the old theory was observed, adapting it to modern computational methods and using it as a fast, accurate and efficient tool for wing design and optimization. Anderson (1980) presented a numerical iterative solution of the classical lifting line theory, suitably modified for post-stall behaviour. The study was performed on straight, rectangular wings of high aspect ratio, with and without leading edge droop. The high angles of attack solutions obtained agreed with available experimental data within a maximum error of around 20%. McCormick (1989) also presented an iterative numerical lifting line model, which was coupled with nonlinear two-dimensional airfoil data. The model predicted with relatively good accuracy complex wing stall phenomenon, such as hysteresis and unsymmetrical spanwise lift distributions with partial stall. Applications and results were once more limited to straight wings, without sweep, twisting or dihedral.

Rasmussen and Smith (1999) developed a new methodology for solving the lifting line equation. Variations in span-wise chord and twisting distributions were taken into consideration by writing them in a Fourier series representation, in addition to a similar decomposition of the span-wise lift distribution. The method converged much faster than previous numerical approaches. A good accuracy was achieved with only a small number of span-wise collocation points and allowed to perform the analysis of wings with taper and twist. Phillips presented several papers on improvements to the classic lifting line theory. One approach (Phillips and Snyder, 2000) used a span-wise distribution of horseshoe vortices and replaced the traditional Kutta - Joukowski law with the three-dimensional vortex lifting law in order to calculate the local lift coefficient as function of the span-wise distribution of bound vorticity. This approach allowed the accurate analysis of wings with arbitrary plan-form, as well as with sweep angle and dihedral angle. Another study took into consideration the effects of geometric and aerodynamic twisting on the calculated wing performance (Phillips, 2004). The solution of the lifting-line equation was obtained using Fourier-series representations, and was further modified in order to become independent of the angle of

attack value, thus allowing only one representation for a given wing geometry, instead of recalculating the entire series for each different angle of attack. The model was used to minimize the induced drag of various wings by introducing a twist distribution. Another improvement concerned the calculation of the wing maximum lift coefficient based on the airfoil section maximum lift coefficient (Phillips and Alley, 2007). The method could be applied to wings of arbitrary plan-form and included the effects of twisting and moderate sweep angles. As in the previous study, a modified Fourier-series representation was used, that considered a coupling with the two-dimensional properties of the wing's airfoil. The obtained results were focused on obtaining the twist distribution capable of maximizing the generated lift for a given plan-form, while reducing the resulting induced-drag.

Phlips (1981) presented an unsteady lifting line theory, by including a detailed three-dimensional representation of the vortex wake and its effects on the lifting surface. The model was successfully used to simulate the flapping motion of bird wings. Spalart (2014) formulated a periodic version of the lifting-line theory, aimed at explaining the spontaneous formation of lift cells on wings in post-stall condition. In order to demonstrate the complex interactions between a stalling wing and its trailing vortex system, a fully nonlinear lift curve was implemented as example. The results showed that the positive or negative value of the lift curve slope could have an important contribution to the flow stability. Gallay and Laurendeau (2015) presented a numerical algorithm for a generalized non-linear lifting line model, with applications to post-stall flows. An iterative, angle of attack correction approach was used, and a strong coupling was achieved by approximating the two-dimensional characteristics of the wing airfoil with polynomials. Good agreement was obtained with existing research on the formation of post-stall lift cells.

The lifting line theory, either in its original or in an improved formulation, has been used by researchers to model the aerodynamic characteristics of different morphing wing concepts. Majji (2007) used this theory to calculate the improvements obtained by a morphing wing with variable twist angle. The obtained results were validated with experimental data obtained through low speed wind tunnel testing. Wickenheiser and Garcia (2007) presented

an extension of Weissinger's lifting line formulation, capable of determining the aerodynamic coefficients of wings with arbitrary span-wise curvature and chord distribution. The method was used to design a gull-like morphing wing concept aimed at improving the lift-to-drag efficiency over a range of different flight conditions. Gamboa et al. (2009) designed a morphing wing concept for a small UAV, capable of wing plan-form changes, in order to reduce its drag coefficient. The wing shapes were determined with a multidisciplinary design optimization tool, coupling aerodynamic shapes optimization with a simplified structural model. The load calculations were performed with a nonlinear lifting line method that could also estimate the viscous drag. Pankonien and Inman (2015) designed an adaptive trailing edge surface aimed to replace the conventional control surfaces without requiring any modification to the wing box. The optimal shapes of the morphing wing were determined with a lifting line model in order to minimize the drag coefficient increase associated with achieving a desired lift coefficient at an off-design flight condition. Experimental wind tunnel testing was performed, and drag reductions of up to 20% were obtained with respect to the baseline design.

1.3 The Vortex Lattice Method

The Vortex Lattice Method (VLM) represents a numerical method for calculating the aerodynamic characteristics of wings. Together with the Doublet Lattice Method (DLM), they represent computational approaches of the lifting surface theory, in which the wing is modeled by a zero-thickness solid surface and a free wake, in these regions the singularity solutions of Laplace's equation for the fluid velocity potential being distributed. Unlike the lifting line theory, that can be applied only for wings with moderate to high aspect ratio and, for the more modern proposed versions of the theory, moderate sweep and dihedral angles, the VLM can be used to calculate the aerodynamic coefficients of any wing geometry, regardless of aspect ratio, sweep angle or taper ratio. This wide application range, together with the low computational requirements, makes the VLM a very useful tool for preliminary wing design or optimization.

In the early versions of the method, the wing surface was divided into panels, and a horseshoe vortex was considered on each panel, with only the middle segment bound on the surface, while the other two segments stretch behind the wing, to form the wake. A linear system of equations was formed to determine the unknown intensities of the horseshoe vortices, and then to compute the aerodynamic coefficients values. Hedman (1966) presented an efficient version of this approach in 1966. Because the modeled wake had to be of zero thickness, all horseshoe vortices had to be in the same plane, thus all wing camber or bending was neglected. Rusak (1985) presented a vortex lattice method in which the wake surface shape was updated iteratively as function of the field of induced velocities. This wake rollup process was proved to converge within only a small number of iterations, and produced good results for modeling the wake of aircraft wings. Levin and Katz (1981) presented a non-steady version of the method that was modified in order to model the phenomenon of leading edge separation. Results were obtained for various motions of a delta wing, including its plunging motion. The proposed wake shedding procedure outperformed previous wake rollup methods for the chosen analysis, in terms of required computational time. Rom (1993) presented a nonlinear VLM that included the wake rollup phenomenon as part of a nonlinear coupled solution procedure. The method was applied to calculate the aerodynamic characteristics and to predict the wake shape for five different wing-canard configurations, at high angle of attack values. The predicted lift and induced drag were in good agreement with the available experimental data, but the pitching moment of the configurations was not calculated well enough with the proposed method.

Katz and Plotkin (1991) presented a new formulation of the traditional VLM, in which the horseshoe vortices distributed over the wing surface were replaced by ring vortices. A vortex ring was placed over each of the geometric panels on the wing surface, and all four sides of the ring were bound to the surface (instead of only one bound segment, for the classic horseshoe vortex approach). The wake was modeled by using free vortex rings, whose intensities were considered known and were linked to the intensities of the trailing edge rings. This new formulation allowed the introduction of the wing surface camber or span-wise bending into the analysis, thus increasing the quality of the results. Vest and Katz

(1996) developed an unsteady version of the VLM formulation with vortex rings, and applied it to calculate the propulsive forces of flapping wings. The results were compared with the experimental results available, but also with analytical methods. Good agreement was found, for both high flapping frequency low span wings and low flapping frequency high span wings. Melin (2000) developed a VLM code based on the horseshoe vortex approach that segmented the two trailing segments of each vortex into several parts. This allowed the analysis of wings with deflected control surfaces, such as ailerons and flaps, since the segmented vortex lines could follow the change in wing camber introduced by such deflections.

The unsteady vortex lattice method has proven to be an accurate tool for predicting non-stationary aerodynamic loads for low-speed regimes, and thus it was used in aeroelasticity and flight dynamics simulations. Murua (2012) presented an exhausted review of the method's application in the above mentioned situations. A new integration was performed with a nonlinear beam model for capturing the wing deformation, therefore the algorithm was re-written in the state-space form and solved with a nonlinear time-marching approach. The numerical studies demonstrated scenarios where the method outperformed other methods traditionally used in aeroelasticity modeling. Bunge and Kroo (2012) developed a compact formulation of the VLM, in which the aerodynamic forces and moments were reduced to quadratic expressions in terms of the flight and control variables. Due to the fact that computation time became independent of the number of vortices used, the method was efficiently integrated into six degrees of freedom flight simulations. Because the method provided analytical equations for the forces and moments, and for their derivatives, it could also be integrated into optimization routines.

Guimaraes Neto (2014) presented a method for using correction factors to improve the accuracy of the vortex lattice method. The positions of the control points of each surface panel were displaced based on steady-state pressure distributions obtained from high-fidelity CFD computations or from wind tunnel tests data. The corrected positions were then used to modify the matrix of the linear system of equations, so that better accuracy was obtained.

Leifsson (2014) developed a wing optimization procedure based on a surrogate model constructed from a corrected low-fidelity aerodynamic model. The aerodynamic model was constructed using a VLM coupled with a two-dimensional compressible viscous analysis of the wing airfoil, while the surrogate model was created using response-surface methodologies. The proposed approach has shown good agreement with CFD results, while being orders of magnitude faster in performing the optimization. Smith et al. (2012) have performed a multi-objective optimization study of a morphing wing system retrofitted on an existing commercial jet aircraft. This study was performed with a coupled aerodynamic, structural and aeroelastic tool, including the VLM for inviscid aerodynamic calculations. The results included a flight range improvement of 4 to 5% over the baseline design, a potential for take-off/landing field-length reduction and climb performance enhancements.

Ghommem et al. (2012) applied an unsteady version of the vortex lattice method in order to optimize the shapes of flapping wing for providing increased forward flight efficiency. The wing shape was parameterized using B-Splines. A sensitivity analysis was performed to identify the parameters that had the highest influence on the flapping wing performance. The optimized shapes provided significantly more thrust, at the cost of a higher power input requirement, but an overall efficiency improvement was obtained. Mariens (2014) presented a quasi-three dimensional aerodynamic solver which provided accurate wing drag results with low computational costs. The method used a vortex lattice method coupled one-way with two-dimensional strip analyses. The effective angles of attack for each strip were corrected with an iterative procedure based on the sweep theory. Validation tests proved that the results obtained were in good agreement with high-fidelity CFD results. The method was then used for the multidisciplinary design optimization of the wing shape of a regional passenger aircraft. The objective of obtaining the same lift but for a reduced structural weight of the wing was achieved.

CHAPTER 2

RESEARCH APPROACH AND THESIS ORGANIZATION

The research performed on the improvement of aerodynamic characteristics through a morphing wing approach that is presented in the current thesis was divided into several phases:

- statement of the problem and design of the morphing concept;
- development and validation of the tools needed for the analysis;
- two-dimensional optimizations performed on the UAS-S4 Éhecatl airfoil;
- three-dimensional optimizations performed on the UAS-S4 Éhecatl wing;
- three-dimensional optimizations and high-fidelity analysis on the MDO 505 wing;

Each of these phases was required in order to successfully achieve the desired objectives and provide further knowledge on the performance, application range and limitations of the morphing wing concept.

2.1 Thesis Research Approach

Achieving a reduction of the drag coefficient provides significant advantages for aircraft, leading to increases in the lift to drag ratio and reductions of the fuel consumption. One possibility of obtaining the desired objectives is an increase in the extent of laminar flow over the wing surface. For a given Reynolds number value, laminar flow exhibits less viscous friction than a turbulent flow, and thus generates lower drag per unit of surface. The transition point between laminar and turbulent flows can be delayed by modifying the pressure distribution over the wing surface so that the recompression occurring after the leading edge suction peak is more gradual and the adverse pressure gradient becomes less strong.

The CRIAQ 7.1 project, that was realized through a collaboration between teams from École de Technologie Supérieure, École Polytechnique de Montréal, Bombardier Aerospace, Thales Canada and the Institute for Aerospace Research-Canadian National Research Center, demonstrated the concept of controlling the upper surface transition point on a rectangular research wing model through morphing. The wing system included a flexible, composite material skin whose shape was modified, according to the flight conditions, by an internally placed SMA (Shape Memory Alloy) actuation mechanism. A number of 35 flight conditions were considered and expressed in terms of Mach number, Reynolds number and angle of attack. Promising results were obtained, with transition point delays of up to 30% of the chord and two-dimensional drag coefficient reductions of up to 22%.

2.1.1 UAS-S4 morphing wing research

Using the experience gained at LARCASE during the project, the same morphing concept was designed for the application on the UAS-S4. For the research performed, a part of the wing upper and lower surfaces was replaced with a flexible skin that could be deformed using an actuation system placed inside the wing structure. The trailing edge limit of the morphing region was limited by the control and high-lift surfaces installed on the wing. A sensitivity analysis of the performances as function of the airfoil shape was performed, and it was established that the highest gains could be achieved for relatively low displacements (of the order of 2.5-3 mm) if the leading edge of the airfoil was modified together with the first half of the upper surface. In order to parameterize the airfoil and to determine the optimal shapes of the morphing skin, a NURBS interpolation was chosen. Other techniques were also considered, but only NURBS allowed for a precise interpolation of the difficult modeling of the leading edge geometry, coupled with a good local control of the deformation through motions of the control points. In addition, the positions and motion of the NURBS control points could directly simulate the actuator displacements at the positions of the actuators along the chord.

A Genetic Algorithm optimization tool was developed for determining the optimal displacements as function of the flight condition. The algorithm was validated using optimization test functions found in literature and it was applied for delaying the upper surface laminar-to-turbulent transition point for the ATR 42 regional turboprop airfoil, and the UAS-S4 airfoil. In order to reduce the required computation time, while not sacrificing the global search characteristics, other population-based algorithms were also investigated. The Artificial Bee Colony Algorithm (ABC) was chosen because it proved faster convergence rates while performing thorough exploration of the search space. A tool was developed and validated using optimization test functions found in literature. Faster convergence acceleration was achieved by coupling the ABC optimizer with the classic, gradient-based Broyden-Fletcher-Goldfarb-Shanno (BFGS) algorithm. The idea was to allow the population-based algorithm to find the region of the global optimum, but without searching for the exact optimum point using its trial-and-error search routine, and, once the region was found, directly converge to the optimum point using the fast gradient-descent routine.

In order to investigate the three-dimensional performance of the morphing wing concept, an aerodynamic solver was needed. The desired solver had to be sufficiently fast as to be suitable for integration with a population-based optimization algorithm, had to allow an easy implementation of geometry modifications, to integrate the effects of the airfoil shape on the wing performance and to predict accurate values of the drag coefficient. An original nonlinear lifting line solver was developed, that used two-dimensional airfoil characteristics in the calculation process. Its performance was validated against experimental data available in scientific literature, and against computations performed with high-fidelity solvers such as ANSYS FLUENT. Comparisons with CFD on several morphed geometries showed that the solver was sensitive enough to capture the drag reductions determined by upper surface wing morphing. In addition, its execution time is much faster than a CFD solver (approximately 300 times faster). Because the lifting line theory is limited in its application range to wings of moderate to high aspect ratio and low to moderate sweep angles, a second solver was developed based on the vortex lattice method (VLM), thus overcoming these limitations. The

novel nonlinear VLM approach was also constructed by coupling the method with two-dimensional airfoil analysis. Validation was performed with experimental data available in literature, and the method showed remarkable accuracy in predicting viscous drag for wings of various plan-forms.

The application of the morphing wing concept to improve the aerodynamic characteristics of the UAS-S4 was performed in two phases, two-dimensional and three-dimensional. The two dimensional optimizations investigated a large range of angles of attack, from normal cruise conditions to post-stall conditions. For low and moderate angle of attack values, the objective was to delay the laminar-to-turbulent transition point and obtain important drag reductions, while for high angles of attack, the analysis investigated the increase of the maximum lift coefficient and the delay of boundary layer separation (stall delay). All the optimizations were also performed with state-of-the-art commercial optimization tools in order to validate the results obtained with the in-house optimization algorithms for the highly nonlinear optimization problem. In the second phase, three-dimensional studies were performed with the objective of improving the wing lift-to-drag ratio. Several span-wise configurations of the morphing wing were proposed and their ability to obtain the desired performance improvements was investigated. The analyses were performed for flight conditions corresponding to cruise, take-off and landing and were validated using high-fidelity CFD computations.

2.1.2 MDO 505 morphing wing research

The CRIAQ MDO 505 project represents a continuation of the CRIAQ 7.1 project, and investigates the effectiveness of a morphing wing model equipped with a flexible upper surface and two controllable ailerons, one rigid and one morphing. The geometry and the structure of the model were designed after the wing tip of a transport aircraft, and are capable of withstanding in-flight loads of 1G. The morphing skin extends between the two wing spars, located at 20% and 65% of the chord and is rigidly attached to the spars and to the root and tip ribs. A sensitivity analysis was performed to determine the optimum number of skin

actuators, as well as their positions along the wing chord. Several configurations were analysed, with the actuators number varying between 1 and 4. It was concluded that 2 actuators, locate at 32% and 48% of the chord are sufficient to generate the desired skin shapes.

The optimal actuator displacements as function of the flight condition were determined using two-dimensional aerodynamic analysis and a Genetic Algorithm optimization tool. Cubic splines were used to generate the required upper skin shapes during the optimization process, because they allow a very good control of the actuation points' location and displacements and they share the same mathematical properties as a beam deflecting under load. To verify the impact of the two-dimensional skin shape optimizations on the overall wing performance, the morphing wing was analysed in 3D using both the fast non-linear VLM code and high-fidelity CFD simulations.

Two distinct approaches were used to generate the three-dimensional shapes of the morphing upper skin. The first approach used spline functions reconstruction, similar to the methodology used for the UAS-S4 analysis. However, in order to accurately reproduce the shapes and thus reduce one source of errors, a second approach was implemented, using high-resolution data obtained by a scanning procedure. In order to ensure that the same meshing parameters were used for all the morphed cases, an automatic mesh generation procedure was implemented through a script created for the ICEM-CFD meshing tool. The three-dimensional computations were performed with FLUENT and validated using experimental wind tunnel data (pressure distribution, upper surface transition location and aerodynamic forces and moments).

2.2 Thesis Organization

As main author, the research performed and included in the thesis was presented in six peer-review journal papers and eight conference papers. Three of the journal papers have been

published and three are currently under review for publication. These scientific papers are presented in the thesis from Chapter 3 to Chapter 8.

Dr. Ruxandra Mihaela Botez, as co-author for all journal and conference papers, supervised the realization and the progress of the performed research. In the first paper, PhD student Andreea Koreanschi worked as co-author by contributing to the development of the genetic algorithm optimizer and to the implementation of cubic splines for the span-wise generation of the morphing wing geometries. In the second and third papers, co-author and Master student Antoine Simon helped perform the comparisons between the results obtained with the in-house optimizer and the commercial, state-of-the-art optimizers, while co-author and PhD student Andreea Koreanschi worked on improving the coupling between the optimization routines and the aerodynamic solver. In the fourth paper, co-author and PhD student Andreea Koreanschi contributed to the implementation of the cubic splines for the span-wise generation of the morphed wing geometries. In the fifth and sixth papers, PhD student Andreea Koreanschi co-authored and worked on the generation of the two-dimensional optimized airfoil shapes for the low aspect ratio MDO 505 wing, and helped with the generation of the three-dimensional geometries constructed from the optimized morphed airfoils.

2.2.1 First journal paper

In Chapter 3, the journal paper “Optimization of an Unmanned Aerial System wing using a flexible skin morphing wing” is presented, that was published in the SAE Journal of Aerospace in October 2013. This paper was also presented at the 2013 SAE Conference that took place in Montreal, and was selected for publication in the *SAE Journal of Aerospace* as it was highly rated by the reviewers. It focused on the development of the aerodynamic solver, the use of splines to reconstruct the morphed geometries and presented preliminary optimization results for the UAS-S4 wing.

In this paper, the new nonlinear lifting line method used a distribution of horseshoe vortices to provide the generation of aerodynamic forces and required two-dimensional strip airfoil analyses, which were performed with the XFOIL solver. Two different approaches were coupled in order to provide the morphed geometries, NURBS for airfoil shape modification and cubic splines for span-wise geometry generation. The genetic algorithm used for the optimizations was presented, and details were given on the mutation and cross-over procedures used. The morphed geometries were used to reduce the wing drag coefficient, and no other constraints were imposed on the other aerodynamic coefficients. Results were presented for one airspeed value, corresponding to the UAS-S4 cruise flight, and for a limited range of angle of attack values, between 0 and 5 degrees.

2.2.2 Second journal paper

In Chapter 4, the research paper entitled “Improving the UAS-S4 Éhecatl airfoil high angles-of-attack performance characteristics using a morphing wing approach” is included, and this paper was published in *Proceedings of the Institution of Mechanical Engineers, Part G: Journal of Aerospace Engineering* in May 2015. In this paper, the morphing wing system was used to delay boundary layer separation and increase the maximum lift coefficient.

The shape changes of the morphing skin were performed with important constraints, in order to limit the displacements to a maximum of 2.5 mm and prevent length variations that would not be feasible from a structural point of view. The two-dimensional simulations were performed with XFOIL, while the Artificial Bee Colony algorithm was presented and used for the optimizations. For validation purposes, the optimizations were also performed with MATLAB. A detailed description of the parameters used for all numerical tools was presented. Results obtained for the morphing airfoil are presented for three Reynolds numbers and angles of attack between 10 and 19 degrees.

2.2.3 Third journal paper

In Chapter 5, the paper “Aerodynamic performance improvement of the UAS-S4 Éhecatl morphing airfoil using novel optimization techniques” is presented, paper that was published in *Proceedings of the Institution of Mechanical Engineers, Part G: Journal of Aerospace Engineering* in August 2015. It focused on using the morphing wing concept to improve flow laminarity on the upper surface of the UAS-S4 airfoil and obtain important drag reductions.

The morphing wing shapes were obtained with respect to structural limitations, and thus the maximum displacements were limited to a value of 2.5 mm. The simulations were performed in two-dimensions using the XFOIL solver, for a range of angles of attack between -4 and 10 degrees. A detailed description of the new optimization tool was presented, including the Artificial Bee Colony algorithm and an augmented version of the Broyden-Fletcher-Goldfarb-Shanno algorithm capable of handling constrained problems. For validation of the results, all the calculations were also performed with the ModeFrontier state-of-the-art commercial optimizer. The parameters used for the configuration of the numerical tool were detailed. The results for the UAS-S4 were obtained with two different objective functions, and the differences between them were presented.

2.2.4 Fourth journal paper

In Chapter 6, the journal article “Analysis of UAS-S4 Éhecatl aerodynamic performance improvement using several configurations of a morphing wing technology” is presented. This paper was submitted to the *Aeronautical Journal* and is currently under review. The paper analyses the impact of the upper surface morphing skin on the lift-to-drag performance and laminar flow increase for the UAS wing, and investigates the effect of the number of span-wise actuation stations on these improvements.

The fast nonlinear lifting line method was used to determine the aerodynamic characteristics, coupled with the Artificial Bee Colony/ Broyden-Fletcher-Goldfarb-Shanno optimizer for

determining the actuator displacements. The morphed geometries were also analysed with the ANSYS FLUENT high-fidelity CFD solver. The turbulence and transition models used for these calculations were presented, as well as the methods for solving the equations. Four configurations of the morphing system were proposed, with a number of span-wise actuation stations that varied between two and five. The stations were distributed so that the shape changes of the skin are as uniform as possible over the entire span of each wing half. The CFD results validated the improved laminar flow on the upper surface and the corresponding lift-to-drag increase. The obtained decrease of profile drag was presented for angles of attack between -4 and 10 degrees.

2.2.5 Fifth journal paper

In Chapter 7, the research paper entitled "A new nonlinear Vortex Lattice Method: applications to wing aerodynamic optimizations" is included. This paper was submitted to the *Chinese Journal of Aeronautics* and is currently in review. The paper focused on the development on the nonlinear VLM, the validation of the solver and the application to analyse the drag reductions obtained for the UAS-S4 and MDO 505 morphing wings.

The mathematical development of the original method was presented, starting from the classic VLM and next introducing the new hypothesis and nonlinear coupling with two-dimensional strip analysis. Several tests were performed to identify the wing surface mesh requirements and the residual convergence characteristics. The model was validated against experimental data available in literature, and validation was done for both low-sweep and high-sweep wings. The VLM was coupled with the NURBS/cubic splines approach for generating morphed geometries and with the Artificial Bee Colony/ Broyden-Fletcher-Goldfarb-Shanno optimizer for determining the actuator displacements. A redesign of the UAS-S4 wing was performed in two stages. The first included only a modification in the plan-form shape and was aimed at obtaining a baseline wing design better suited for long surveillance flights, while the second step included the optimization of the airfoil to improve upper surface flow laminarity and reduce the drag coefficient. The redesign was performed

using a multi-point optimization approach, covering 7 typical cruise flight conditions. Another application of the VLM was to analyse the drag reductions obtained for the MDO 505 project model, a low aspect ratio wing equipped with a flexible upper surface. The airfoil optimizations were performed in two-dimensions for 9 flight cases, and then the impact, on the three-dimensional wing, of using the morphed airfoils instead of the baseline airfoil was presented.

2.2.6 Sixth journal paper

In Chapter 8, the paper "Numerical Simulation and Wind Tunnel Tests Investigation and Validation of a Morphing Wing-Tip Demonstrator Aerodynamic Performance" is presented, paper that was submitted to the *Aerospace Science and Technology* and is currently under review. The paper presents the comparisons between the numerical CFD simulations and the wind tunnel experimental results for the MDO 505 project morphing wing.

Details about the morphing wing technology demonstrator were presented. Optimizations were performed in order to determine the required actuator displacements as function of the flight condition. The resulting skin shapes were scanned using high-precision photogrammetry and used for constructing the three-dimensional geometries. A grid convergence study was performed to determine the required meshing characteristics, and a script was created to automatize the mesh generation procedure. The morphed geometries were analysed with the ANSYS FLUENT high-fidelity CFD solver. The turbulence and transition models used for these calculations were presented, as well as the methods for solving the equations. Experimental tests were performed at the NRC subsonic wind tunnel and included upper surface transition measurements using Infra-Red thermography, pressure sensors acquisitions and aerodynamic loads measurements using a high-precision balance. The comparisons between the numerical and experimental results were presented.

2.3 Concluding Remarks

Following the aforementioned research steps, the flight performance of the wing of the unmanned aerial vehicle was improved using a morphing wing system, from establishing the concept of the flexible upper skin, developing fast and accurate methods for performing the optimizations and evaluating the aerodynamic characteristics and determining two-dimensional and three-dimensional morphed shapes according the desired objectives, for flight conditions cover a significant part of the aircraft's flight envelope.

CHAPTER 3

OPTIMIZATION OF AN UNMANNED AERIAL SYSTEM WING USING A FLEXIBLE SKIN MORPHING WING

Oliviu Şugar Gabor, Andreea Koreanschi and Ruxandra Mihaela Botez
LARCASE Laboratory of Applied Reasearch in Active Controls,
Avionics and Aeroservoelasticity
École de Technologie Supérieure, 1100 rue Notre Dame Ouest,
Montréal, H3C1K3, Québec, Canada

This article was published in *SAE International Journal of Aerospace*, vol. 6, no 1, p. 115-121

Résumé

Dans cet article, nous décrivons une méthodologie pratiquement efficace pour améliorer les caractéristiques aérodynamiques de l'aile d'un système autonome de vol en utilisant une approche de changement de forme. Nous avons remplacé une partie des surfaces supérieures et inférieures des ailes originales avec une peau flexible en matériaux composites dont sa forme peut être modifiée, selon les conditions de vol variables, à l'aide des actionneurs placés à l'intérieur de l'aile. Les déplacements optimaux des actionneurs, en fonctions des caractéristiques de l'écoulement externe, sont déterminées en utilisant un nouvel optimiseur basé sur un algorithme génétique, couplé avec une extension numérique en trois dimensions du modèle classique de la ligne portante pour l'estimation des coefficients aérodynamiques des ailes modifiées. Nous avons utilisé l'outil d'optimisation pour réduire le coefficient de traînée globale de l'aile d'un système autonome de vol militaire équipée avec la peau flexible. Nous avons obtenu de bonnes solutions pour une très petite fraction du coût de calcul nécessaire lors de l'exécution d'un même type de calcul pour un écoulement visqueux.

Abstract

In this paper, we describe a practically efficient methodology of improving the aerodynamic characteristics of an unmanned aerial system's wing using a morphing approach. We have replaced a part of the original wings' upper and lower surfaces with a flexible, composite material skin whose shape can be modified, according to the variable airflow conditions, using internally placed actuators. The optimal displacements of the actuators, as functions of the external flow characteristics, are determined using a genetic algorithm based optimizer, coupled with a three - dimensional numerical extension of the classical lifting line model for estimating the modified wing aerodynamic coefficients. We have used the optimization tool to decrease the overall drag coefficient of a military grade unmanned aerial system's wing equipped with the flexible skin. We have obtained good quality solutions for only a fraction of the computational cost needed when performing viscous flow field calculations.

3.1 Introduction

In recent years, Unmanned Aerial Systems (UAS) have become increasingly used in both military and civil aviation. Their main goal has been performing long time surveillance flights, at various altitudes and flight speeds, and sometimes in rapidly changing weather conditions. Because of the increasing demand of UAS's, engineers and designers have searched for methods to improve their flight performances, in order to make them more adaptable for various flight missions, to improve their aerodynamic efficiency and to increase their effective range and payload.

One answer to all these aircraft design challenges is to use a morphing technique, to provide the aircraft with the capacity of detecting the changes occurring in the airflow around it and to adapt to them by modifying its geometry, usually the wing, during flight. Sofla et al. (2010) conducted a comprehensive study of the various aircraft morphing solutions proposed by different authors.

A remarkable project into developing a functional morphing aircraft was Lockheed Martin's unmanned combat air vehicle (UCAV), which had wing folding capabilities (Love et al., 2007), (Rodriguez, 2007). The UCAV would be capable of long range cruise by minimizing fuel burn using an extended wing span, as well as transitioning into the attack mode, with higher maximum speed and increased manoeuvrability by decreasing its wing span. A functional model of the UCAV was designed, fabricated and tested in the wind tunnel, at speeds ranging from the subsonic incompressible regime up to transonic conditions (Ivanco et al., 2007).

Gamboa et al. (2007) presented another concept of a morphing wing developed for a small Unmanned Aerial Vehicle. The morphing wing created had both span and chord expansion capabilities, its purpose was to obtain the overall drag reduction with respect to the original, fixed wing, for low speeds ranging from 15 m/s up to 50 m/s. Drag reductions between 14.7% at a speed of 20 m/s and 34.5% at a speed of 50 m/s have been obtained.

NEXTGEN Aeronautics proposed an UAV design with a wing structure capable of being transformed from a high span configuration for slow speed flights, to a configuration with a reduced wing span, adapted to high speed flight (Flanagan et al., 2007). In this proposed solution, the wing was based on a moveable truss structure that could be controlled using electro - mechanical actuators, in order to adjust the wing span, area and shape according to variable flight conditions. In August 2006, NEXTGEN performed a successful flight test of the prototype.

The CRIAQ 7.1 project took place between 2006 and 2009 and was realized following a collaboration approach between teams from École de Technologie Supérieure (ÉTS), École Polytechnique de Montréal, Bombardier Aerospace, Thales Canada and the Institute for Aerospace Research – National Research Canada (IAR - NRC). The objective of the project was to improve and control the laminarity of the flow past a morphing wing, in order to obtain important drag reductions.

In this project, the active structure of the morphing wing combined three main subsystems: a flexible, composite material upper surface, stretching between 3% and 70% of the airfoil chord; a rigid inner surface; a Shape Memory Alloy (SMA) actuator group located inside the wing box, which could morph the flexible skin at two points, located at 25.3% and 47.6% of the chord (Brailovski et al., 2008). The reference airfoil chosen was the WTEA laminar airfoil. The morphing airfoil was designed for low subsonic flow conditions. A theoretical study of the morphing wing system was performed by Pages (2007) and very promising results were obtained; the morphing system was able to delay the transition location downstream by up to 30% of the chord, and to reduce the airfoil drag by up to 22%. The wind tunnel tests were performed in the 2 m by 3 m atmospheric closed circuit subsonic wind tunnel at IAR - NRC and validated the numerical simulations (Sainmont et al., 2009).

3.2 Finite Span Wing Model

Prandtl's classical lifting line theory, first published in 1918 (Prandtl, 1918), represented the first analytical model capable of accurately predicting the lift and induced drag of a finite span lifting surface. The aerodynamic characteristics predicted by the theory were repeatedly proven to be in close agreement with experimental results, for straight wings with moderate to high aspect ratio.

The solution of Prandtl's classical equation is in the form of an infinite sine series for the bound vorticity distribution. Traditionally, the series is truncated to a finite number of terms, and collocation methods are used to determine the sine series coefficients, method that was firstly presented by Glauert (1983). Popular methods of determining the bound vorticity distribution included those developed by Tani (1934) and Multhopp and Schwabe (1938). Other authors have proposed modified versions of the original lifting line theory, modifications that increase the quality of the obtained results (Jones, 1941), increase the applicability or the model (Weissinger, 1947) or make use of information regarding the wing's airfoil sections (Sivells and Neely, 1947). More modern solutions include that of

Rasmussen and Smith (1999), who presented a more rigorous method based on a Fourier series expansion.

With the development of more efficient and powerful computers, several authors have also proposed purely numerical methods for solving Prandtl's lifting line equation. Among these, we can mention McCormick (1995), Anderson and Corda (1980) or Katz and Plotkin (1991).

However, all the above mentioned numerical methods were based on Prandtl's assumptions of a straight distribution of bound vorticity, and therefore are subjected to all the limitations of the classical lifting line model: a single lifting surface of moderate to high aspect ratio, with no sweep angle and no means of considering the effects of the various wing sections airfoils.

The method used in this paper is based on the original work of Phillips and Snyder (2000). Whereas the classical lifting line theory is based on the assumption of a straight lifting surface and the application of the two - dimensional Kutta - Joukowski vortex lifting law for a three dimensional flow, the modern adaptation uses a general horseshoe vortex distribution and uses a fully three - dimensional vortex lifting law. Because of these characteristics, the method has a much wider applicability range compared to the original theory, including multiple lifting surfaces and wings arbitrary camber, sweep and dihedral angle.

3.2.1 Wing calculation method

In numerical lifting line models, the continuous distribution of bound vorticity over the lifting surface and the continuous distribution of trailing vorticity are approximated using a finite number of horseshoe vortices. The bound portion of the vortices can be aligned with the wing's quarter chord line, thus taking into consideration the local values of the sweep and dihedral angles, while the trailing portions remain aligned with the free stream velocity, as shown in Figure 3.1.

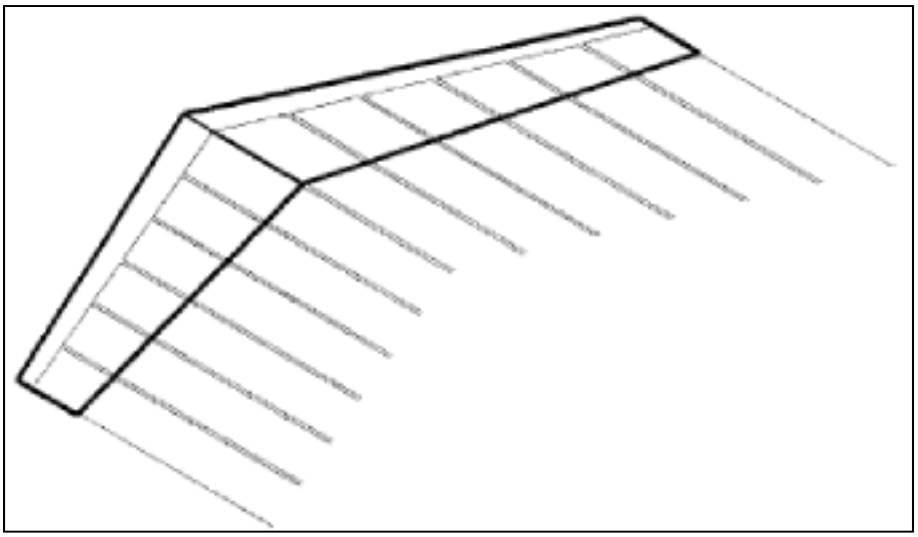

Figure 3.1 Horseshoe vortices distributed along the wingspan
Taken from Phillips and Snyder (2000)

Each horseshoe vortex is made up of three straight vortex segments. To calculate the velocity induced, at an arbitrary point in space, by a vortex segment, we apply the Biot - Savart law (Katz and Plotkin, 1991):

$$\mathbf{V} = \frac{\Gamma}{4\pi} \frac{\mathbf{r}_1 \times \mathbf{r}_2}{\left|\mathbf{r}_1 \times \mathbf{r}_2\right|^2} \mathbf{r}_0 \left(\frac{\mathbf{r}_1}{\mathbf{r}_2} - \frac{\mathbf{r}_2}{\mathbf{r}_1} \right) \tag{3.1}$$

In the above equation Γ is the vortex segment intensity, $\mathbf{r}_1$ and $\mathbf{r}_2$ are the spatial position vectors from the starting and ending points of the vortex segment to an arbitrary point in space and $\mathbf{r}_0$ is the vector along the straight vortex segment. Phillips and Snyder (2000) propose a form more suitable from a numerical point of view:

$$\mathbf{V} = \frac{\Gamma}{4\pi} \frac{\left(r_1 + r_2\right)\left(\mathbf{r}_1 \times \mathbf{r}_2\right)}{r_1 r_2 \left(r_1 r_2 + \mathbf{r}_1 \mathbf{r}_2\right)} \tag{3.2}$$

Figure 3.2 presents the typical geometry of one horseshoe vortex. When we apply equation (3.2) for all segments of the horseshoe vortex, we can determine the velocity induced at an arbitrary point in space:

$$\mathbf{V}=\frac{\Gamma}{4\pi}\frac{\mathbf{v}_\infty\times\mathbf{r}_2}{r_2\left(r_2-\mathbf{v}_\infty\mathbf{r}_2\right)}+\frac{\Gamma}{4\pi}\frac{\left(r_1+r_2\right)\left(\mathbf{r}_1\times\mathbf{r}_2\right)}{r_1r_2\left(r_1r_2+\mathbf{r}_1\mathbf{r}_2\right)}-\frac{\Gamma}{4\pi}\frac{\mathbf{v}_\infty\times\mathbf{r}_1}{r_1\left(r_1-\mathbf{v}_\infty\mathbf{r}_1\right)} \tag{3.3}$$

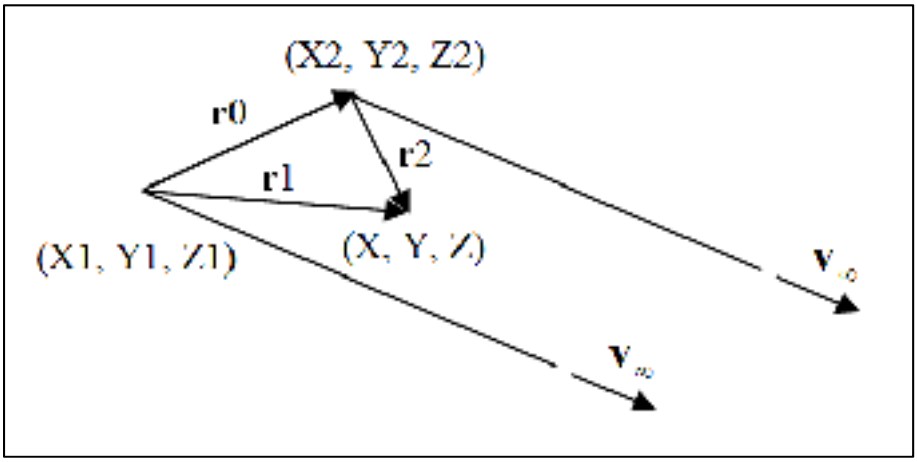

Figure 3.2 Geometry and position vectors for one horseshoe vortex

When considering the distribution of horseshoe vortices over the lifting surface, equation (3.3) can be used to compute the velocity induced at any point on the lifting surface, by any of the horseshoe vortices, provided that the intensities Γ are known.

If we approximate the continuous distribution of bound vorticity with a finite number of N distinct horseshoe vortices, each one having its own intensity Γ_i, we will need a mathematical system of N equations relating these intensities to some known properties of the wing. In order to find such a relation, we turn to the three dimensional vortex lifting law (Saffman, 1992). Using the same approach as that suggested by Saffman (1992) or by Phillips and Snyder (2000), the non - viscous force acting on a horseshoe element of the lifting surface is equal to:

$$\mathbf{dF}_i = \rho \Gamma_i \mathbf{V}_i \times \mathbf{dl}_i \tag{3.4}$$

In the above equation, ρ is the air density, Γ_i is the unknown intensity of the horseshoe vortex, $\mathbf{V}_i$ is the local airflow velocity and $\mathbf{dl}_i$ is a spatial vector along the bound segment of the horseshoe vortex, aligned in the direction of the local circulation.

In order to calculate the local velocity, with each horseshoe vortex we have to associate a control point at which the induced velocities will be determined. We consider the control points to be situated on the wing surface, at equal distance between the two semi-infinite trailing legs of the horseshoe vortex, at the three quarter chord point, as measured from the local section leading edge. The importance of choosing the three quarter chord point has been revealed by various authors (Multhopp and Schwabe, 1938), (Weissinger, 1947), (Katz and Plotkin, 1991). Thus, the local velocity at each control point becomes:

$$\mathbf{V}_i = \mathbf{V}_\infty + \sum_{j=1}^{N} \Gamma_j \mathbf{v}_{ij} \tag{3.5}$$

We denote by $\mathbf{V}_\infty$ the free stream velocity, while $\mathbf{v}_{ij}$ represents the velocity induced by the horseshoe vortex j, considered to be of strength equal to unity, at the control point i, and is given by equation (3.3).

From wing theory, we know that the magnitude of the lifting force acting on an A_i area section of the wing located at a control point i can be written as:

$$\left\| \mathbf{F} \right\|_i = \frac{1}{2} \rho V_\infty^2 A_i C_{l_i} \tag{3.6}$$

The lift coefficient C_{l_i} is that of the local airfoil situated at the wingspan section corresponding to control point i and it depends on the local effective angle of attack. If the lift

coefficient can be determined using other means, such as experimentally determined lift curves or using a two - dimensional airfoil calculation solver, then, by replacing the local velocity given by equation (3.5) into equation (3.4), and then equating the modulus of the three - dimensional vortex lifting force with the expression give in equation (3.6), we obtain the following relation:

$$\left\| \rho\Gamma_i \left(\mathbf{V}_\infty + \sum_{j=1}^{N} \Gamma_j \mathbf{v}_{ij} \right) \times \mathbf{dl}_i \right\| = \frac{1}{2} \rho V_\infty^2 A_i C_{l_i} \tag{3.7}$$

By writing equation (3.7) for all control points along the wing span, we obtain a nonlinear system of N equations for the calculation of the unknown horseshoe vortex intensities. The system can be solved in an iterative fashion, using Newton's method. However, in order to avoid the necessity of analytically calculating all the entries in the system's Jacobian matrix, we use Broyden's quasi - Newton method (Broyden, 1965), in which the Jacobian is replaced by an approximation that is updated at each iteration.

Once the intensities of the horseshoe vortices have been determined, the total non - viscous aerodynamic force can be readily calculated by summing up all the individual forces given by equation (3.4), resulting:

$$\mathbf{F} = \sum_{i=1}^{N} \left[\rho\Gamma_i \left(\mathbf{V}_\infty + \sum_{j=1}^{N} \Gamma_j \mathbf{v}_{ij} \right) \times \mathbf{dl}_i \right] \tag{3.8}$$

The calculation method presented, like that developed by Sivells and Neely (1947), can be used to approximate the profile drag coefficient of the wing, since the spanwise lift distribution will not only verify all the constraints imposed by the numerical lifting line theory, but also those imposed by several wingspan airfoil characteristics. As presented in (Sivells and Neely, 1947), the profile drag coefficient of the wing is given by:

$$C_{D0} = \frac{1}{S}\int_{-b/2}^{b/2} C_d(y)c(y)dy \approx \frac{1}{S}\sum_{i=1}^{N} C_{d_i} c_i \Delta y_i \tag{3.9}$$

In the above equation, S represents the total wing area, b is the wing span, C_{d_i} is the profile drag coefficient of wingspan section i, as calculated from the available experimental data or calculated by the two - dimensional solver, while c_i is the wing's chord at the given control point section.

3.2.2 Two - dimensional flow solver

The code used for the calculation of the two - dimensional aerodynamic characteristics of the wing's control sections is XFOIL, version 6.96, developed by Drela and Youngren (2001). The XFOIL code was chosen because it has proven its precision and effectiveness over time, and because it reaches a converged solution very fast. The inviscid calculations in XFOIL are performed using a linear vorticity stream function panel method. A Karman - Tsien compressibility correction is added, allowing good predictions all the way to transonic flow. For the viscous calculations, XFOIL uses a two - equation lagged dissipation integral boundary layer formulation, and incorporating the e^N transition criterion. The flow in the boundary layer and in the wake is interacted with the inviscid potential flow by using the surface transpiration model (Drela and Youngren, 2001).

3.3 Wing Morphing Technique

The main idea behind the morphing concept is to replace a part of the wing's upper and lower surfaces with a flexible skin that can be modified using actuators placed inside the wing body. To perform the optimization, the flexible skin will be chosen to start on the wing's lower surface, at 20% of the chord (as measured from the leading edge), it will go around the wing's leading edge and continue on the upper surface until 65% of the chord (as measured from the leading edge). A section of the wing equipped with the morphing skin is shown in Figure 3.3.

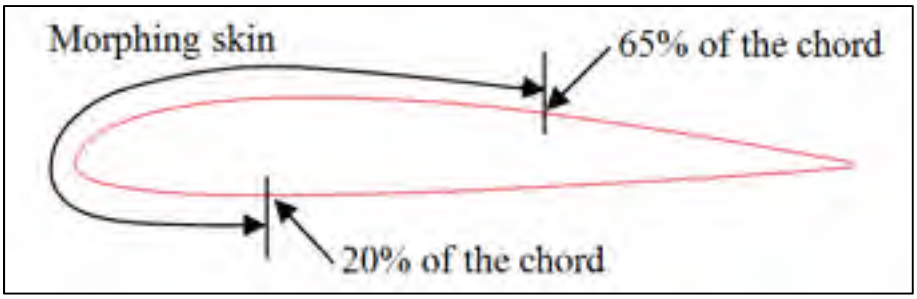

Figure 3.3 Extent of the morphing skin for one spanwise station

Along the wingspan direction, at several predetermined stations, we place the actuator lines. Each of the actuation lines is aligned with the local chord of the spanwise station. To modify the shape of the flexible skin, we chose a number of 10 actuation points for each spanwise actuator line, points that are distributed along the length of the skin, but with a greater density around the leading edge. The choice of this high number was found necessary in order to accurately control the deformation of the leading edge and to avoid unrealistic shapes during the optimization process.

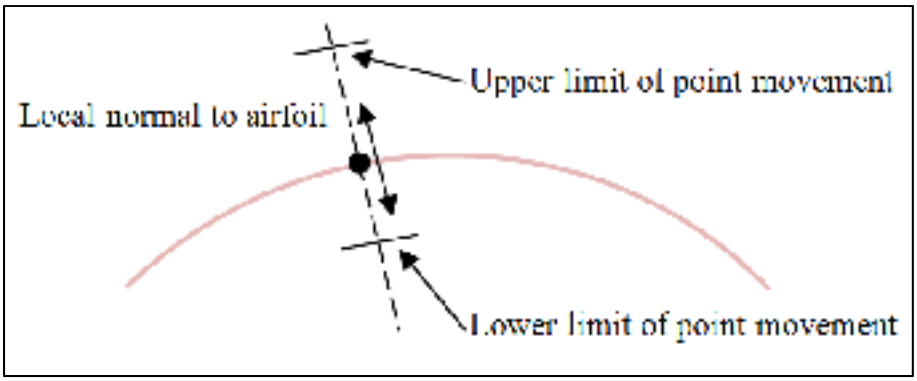

Figure 3.4 Constraints for actuation points movement

Each actuation point is constrained to move only on the direction given by the local normal vector to the airfoil surface. Also, the magnitude of the displacement is limited between the values of 1% of the local wing chord when the actuation point is pushed towards the outside of the original airfoil curve and 0.5% of the local wing chord when the actuation point is

pulled towards the inside of the original airfoil curve. The constraint method for the actuators is explained in Figure 3.4.

The distribution of actuation points for any spanwise airfoil section is depicted in Figure 3.5. In order to regenerate the airfoil shape of each of the spanwise stations, regeneration necessary after each movement of any of the actuation points, we have used a Non Uniform Rational B - Splines (NURBS) parameterization of the airfoil curve (Piegl and Tiller, 1997).

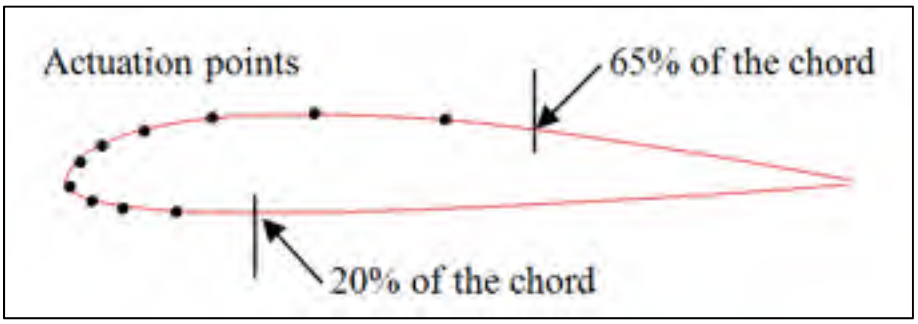

Figure 3.5 Position of the actuation points for one spanwise station

3.4 Wing Optimization Technique

The objective of the aerodynamic optimization is to decrease the wing's drag coefficient. The optimization procedure consists in finding the optimal displacements of all the actuation points, for all the spanwise calculation sections, in such a way that, for any given combination of free stream Mach number and geometric angle of attack, the drag of the wing equipped with the morphing skin is as small as possible. The optimization tool is a genetic algorithm code, coupled with the numerical lifting line code for the calculation of the wing's aerodynamic coefficients.

Genetic algorithms are numerical optimization algorithms inspired by natural selection and genetics of living organisms. The algorithm is initialized with a population of guessed individuals, and uses three operators namely selection, crossover and mutation to direct the

population towards convergence to the global optimum, over a series of generations (Coley, 1999), (Herrera, 1998).

Each individual in the population is defined by a matrix of real values, that of the displacements of all the control points $\delta(i,j)$ where $i=1,2,...,10$ and $j=1,2,...,N$. The number of rows is equal to the number of actuation points on each spanwise section, while the number of columns is equal to the predetermined number of spanwise actuation lines.

In order to evaluate all individuals in the population, an objective function, called the fitness function, must be defined. Because the goal of the optimization is to decrease the wing's drag coefficient, the following fitness function was used in the algorithm:

$$Fitness = \frac{1}{C_D} \tag{3.10}$$

The fitness function is calculated for all individuals of a given generation. The higher the values of the fitness function, the higher are the chances of the individual to be selected for building the next generation.

The outline of the optimization method and all the steps of the genetic algorithm are presented in Figure 3.6. The process of evaluation of the fitness function, selection of the best individuals to become parents, crossover and mutation of the new individuals continues in an iterative way, until the maximum number of generations is reached. Tournament selection, simulated binary crossover (Herrera, 1998) and polynomial mutation (Herrera, 1998) with a probability of 0.01 were used. The termination criterion was simply a given number of generations.

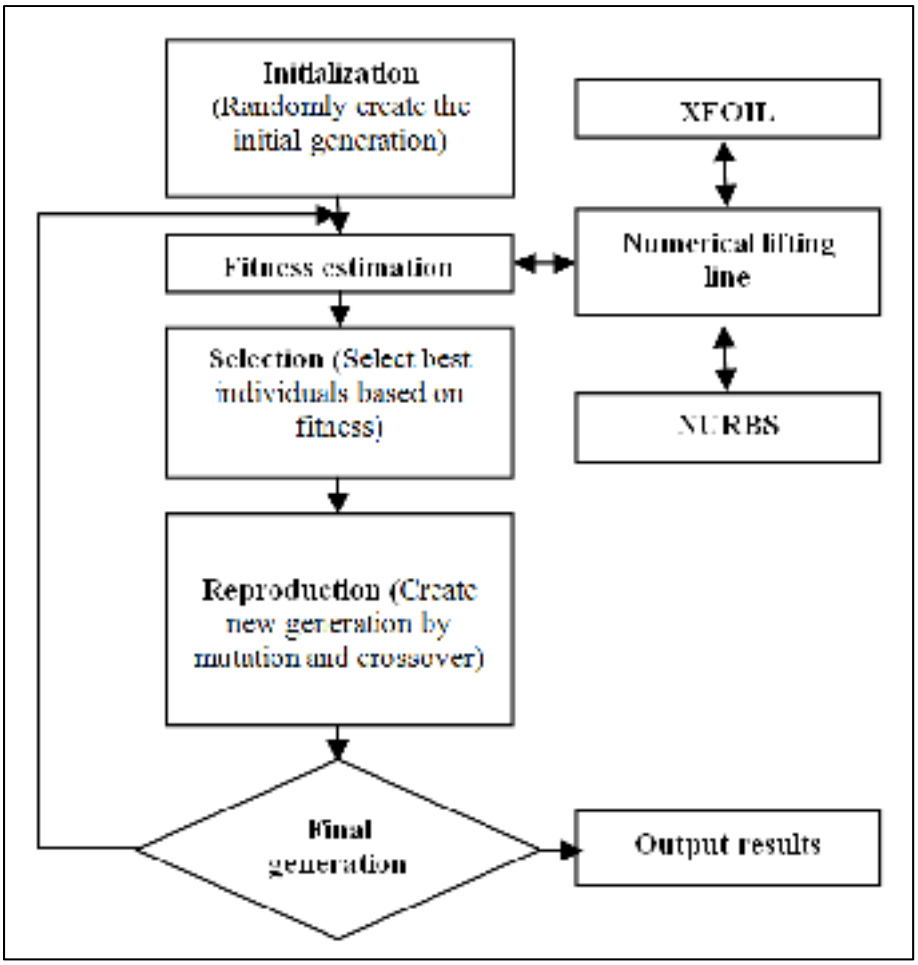

Figure 3.6 Outline of the genetic algorithm optimization tool

The optimization tool has already demonstrated its capabilities with the problem of increasing the laminarity of the flow and decreasing the viscous drag coefficient of the ATR 42 airfoil, for several different flight conditions (Sugar Gabor, 2012). The optimization was performed for the ATR 42 airfoil, with a chord of 0.244 meters. The morphing skin stretched between 10% and 70% of the chord, only on the upper surface, with only two actuators, situated at 30% and 50% of the chord. The optimization was performed in the subsonic incompressible flow regime for three angle of attack values, -2, 0 and 2 degrees, while the Mach number varied between 0.1 and 0.2 and the Reynolds number varied between 578000 and 1156000. It has been possible to delay the transition point on the upper surface of the airfoil by as much as 24.81%, and to reduce the drag coefficient with up to 26.73%.

3.5 Brief Description of the UAS

The wing optimization procedure shall focus on replacing the conventional, rigid wing of the Hydra Technologies S4 Éhecatl Unmanned Aerial System with a morphing wing. The S4 was designed and built in Mexico, and it was created as an aerial unmanned surveillance system, directed towards providing security and surveillance capabilities for the Armed Forces, as well as civilian protection in hazardous situations. It is a high performance vehicle, capable of reaching altitudes of 4500 m and cruising speeds of over 100 knots. The purpose of replacing the conventional wing with a morphing one is the ability to dynamically change its shape during flight, reduce the wing's drag coefficient, and thus, reduce engine fuel consumption. This will grant the S4 UAS extended flight times and a longer effective range, improving the cost efficiency of its operation.

Figure 3.7 Hydra Technologies S4 Éhecatl

3.6 Optimization of the S4 Wing

Concerning the aerodynamic optimization of the complete wing, the objective of the optimization was to decrease the overall drag coefficient, including the induced drag and the estimated wing profile drag. The optimization was performed for three values of the Mach, namely Mach = 0.10, 0.15, 0.20, and for a limited range of angles of attack, between

0 degrees and 5 degrees. Because we have also tried to reduce the induced drag of the wing, no constraints were imposed on the variation of the lift coefficient.

Figure 3.8 presents the variation between the coefficients of the morphed and original wing, in percentages, for the lift coefficient CL, overall drag coefficient CD and pitching moment coefficient about the root chord leading edge Cm, for a Mach number of 0.10. A negative percentage value means that the morphed wing coefficients are smaller than those of the original wing.

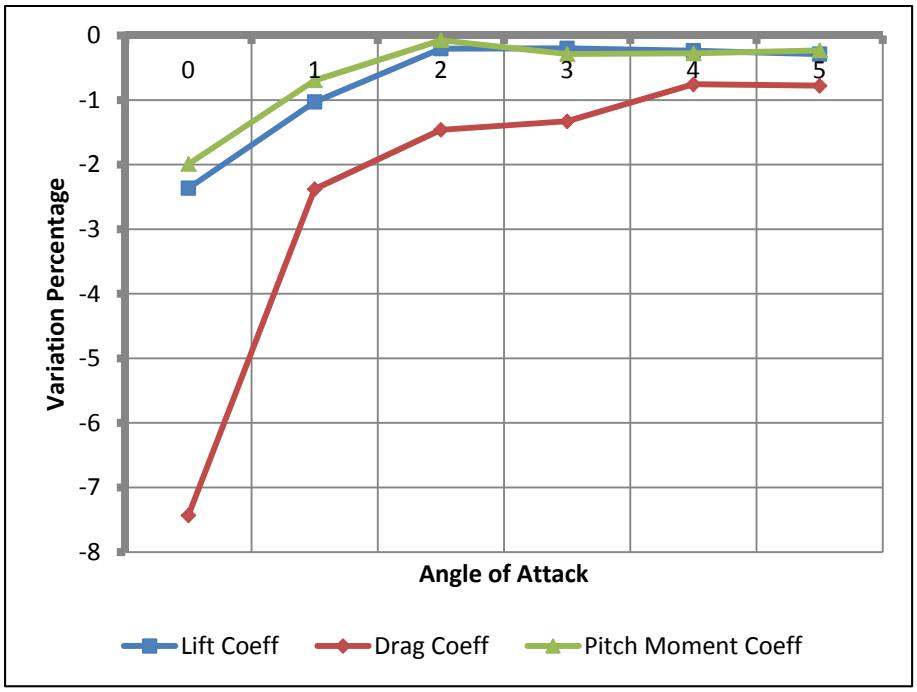

Figure 3.8 Variation percentages for Mach = 0.10

Figure 3.9 presents the variation between the coefficients of the morphed and original wing, in percentages, for the lift coefficient CL, overall drag coefficient CD and pitching moment coefficient about the root chord leading edge Cm, for a Mach number of 0.15. A negative percentage value means that the morphed wing coefficients are smaller than those of the original wing.

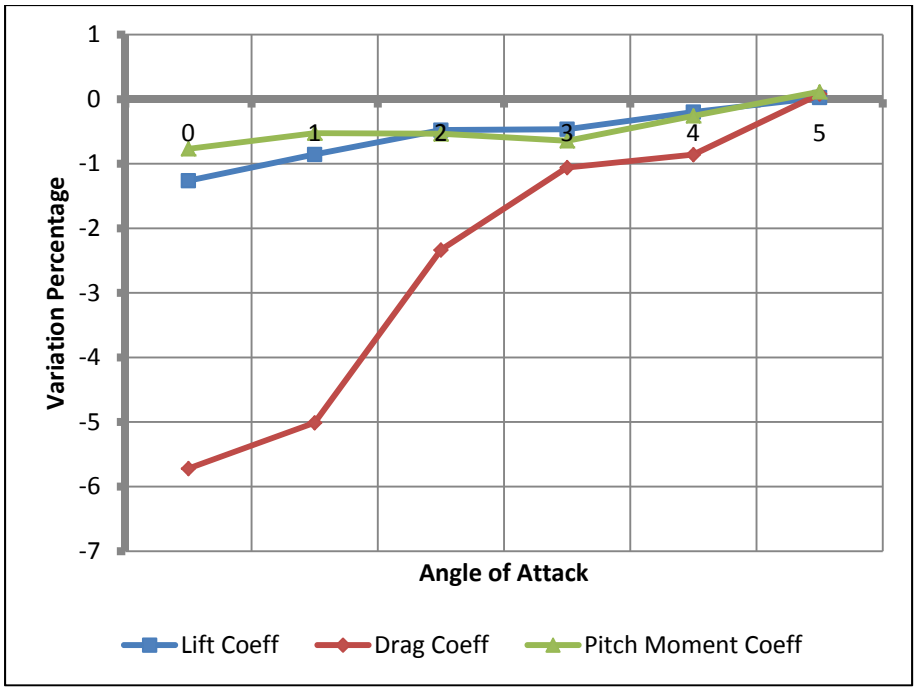

Figure 3.9 Variation percentages for Mach = 0.15

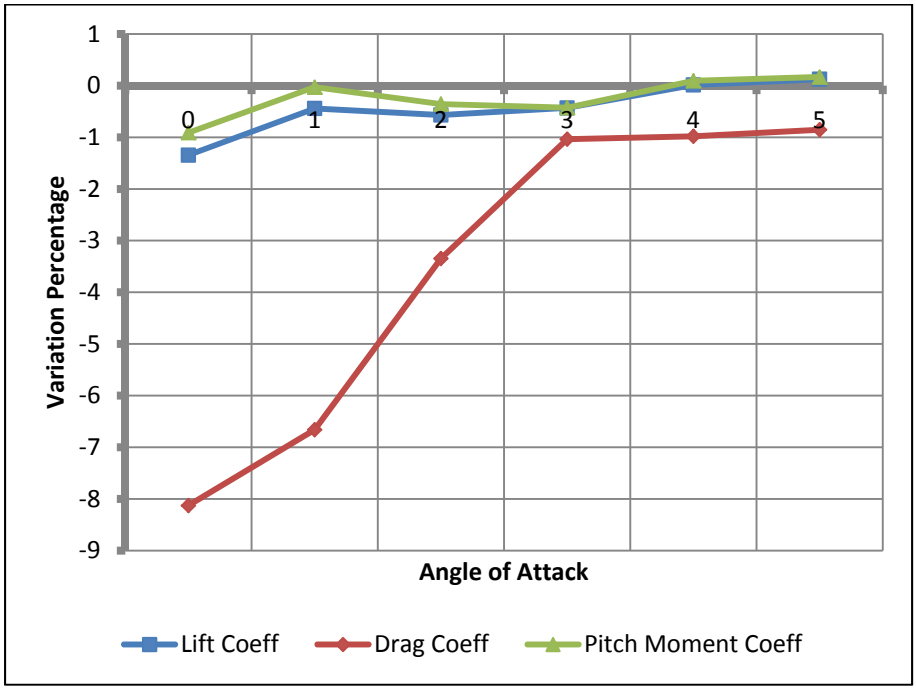

Figure 3.10 Variation percentages for Mach = 0.20

Figure 3.10 presents the variation between the coefficients of the morphed and original wing, in percentages, for the lift coefficient CL, overall drag coefficient CD and pitching moment coefficient about the root chord leading edge Cm, for a Mach number of 0.20. A negative percentage value means that the morphed wing coefficients are smaller than those of the original wing.

3.7 Conclusions

We have successfully obtained the reduction of the overall drag coefficient of the S4 UAS wing. The reduction drastically decreases as the angle of attack increases, because of the increasingly significant contribution of the induced drag, which cannot be effectively modified using this type of wing morphing. For a Mach number of 0.10, the drag reductions vary between 7.51% and 0.76%. For a Mach number of 0.15, the drag reductions vary between 5.76% and 0.12%. For a Mach number of 0.20, the drag reductions vary between 8.07% and 0.92%. The drag reduction obtained is mainly caused by the reduction of the profile drag coefficient, indicating an increased laminarity of the flow. Although we have imposed no constraints on the lift coefficient, the variations obtained are relatively small, with an average reduction of less than 1%, and a maximum reduction of 2.30%.

Acknowledgments

We would like to thank the Hydra Technologies Team in Mexico for their continuous support, and especially Mr. Carlos Ruiz, Mr. Eduardo Yakin and Mr. Alvaro Gutierrez Prado.

CHAPTER 4

IMPROVING THE UAS-S4 EHECATL AIRFOIL HIGH ANGLE OF ATTACK PERFORMANCE CHARACTERISTICS USING A MORPHING WING APPROACH

Oliviu Şugar Gabor, Antoine Simon, Andreea Koreanschi and Ruxandra Mihaela Botez
LARCASE Laboratory of Applied Reasearch in Active Controls,
Avionics and Aeroservoelasticity
École de Technologie Supérieure, 1100 rue Notre Dame Ouest,
Montréal, H3C1K3, Québec, Canada

This article was published in *Proceedings of the Institution of Mechanical Engineers, Part G: Journal of Aerospace Engineering*, DOI: 10.1177/0954410015587725

Résumé

Dans ce papier, une approche de type aile déformable qui utilise une nouvelle méthodologie et ses résultats pour l'optimisation a des grands angles d'attaque du profil aérodynamique du système autonome de vol S4 sont décrits. Le délai de la séparation de la couche limite, couplé à l'augmentation du coefficient de portance maximal, a été réalisé en utilisant un outil interne d'optimisation basée sur l'algorithme de la Colonie des Abeilles Artificielles, couplé avec l'algorithme Broyden-Fletcher-Goldfarb-Shanno dans le but de fournir un raffinement final de la solution. Les résultats obtenus ont été validés avec un logiciel avancé d'optimisations multi-objectifs, disponible dans le commerce. Les calculs aérodynamiques ont été effectués en utilisant un procédé linéaire de panneau en 2D, couplé à un modèle de couche limite incompressible et à un critère d'estimation de transition. Pour des très petits déplacements de la surface supérieure de l'aile, de moins de 2,5 mm, des augmentations du coefficient de portance jusqu'à 18%, avec des réductions de traînée pertinentes ont été atteints, en retardant la séparation avec succès pour les angles d'attaque élevés.

Abstract

In this paper, a morphing wing approach with a new methodology and its results for the high angles of attack optimization of the S4 unmanned aerial system airfoil are described. The boundary layer separation delay, coupled with an increase of the maximum lift coefficient, was achieved using an in-house optimization tool based on the Artificial Bee Colony algorithm, coupled with the Broyden-Fletcher-Goldfarb-Shanno algorithm to provide a final refinement. The obtained results were validated with an advanced, multi-objective, commercially available optimizing tool. The aerodynamic calculations were performed using a 2D linear panel method, coupled with an incompressible boundary layer model and a transition estimation criterion. For very small displacements of the airfoil surface, of less than 2.5 mm, lift coefficient increases of up to 18% together with relevant drag reductions have been achieved, successfully delaying separation for the high angles of attack range.

4.1 Introduction

The flow separation phenomenon represents the breakaway or detachment of the fluid flow from a solid surface, most often caused by a severe adverse pressure gradient (Simpson, 1996) or by the surface geometrical characteristics (Kim, 1980). Separation is generally accompanied by a significant thickening of the rotational flow region adjacent to the airfoil/wing surface, and leads to important lift loss and drag increase. Since the early years of aviation, engineers have been preoccupied with developing the means to control the separation phenomenon, or to avoid it completely if possible. The use of steady blowing and suction through slots placed at various locations on the wing surface has been known since the 1950s (Lachmann, 2014), and the system has been implemented on production aircraft, but due to its technical complexity and increased weight, it has been considered inefficient (Attinello, 1961). Another method of separation control, introducing periodic perturbations in the flow via an excitation mechanism, has proven to be significantly more effective than suction and/or blowing. Its success has been demonstrated in a wide variety of configurations (various airfoils, delta wings, bluff bodies) (Greenblatt and Wygnanski, 2000). In the 1990s,

other theoretical and technical solutions were developed for separation control, such as energy efficient micro-electro-mechanical systems (MEMS) (McMichael, 1996) or the use of adaptive, intelligent structures (Friedman and Millott, 1995).

In this paper, a structurally feasible and efficient wing morphing technique is used to delay boundary layer separation and improve the aerodynamic characteristic of an airfoil at high angles of attack. By actively modifying the wing shape using this morphing technique, an optimal shape for the wing and/or airfoil can be provided during each distinct phase of aircraft flight. The main advantage of morphing is that the same system used for improving high angles of attack behaviour can be used for other purposes, such as increasing flow laminarity and obtaining a reduction of drag in cruise conditions (Sugar Gabor, 2013), (Sugar Gabor, 2012). In addition to achieving important reductions in drag and fuel consumption, recent research has shown that adaptive morphing wings can also be effectively used to replace conventional high-lift devices or conventional control surfaces (Pecora et al., 2011), (Barbarino et al., 2011), (Diodati et al., 2013), (Pecora, 2012), (Pecora et al., 2014), (Pecora et al., 2014) thus showing great promise for the development of the next generation aircraft.

In recent years, there has been increasing interest in the development and application of morphing solutions on Unmanned Aerial Vehicles (UAVs), due to increasingly higher efficiency requirements and much simplified certification issues. Using a telescopic pneumatic actuator, Neal et al. (2004) designed and validated a variable wing plan-form UAV, capable of significant span and sweep changes. Wind tunnel testing showed that only three configurations were necessary to increase the lift to drag ratio over the entire flight envelope. Supekar (2007) evaluated the aerodynamic performance of a two-segment, telescopic UAV wing that could also change the dihedral of the outer segment. Gamboa et al. (2007) designed a UAV wing capable of independent span and chord changes, with the aid of a telescopic spar and rib system. The numerical analysis demonstrated drag reductions of up to 23% when compared to the non-morphing geometry. Falcao (2011) designed and tested a morphing winglet for a military UAV, achieving important performance improvement by simply changing the winglet cant and toe angles. Do Vale et al. (2011) proposed a UAV

morphing wing capable of telescopic span changes and independent conformal camber changes.

One of the most advanced morphing projects was Lockheed Martin's Agile Hunter UAV (Bye and McClure, 2007), (Ivanco et al., 2007), (Love et al., 2007). The wind tunnel prototype was capable of folding the inner wing sections over the fuselage, in order to reduce the drag during transonic cruise. Another important project was NextGen Aeronautic MFX1 UAV, with variable wing sweep and wing area (Andersen, 2007), (Flanagan et al., 2007). The prototype was successfully flight tested, demonstrating the capability of achieving significant plan-form changes during various flight scenarios. Sofla et al. (2010) developed a morphing wing concept in which the wing could perform uniform, out-of-plane flexing, with the aid of Shape Memory Alloy (SMA) actuators. A numerical analysis was conducted in order to evaluate the performance of the UAV equipped with the morphing wing concept.

Gano and Renaud (2002) presented a concept to increase the aerodynamic efficiency of a UAV by gradually decreasing the wing thickness as the fuel inside the wing-mounted tank is consumed, thus decreasing the drag coefficient. Shyy (2010) presented research on small UAV airfoils that passively morph in response to changes in external aerodynamic forces, instead of using an active deformation mechanism. The flexibility of the wing improved performance by limiting flow separation at high angles of attack. Bartley-Cho et al. (2004) presented a variable camber wing, actuated by piezoelectric motors and integrated into a Northrop-Grumman combat UAV. Bilgen et al. (2007), (2009) designed and tested a concept of replacing the ailerons with local, continuous wing camber changes. Wind tunnel experiments and the flight testing of the UAV equipped with the morphing wing demonstrated the effectiveness of the concept at providing roll control.

The research presented in this paper continues that of the CRIAQ 7.1 project, whose objective was to improve and control the laminarity of the flow past a morphing wing, in order to obtain significant drag reductions (Botez, 2007). In CRIAQ 7.1, the active structure of the morphing wing combined three main subsystems: a flexible, composite material upper

surface, stretching between 3% and 70% of the airfoil chord, a rigid inner surface and a Shape Memory Alloy (SMA) actuator group located inside the wing box. The actuator group could morph the flexible skin at two points, located at 25.3% and 47.6% of the chord (Brailovski et al., 2008). The reference airfoil chosen for the project was the WTEA laminar airfoil and the morphing system was designed for low subsonic flow conditions. A theoretical study of the morphing wing system was performed (Pages, 2007), and very promising results were obtained: the morphing system was able to delay the transition location downstream by up to 30% of the chord, and to reduce the airfoil drag by up to 22%.

Two control approaches were used to provide the optimal SMA actuator displacements for each different flight condition. In the open loop configuration, the desired displacements were directly imposed on the system (Popov et al., 2010), while a novel, adaptive, neuro-fuzzy approach was used to predict and control the morphing wing performance (Grigorie, 2009). In the closed loop configuration, the displacements were automatically determined as a function of the pressure readings from the wing upper surface (Popov et al., 2010). The wind tunnel tests were performed in the 2 m by 3 m atmospheric closed circuit subsonic wind tunnel at IAR-CNRC, validating the numerical wing optimisations (Sainmont et al., 2009) and the designed control techniques (Grigorie, 2012).

The optimization procedure is focused on enhancing the aerodynamic characteristics of the Hydra Technologies S4 Éhecatl UAS airfoil. The S4 was designed and build in Mexico, and was created as an aerial unmanned surveillance system, directed towards providing security and surveillance capabilities for the Armed Forces, as well as civilian protection in hazardous situations. General information about the characteristics and flight performance of the S4 UAS is presented in Table 4.1. The purpose of optimizing the original airfoil using a morphing wing technology is to grant the S4 UAS increased aerodynamic efficiency, extended flight time and a longer effective range, improving its cost effectiveness.

Table 4.1 General information about the Hydra S4 UAS

Characteristic	Value
Maximum Takeoff Weight	80 kg
Wingspan	4.2 m
Mean Aerodynamic Chord	0.57 m
Wing Area	2.3 m^2
Operational Ceiling	15,000 ft
Maximum Airspeed	135 knots
Loitering Airspeed	35 knots
Operational Range	120 km

4.2 Morphing Wing Concept

Implementing an airfoil morphing technique on the real UAS-S4 requires that only a limited portion of the entire airfoil curve will be allowed to change, and that the modifications will be small enough in order to be feasible from a structural point of view. Any numerical optimization performed must be done by considering the technological possibilities and constraints required by the practical manufacture of the morphing wing structure. The concept presented in this paper is to replace a part of the UAS's conventional wing skin with a flexible skin that could be morphed using electrical actuators placed inside the wing structure. Figure 4.1 shows the basic idea of the morphing wing.

The imposed condition is that the flexible skin starts at 5% of the chord on the airfoil lower surface, goes around the leading edge and stretches up to 55% of the chord on the upper surface. The starting point was chosen on the airfoil's lower surface to allow a good control of the leading edge shape, while the skin's extent on the upper surface is limited by the presence of the wing control surfaces, such as the aileron and the flap. The skin is attached to the rigid part of the wing at both its ends, providing a smooth transition between the flexible and the fixed regions.

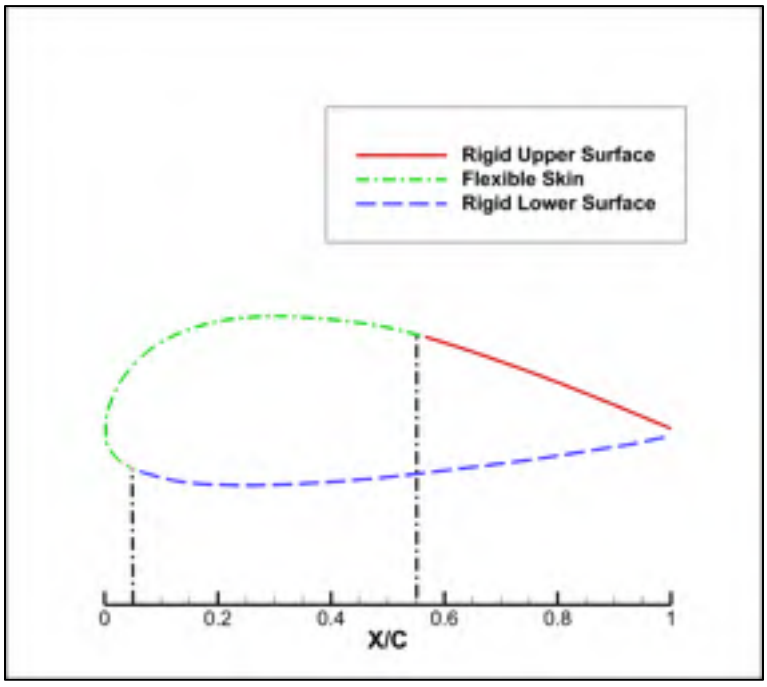

Figure 4.1 The morphing skin for the airfoil

4.2.1 Airfoil parameterization using NURBS

From a numerical perspective, the airfoil was parameterized using Non-Uniform Rational B-Splines (NURBS) (Piegl and Tiller, 1997). The NURBS are a generalization of B-Splines and Bézier curves, offering great flexibility and precision in representing and manipulating analytical curves. From a mathematical point of view, a NURBS curve is defined by its order, a polygon of weighted control points, and a knot vector:

$$\mathbf{C}(u) = \sum_{i=1}^{K} \frac{N_{i,n} w_i}{\sum_{j=1}^{K} N_{j,n} w_j} \mathbf{P}_i \tag{4.1}$$

In the above equation, u is the curve parameter, ranging from 0 (the start of the curve) to 1 (the end of the curve), K is the number of control points, $N_{i,n}$ is the i^{th} basis function, having the order n, w_i is the weight associated with the i^{th} control point, and $\mathbf{P}_i = [x_i, y_i]$ is the

control point. The basis functions are determined using the De Boor recursive formula (De Boor, 1978):

$$N_{i,1} = \begin{cases} 1, if\ t_i \le u \le t_{i+1} \\ 0, otherwise \end{cases}$$
$$N_{i,n} = \frac{u - t_i}{t_{i+n} - t_i} N_{i,n-1} + \frac{t_{i+n+1} - u}{t_{i+n+1} - t_{i+1}} N_{i+1,n-1} \tag{4.2}$$

where u is the curve parameter, n is the order of the basis function and t_i represents the i^{th} knot of the curve knot vector. The morphing part of the airfoil and the NURBS control polygon associated with it are presented in Figure 4.2.

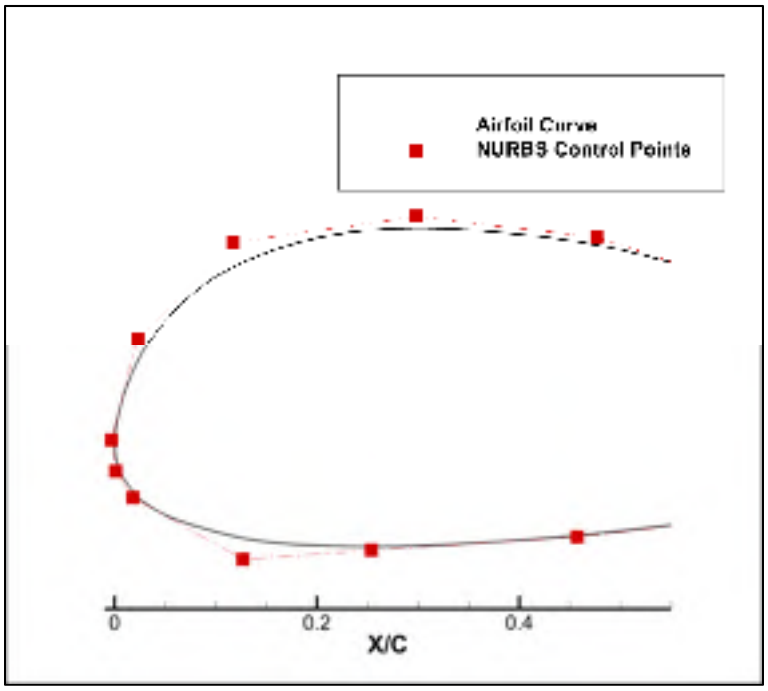

Figure 4.2 The NURBS control points for the original airfoil

The airfoil curve was parameterized with a 3rd degree NURBS curve, which ensures smoothness up to the second derivative, and seven control points corresponding to the flexible skin portion. This number of control points was found necessary in order to properly

control the deformation of the leading edge, and to exactly reconstruct the original airfoil when all the internal actuator displacements are set to zero.

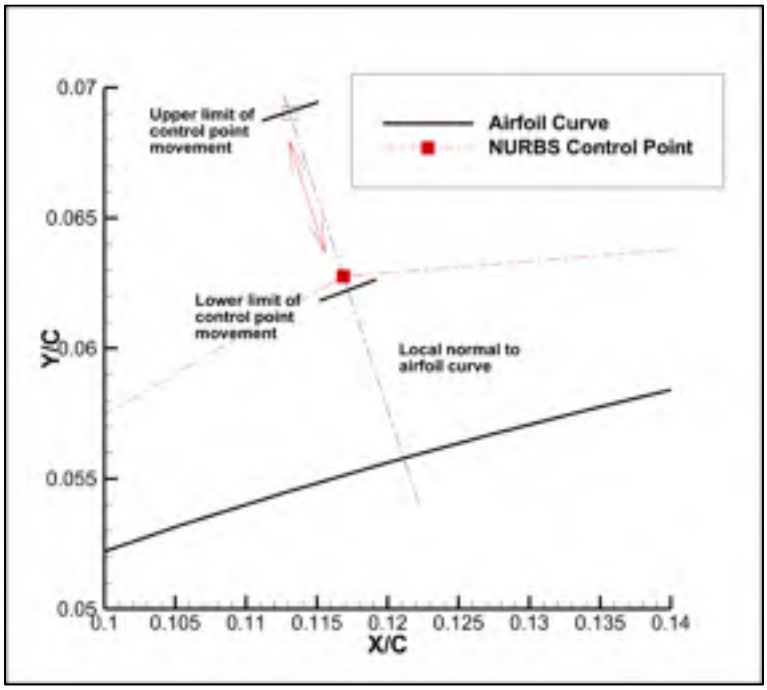

Figure 4.3 Direction of motion and imposed limits for a control point

In the numerical optimization, the change of the airfoil curve shape is achieved by changing the coordinates of the NURBS control points. The motion of the seven control points that morph the flexible skin is strictly controlled. For each control point, the vector normal to the airfoil curve is calculated, vector that also passes through the control point, or as close as possible to it, within an acceptable error margin. The motion of the seven points is then restricted in the direction given by the normal vector. In addition, the control point cannot move for more than a given length along this direction, in order to maintain the deformations of the flexible skin within acceptable and predefined limits. For all control points, the range of movement has been limited between their original position (as the lower limit) and a maximum outwards displacement equal to 0.45% of the airfoil chord (as the upper limit). Figure 4.3 shows the direction of motion and the limits imposed on one of the NURBS control points.

4.2.2 The aerodynamic solver

The code that has been used for the calculation of the two-dimensional aerodynamic characteristics of the UAS-S4 airfoil is XFOIL, version 6.96, developed by Drela and Youngren (Drela and Youngren, 2001). The XFOIL code was chosen because it has proven its precision and effectiveness over time and it reaches a converged solution very quickly, thus being suited for integration into an optimization procedure requiring a very high number of objective function evaluations.

The inviscid calculations in XFOIL are performed using a linear vorticity stream function panel method (Drela, 1989). A Karman-Tsien compressibility correction is included, allowing good predictions for subsonic, compressible flows. For the viscous calculations, XFOIL uses a two-equation lagged dissipation integral boundary layer formulation (Drela, 1989), and the e^N criterion for determining the laminar to turbulent transition point (Drela, 2003). The flow in the boundary layer and in the wake interacts with the inviscid potential flow by use of the surface transpiration model.

XFOIL provides accurate results for angles of attack up to the stall conditions (Drela, 1989), (Gross and Fasel, 2010). Comparisons with experimental data and with high fidelity LES (Large Eddy Simulation) and DNS (Direct Numerical Simulation) computations (Gross and Fasel, 2010), (Mack et al., 2008) show its performance and the expected errors in its results for angles of attack immediately after stall.

4.3 In-house Optimization Code

The tool used to perform the optimization of the UAS-S4 wing airfoil is an in-house code based on the Artificial Bee Colony (ABC) algorithm, coupled with the Broyden-Fletcher-Goldfarb-Shanno (BFGS) algorithm for providing a final refinement of the solution.

4.3.1 Artificial Bee Colony algorithm

The ABC algorithm is an optimization algorithm based on the intelligent behaviour of a honeybee swarm. First presented by Karaboga (2007), it has been continuously further developed. In this algorithm, the colony contains three different types of bees: employed, onlooker and scouts, while the food sources exploited by these bees represent the possible solutions of the optimization problem.

The ABC algorithm is initialized using a random distribution of food sources, equal to the number of employed bees. Each employed bee visits one food source, evaluates the nectar amount of that food source (the quality of that possible solution) and then searches for a new food source in its vicinity. If the quality of this newly found source is higher, the employed bee memorizes its position and forgets about the old food source. The onlooker bees wait in the hive of the bee swarm until all the employed bees have finished their search and have returned to the hive. Each onlooker bee individually chooses one of the food sources exploited by the employed bees, with a probability based on the quality of that food source. Because the choice is made based on quality, more than one onlooker bee can choose the same food source if its quality is high. The onlooker bee then carries out the same exploration process as an employed bee, searching for a higher quality source in the vicinity of its chosen source. Scout bees randomly search for new food sources, in order to replace the exhausted ones. In the algorithm, an employed bee becomes a scout if the food source that it is exploiting cannot be improved after a predetermined number of visits. The process of sending out the employed bees, the onlooker bees and the scouts continues in an iterative manner for a predetermined number of cycles. The general outline of the ABC algorithm is presented in Figure 4.4.

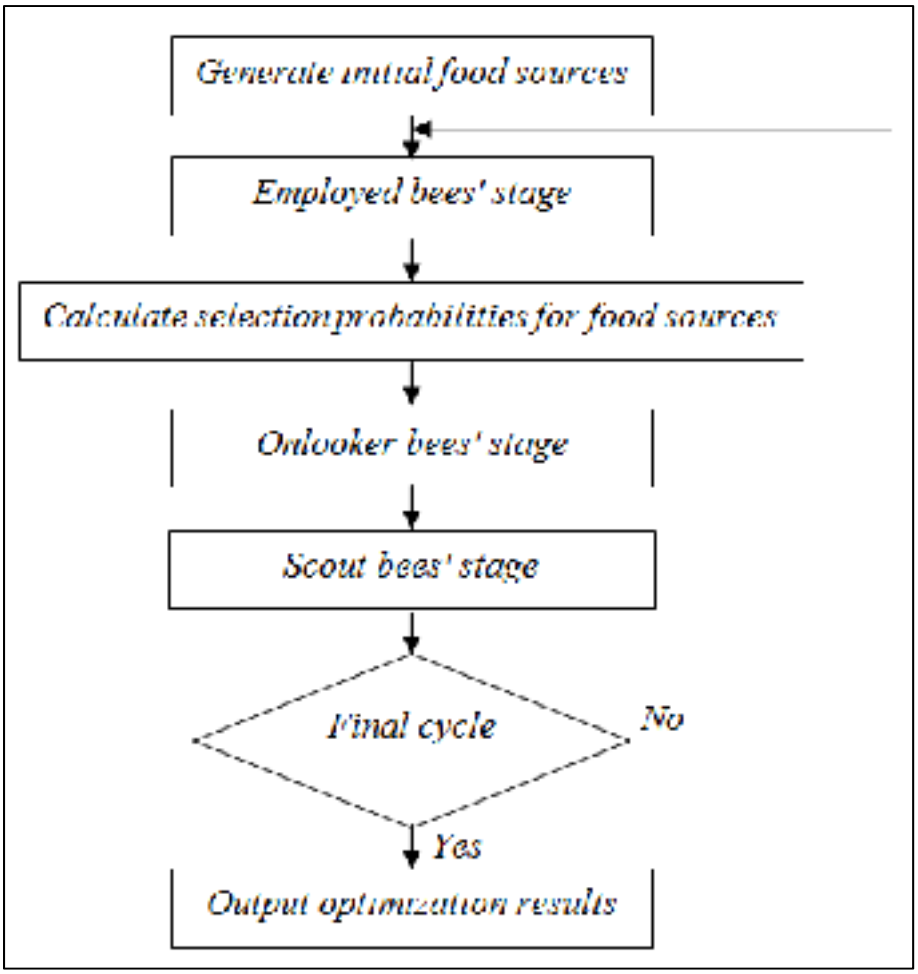

Figure 4.4 General outline of the ABC algorithm

The original ABC algorithm was developed only for unconstrained optimization problems and it has slow convergence properties (Karaboga and Basturk, 2007). Karaboga proposed a revised version of the algorithm capable of solving constrained optimization problems by replacing the standard food source selection process with Deb's constraint handling method (Deb and Goldberg, 1991). Other authors have proposed methods for the enhancement of the convergence properties of the algorithm, such as dynamically adjusting the frequency and magnitude of the perturbations (Akay and Karaboga, 2012), steering the solutions towards the region of the global optimum (Zhu and Kwong, 2010) or influencing the behaviour of the bees using elements of chaos theory (Xu, 2010).

4.3.2 Broyden-Fletcher-Goldfarb-Shanno algorithm

In order to determine the effectiveness of the optimization routine based on the ABC algorithm, several tests were performed on a reduced order problem, where only two control points change the shape of the flexible skin. The effect of changing the shape of the skin could be analysed by a Monte-Carlo simulation and plotting the response surface of the objective function, for all combinations of allowed displacements. It was found that the ABC algorithm converged very quickly to the vicinity of the global optimum, but in some cases, when the optimum lies within an almost flat surface, a high number of additional cycles are needed to find the exact global optimum point. For this reason, the option of performing a final refinement of the solution using the Broyden-Fletcher-Goldfarb-Shanno (BFGS) algorithm was implemented (Bonnans et al., 2006). The BFGS algorithm is an iterative quasi-Newton method used for unconstrained optimization, in which the Hessian matrix of second order derivatives is approximated and updated using the gradient evaluations. The objective function gradient is estimated using finite difference approximations. Since the BFGS method can be applied only for unconstrained optimization, it was coupled with the Augmented Lagrangian Method (ALM) (Powell, 1969) in order to introduce the desired optimization constraints.

4.3.3 Optimization tool used for validation of the in-house code

The second tool that has been used for the optimization of the UAS-S4 wing airfoil, with the aim to validate the results of the in-house solver, is the Optimization Toolbox included in the commercially available software package MATLAB (MathWorks, 2015). A developed script allowed us to perform the optimization of the airfoil, by coupling one of the several integrated optimization algorithms with the external NURBS parameterization routines and the aerodynamic solver. The Toolbox implemented genetic algorithm was chosen for the present work. The algorithm was configured with a *feasible-type initial population*, *fitness function scaling based on the top individual fitness*, *roulette-type selection*, *elitism*, *uniform mutation* and *double point crossover*. After the genetic algorithm terminates its execution, a

final refinement of the solution is performed with the Interior Point algorithm implemented in the MATLAB Toolbox. The algorithm was configured with *finite difference approximations* to evaluate the derivatives, a *BFGS-type approximation of the Hessian matrix* and *conjugate gradient steps* for the solution advancement.

4.4 Results and Discussions

The optimization of the UAS-S4 wing airfoil was performed with the objective of delaying the boundary layer separation at high angles of attack. In order to achieve this goal, the separation point is determined by analysis of the skin friction coefficient distribution over the airfoil upper surface. The actual chord-wise position of the separation point was used as the objective function, while imposing the constraint of increasing the value of the lift coefficient with respect to the lift coefficient of the original airfoil. Thus, the general optimization objective function and constraints are:

$$\begin{aligned} \min f &= w_1 C_L + w_2 \frac{(X/C)_{sep}^0}{(X/C)_{sep}} \\ C_L - C_L^0 &> 0 \\ \delta_{min} \leq \delta_i &\leq \delta_{max} \\ \left| \frac{l}{l^0} - 1 \right| &\leq 0.0075 \end{aligned} \tag{4.3}$$

Here, $(X/C)_{sep}$ is the chordwise position of the boundary layer separation point for the morphed airfoil, $(X/C)_{sep}^0$ is the separation point for the original airfoil, C_L and C_L^0 are the lift coefficients of the morphed and original airfoils, δ_i is the displacement of a control point, δ_{max} is the upper limit for displacement, l and l^0 are the skin lengths for the morphed and original airfoils, while w_1 and w_2 are user defined weights.

For the angles of attack where the flow is completely attached the weight w_1 was set to one, w_2 was set to zero and the constraint on the lift is ignored. For angles of attack with detached

boundary layer, the weight w_1 was set to zero, w_2 was set to one, and all constraints are considered active.

4.4.1 Aerodynamic analysis setup

The analyses were performed at three airspeed values, 34 m/s, 51 m/s and 68 m/s, corresponding to Mach number values of 0.10, 0.15 and 0.20. The highest value represents the maximum velocity of the UAS-S4, while the middle value represents its cruise speed. The Reynolds numbers corresponding to the three airspeeds are relatively small, 1.412E+06, 2.171E+06 and 2.823E+06. The range of angles of attack is between 10 deg and 19 deg, while the turbulent intensity of the incoming airflow was set at 0.07%.

4.4.2 Morphing airfoil setup

The NURBS parameterization of the airfoil was performed using seven control points for the flexible skin region situated between 5% of the chord on the airfoil lower surface and 55% of the chord on the upper surface. The number of control points was chosen by taking into account a compromise between the accuracy of the NURBS representation of the airfoil and the total number of optimization variables. The lower limits of the control point movements were set to zero, corresponding to the original airfoil shape, while the upper limits were limited to 2.5 mm. This value was found high enough in order to obtain the needed range of aerodynamic performance improvements, while keeping the variation of the flexible skin's length below 0.75%.

4.4.3 In-house optimizer setup

The ABC algorithm considered 30 employed bees, 30 onlooker bees, and a maximum number of cycles equal to 50, giving a total possible number of objective function evaluations equal to 3000. The initial values of the scaling factor and the solution modification rate were set to 1.0, and were dynamically updated during the simulation every

10 cycles. The limit of cycles after which non-improved solutions were abandoned was set equal to the maximum number of cycles, since it was determined that this parameter does not significantly influence convergence for the particular problem of the airfoil optimization. The attraction factor of the best solution was set to 1.5. Concerning the convergence of the algorithm, if the best-found solution does not improve for 20 cycles, then it is considered the optimal solution. If the ABC algorithm has not converged after the maximum of 50 cycles, the ABC loop is exited and the ALM-BFGS loop begun. Because the initial guess used for starting the calculations is already very close to the optimum, a small number of iterations were found to be enough for convergence. A maximum number of 2 ALM iterations, 10 BFGS iterations and 10 approximate line search iterations were imposed. However, the modulus of the gradient usually became smaller than 1E-05 after only 2 or 3 BFGS iterations, within the first ALM iteration. The ALM penalty coefficient and the Lagrangian multipliers were initialized with a value of 10.

4.4.4 MATLAB Optimization Toolbox setup

In order to run the genetic algorithm, a population of 100 individuals was used, and 30 generations were imposed, giving a total possible number of objective function evaluations equal to 3000. The mutation rate was set equal to 0.05, the crossover fraction was set at 0.85 and the number of elitist individuals was limited to 3. Because the initial guess of the Interior Point refinement is the best solution found by the genetic algorithm, only a small number of iterations are needed. A maximum number of 20 algorithm iterations were imposed, with function and constraints tolerances of 1E-05.

4.4.5 Results obtained for the separation delay

In Figures 4.5 to 4.7, a comparison is presented for the pressure coefficient and the skin friction coefficient distributions, for the original and the optimized airfoils, at an airspeed of 34 m/s (Mach number equal to 0.10 and Reynolds number equal to 1.412E+06) and three values for the angles of attack, 10 deg, 15 deg and 19 deg.

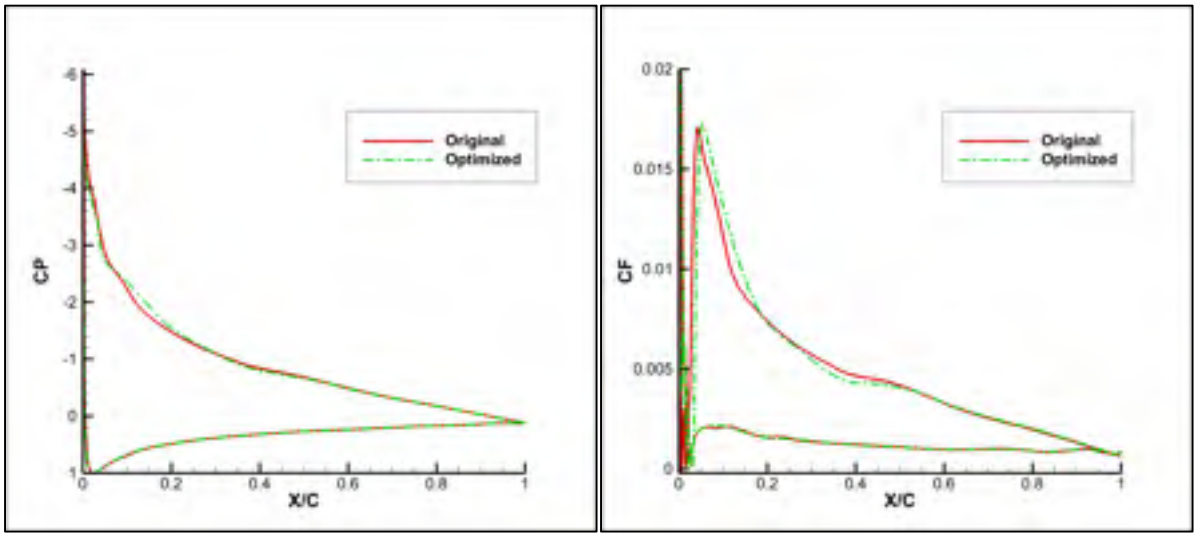

Figure 4.5 Pressure distributions and skin friction coefficient comparisons
at 34 m/s and 10 deg angle of attack

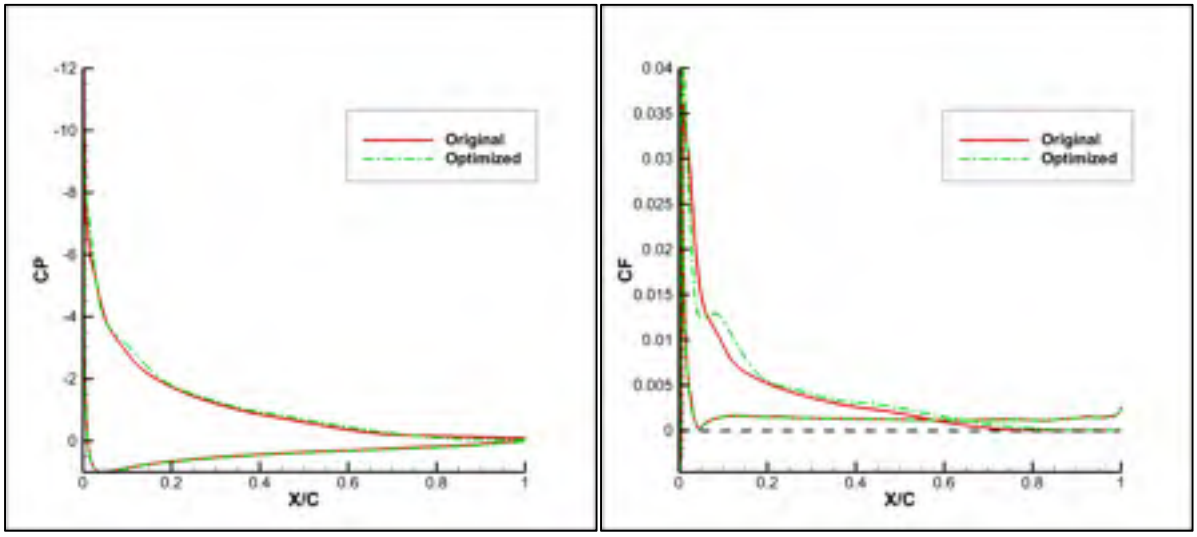

Figure 4.6 Pressure distributions and skin friction coefficient comparisons
at 34 m/s and 15 deg angle of attack

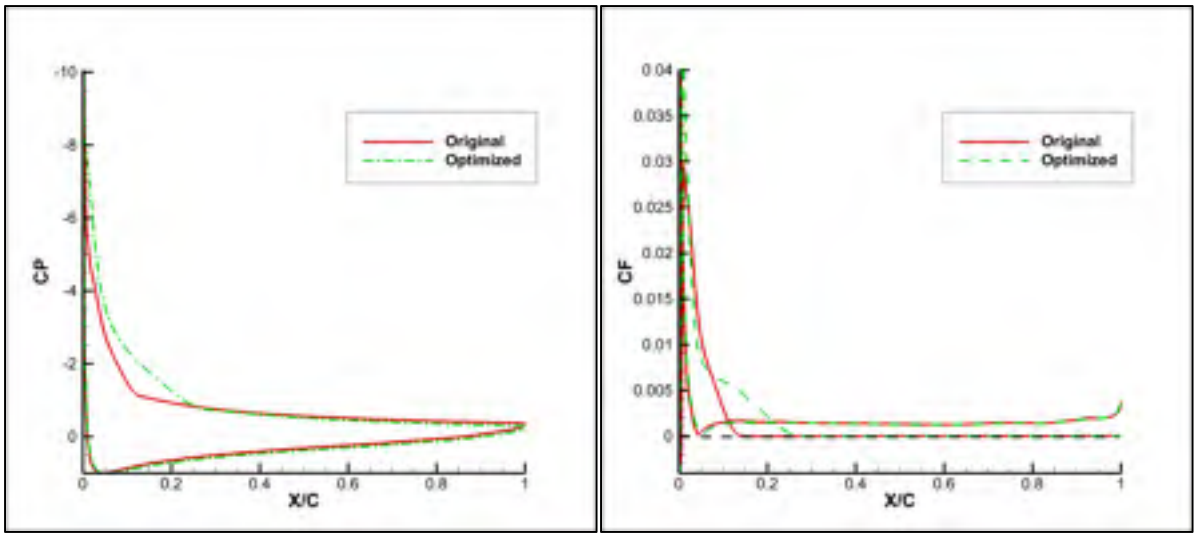

Figure 4.7 Pressure distributions and skin friction coefficient comparisons at 34 m/s and 19 deg angle of attack

At an angle of attack of 10 deg, the boundary layer remains attached over the entire length of the airfoil upper surface. The flexible skin produces a modification of the pressure distribution in the leading edge area, resulting in a smoother pressure peak and an adverse pressure gradient that is not as intense as for the original airfoil. As consequence, there is a delay in the onset of turbulent flow, the laminar region being extended with 3% of the chord.

As the angle of attack is increased to 15 deg, trailing edge separation appears, as seen in Figure 4.6. For the original airfoil, the chord-wise point where the turbulent skin friction coefficient vanishes is located at 72% of the chord, while the morphed airfoil shows an extended attached boundary layer, separation occurring at 81% of the chord.

At 19 deg angle of attack, the original airfoil experiences leading edge separation, as seen in Figure 4.7, the detachment point being located at 13% of the chord. By adapting the shape of the airfoil through morphing, separation can be delayed with 15% of the chord, as seen from the skin friction coefficient plot. The separation delay is coupled with a less abrupt adverse pressure gradient, and a corresponding reduction of the airfoil pressure drag.

Figure 4.8 presents the variation of the UAS-S4 airfoil lift and drag coefficients with the angle of attack, for the original airfoil and for both optimized airfoils (obtained by the in-house code and MATLAB), at a Mach number of 0.10 (airspeed of 34 m/s). It is seen that a significant lift increase for the entire range of angles of attack was obtained by both optimization codes. The lift coefficient increase of the morphing airfoil, compared to the original airfoil lift coefficient (in percentages), for each angle of attack included in the analysis range, is detailed in Table 4.2.

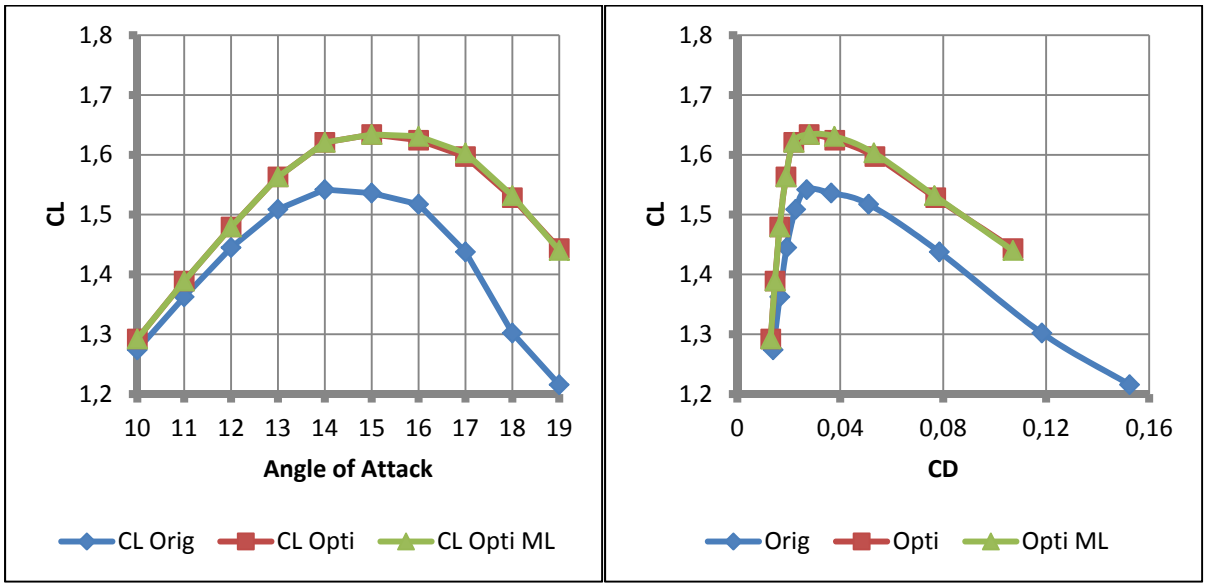

Figure 4.8 Original and optimized airfoils lift and drag variations comparison at Mach 0.10

The results obtained by the in-house code almost perfectly match the results obtained by the MATLAB Toolbox. The improvement of the lift coefficient with respect to the lift coefficient of the original airfoil has values of up to almost 19%. In addition, an increase of 6.4% is obtained for the maximum lift coefficient. Because the pressure drag component is smaller for the morphed airfoil (as seen from the drag variations with the angle of attack in Figure 4.8), due to the delay of the boundary layer separation, then a significant improvement of the airfoil lift-to-drag ratio was obtained, as shown in Figure 4.9.

Table 4.2 Comparison of lift coefficient values versus the angle of attack for the original and the optimized airfoils

Alpha [deg]	Original CL	In-house Optimized CL	In-house Improvement [%]	MATLAB Optimized CL	MATLAB Improvement [%]
10	1.2740	1.2921	1.42	1.2917	1.39
11	1.3624	1.3889	1.95	1.3875	1.84
12	1.4448	1.4793	2.39	1.4793	2.39
13	1.5089	1.5630	3.59	1.5630	3.59
14	1.5417	1.6205	5.13	1.6206	5.13
15	1.5360	1.6330	6.38	1.6342	6.39
16	1.5173	1.6245	7.07	1.6265	7.19
17	1.4375	1.5970	11.10	1.5965	11.06
18	1.3020	1.5317	17.67	1.5298	17.50
19	1.2156	1.4432	18.72	1.4405	18.50

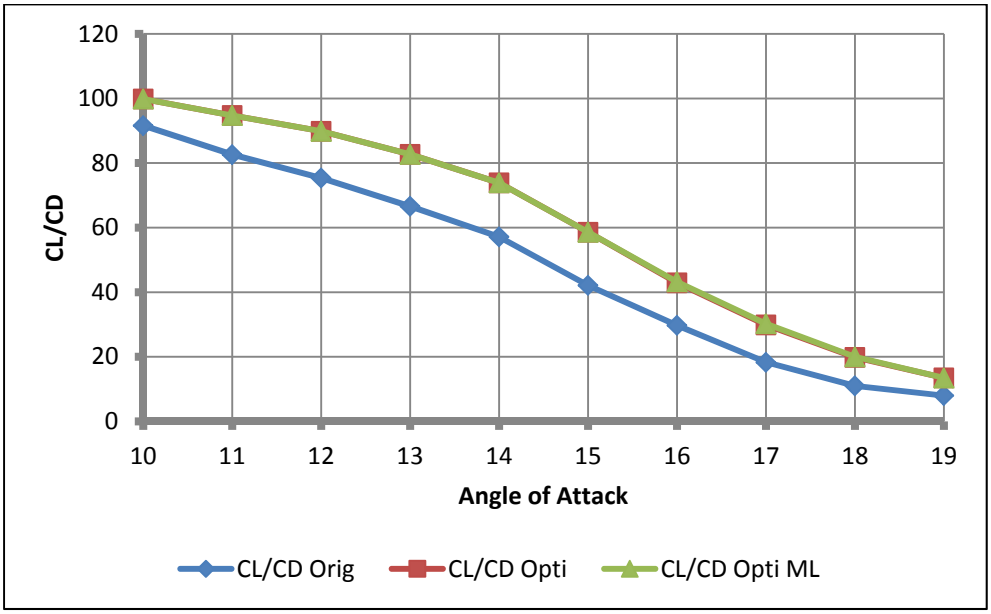

Figure 4.9 Original and optimized airfoils lift/drag ratio comparison at Mach 0.10

The morphing airfoil behaviour observed at a Mach number of 0.10 remains relatively the same for the other two considered airspeeds. In Figures 4.10 to 4.12, a comparison is presented for the pressure coefficient and the skin friction coefficient distributions, for the original and the optimized airfoil, at an airspeed of 51 m/s (corresponding to a Mach number of 0.15 and a Reynolds number of 2.171E+06) and at the same values for the angle of attack as before, 10 deg, 15 deg and 19 deg.

At 10 deg angle of attack, the boundary layer remains attached over the entire length of the airfoil upper surface. The morphing airfoil has a delay in the onset of turbulent flow, as shown in the skin friction coefficient plot of Figure 4.10.

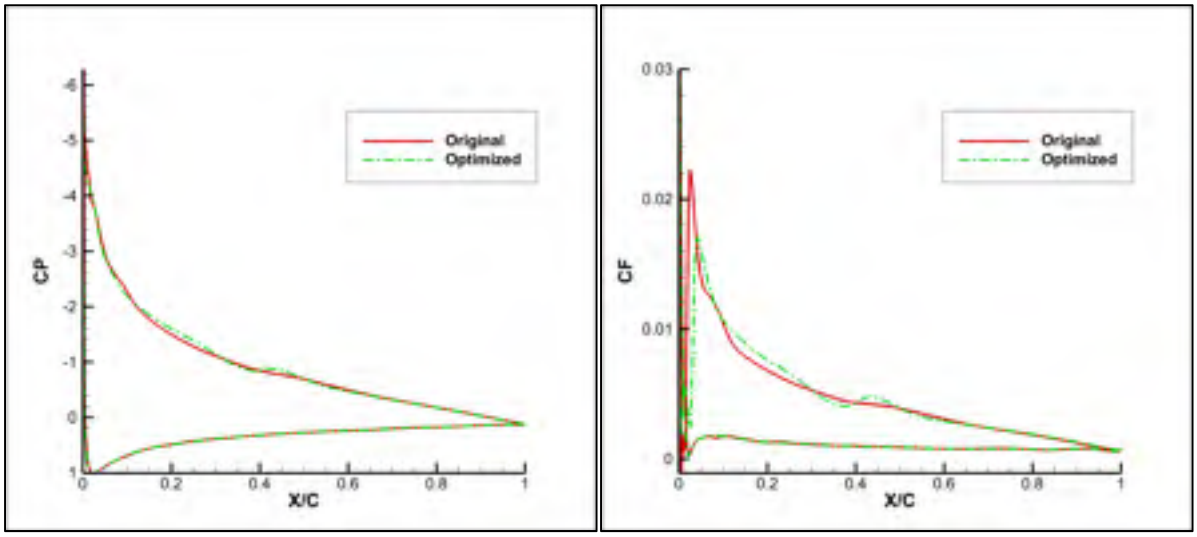

Figure 4.10 Pressure distributions and skin friction coefficient comparisons
at 51 m/s and 10 deg angle of attack

As the angle of attack is increased to 15 deg, trailing edge separation appears, as seen in Figure 4.11. The difference in the boundary layer separation point between the morphed and original airfoils is small, with a delay of approximately 3% of the chord. At 19 deg angle of attack, the original airfoil experiences leading edge separation, as seen in Figure 4.12, the detachment point being located at 15% of the chord. For the morphed airfoil, the detachment point is located at 25% of the chord, thus a delay of 10% of the chord was obtained.

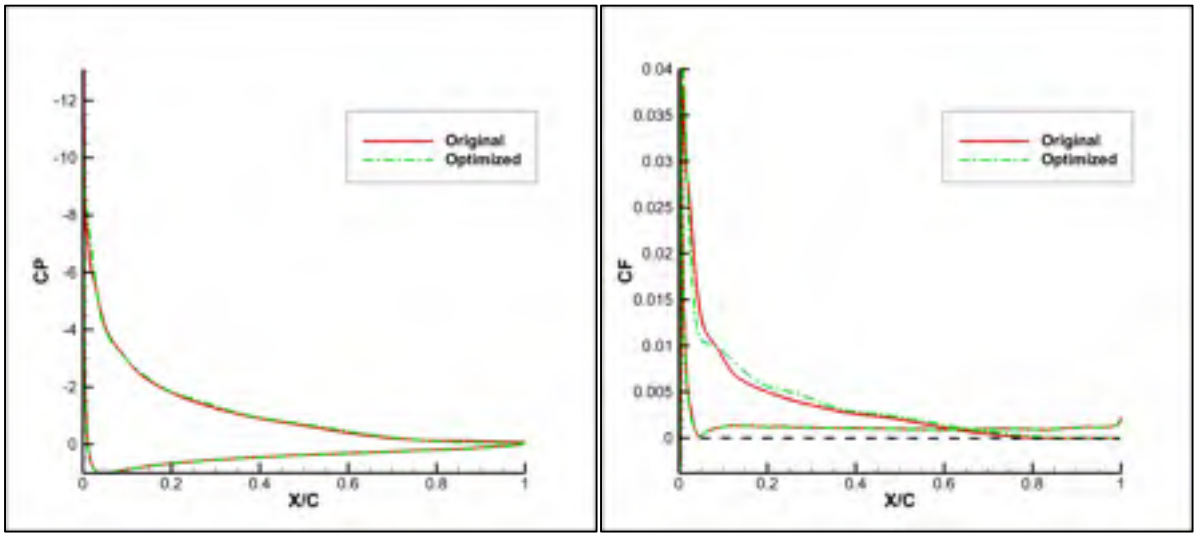

Figure 4.11 Pressure distributions and skin friction coefficient comparisons at 51 m/s and 15 deg angle of attack

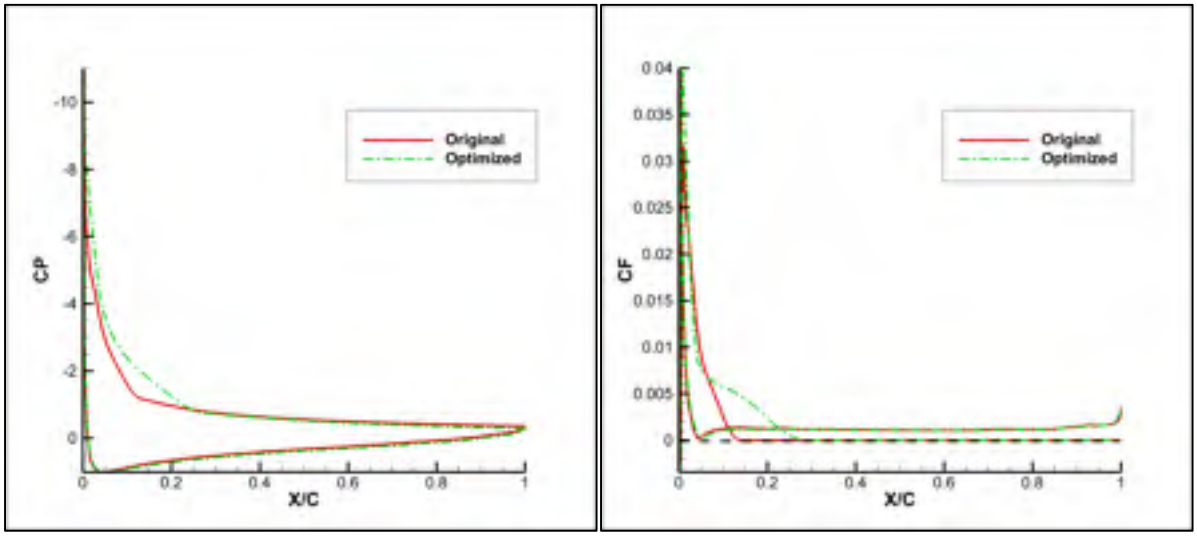

Figure 4.12 Pressure distributions and skin friction coefficient comparisons at 51 m/s and 19 deg angle of attack

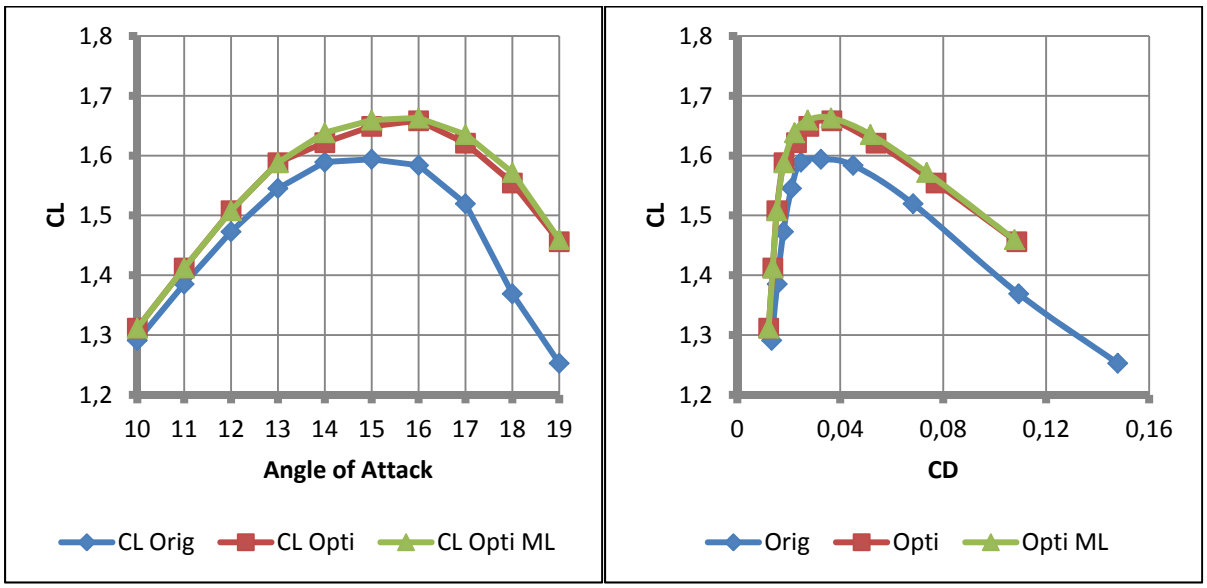

Figure 4.13 Original and optimized airfoils lift and drag variations comparison at Mach 0.15

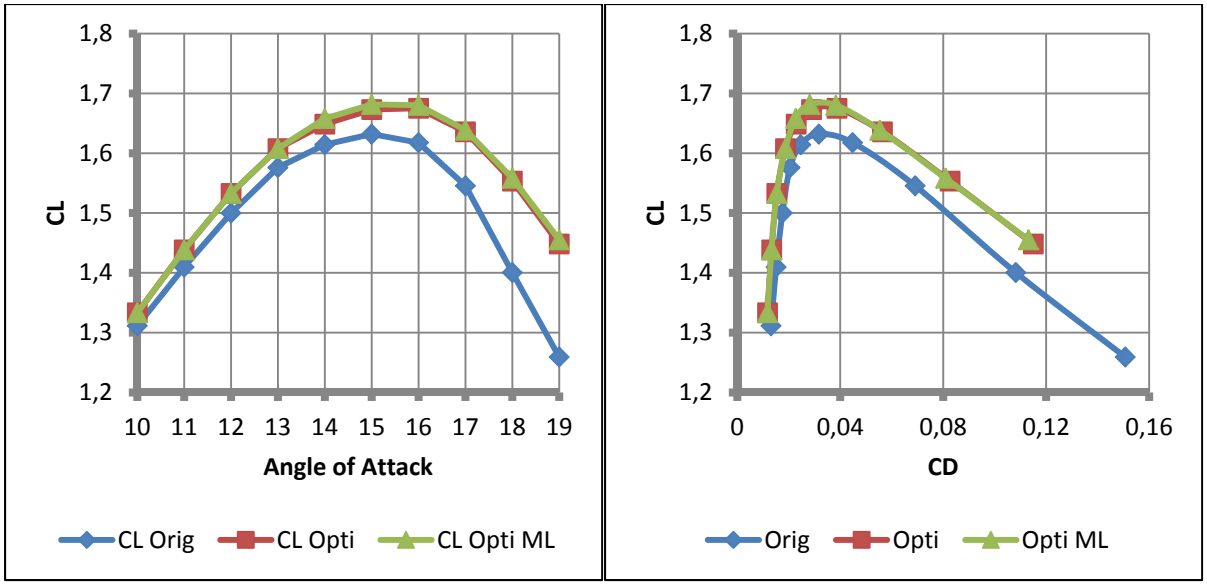

Figure 4.14 Original and optimized airfoils lift and drag variations comparison at Mach 0.20

Both optimizer codes obtained consistent lift increases and drag reductions for the entire range of angles of attack. Figures 4.13 and 4.14 present the lift and drag variations with the angle of attack, for the original and morphing airfoils, for the Mach numbers equal to 0.15 (Figure 4.13) and 0.20 (Figure 4.14).

In Figure 4.15, the chord-wise position of the boundary layer separation point is presented, for the original airfoil and for the morphing airfoil, for all three considered Reynolds numbers, 1.412E+06, 2.171E+06 and 2.823E+06. The improvement obtained by the airfoil morphing technique increases as the angle of attack increases, the most important separation delay occurring at 19 deg angle of attack. In addition, the obtained improvement is largest for the smallest Reynolds number, and decreases as the Reynolds number and airspeed increase.

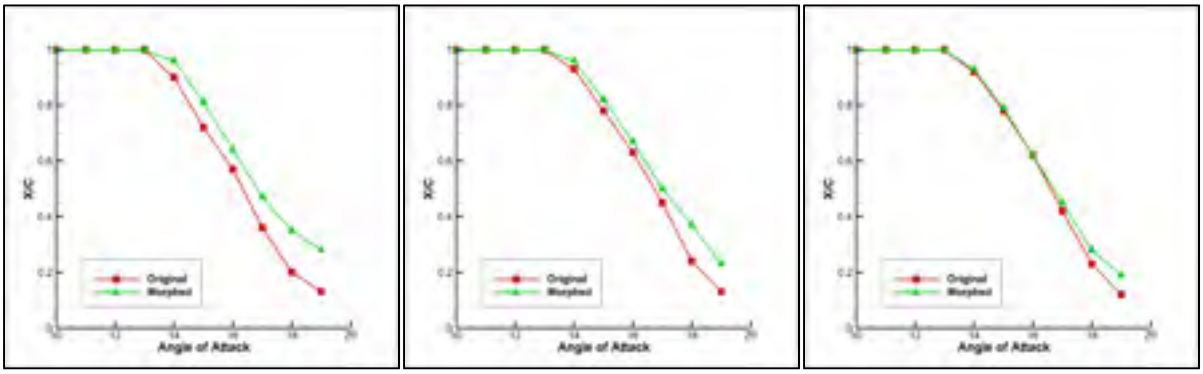

Figure 4.15 Chord-wise positions of the boundary layer separation points for Re = 1.41 million (left), Re = 2.17 million (center) and Re = 2.82 million (right)

4.4.6 Morphed airfoil geometries

The results obtained here require only very small modifications of the morphing airfoil flexible skin shape. The changes in the NURBS control points positions should be small enough to keep the modifications feasible from a structural point of view, and to prevent great changes of the flexible skin length. In Table 4.3, the normal direction displacements of the NURBS control points are given, at a Mach number of 0.20. It must be noted that this particular optimization case obtained the highest average actuator displacements, so it can be

considered a limit case, from the point of view of the actual loads the morphing skin has to withstand.

Figure 4.16 shows the original UAS-S4 airfoil and three different reconstructed airfoils, for three angle of attack values (15 deg, 17 deg and 19 deg), based on the displacement values of Table 4.3, as well as a magnified view of the region on the upper skin where the most significant displacements occur.

Table 4.3 Normal direction NURBS control points displacements for Mach 0.20

Angle of attack [deg]	**Skin length variation [%]**	**Control points normal displacements [m]**						
		Point 1	**Point 2**	**Point 3**	**Point 4**	**Point 5**	**Point 6**	**Point 7**
10	0.11	7.50E-04	1.50E-03	2.15E-03	2.20E-03	1.25E-03	2.50E-03	2.25E-03
11	-0.02	1.75E-03	9.50E-04	2.45E-03	2.50E-03	2.50E-03	2.30E-03	2.50E-03
12	0.10	2.50E-03	2.50E-03	2.50E-03	2.50E-03	1.85E-03	4.00E-04	2.45E-03
13	0.16	5.00E-04	4.00E-04	2.50E-04	2.50E-03	2.50E-03	0.00	2.50E-03
14	0.29	1.00E-04	1.50E-04	0.00	3.00E-04	2.50E-03	2.20E-03	2.50E-03
15	0.31	6.50E-04	0.00	0.00	1.65E-03	2.50E-03	1.60E-03	2.50E-03
16	0.17	1.05E-03	1.50E-04	5.00E-05	0.00	2.50E-03	9.50E-04	2.50E-03
17	0.14	1.90E-03	1.00E-03	0.00	0.00	0.00	5.00E-05	2.50E-03
18	0.20	1.90E-03	2.45E-03	1.25E-03	3.00E-04	0.00	0.00	2.50E-03
19	0.18	2.25E-03	2.50E-03	2.45E-03	1.20E-03	0.00	0.00	2.50E-03

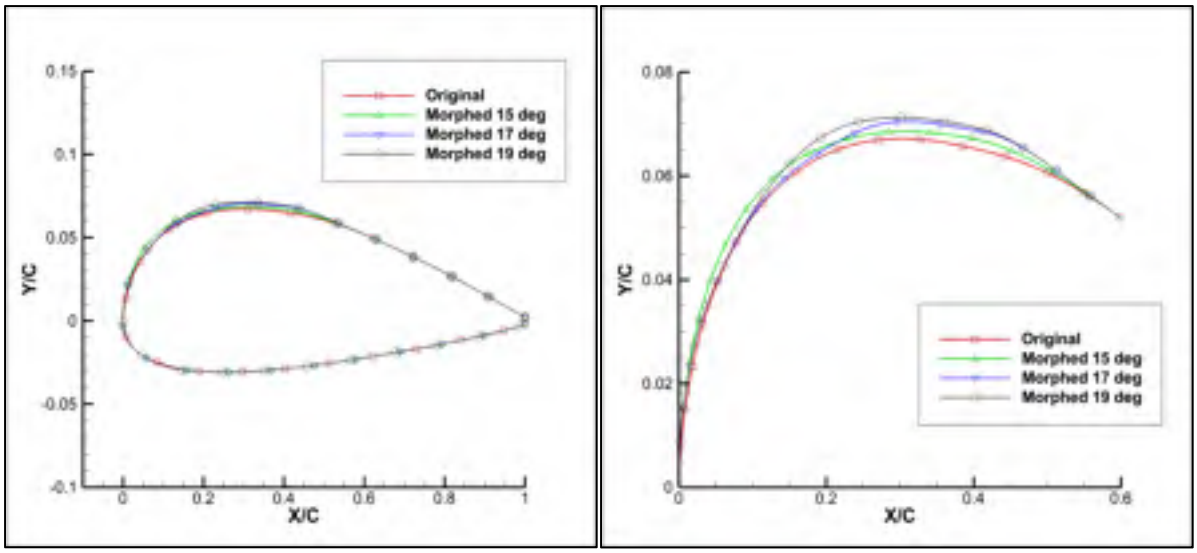

Figure 4.16 Comparison between the original airfoil and three optimized airfoils

4.5 Conclusions

In this paper, we have presented numerical results obtained for the optimization of the Hydra Technologies S4 UAS airfoil. The airfoil modification procedure is based on a morphing wing approach, and the upper and lower surface changes have been done keeping in mind possible structural constraints. A new optimization code, based on a hybrid ABC-BFGS algorithm was used to determine the optimal displacements of the NURBS control points. The results have been validated using a state-of-the-art, commercially available optimisation software.

The morphing skin was used to increase the aerodynamic performance of the airfoil at high angles of attack. To achieve the objective, the focus was placed on delaying the boundary layer separation and also on increasing the lift coefficient. For each of three considered airspeeds, significant lift increases have been obtained, coupled with equally important reductions of the pressure drag, leading to an increase in aerodynamic efficiency. The morphing skin provides the most important improvements at the highest values of the angle of attack, where the boundary layer separation occurs close to the leading edge of the airfoil.

The lift coefficient improvements, as important as 19%, and the delay in the boundary layer separation, up to 15% of the chord, have been obtained using very small displacements of the airfoil flexible skin. In addition, only a limited portion of the airfoil is flexible, between 5% of the chord on the lower surface and 55% of the chord on the upper surface. Thus, we were able to limit the displacements of the actuation system used to change the flexible skin shape, and we prevent significant variation of the skin length, in order to make the modifications feasible for the implementation on the UAS-S4.

4.6 Future work

The work presented in the paper, focused on the two-dimensional behaviour of a morphing airfoil, will be followed by a three-dimensional analysis of the proposed concept. The spanwise limits of the morphing skin, as well as the spanwise variations of the skin displacements will be established. A material suitable for achieving the desired skin displacements must be chosen. Based on the errors between the aerodynamic target shapes and the finite element model calculated shapes, several configurations will be analysed: keeping the morphing skin an active structural component of the UAS wing or redesigning the spars and ribs so that the skin can be freed from the loads induced by wing bending and torsion. An internal actuation system must be designed, capable of providing the desired displacements while constrained by the available internal space and position of spars and ribs. Once the skin material and the final wing structure are established, an energy consumption analysis of the morphing system under combined aerodynamic and structural forces will be performed, thus quantifying the overall power consumption gains of the concept.

Acknowledgments

We would like to thank the Hydra Technologies Team in Mexico for their continuous support, and especially Mr. Carlos Ruiz, Mr. Eduardo Yakin and Mr. Alvaro Gutierrez Prado. We would also like to thank to the Natural Sciences and Engineering Research

Council of Canada (NSERC) for the funding of the Canada Research Chair in Aircraft Modeling and Simulation Technologies. In addition we would like to thank to the Canada Foundation of Innovation (CFI), to the Ministère du Développement économique, de l'Innovation et de l'Exportation (MDEIE) and to Hydra Technologies for the acquisition of the UAS-S4 using the Leaders Opportunity Funds.

CHAPTER 5

AERODYNAMIC IMPROVEMENT OF THE UAS-S4 ÉHECATL MORPHING AIRFOIL USING NOVEL OPTIMIZATION TECHNIQUES

Oliviu Şugar Gabor, Antoine Simon, Andreea Koreanschi and Ruxandra Mihaela Botez
LARCASE Laboratory of Applied Reasearch in Active Controls,
Avionics and Aeroservoelasticity
École de Technologie Supérieure, 1100 rue Notre Dame Ouest,
Montréal, H3C1K3, Québec, Canada

This article was published in *Proceedings of the Institution of Mechanical Engineers, Part G: Journal of Aerospace Engineering*, DOI: 10.1177/0954410015605548

Résumé

Dans cet article, nous présentons un concept d'aile déformable pour la surface portante du système autonome de vol S4, la nouvelle méthodologie d'optimisation et les résultats obtenus pour plusieurs conditions de vol. La réduction du coefficient de traînée a été réalisée en utilisant un outil interne d'optimisation, basée sur le nouvel algorithme de la Colonie des Abeilles Artificielles, couplé avec l'algorithme Broyden-Fletcher-Goldfarb-Shanno pour fournir un raffinement final de la solution. Une large gamme de vitesses et d'angles d'attaque a été étudiée. Un logiciel avancé d'optimisation multi-objectif, disponible dans le commerce, a permis de valider la stratégie d'optimisation proposée et les résultats obtenus. Les calculs aérodynamiques ont été effectués en utilisant le solveur XFOIL, avec un méthode linéaire de panneau en 2D, couplé à un modèle de couche limite incompressible et un critère d'estimation de transition, afin de fournir des estimations précises du coefficient de traînée aérodynamique. Des réductions de la traînée allant jusqu'à 14% ont été réalisées pour un large éventail de conditions de vol différentes, en utilisant de très petits déplacements de la surface du profil, de seulement 2,5 mm.

Abstract

In this paper, we present a morphing wing concept of the airfoil of the S4 unmanned aerial system, the new optimization methodology and the results obtained for multiple flight conditions. The reduction of the airfoil drag coefficient has been achieved using an in-house optimization tool based on the relatively new Artificial Bee Colony algorithm, coupled with the Broyden-Fletcher-Goldfarb-Shanno algorithm to provide a final refinement of the solution. A broad range of speeds and angles of attack have been studied. An advanced, multi-objective, commercially available optimizing tool was used to validate the proposed optimization strategy and the obtained results. The aerodynamic calculations were performed using the XFOIL solver, a 2D linear panel method, coupled with an incompressible boundary layer model and a transition estimation criterion, to provide accurate estimations of the airfoil drag coefficient. Drag reductions of up to 14% have been achieved for a wide range of different flight conditions, using very small displacements of the airfoil surface, of only 2.5 mm.

5.1 Introduction

The reduction of fuel consumption represents a major area of research in the today aerospace industry. Flight experiments have demonstrated that a 20% reduction in airplane drag leads to an 18% reduction in fuel consumption (Iannotta, 2002). Drag reduction on a wing could be achieved by actively modifying the wing shape, for purposes such as the promotion of a larger laminar flow region on the wing upper surface. Because laminar flow exhibits less viscous friction than a turbulent one, a substantial viscous drag reduction is expected (Zingg, 2006). Authors have proposed solutions for increasing the extent of laminar flow over the wing surface, among which the automated trailing edge cruise flap (McAvoy and Gopalarathnam, 2002), (Drela, 1990) or various active suction-type laminar flow control devices (Braslow, 1999). The main advantage of actively modifying the wing shape using a morphing technique is that an optimal shape for the wing and/or airfoil can be provided for different performance improvement objectives and during each distinct phase of aircraft

flight, while preserving suitably smooth shapes, thus avoiding the off-design performace loss associated with single point optimized rigid shapes (Drela, 1998). In addition to achieving important reductions in fuel consumption, adaptive, morphing wings can also be effectively used to replace conventional high-lift devices (Pecora et al., 2011), (Diodati et al., 2013), or the conventional control surfaces (Pecora, 2012).

In recent years, a great interest has appeared for the development and application of morphing solutions on Unmanned Aerial Vehicles (UAVs), because of increasingly greater efficiency requirements and of much simpler certification issues. Neal et al. (2010) designed and validated a variable wing plan-form UAV, capable of significant span and sweep changes, using a telescopic pneumatic actuator. The wind tunnel testing showed that only three configurations were necessary to increase the lift to drag ratio over the entire flight envelope. Supekar (2007) evaluated the aerodynamic performance of a two-segment, telescopic UAV wing that could also change the dihedral of the outer segment. Gamboa et al. (2007) designed an UAV wing capable of independent span and chord changes, with the aid of a telescopic spar and rib system. The numerical analysis demonstrated drag reductions of up to 23% when compared to the non-morphing geometry. Falcao (2011) designed and tested a morphing winglet for a military UAV, achieving important performance improvement by simply changing the winglet cant and toe angles. Do Vale et al. (2011) proposed a UAV morphing wing capable of telescopic span changes and independent conformal camber changes.

One of the most advanced morphing projects was Lockheed Martin's Agile Hunter UAV (Bye and McClure, 2007), (Ivanco et al., 2007), (Love et al., 2007). The wind tunnel prototype was capable of folding the inner wing sections over the fuselage, in order to reduce the drag during transonic cruise. Another important project was NextGen Aeronautic MFX1 UAV, with variable wing sweep and wing area (Andersen, 2007), (Flanagan et al., 2007). The prototype was successfully flight tested, demonstrating the capability of achieving significant plan-form changes during various flight scenarios. Sofla et al. (2010) developed a morphing wing concept in which the wing could perform uniform, out-of-plane flexing, with

the aid of Shape Memory Alloy (SMA) actuators. A numerical analysis was performed in order to evaluate the performance of an UAV equipped with the morphing wing.

Gano and Renaud (2002) presented a concept to increase the aerodynamic efficiency of an UAV by gradually decreasing the wing thickness as the fuel inside the wing-mounted tank is consumed, thus decreasing the drag coefficient. Shyy (2010) presented research on small UAV airfoils that passively morph is response to changes in external aerodynamic forces, instead of using an active deformation mechanism. The flexibility of the wing improved performance by limiting flow separation at high angles of attack. Bartley-Cho et al. (2004) presented a variable camber wing, actuated by piezoelectric motors and integrated into a Northrop-Grumman combat UAV. Bilgen et al. (2007), (2009) designed and tested a concept of replacing the ailerons with local, continuous wing camber changes. The wind tunnel experiments and the flight testing of an UAV equipped with the morphing wing demonstrating the effectiveness of the concept at providing adequate roll control.

The CRIAQ 7.1 project took place between 2006 and 2009 and was realized following a collaboration approach between teams from École de Technologie Supérieure (ÉTS), École Polytechnique de Montréal, Bombardier Aerospace, Thales Canada and the Institute for Aerospace Research-Canadian National Research Center (IAR-CNRC). The objective of the project was to improve and control the laminarity of the flow past a morphing wing, in order to obtain important drag reductions (Botez, 2007).

In this project, the active structure of the morphing wing combined three main subsystems: a flexible, composite material upper surface, stretching between 3% and 70% of the airfoil chord, a rigid inner surface and a Shape Memory Alloy (SMA) actuator group located inside the wing box, which could morph the flexible skin at two points, located at 25.3% and 47.6% of the chord (Brailovski et al., 2008). The reference airfoil chosen for the project was the WTEA laminar airfoil and the morphing system was designed for low subsonic flow conditions. A theoretical study of the morphing wing system was performed (Pages, 2007), and very promising results were obtained: the morphing system was able to delay the

transition location downstream by up to 30% of the chord, and to reduce the airfoil drag by up to 22%.

Two control approaches were used for providing the optimal SMA actuator displacements for each different flight condition. In the open loop configuration, the desired displacements were directly imposed on the system (Popov et al, 2010) , while a novel, adaptive, neuro-fuzzy approach was used to predict and control the morphing wing performance (Grigorie, 2009). In the closed loop configuration, the displacements were automatically determined as a function of the pressure readings from the wing upper surface (Popov et al., 2010). In addition, a new controller based on an optimal combination of the bi-positional and PI laws was developed (Grigorie et al., 2012). The wind tunnel tests were performed in the 2 m by 3 m atmospheric closed circuit subsonic wind tunnel at IAR-CNRC and validated the numerical wing optimisations (Sainmont et al., 2009) and the designed control techniques (Grigorie, 2012).

The optimization procedure is focused on enhancing the aerodynamic characteristics of the Hydra Technologies S4 Éhecatl UAS airfoil. The S4 was designed and build in Mexico, and was created as an aerial unmanned surveillance system, directed towards providing security and surveillance capabilities for the Armed Forces, as well as civilian protection in hazardous situations. It is a high performance vehicle, capable of reaching altitudes of 15000 ft and cruising speeds of over 100 knots. The purpose of optimizing the original airfoil using a morphing wing technology is to grant the S4 UAS increased aerodynamic efficiency, extended flight times and a longer effective range, improving the cost effectiveness of its operation.

5.2 Optimization Approach

In order to improve the aerodynamic qualities of the UAS-S4 airfoil, the standard form of a continuous optimization problem can be used (Boyd and Vandenberghe, 2004):

$$\begin{aligned} &\text{minimize} \quad f(x) \\ &\text{subject to} \begin{cases} g_i(x) \le 0, \ i = 1, \ \dots, m \\ h_j(x) = 0, \ j = 1, \ \dots, p \end{cases} \end{aligned} \tag{5.1}$$

In the above mathematical formulation, $f(x)$ is the objective function to be minimized with respect to the variable x, $g_i(x)$ are the inequality constraints and $h_j(x)$ are the equality constraints that apply to the specific optimization problem.

5.2.1 Morphing wing concept

When considering the external flow over an airfoil, all the aerodynamic properties of that airfoil will be a function of its shape. The optimization problem is to find the optimal shape of the airfoil that allows the minimization of a specific aerodynamic characteristic (such as the drag coefficient), while respecting multiple constraints (the displacements of the airfoil curve should be within the desired limits, smoothness of the airfoil curve must be kept at all times, the other aerodynamic coefficient should not vary too much around some given values, etc.).

The actual implementation of an airfoil deformation technique on the real UAS-S4 requires that only a limited portion of the entire airfoil curve would be allowed to change, and that the modifications would be small enough in order to be feasible from a structural point of view. Any numerical optimization performed must be done with regard to the technological possibilities and constraints required by the practical development of the morphing wing structure. Our idea was to replace a part of the UAS's conventional, rigid wing skin by a flexible skin that could be deformed using electrical actuators placed inside the wing structure. Figure 5.1 shows the basic idea of the morphing wing.

We imposed that flexible skin starts at 5% of the chord on the airfoil lower surface, goes around the leading edge and stretches up to 55% of the chord on the upper surface. The starting point was chosen on the airfoil's lower surface in order to allow a good control of the

leading edge shape, while the skin's extent on the upper surface was limited by the presence of the wing control surfaces, such as aileron and flaps. The skin is attached to the rigid part of the wing at both ends, providing a smooth transition between the flexible and fixed regions.

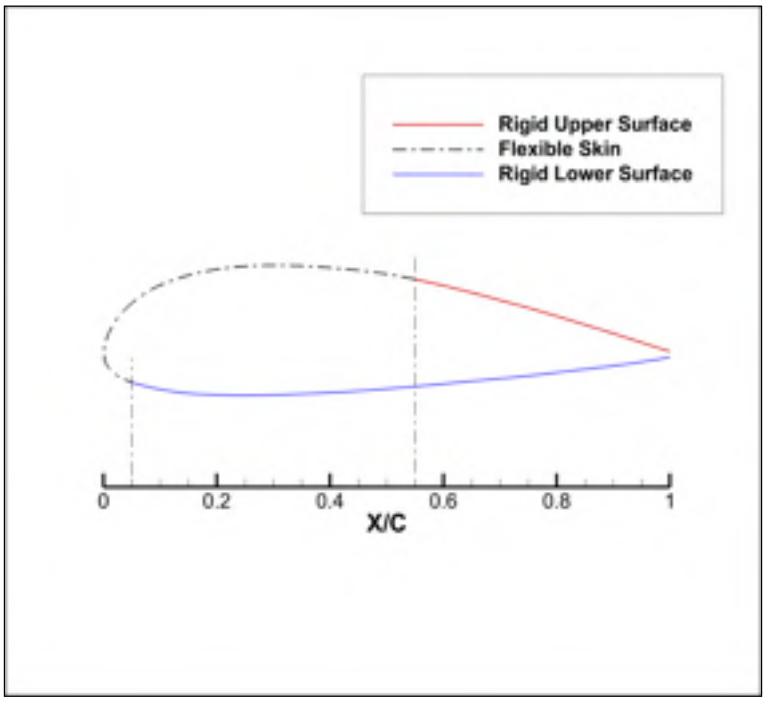

Figure 5.1 The morphing skin for the airfoil

5.2.2 Airfoil parameterization using NURBS

From a numerical point of view, the airfoil was parameterized using Non-Uniform Rational B-Splines (NURBS) (Piegl and Tiller, 1997), (Gerald, 1999). The NURBS are a generalization of B-Splines and Bézier curves, offering great flexibility and precision in representing and manipulating analytical curves. From a mathematical point of view, its order, a polygon of weighted control points, and a knot vector define a NURBS curve:

$$\mathbf{C}(u) = \sum_{i=1}^{k} \frac{N_{i,n} w_i}{\sum_{j=1}^{k} N_{j,n} w_j} \mathbf{P}_i \tag{5.2}$$

In the above formula, u is the curve parameter, ranging from 0 (the start of the curve) to 1 (the end of the curve), k is the number of control points, $N_{i,n}$ is the $i-th$ basis function, of order n, w_i is the weight associated with the $i-th$ control point, and $\mathbf{P}_i = [x_i, y_i]$ is the control point. The basis functions are determined using the De Boor recursive formula (De Boor, 1978):

$$N_{i,1} = \begin{cases} 1 \text{ , if } t_i \le u \le t_{i+1} \\ 0 \text{ , otherwise} \end{cases}$$
$$N_{i,n} = \frac{u - t_i}{t_{i+n} - t_i} N_{i,n-1} + \frac{t_{i+n+1} - u}{t_{i+n+1} - t_{i+1}} N_{i+1,n-1} \tag{5.3}$$

where u is again the curve parameter, n is the order of the basis function, while t_i represents the $i-th$ knot of the curve knot vector. In Figure 5.2, we present the deformable part of the airfoil and the NURBS control polygon associated with it.

For the parameterization of the airfoil curve, we have used a 3rd degree NURBS curve, which grants smoothness up to the second derivative, and a number of seven control points corresponding to the flexible skin part. This number of control points was found necessary in order to properly control the deformation of the leading edge, and to be able to exactly reconstruct the original airfoil when all the internal actuator displacements are set to zero.

In the numerical optimization, the change of the airfoil curve shape was achieved by changing the coordinates of the NURBS control points. The motion of the seven control points that influences the flexible skin was strictly controlled. For each control point, we calculated the vector normal to the airfoil curve, vector that also passes through the control point, or as close as possible to it, within an acceptable error margin. The motion of the seven points is then restricted to the direction given by the normal vector. In addition, the control point cannot move for more than a given length along this direction, in order to maintain the deformations of the flexible skin within some acceptable, predefined limits. Figure 5.3 shows the direction of movement and the limits imposed on one of the NURBS control points.

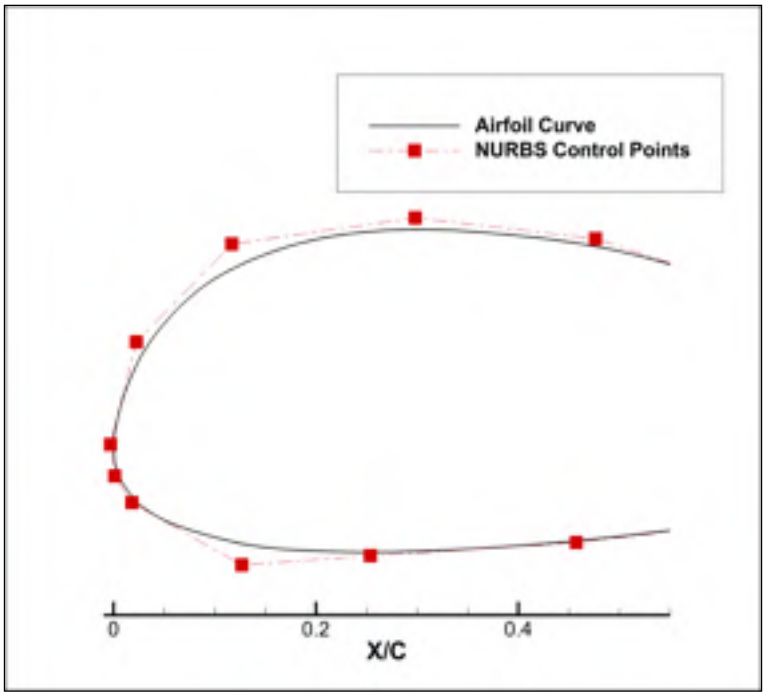

Figure 5.2 The NURBS control points for the original airfoil

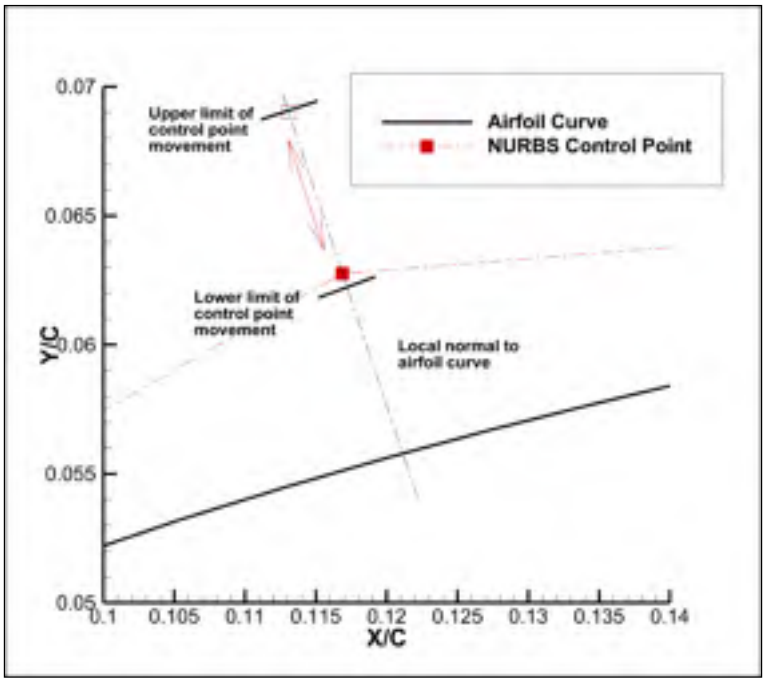

Figure 5.3 Direction of movement and imposed limits for a control point

5.2.3 The aerodynamic problem

Once the suitable mathematical description of the airfoil shape had been achieved, we were able to formulate different optimization objectives, concerning various aerodynamic properties of the airfoil. If, for example, the goal would be to minimize the drag coefficient, for any given airspeed and angle of attack, while keeping the lift coefficient constant, then the numerical optimization problem would be:

$$\begin{aligned} &\text{minimize} \quad C_D(\delta_1, \delta_2, \ \ldots, \delta_7) \\ &\text{subject to} \begin{cases} \delta_i \le \delta_{\max}, \ i = 1, \ \ldots, 7 \\ -\delta_j \le \delta_{\min}, \ j = 1, \ \ldots, 7 \\ C_L = \text{constant} \end{cases} \end{aligned} \tag{5.4}$$

In the above equation, δ_i represents the displacement of any of the seven control points that correspond to the flexible skin, while $\delta_{\min}$ and $\delta_{\max}$ are the allowed limits of the control point movement along the normal direction vector.

The code we have used for the calculation of the two-dimensional aerodynamic characteristics of the UAS airfoil is XFOIL, version 6.96, developed by Drela and Youngren (Drela and Youngren, 2001). The XFOIL code was chosen because it has proven its precision and effectiveness over time, and because it reaches a converged solution very fast. The inviscid calculations in XFOIL are performed using a linear vorticity stream function panel method (Drela, 1989). A Karman-Tsien compressibility correction is included, allowing good predictions for subsonic, compressible flows. For the viscous calculations, XFOIL uses a two-equation lagged dissipation integral boundary layer formulation (Drela, 1989), and incorporates the e^N transition criterion (Drela, 2003). The flow in the boundary layer and in the wake interacts with the inviscid potential flow by use of the surface transpiration model.

5.3 In-house Optimization Code

One of the tools used to perform the optimization of the UAS-S4 wing airfoil is an in-house code based on the Artificial Bee Colony (ABC) algorithm, coupled with the Broyden-Fletcher-Goldfarb-Shanno (BFGS) algorithm for providing a final refinement of the solution.

5.3.1 Artificial Bee Colony algorithm

The ABC algorithm is an optimization algorithm based on the intelligent behaviour of a honeybee swarm. It was conceived by Karaboga and Basturk (2007) and has been continuously developed and adapted. In this algorithm, the colony contains three different types of bees: employed, onlooker and scouts, while the food sources exploited by these bees represent the possible solutions of the optimization problem.

The ABC algorithm is initialized with a random distribution of food sources, equal to the number of employed bees. Each employed bee visits one food source, evaluates the nectar amount of that food source (the quality of the possible solution) and then searches for a new food source in its vicinity. If the quality of this newly found source is higher, the employed bee memorizes its position and forgets about the previous food source. The onlooker bees wait in the hive of the bee swarm until all the employed bees have finished their search and have returned to the hive. Each onlooker bee individually chooses one of the food sources exploited by the returned employed bees, with a probability based on the quality of that food source. Then, it carries out the same exploration process as an employed bee, searching for a higher quality source in the vicinity of the chosen one. Scout bees are randomly searching for new food sources, in order to replace the exhausted ones. In the algorithm, an employed bee becomes a scout if the food source that it is exploiting cannot be improved after a given number of visits. The process of sending out the employed bees, the onlooker bees and the scouts continues in an iterative manner for a predetermined number of cycles. The general outline of the ABC algorithm is presented in Figure 5.4.

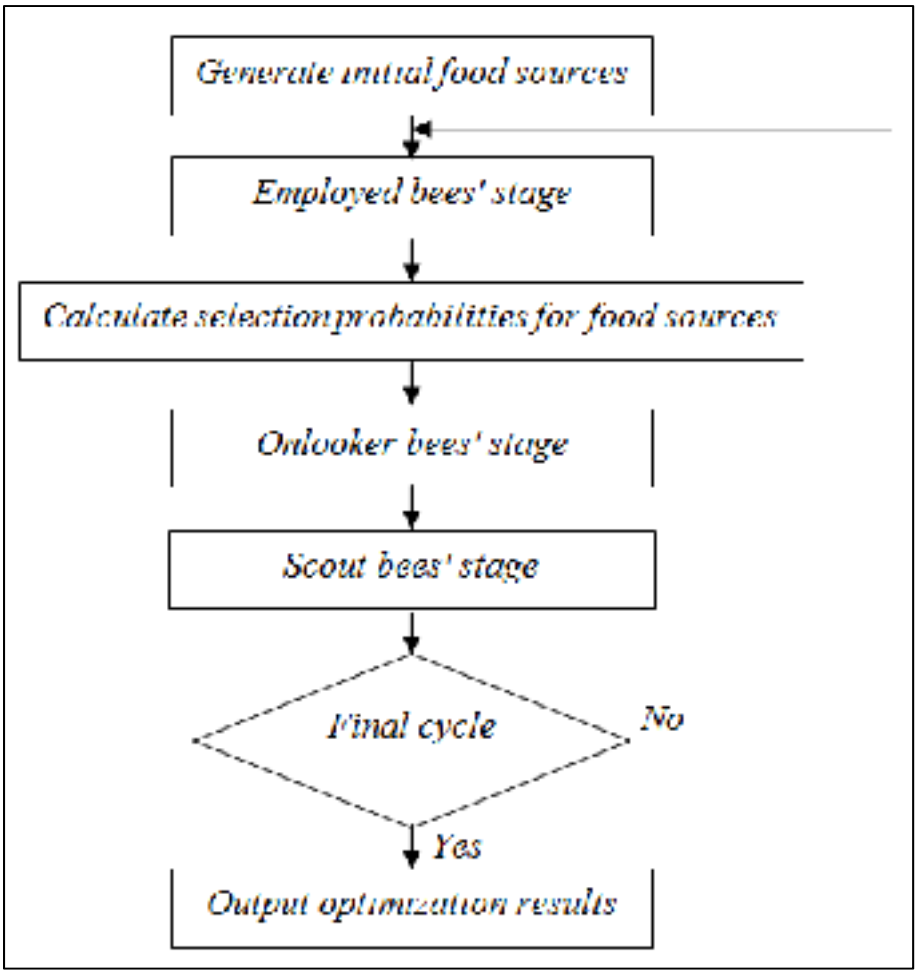

Figure 5.4 General outline of the ABC algorithm

The original ABC algorithm was developed only for unconstrained optimization problems, but Karaboga demonstrated that it could be applied for constrained optimization with only minor modifications (Karaboga and Basturk, 2007). In the original algorithm, the employed and onlooker bees perform a greedy selection process when searching for new food sources, immediately forgetting about the previous source if the new food source has better quality. In order to handle constrained optimization, the greedy selection is simply replaced by Deb's constraint handling method (Deb and Goldberg, 1991).

The performance of the ABC algorithm has been compared with that of several other population-based optimization algorithms, such as genetic algorithm, particle swarm

optimization, evolution strategies and differential evolution algorithm. Results for a number of 50 different minimization problems showed that the ABC algorithm outperformed the other population-based algorithms, with the advantage of employing fewer control parameters (Karaboga and Akay, 2009). Various authors have proposed methods for further enhancing the convergence properties of the algorithm, such as dynamically adjusting the frequency and magnitude of the perturbations (Akay and Karaboga, 2010), steering the solutions towards the region of the global optimum (Zhu and Kwong, 2010) or influencing the behaviour of the bees using elements of chaos theory (Xu, 2010).

5.3.2 Broyden-Fletcher-Goldfarb-Shanno algorithm

In order to determine the effectiveness of the optimization routine, we have performed several tests on a reduced order problem, in which only two control points change the shape of the flexible skin. The effect of deforming the skin could be clearly analysed by performing a Monte-Carlo simulation and plotting the response surface of the objective function, for all combinations of allowed displacements. It was found that the ABC algorithm converged very quickly to a vicinity of the global optimum, but in some cases, when the optimum lies within an almost flat valley, it needs a great number of additional cycles to find the exact optimal point. For this reason, we have implemented the option of performing a final refinement of the solution using the Broyden-Fletcher-Goldfarb-Shanno (BFGS) algorithm (Bonnans et al., 2006).

The BFGS method is an iterative, quasi-Newton method for unconstrained optimization, in which the Hessian matrix of second derivatives is approximated and updated using the gradient evaluations. The algorithm starts with an initial guess of the solution, $\mathbf{x}_k$ (in our case, the final solution provided by the ABC method), and an initial guess of the approximate Hessian matrix $\mathbf{B}_k$. The search direction $\mathbf{p}_k$ is given by solving the Newton-like linear system:

$$\mathbf{B}_k \mathbf{p}_k = -\nabla f(\mathbf{x}_k) \tag{5.5}$$

In the above equation $\nabla f(\mathbf{x}_k)$ represents the gradient of the function that should be minimized and that is calculated at the available solution. Next, a line search is performed to determine the acceptable advancement step α_k, and the solution is updated:

$$\mathbf{x}_{k+1} = \mathbf{x}_k + \alpha_k \mathbf{p}_k \tag{5.6}$$

The final step of the algorithm consists in the update of the approximate Hessian matrix:

$$\mathbf{B}_{k+1} = \mathbf{B}_k + \frac{\mathbf{y}_k \mathbf{y}_k^T}{\mathbf{y}_k^T \mathbf{s}_k} - \frac{\mathbf{B}_k \mathbf{s}_k \mathbf{s}_k^T \mathbf{B}_k}{\mathbf{s}_k^T \mathbf{B}_k \mathbf{s}_k} \tag{5.7}$$

where $\mathbf{y}_k = \nabla f(\mathbf{x}_{k+1}) - \nabla f(\mathbf{x}_k)$ represents the difference between two successive calculations of the objective function's gradient vector, while $\mathbf{s}_k = \alpha_k \mathbf{p}_k$. The convergence of the method is checked by monitoring the norm of the gradient vector, $\|\nabla f(\mathbf{x}_{k+1})\|$, until it becomes smaller than a given error criteria ε.

Since the BFGS method can be applied only for unconstrained optimization, it was coupled with the Augmented Lagrangian Method (ALM) (Powell, 1969), in order to introduce the desired optimization constraints. The ALM method replaces the constrained optimization problem by an iterative series of unconstrained optimization problems, targeting a modified objective function. The constrained problem can be written as:

$$\begin{aligned} &\text{minimize} \quad f(\mathbf{x}) \\ &\text{subject to} \quad g_i(\mathbf{x}) = 0, \; i = 1, \; \ldots, m \end{aligned} \tag{5.8}$$

The objective function $f(\mathbf{x})$ is replaced by a modified function $\phi(x)$ in which the constrains are introduced under the form of a penalty term and a Lagrangian multipliers term:

$$\phi(\mathbf{x}) = f(\mathbf{x}) + \mu \sum_{i=1}^{m} g_i(\mathbf{x})^2 - \sum_{i=1}^{m} \lambda_i g_i(\mathbf{x}) \tag{5.9}$$

where μ represents the penalty coefficient and λ_i represent the Lagrangian multipliers. The modified function $\phi(\mathbf{x})$ can be minimized using the unconstrained BFGS algorithm, until the convergence of the solution is obtained. Using the determined optimal solution, denoted by $\mathbf{x}^*$, the two variables controlling the enforcement of the constraints can be updated:

$$\begin{aligned} \mu &= \beta\mu \\ \lambda_i &= \lambda_i - \mu g_i(\mathbf{x}^*) \end{aligned} \tag{5.10}$$

In the above equations, β is a parameter that controls the rate at which μ increases from one ALM iteration to the next iteration. With the new values of μ and λ_i, the modified function $\phi(x)$ is recalculated and the unconstrained problem is solved again to obtain a better estimation of the constrained optimum. The algorithm continues running until all the constraints are respected, $g_i(\mathbf{x}) = 0$, and the modified function $\phi(x)$ becomes identical to the original objective function $f(x)$.

5.3.3 Optimization tool for validation

The second tool we have used for the optimization of the UAS-S4 wing airfoil, and validate the results of the in-house optimizer, is the commercially available software package called modeFrontier (ESTECO, 2015). It is an integration platform, allowing multi-disciplinary and multi-objective optimization of engineering designs. The software allows us to perform the optimization of the airfoil, by coupling the integrated algorithms with the external NURBS

parameterization routines and aerodynamic solver. Figure 5.5 presents the necessary setup of the problem inside modeFrontier.

The figure also clearly identifies all the different components needed for the creation of the optimization system:

- A) The *displacements of the seven control points* of the flexible skin are arranged into an input matrix, together with the acceptable lower and upper bounds of each displacement and the displacement step;
- B) The *Design of Experiment* allows the choice of the number n of different designs to be analysed in the study; a design comprises a random combination of the optimisation problem variables, in the present study, a combination of displacements for all the seven control points; the initial designs are generated using the Uniform Latin Hypercube algorithm, guaranteeing a uniform distribution of the initial designs over the entire allowable variables range;
- C) The *Optimization Algorithm Selection* allows a choice between several different algorithms; the implemented multi-objective genetic algorithm MOGA-II (Poles, 2003) was chosen for the current study; it uses a *multi-search elitist approach* and a *directional crossover operator*, characteristics that ensure robustness and avoid its premature convergence to local optima; *directional crossover* is a proprietary genetic operator, that always tries to create a new individual with better characteristics than its parents; Figure 5.6 presents the setup of the algorithm parameters;
- D) *External routines* used for the generation of the morphed airfoil coordinates, using the NURBS parameterization, based on the modifications of the control points coordinates provided by the MOGA-II optimization algorithm;
- E) The *creation of the input file* needed for the configuration of the XFOIL aerodynamic solver; in this file, we specify the flight conditions (airspeed, angle of attack, Reynolds number) for which the optimization is performed;
- F) The *external aerodynamic solver* XFOIL used to calculate the properties of the morphed airfoil;
- G) The desired objective of the optimization;

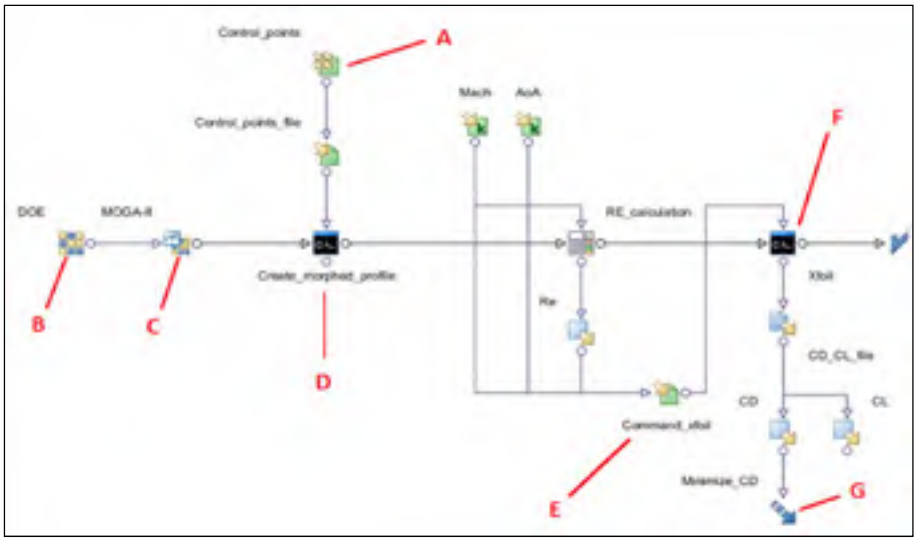

Figure 5.5 Setup for airfoil optimization problem using modeFrontier

Parameters		
Number of Generations	[1,5000]	15
Probability of Directional Cross-Over	[0.0,1.0]	0.5
Probability of Selection	[0.0,1.0]	0.05
Probability of Mutation	[0.0,1.0]	0.1
Advanced Parameters		
DNA String Mutation Ratio	[0.0,1.0]	0.05
Elitism		Enabled
Treat Constraints		Penalising Objectives
Algorithm Type		MOGA - Generational Evolution
Random Generator Seed	[0,999]	1
Category Parameters		
Categorize Generations		
Categorize Operators		

Figure 5.6 Choice of parameters for MOGA-II algorithm

5.4 Results and Discussions

The optimization of the UAS-S4 wing airfoil was performed with the objective of reducing the drag coefficient. In order to achieve this goal, two distinct approaches were used. In the first one, the actual drag coefficient of the airfoil was used as the objective function, while imposing the constraint of not allowing the lift coefficient to become lower than the lift coefficient of the original airfoil. In the second approach, a more indirect strategy was used, in which the objective function was to increase the extent of laminar flow over the airfoil

upper surface, while imposing the same constraint as mentioned before on the variation of the lift coefficient.

5.4.1 Aerodynamic analysis setup

The analyses were performed at three airspeed values, 34 m/s, 51 m/s and 68 m/s, corresponding to Mach number values of 0.10, 0.15 and 0.20. The highest value represents the maximum velocity of the UAS-S4, while the middle value represents its cruise speed. The Reynolds numbers corresponding to the three airspeeds are relatively small, 1.412E+06, 2.171E+06 and 2.823E+06. The range of angles of attack is between -2 deg and 10 deg and covers the typical values expected in any normal flight scenario of the UAS. The turbulent intensity of the incoming airflow was set at 0.07%.

5.4.2 Morphing airfoil setup

The NURBS parameterization of the airfoil was performed using seven control points for the flexible skin region stretching between 5% of the chord on the airfoil lower surface and 55% of the chord on the upper surface. The number of control points was chosen as a compromise between the accuracy of the NURBS representation of the airfoil and the total number of optimization variables. The lower limits of the control point movements were set to zero, corresponding to the original airfoil shape, while the upper limits were limited to 2.5 mm. This value was found high enough in order to obtain a good range of improvements, while keeping the variation of the flexible skin's length smaller than 0.75%.

5.4.3 In-house optimizer setup

The ABC algorithm considered 30 employed bees, 30 onlooker bees, and a maximum number of cycles equal to 50, giving a total possible number of objective function evaluations equal to 3000. The initial values of the scaling factor and the modification rate were set to 1.0, and were dynamically updated during the simulation every 10 cycles. The

limit of cycles after which non-improved solutions were abandoned was set equal to the maximum number of cycles, since it was found this parameter does not significantly influence convergence for the particular problem of the airfoil optimization. The attraction factor of the best solution was set to 1.5. Concerning the convergence of the algorithm, if the best-found solution does not improve for 20 cycles, it is considered the optimal solution. If the ABC algorithm has not converged after the maximum 50 cycles, we exit the ABC loop and enter the ALM-BFGS loop. Because the initial guess used for starting the calculations is already very close to the optimum, a small number of iterations were found sufficient for convergence. A maximum number of ALM iterations equal to 2, of BFGS iterations equal to 10 and of approximate line search iterations equal to 10 were imposed. However, the modulus of the gradient usually became smaller that 1E-05 after only 2 or 3 BFGS iterations, within the first ALM iteration. The ALM penalty coefficient and the Lagrangian multipliers were initialized with a value of 10.

5.4.4 modeFrontier setup

For the MOGA-II algorithm, a population of 100 individuals was used, and 15 generations were imposed, giving a total possible number of objective function evaluations equal to 1500. We have set the probability of directional crossover equal to 0.5, the probability of mutation equal to 0.1 and the mutation ratio equal to 0.05. In addition, we have enabled the use of elitism, and we have selected to treat the optimization constraints as penalties that negatively affect the performance of the individuals.

5.4.5 Results obtained for drag reduction

The results obtained with both optimization tools, for the first approach, when the drag coefficient of the airfoil was used as objective function, are presented here. Figure 5.7 presents the variation of the UAS airfoil drag coefficient with the lift coefficient, for the original airfoil and for both optimized airfoils (obtained by the in-house code and modeFrontier), for a Mach number of 0.15.

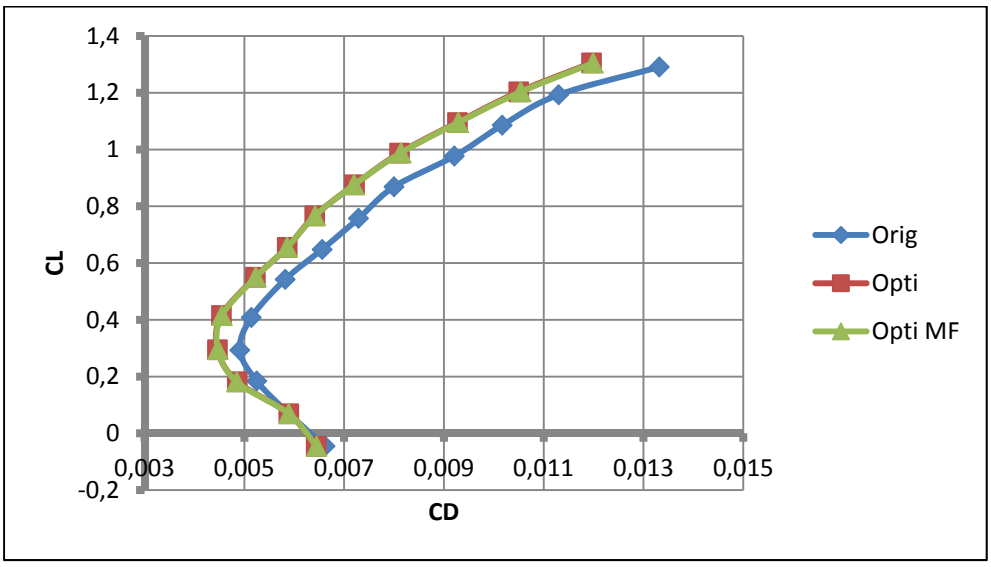

Figure 5.7 Original and optimized airfoils drag polar comparison for Mach = 0.15

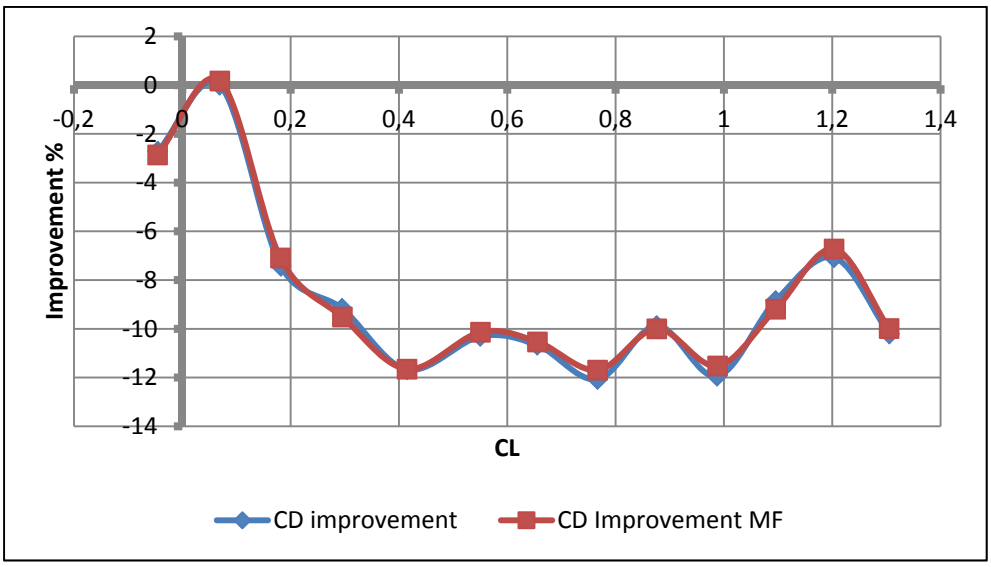

Figure 5.8 Drag coefficient reduction over the lift coefficient range for Mach = 0.15

It is seen that both optimizer codes obtained a consistent drag reduction for the entire range of flight conditions. The drag reduction, in percentages, compared to the original airfoil coefficient, for each lift coefficient obtained in the analysis range, is depicted in Figure 5.8.

The results obtained by the in-house code almost perfectly match the results of modeFrontier. Except for the conditions close to zero lift, where the improvements are small, drag reductions of over 7%, were obtained, with a maximum reduction of 12% for *CL* values of 0.4, 0.8 and 1.0 (corresponding to angle of attack values of 2 deg, 5 deg and 7 deg). Because keeping the lift coefficient at least to the value of the original airfoil was a constraint of the optimization, then a significant improvement of the airfoil lift-to-drag ratio was obtained, as shown in Figure 5.9.

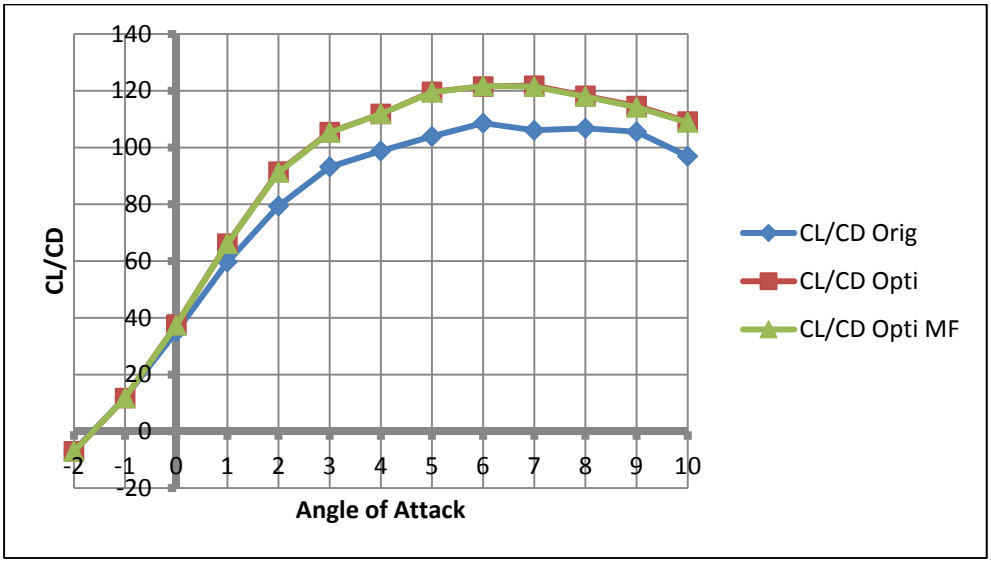

Figure 5.9 Original and optimized airfoils lift over drag ratio comparison for Mach = 0.15

In order to make a qualitative assessment of the influence that the morphed skin has on the behaviour of the airfoil boundary layer, and clearly identify the origin of the drag reduction, a comparison is presented for the pressure coefficient distribution and the skin friction coefficient distribution, for the original airfoil and the optimized airfoil, at an airspeed of 51 m/s and 2 deg angle of attack.

It can be observed, from the pressure coefficient plot in Figure 5.10, that the morphed airfoil presents a smoother pressure peak, and that the adverse pressure gradient is not as strong as it is for the original airfoil, thus creating favourable conditions for an extended laminar flow. The skin friction coefficient in Figure 5.10 clearly indicates that the laminar-to-turbulent transition region is delayed by almost 15% of the chord, from the initial position at 35% of the chord, in the case of the original airfoil, up to a position at 50% of the chord.

As the angle of attack is increased, the drag coefficient reduction is achieved through both a small increase in the extent of laminar flow, and through a reduction of pressure drag. In Figure 5.11, an important difference in the pressure coefficient peak, between the original and optimized airfoil can be observed. In addition, the skin friction coefficient indicates a small increase in the laminar flow region, although the flow remains turbulent over 90% of the chord.

The optimized airfoil behaviour observed at a Mach number of 0.15 remains relatively the same for the other two considered airspeeds. Both optimizer codes obtained consistent drag reductions for the entire range of angles of attack. Figure 5.12 and Figure 5.13 present the actual drag coefficient reductions, in percentages, compared to the original airfoil coefficients, for the Mach numbers equal 0.10 (Figure 5.12) and 0.20 (Figure 5.13).

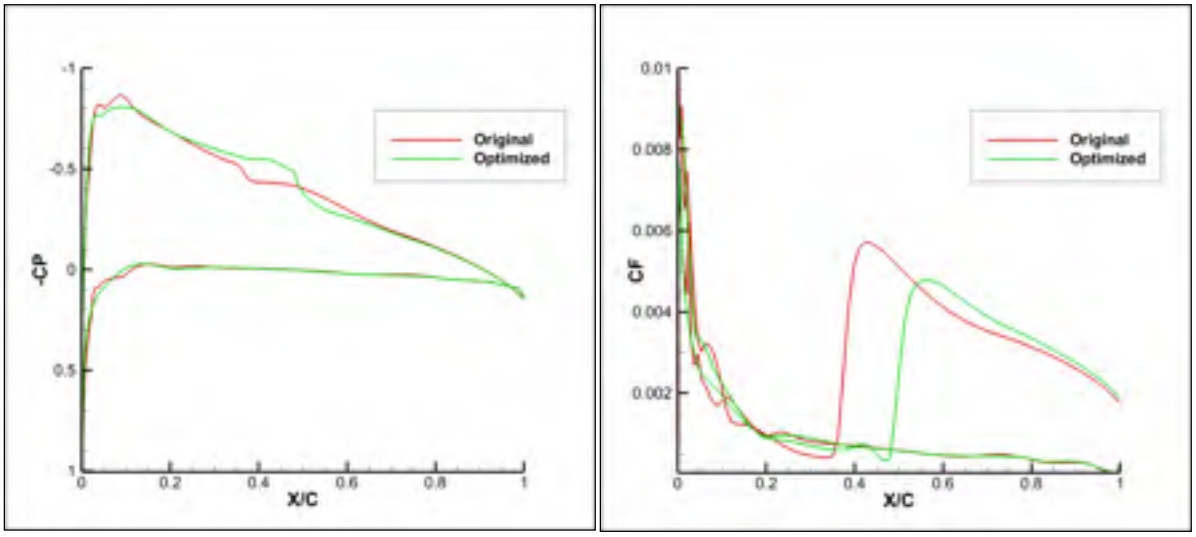

Figure 5.10 Pressure distributions and skin friction coefficient comparisons at 51 m/s and 2 deg angle of attack

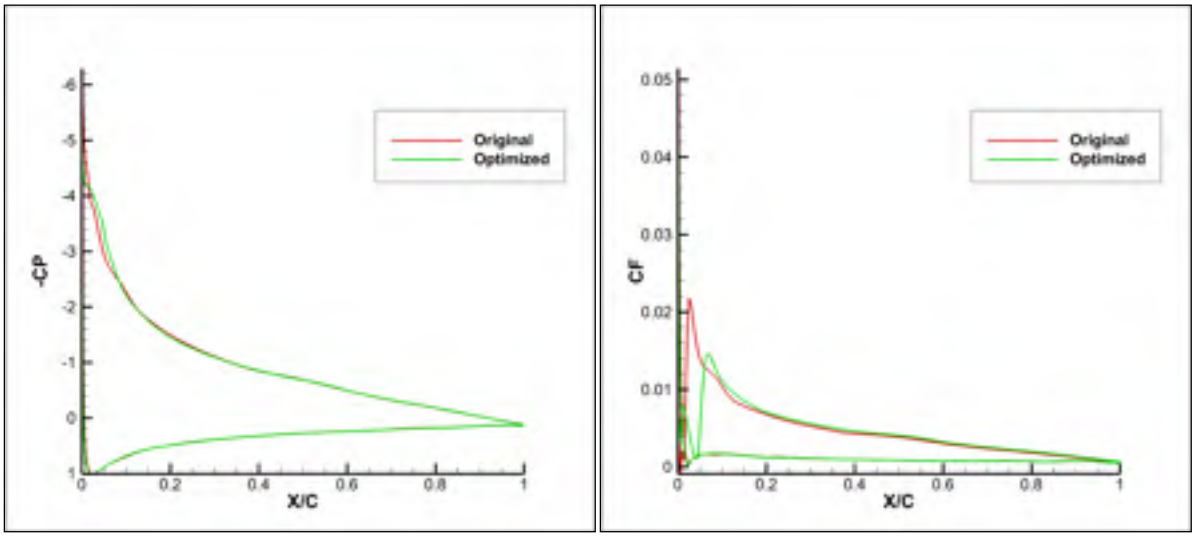

Figure 5.11 Pressure distributions and skin friction coefficient comparisons at 51 m/s and 10 deg angle of attack

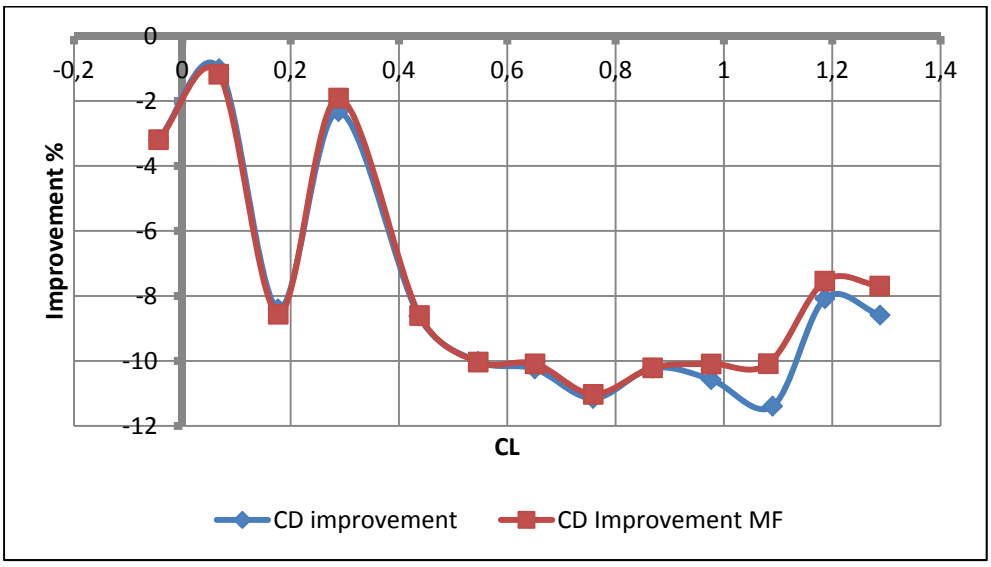

Figure 5.12 Drag coefficient reduction over the lift coefficient range for Mach = 0.10

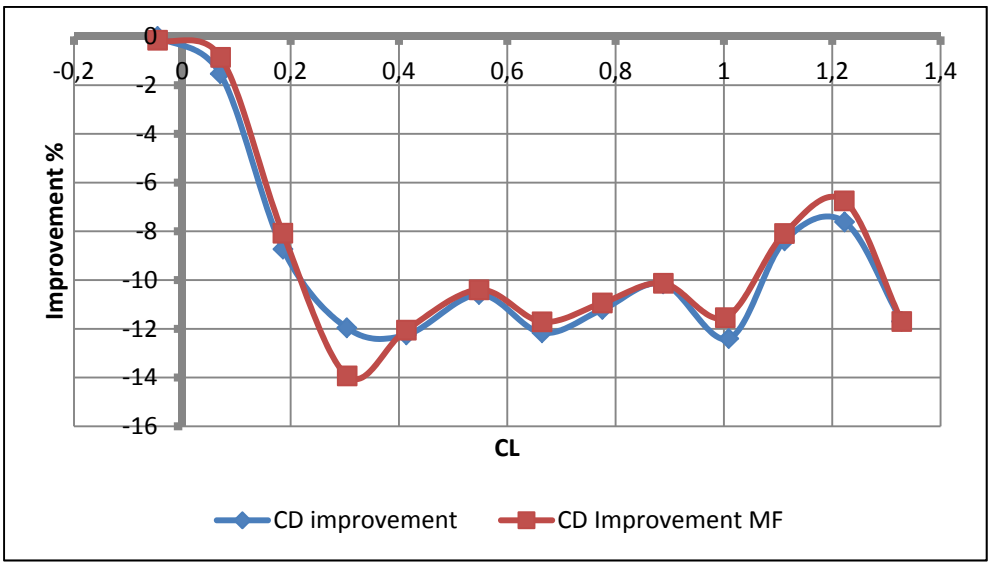

Figure 5.13 Drag coefficient reduction over the lift coefficient range for Mach = 0.20

5.4.6 Results obtained for transition delay

The results obtained with both optimization tools, for the second approach, when the objective function is the increase of the extent of laminar flow over the airfoil upper surface, while imposing the constraint of not allowing the lift coefficient to become lower than the lift coefficient of the original airfoil, are presented. Figure 5.14, shows a comparison between the chord-wise positions of the upper surface laminar-to-turbulent transition point, for the original and optimized airfoils. The comparison is made again at a Mach number of 0.15, the UAS-S4 cruise regime. The angle of attack range is restricted between -2 and 3 deg, in order to keep the flow naturally laminar over an extended region of the airfoil chord.

It can be observed that for angles of attack smaller than 0 deg, no improvements can be obtained. This can be explained by the fact that the transition point is naturally situated at over 60% of chord, as measured from the leading edge, downstream of the morphing skin termination point. Thus, its position cannot be actively controlled by modifying the airfoil shape within the predetermined limits. For angles of attack greater than 1 deg, transition delays of over 10% of the chord are obtained. The increase in flow laminarity causes a reduction in the airfoil drag coefficient, as can be observed in Figure 5.15.

Figure 5.16 shows the comparison between the original and optimized airfoils pressure coefficient distribution, at the airspeed of 51 m/s, at -1 deg angle of attack (left) and at 3 deg angle of attack (right).

The 3 deg angle of attack pressure coefficient distribution plot indicates the same behaviour of the optimized airfoil as observed for the first optimization approach. A smoother pressure peak and an adverse pressure gradient that is not as strong as for the original airfoil, creating favourable conditions for laminar flow, are obtained. At -1 deg, the flow is laminar beyond the extent of the morphing skin, but an influence on the leading edge pressure distribution can be observed.

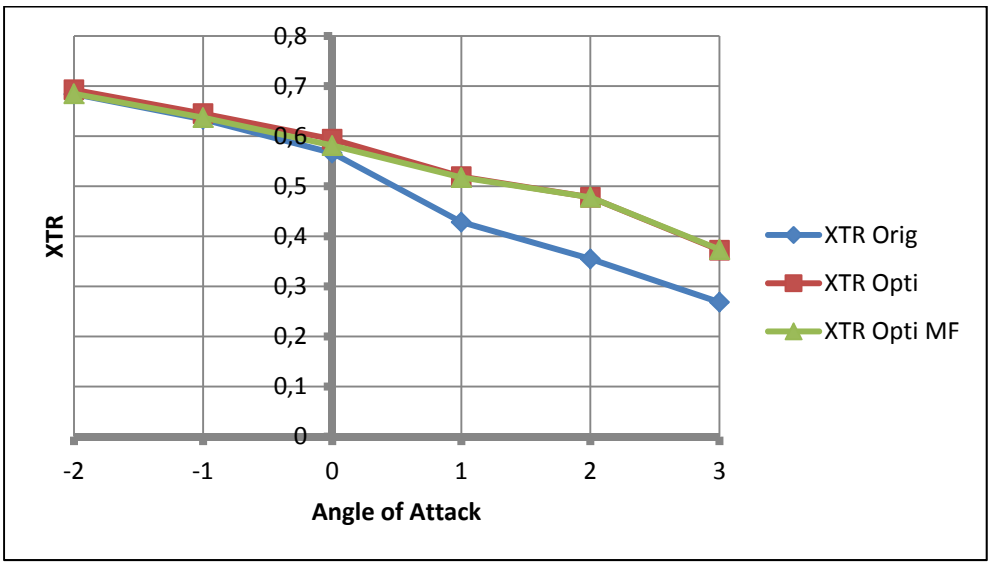

Figure 5.14 Comparison of the upper surface transition location with the angle of attack for Mach 0.15

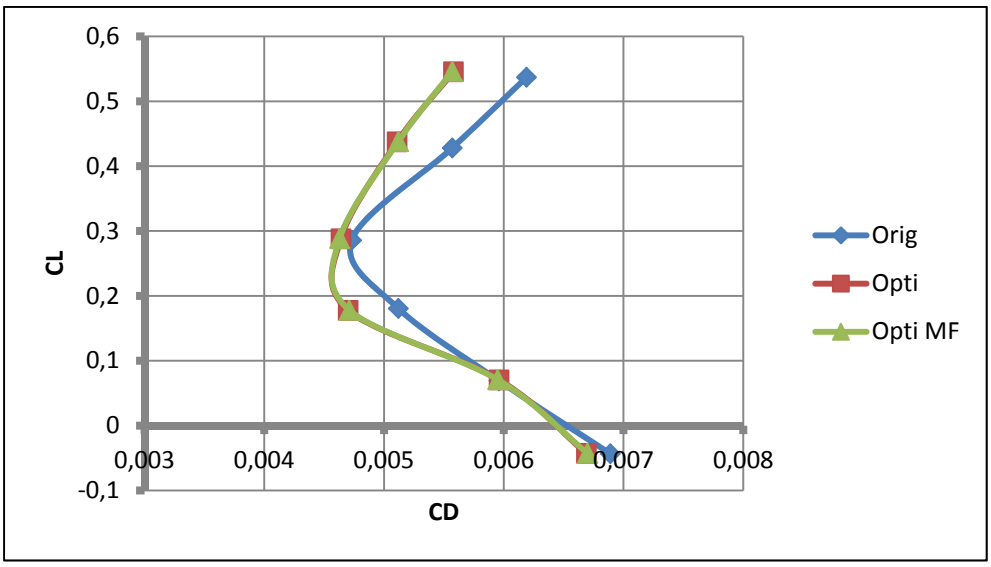

Figure 5.15 Original and optimized airfoils drag polar comparison for Mach = 0.15

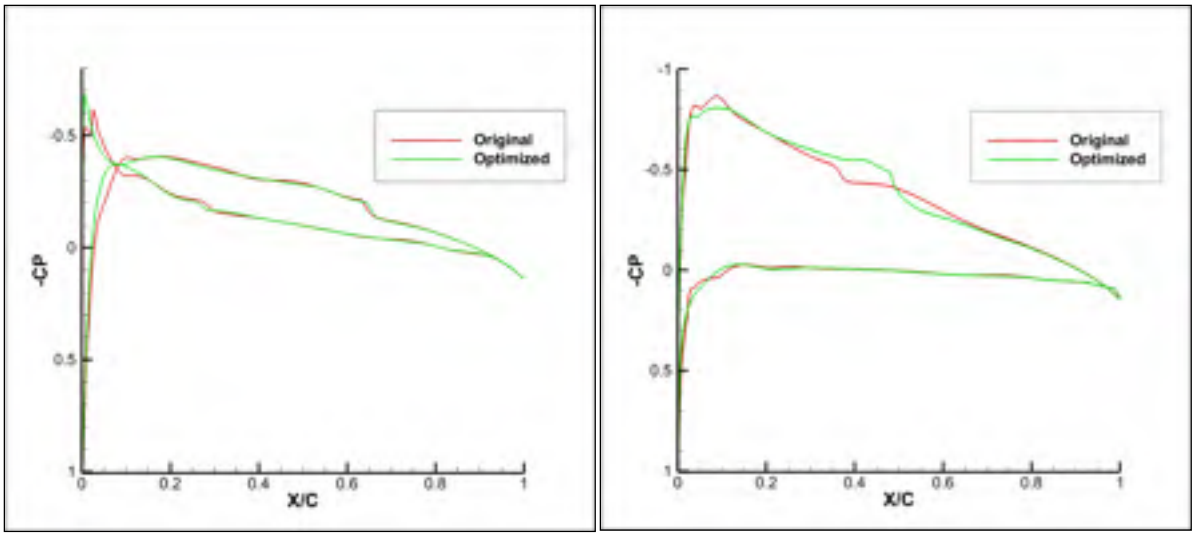

Figure 5.16 Pressure distributions comparisons at 51 m/s and -1 deg angle of attack (left) and 3 deg angle of attack (right)

The optimized airfoil behaviour observed at a Mach number of 0.15 remains relatively the same for the other two considered airspeeds. Both optimizer codes obtained important delays in the transition point location, provided that its initial location lies in the flexible skin region. Figure 5.17 and Figure 5.18 present the chord-wise positions of the upper surface laminar-to-turbulent transition point, for the Mach numbers equal 0.10 (Figure 5.17) and 0.20 (Figure 5.18).

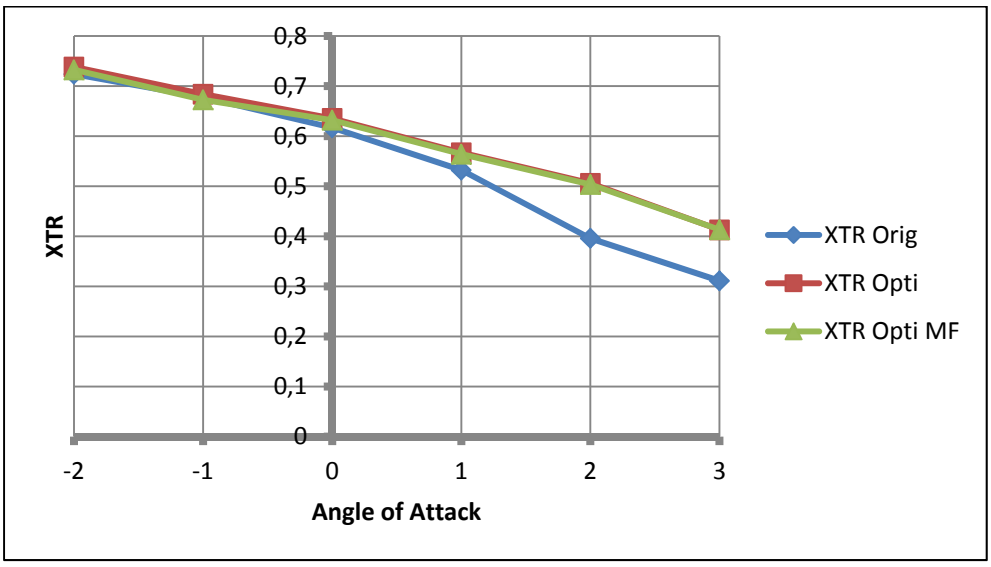

Figure 5.17 Comparison of the upper surface transition location with the angle of attack for Mach 0.10

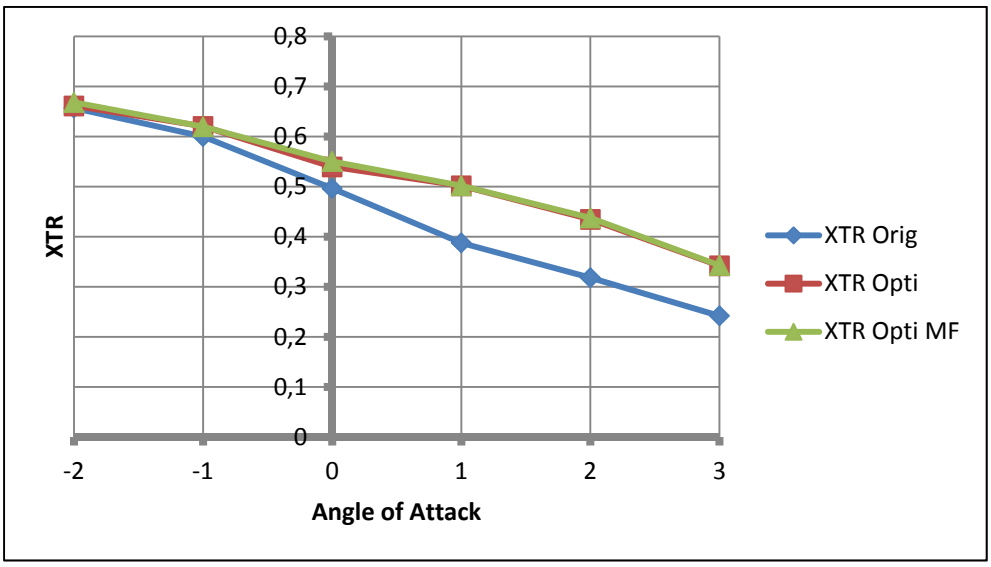

Figure 5.18 Comparison of the upper surface transition location with the angle of attack for Mach 0.20

5.4.7 Comparison between the optimization strategies

Both optimization approaches obtained good results, and the obtained morphed geometries outperform the original airfoil for their respective flight conditions. At the same time, the skin friction coefficient plot in Figure 5.10 shows that the airfoil optimized with respect to the drag coefficient achieves a higher extent of laminar flow, while the polar plot of Figure 5.15 shows that the airfoils optimized for increase laminar flow have smaller drag, compared to the original geometry. Table 5.1 presents a comparison between the drag polars of the optimized morphed geometries obtained with the two different strategies, while Table 5.2 presents a comparison between the chord-wise positions of the upper surface laminar-to-turbulent transition points of the morphed geometries obtained with the two approaches. Both comparisons are performed at a Reynolds number of 2.171E+06 and a Mach number of 0.15.

Table 5.1 Comparison of drag coefficient obtained with the two optimization strategies

CL	CD original airfoil	CD obtained with drag-focused optimization	CD obtained with transition-focused optimization
-0.0451	0.00662	0.00644	0.00655
0.0698	0.00589	0.00588	0.00589
0.1841	0.00525	0.00486	0.00487
0.2931	0.00491	0.00446	0.00450
0.4081	0.00514	0.00454	0.00454
0.5423	0.00582	0.00522	0.00522

It can be seen that the results of the two different optimizations achieve the desired goals, with respect to the original airfoil performance and the chosen objective. The morphed geometries obtained are very similar, obtaining almost the same performance improvement, but they are not identical. For the -2 deg case, clear differences exist in the morphed airfoils shapes, as seen from the drag coefficient difference. Between -1 deg and 1 deg angle of attack, the two morphed geometries are only differentiated by very small displacements and performance differences, according to the optimization objective, while for the 2 deg and 3 deg cases, the differences are negligible.

Table 5.2 Comparison of upper surface transition obtained with the two optimization strategies

Angle of Attack [deg]	X_{TR} original airfoil	X_{TR} obtained with drag-focused optimization	X_{TR} obtained with transition-focused optimization
-2	0.6839	0.6856	0.6928
-1	0.6336	0.6371	0.6451
0	0.5664	0.5842	0.5941
1	0.4284	0.5167	0.5193
2	0.3549	0.478	0.478
3	0.2685	0.3724	0.3724

The results obtained with the two objective functions could be even more similar by imposing a desired control point displacement precision during the optimization procedure. By imposing this precision limit, calibrated according to the precision of available actuation systems, the currently continuous space of allowed displacements would be transformed into a discrete set of allowed displacements, spanning between the lower and upper movement limits.

5.4.8 Morphed airfoil geometries

The results obtained for both objective functions require only very small modifications of the airfoil geometry. The changes in the NURBS control points positions should be small enough to keep the modifications feasible from a structural point of view, and to prevent great changes of the flexible skin length. In Table 5.3, we present the normal direction displacements of the NURBS control points, for the optimization performed with the aim of reducing the airfoil drag coefficient, at a Mach number of 0.20. It must be noted that this particular optimization case needed the greatest average displacements of the actuators, so it can be considered a limit case, from the point of view of the actual loads the morphing skin has to withstand.

Figure 5.19 shows the original S4 UAS airfoil and three different reconstructed airfoils, for three angle of attack values (0 deg, 4 deg and 7 deg), based on the displacement values of Table 5.3.

Table 5.3 Normal direction NURBS control points displacements for Mach 0.20

Angle of attack [deg]	Skin length variation [%]	Control points normal displacements [mm]						
		Point 1	Point 2	Point 3	Point 4	Point 5	Point 6	Point 7
-2	0.37	0.07	0.68	0.88	0.29	0.00	2.10	0.00
-1	0.30	0.01	0.19	0.02	0.44	0.00	1.40	0.00
0	0.37	0.73	0.43	0.13	0.33	0.00	0.87	1.00
1	0.47	2.50	1.70	1.20	0.09	0.00	0.10	1.96
2	0.40	2.50	2.49	1.66	0.43	0.00	0.00	1.25
3	0.34	0.02	2.50	2.50	1.05	0.05	0.00	0.57
4	0.29	0.07	0.04	2.50	1.92	0.02	0.00	0.02
5	0.31	0.00	0.00	2.48	2.50	0.20	0.00	0.02
6	0.33	0.00	0.00	0.04	2.50	1.11	0.02	0.25
7	0.76	1.25	1.32	1.25	2.43	0.39	1.72	1.62
8	0.55	0.04	0.00	0.00	0.00	2.50	1.97	1.14
9	0.62	0.00	0.25	0.94	0.00	2.50	2.50	1.39

5.5 Conclusions

In this paper, we have presented numerical results obtained for the optimization of the Hydra Technologies UAS-S4 airfoil. The airfoil modification procedure is based on a morphing wing approach, and the upper and lower surface changes have been done keeping in mind possible structural constraints. A new optimization code, based on a hybrid ABC-BFGS algorithm was used to determine the optimal displacements of the NURBS control points. The results have been validated with the help of a state-of-the-art, commercially available optimisation software.

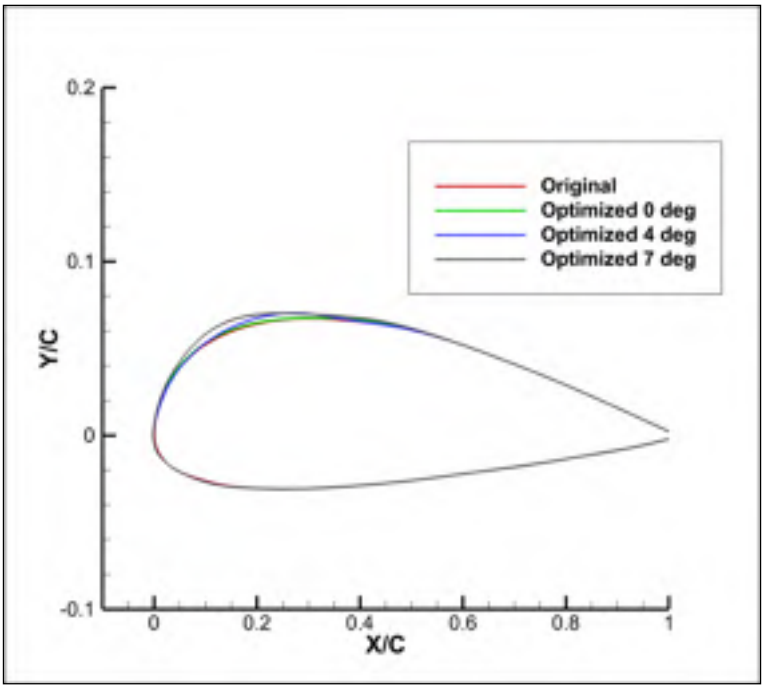

Figure 5.19 Comparison between the original airfoil and three optimized airfoils

The morphing skin was used to decrease the airfoil drag coefficient, using two different approaches. In the first one, we have focused on the actual drag coefficient value, while in the second approach we have tried to maximize the extent of the laminar flow on the airfoils' upper surface. For each of three considered airspeeds, significant drag coefficient reductions have been obtained for the positive values of the angle of attack. At low angles of attack, the drag reduction is linked to the increased extent of laminar flow, while at higher angle of attack values pressure drag reduction has a higher weight in achieving the proposed objective.

The drag coefficient reduction, as important as 14%, and the delay in the laminar-to-turbulent transition location, up to 15% of the chord, have been obtained using very small displacements of the airfoil surface. In addition, only a limited portion of the airfoil is flexible, between 5% of the chord on the lower surface and 55% of the chord on the upper surface. Thus, we have made sure to limit the displacements of the actuation system used to deform the flexible skin, and we prevent significant variation of the skin length, in order to

make the modifications feasible for the implementation on the UAS-S4. These modifications will make it possible for the UAS-S4 to achieve increased efficiency.

Acknowledgments

We would like to thank the Hydra Technologies Team in Mexico for their continuous support, and especially Mr. Carlos Ruiz, Mr. Eduardo Yakin and Mr. Alvaro Gutierrez Prado. We would also like to thank to the Natural Sciences and Engineering Research Council of Canada (NSERC) for the funding of the Canada Research Chair in Aircraft Modeling and Simulation Technologies. In addition we would like to thank to the Canada Foundation of Innovation (CFI), to the Ministère du Développement économique, de l'Innovation et de l'Exportation (MDEIE) and to Hydra Technologies for the acquisition of the UAS-S4 using the Leaders Opportunity Funds.

CHAPTER 6

OPTIMIZATION OF UNMANNED AERIAL SYSTEM WING AERODYNAMIC PERFORMANCE USING SEVERAL CONFIGURATIONS OF A MORPHED WING CONCEPT

Oliviu Şugar Gabor, Andreea Koreanschi and Ruxandra Mihaela Botez
LARCASE Laboratory of Applied Reasearch in Active Controls,
Avionics and Aeroservoelasticity
École de Technologie Supérieure, 1100 rue Notre Dame Ouest,
Montréal, H3C1K3, Québec, Canada

This article was submitted to *The Aeronautical Journal*

Résumé

L'article présente les résultats de l'optimisation aérodynamique d'un système autonome de vol en utilisant une approche d'aile déformable. La déformation de la forme de l'aile est réalisée en plaçant les lignes d'actionneurs à plusieurs positions selon son envergure. Pour chaque condition de vol, les déplacements optimaux sont trouvés en utilisant une combinaison du nouvel algorithme de la Colonie des Abeilles Artificielles et une routine de recherche classique, basée sur le gradient. Les caractéristiques aérodynamiques de l'aile sont calculées par une méthode efficace de ligne portante non linéaire, couplé à un solveur d'écoulement visqueux bidimensionnel. Les optimisations sont effectuées à des angles d'attaque plus petits que l'angle de portance maximale, avec le but d'améliorer la finesse aérodynamique de l'aile du système autonome de vol UAS-S4 Éhecatl. Plusieurs configurations de l'aile déformable sont proposées, chacune avec un nombre différent de lignes d'actionnement, et les améliorations obtenues par ces configurations sont analysées et comparées.

Abstract

The paper presents the results of the aerodynamic optimization of an Unmanned Aerial System wing using a morphing approach. The shape deformation of the wing is achieved by placing actuator lines at several positions along its span. For each flight condition, the optimal displacements are found using a combination of the new Artificial Bee Colony algorithm and a classical gradient-based search routine. The wing aerodynamic characteristics are calculated with an efficient nonlinear lifting line method coupled with a two-dimensional viscous flow solver. The optimizations are performed at angles of attack below the maximum lift angle, with the aim of improving the Hydra Technologies UAS-S4 wing lift-to-drag ratio. Several configurations of the morphing wing are proposed, each with a different number of actuation lines, and the improvements obtained by these configurations are analysed and compared.

6.1 Introduction

One of the major research efforts of the present day aerospace industry is concentrated on reducing fuel consumption and making airplanes more efficient. Flight tests have demonstrated that a 20% reduction in airplane drag could lead to an 18% reduction in fuel consumption (Okamoto and Rhee, 2005). The active modification of the wing shape, for purposes such as promoting a larger laminar flow region on the wing surface, could lead to a substantial drag reduction (Zingg, 2006). The main advantage of actively modifying the wing shape using a morphing technique is that an optimal shape for the wing and/or airfoil can be provided during each distinct phase of aircraft flight, for each of the various airflow conditions. In addition to achieving important reductions in fuel consumption, adaptive, morphing wings can also be effectively used to replace conventional high-lift devices (Pecora et al., 2011), (Barbarino et al., 2011), (Diodati et al., 2013), or the conventional control surfaces (Pecora, 2012).

In recent years, the development and application of morphing solutions on Unmanned Aerial Vehicles (UAVs) has garnered considerable interest, due to the increasingly greater efficiency requirements and their much simpler certification issues, compared to manned airplanes. Various researchers have presented concepts for morphing UAVs that achieved performance improvements over the traditional, fixed geometry versions. Neal et al. (2004) and Supekar (2007) used telescopic pneumatic actuators to change the UAV wing planform and achieve an increase in the lift-to-drag ratio over the entire flight envelope. Gamboa et al. (2007) designed a UAV wing capable of independent span and chord changes that achieved drag reductions of up to 23% when compared to the non-morphing geometries.

Gano and Renaud (2002) presented a concept to increase the aerodynamic efficiency of a UAV by gradually decreasing the wing thickness as the fuel inside the wing-mounted tank was consumed, while Shyy (2010) presented research on small UAV airfoils that passively morphed in response to changes in external aerodynamic forces. Do Vale et al. (2011) developed a morphing wing capable of span changes through a telescopic system, but in addition achieved conformal changes of its airfoil camber. The two morphing mechanisms could independently change the wing shape, and were designed for a UAV application, by using a coupled aerodynamic-structural optimization process. Falcao et al. (2011) proposed a new design of a morphing winglet for a military class UAV. By changing the winglet cant and toe angles, the system could achieve important performance improvements by effectively controlling the lift distribution at the wingtip region according to different flight conditions. Previtali et al. (2014) performed numerical studies to investigate the roll control performance of a morphing wing concept that used compliant ribs and that were aimed to replace the conventional ailerons. Bartley-Cho et al. (2004) presented a variable camber wing, actuated by piezoelectric motors and integrated into a Northrop-Grumman combat UAV. Bilgen et al. (2007), (2009) designed and tested a concept of replacing the ailerons with local, continuous wing camber changes.

In addition to the academic environment, aircraft manufacturing companies have also shown interest in the development of next-generation morphing UAVs. Lockheed Martin's Agile

Hunter UAV concept (Bye and McClure, 2007), (Ivanco et al., 2007), (Love et al., 2007) was developed into a wind tunnel prototype capable of folding the inner wing sections over the fuselage to reduce the drag during transonic cruise. NextGen Aeronautic created the MFX1 UAV prototype (Andersen, 2007), (Flanagan et al., 2007), with variable wing sweep and wing area, and demonstrated its significant in-flight planform changing capabilities in several successful flight tests.

The objective of the CRIAQ 7.1 project was to improve and control the laminarity of the flow past a morphing wing wind tunnel model, in order to obtain important drag reductions (Botez, 2007). The wing was equipped with a flexible composite material upper surface whose shape could be changed using internally-placed Shape Memory Alloy (SMA) actuators (Brailovski et al., 2008). The numerical study revealed very promising results: the morphing system was able to delay the transition location downstream by up to 30% of the chord and reduce the airfoil drag by up to 22% (Pages, 2007). The actuator optimal displacements for each of the flight conditions were provided using both a direct open loop approach (Popov et al., 2010), (Grigorie, 2009) and a closed loop configuration based on real time pressure readings from the wing upper surface (Popov et al., 2010). In addition, a new controller based on an optimal combination of the bi-positional and PI laws was developed (Grigorie et al., 2012). The wind tunnel tests were performed in the 2 m by 3 m atmospheric closed circuit subsonic wind tunnel at IAR-CNRC, and validated the numerical wing optimisations (Sainmont et al., 2009) and the designed control techniques (Grigorie and Botez, 2010), (Grigorie, 2012), (Grigorie et al., 2012).

6.2 Morphing Wing Concept

The actual implementation of a wing surface morphing technique on the real UAS-S4 requires that only a limited portion of the entire wing surface would be allowed to change, and that the modifications would be small enough to be feasible from structural and control point of views. Thus, all the numerical optimizations were performed with regard to the technological possibilities and constraints required by the practical implementation of the

morphing wing concept. Only a limited part of the UAS's conventional, rigid wing skin was replaced using a flexible skin whose shape can be modified using actuators placed inside the wing structure. Figure 6.1 presents a chordwise section through the wing, identifying the morphing and the rigid parts of the wing skin (left), and shows a top view of the wing, with the spanwise limits of the morphing skin (right).

The morphing skin replaces a part of the wing's rigid upper surface. In the chordwise direction, the skin starts close to the leading edge, at $X/C = 0.01$ and extends on the upper surface up to $X/C = 0.55$, where C represents the local chord of the wing airfoil. The ending point of the flexible skin is limited by the presence of the wing control surfaces, such as the flaps and the ailerons. The attachment between the rigid and flexible portions is made in a way that ensures continuity and a smooth transition between the two regions. In the spanwise direction, the morphing skin starts close to the UAV wing/fuselage junction, at $Y/B = 0.19$ and extends to the wing tip, at $Y/B = 0.98$, where B represents the wing half-span, as measured from the fuselage centerline up to the wing tip.

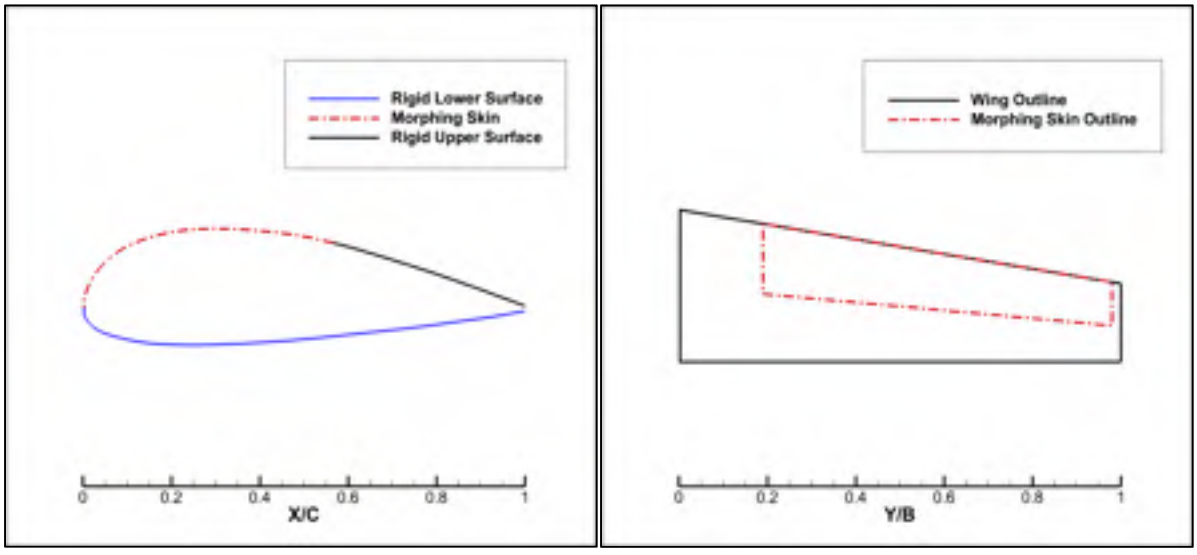

Figure 6.1 Chordwise section through the morphing wing (left) and topside view of the morphing skin (right)

In order to provide the required deformations of the morphing skin, the internal actuators are arranged into a number of chordwise actuation lines, each line consisting of several actuators placed at a desired Y/B spanwise position. For the purpose of the numerical analysis, the wing spanwise sections that correspond to the actuation lines are parameterized using Non-Uniform Rational B-Splines (NURBS) (Piegl and Tiller, 1997), (Farin, 1999). The NURBS are a generalization of B-Splines and Bézier curves, being defined by their order, a polygon of weighted control points and a knot vector, and making use of the De Boor recursive formula (De Boor, 1978) to calculate the values of the basis functions:

$$\mathbf{C}(u) = \sum_{i=1}^{k} \frac{N_{i,n} w_i}{\sum_{j=1}^{k} N_{j,n} w_j} \mathbf{P}_i$$

$$N_{i,1} = \begin{cases} 1, & if\ t_i \le u \le t_{i+1} \\ 0, & otherwise \end{cases} \tag{6.1}$$

$$N_{i,n} = \frac{u - t_i}{t_{i+n} - t_i} N_{i,n-1} + \frac{t_{i+n+1} - u}{t_{i+n+1} - t_i} N_{i+1,n-1}$$

In Equation (6.1), u is the curve parameter, ranging from 0 (the start of the curve) to 1 (the end of the curve), k is the number of control points, n is the order of the curve, w_i are the weights associated with the control points, t_i are the knots, $N_{i,n}$ are the basis functions and $\mathbf{P}_i = [x_i, y_i, z_i]$ are the control points.

In the numerical optimization, the change of the morphing skin shape is achieved by changing the coordinates of the NURBS control points, a motion that is strictly controlled. For each spanwise actuation line and for each control point of that line, a vector that passes through the control point and that is normal to the local airfoil curve is calculated. The motion of the control points is then restricted to the direction given by this vector. In addition, the control points cannot move for more than a given length along this direction, in order to maintain the deformations of the flexible skin within acceptable, predefined limits. Figure 6.2 shows the NURBS control points that correspond to one spanwise section of the

wing (left), and also presents the direction of motion and the limits imposed on one of the control points (right).

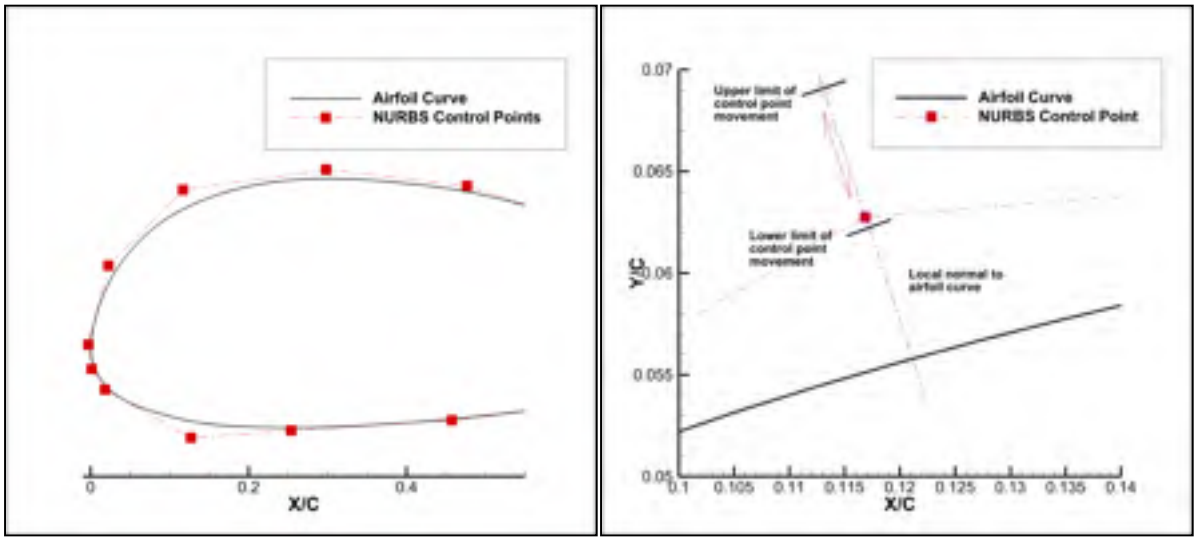

Figure 6.2 Control points for one spanwise section (left) and the movement constraints for one selected point (right)

6.3 Wing performance Calculation Methodology

The aerodynamic performance of the wing is calculated using a three-dimensional numerical extension of the classical lifting-line method, in which two-dimensional aerodynamic data from several spanwise wing sections is integrated into the three-dimensional global mathematical model, in order to determine the wing aerodynamic characteristics (Sugar Gabor, 2013). The method follows the methodology proposed by Phillips and Snyder (2000).

6.3.1 Nonlinear lifting line method

The continuous distributions of bound vorticity over the wing surface and of trailing vorticity in the wing wake are approximated using a finite number of horseshoe vortices. The bound segment of the vortices is aligned with the wing quarter chord line, while the trailing segments are aligned with the direction of the freestream, as presented in Figure 6.3.

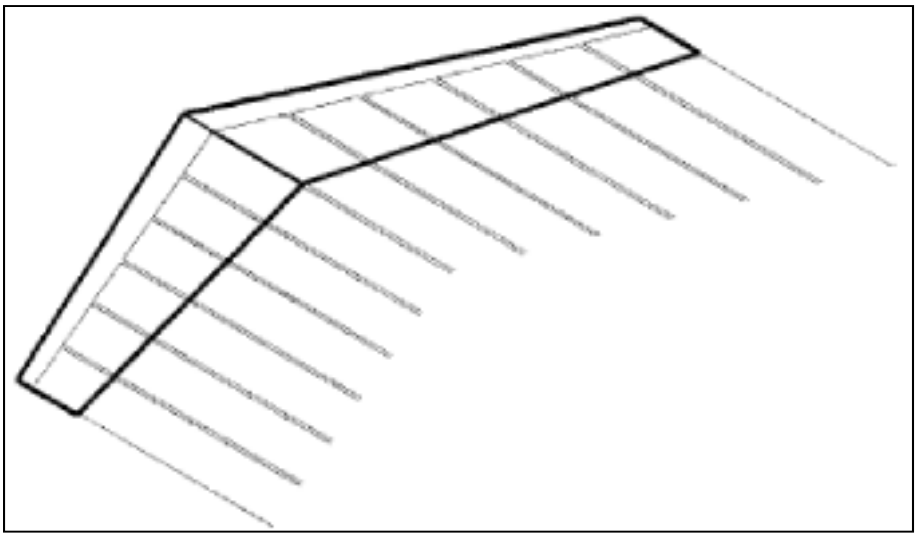

Figure 6.3 Horseshoe vortices distribution over the wing surface
Taken from Phillips and Snyder (2000)

The velocity induced by a straight vortex segment at an arbitrary point in space, such as any of the three segments making a horseshoe vortex, is given by the Biot-Savart formula (Katz and Plotkin, 1991), (Phillips and Snyder, 2000):

$$\mathbf{V} = \frac{\Gamma}{4\pi}\frac{\mathbf{r}_1 \times \mathbf{r}_2}{|\mathbf{r}_1 \times \mathbf{r}_2|^2}\mathbf{r}_0\left(\frac{\mathbf{r_1}}{\mathbf{r}_2} - \frac{\mathbf{r_2}}{\mathbf{r}_1}\right) = \frac{\Gamma}{4\pi}\frac{(r_1 + r_2)(\mathbf{r}_1 \times \mathbf{r}_2)}{r_1 r_2(r_1 r_2 + \mathbf{r}_1\mathbf{r}_2)} \tag{6.2}$$

In Equation (6.2) Γ is the vortex intensity, $\mathbf{r}_1$ and $\mathbf{r}_2$ are the spatial vectors from the starting and ending points of the vortex segment to the arbitrary point in space, r_1 and r_2 are the moduli of the spatial vectors and $\mathbf{r}_0$ is the spatial vector along the length of the vortex segment.

Each horseshoe vortex is made up of three straight vortex lines, one of them is bound to the wing quarter chord line and the other two are aligned with the freestream velocity. The typical geometry of a horseshoe vortex is presented in Figure 6.4.

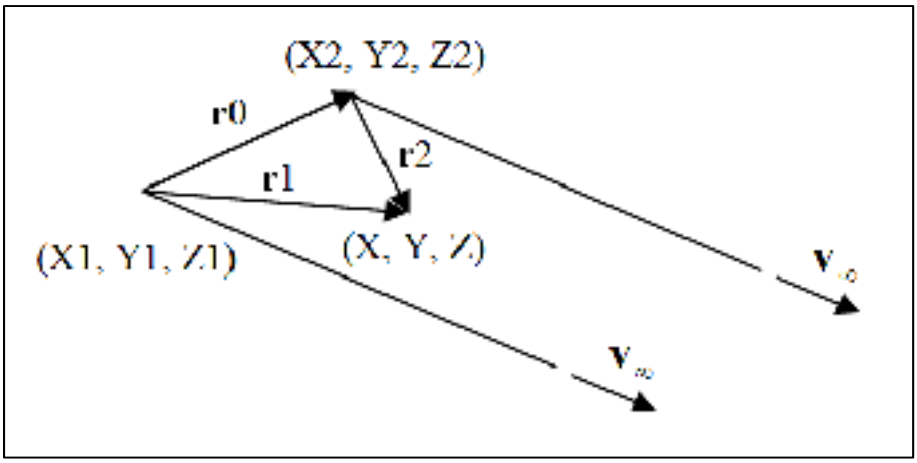

Figure 6.4 Geometry details for a typical horseshoe vector

By applying Equation (6.2) on all of the segments of the horseshoe vortex, and summing the obtained velocities, the velocity induced at an arbitrary point in space can be determined:

$$\mathbf{V} = \frac{\Gamma}{4\pi}\frac{\mathbf{v}_\infty \times \mathbf{r}_2}{r_2(r_2 - \mathbf{v}_\infty \mathbf{r}_2)} + \frac{\Gamma}{4\pi}\frac{(r_1 + r_2)(\mathbf{r}_1 \times \mathbf{r}_2)}{r_1 r_2(r_1 r_2 + \mathbf{r}_1 \mathbf{r}_2)} - \frac{\Gamma}{4\pi}\frac{\mathbf{v}_\infty \times \mathbf{r}_1}{r_1(r_1 - \mathbf{v}_\infty \mathbf{r}_1)} \tag{6.3}$$

The continuous distribution of vorticity over the wing surface and in the wing wake is approximated with N horseshoe vortices, each vortex having its own intensity Γ_i. To determine the unknown values of the vortex intensities, the three-dimensional vortex lifting law (Saffman, 1992), (Phillips and Snyder, 2000) is applied to express the inviscid force $\mathbf{dF}_i$ acting on the bound segment of each horseshoe vortex:

$$\mathbf{dF}_i = \rho \Gamma_i \mathbf{V}_i \times \mathbf{dl}_i \tag{6.4}$$

In Equation (6.4), $\mathbf{dF}_i$ is the local force acting on a differential segment of the lifting line, a segment that is identical to the bound segment of the horseshoe vortex with an intensity of Γ_i, ρ is the fluid density, $\mathbf{V}_i$ is the local airspeed vector and $\mathbf{dl}_i$ is the spatial vector along the lifting line differential segment, aligned according to the local vorticity. The local airspeed vector over one bound vortex segment is equal to the sum of the freestream velocity $\mathbf{V}_\infty$ and

the velocities induced by all the other horseshoe vortices distributed over the wing surface and wake:

$$\mathbf{V}_i = \mathbf{V}_\infty + \sum_{j=1}^{N} \Gamma_j \mathbf{v}_{ij} \tag{6.5}$$

In the above Equation (6.5), $\mathbf{v}_{ij}$ is the velocity induced at the bound segment of horseshoe vortex i by the unit strength horseshoe vortex j and is given by Equation (6.3), in which the vortex intensity is considered to be $\Gamma = 1$.

From classical wing theory, the magnitude of the inviscid force acting on a wing strip of area A_i and having a local airfoil lift coefficient C_{l_i} is given by Equation (6.6):

$$\|\mathbf{F}_i\| = \frac{1}{2}\rho V_\infty^2 A_i C_{l_i} \tag{6.6}$$

The local airfoil lift coefficient can be determined using other means, such as experimentally determined lift curves or 2D simulations using fast, coupled panel methods/boundary layer codes, provided that the local strip angle of attack is known. This local angle of attack α_i can be calculated using the local strip velocity $\mathbf{V}_i$, the local airfoil chordwise unit vector $\mathbf{c}_i$ and the unit vector normal to the local airfoil chord $\mathbf{n}_i$, and is given by Equation (6.7):

$$\propto_i = \tan^{-1}\left(\frac{\mathbf{V}_i \mathbf{n}_i}{\mathbf{V}_i \mathbf{c}_i}\right) \tag{6.7}$$

If the wing strips are taken such that each horseshoe vortex-bound segment corresponds to one strip, then the modulus of the force given by Equation (6.4) can be set equal to the one given by Equation (6.6), since the bound segment is the only segment upon which the surrounding fluid exerts a force, the trailing segments being aligned with the freestream. Thus, for each vortex over the wing surface, the following equation can be written:

$$\left\| \rho \Gamma_i \left(\mathbf{V}_\infty + \sum_{j=1}^{N} \Gamma_j \mathbf{v}_{ij} \right) \times \mathbf{dl}_i \right\| - \frac{1}{2} \rho V_\infty^2 A_i C_{l_i} = 0, \;\; i = 1,2,\dots,N \tag{6.8}$$

The nonlinear system of equations obtained by combining the N equations written for each horseshoe vortex can be solved using Newton's classical method for nonlinear systems to provide the unknown vortex intensities. Once all of the horseshoe vortices' intensities have been calculated, the aerodynamic force and moment about the root chord quarter chord point can be determined, using Equations (6.9) and (6.10):

$$\mathbf{F} = \rho \sum_{i=1}^{N} \left[\left(\mathbf{V}_\infty + \sum_{j=1}^{N} \Gamma_j \mathbf{v}_{ij} \right) \Gamma_i \times \mathbf{dl}_i \right] \tag{6.9}$$

$$\mathbf{M} = \rho \sum_{i=1}^{N} \mathbf{r}_i \times \left[\left(\mathbf{V}_\infty + \sum_{j=1}^{N} \Gamma_j \mathbf{v}_{ij} \right) \Gamma_i \times \mathbf{dl}_i \right] + \mathbf{dM}_i \tag{6.10}$$

The great advantage of this method is that it can provide the wing viscous drag in addition to the inviscid wing characteristics, since the calculated spanwise vorticity distribution has been constrained not only by the lifting line hypothesis, but also by the local airfoil characteristics, which have been determined taking into consideration the fluid viscosity effects. In addition, if the strip airfoil shapes are changed by the morphing technique, then the effects of this deformation on the wing performance are automatically determined. The wing viscous drag coefficient is given by Equation (6.11):

$$C_{D_0} = \frac{1}{S} \int_{-b/2}^{b/2} C_d(y) c(y) dy \cong \frac{1}{S} \sum_{i=1}^{N} C_{d_i} c_i \Delta y_i \tag{6.11}$$

Here, S represents the wing area, b is the wingspan, C_{d_i} is the local airfoil drag coefficient, calculated together with the local lift coefficient C_{l_i}, c_i represents the local wing chord and Δy_i is the span of the local wing strip.

6.3.2 Calculation of the strip airfoil aerodynamic properties

The 2D airfoil calculations are performed using the XFOIL code (Drela and Youngren, 2001). The inviscid estimation of the velocity field over the airfoil surface is done using a linear vorticity stream function panel method (Drela, 1989). The boundary layer properties are determined with a two-equation, lagged dissipation integral boundary layer formulation (Drela, 1989), incorporating a modified, implicit version of the e^N laminar-to-turbulent transition criterion (Drela, 2003). The boundary layer and the wake flow interact with the inviscid potential flow by means of the surface transpiration model, and the two sets of equations are solved simultaneously, using Newton's method for nonlinear systems.

6.4 The Optimization Approach

For each different flight condition, the optimal displacements of the morphing wing internal actuators are determined using an original, in-house developed optimization code (Sugar Gabor, 2014), based on a coupling of the Artificial Bee Colony (ABC) algorithm with the Broyden-Fletcher-Goldfarb-Shano (BFGS) algorithm, and using the numerical lifting line methodology for estimating the morphed wing aerodynamic performance.

The ABC algorithm is an optimization algorithm based on the intelligent behaviour of a honeybee swarm. Karaboga and Basturk (2007) conceived the original algorithm in 2007, and it was applicable only to the unconstrained optimization of linear and nonlinear problems. Other authors have proposed methods for enhancing the algorithm's capabilities, such as the handling of constrained optimization problems (Karaboga and Basturk, 2007) or the significant improvement of its convergence properties (Zhu and Kwong, 2010). Because the ABC algorithm simultaneously performs a global search throughout the entire definition

domain of the objective function and a local search around the more promising solutions already found, it can efficiently avoid converging towards a local minimum point of the objective function, and thus is able to approximate the global optimum point.

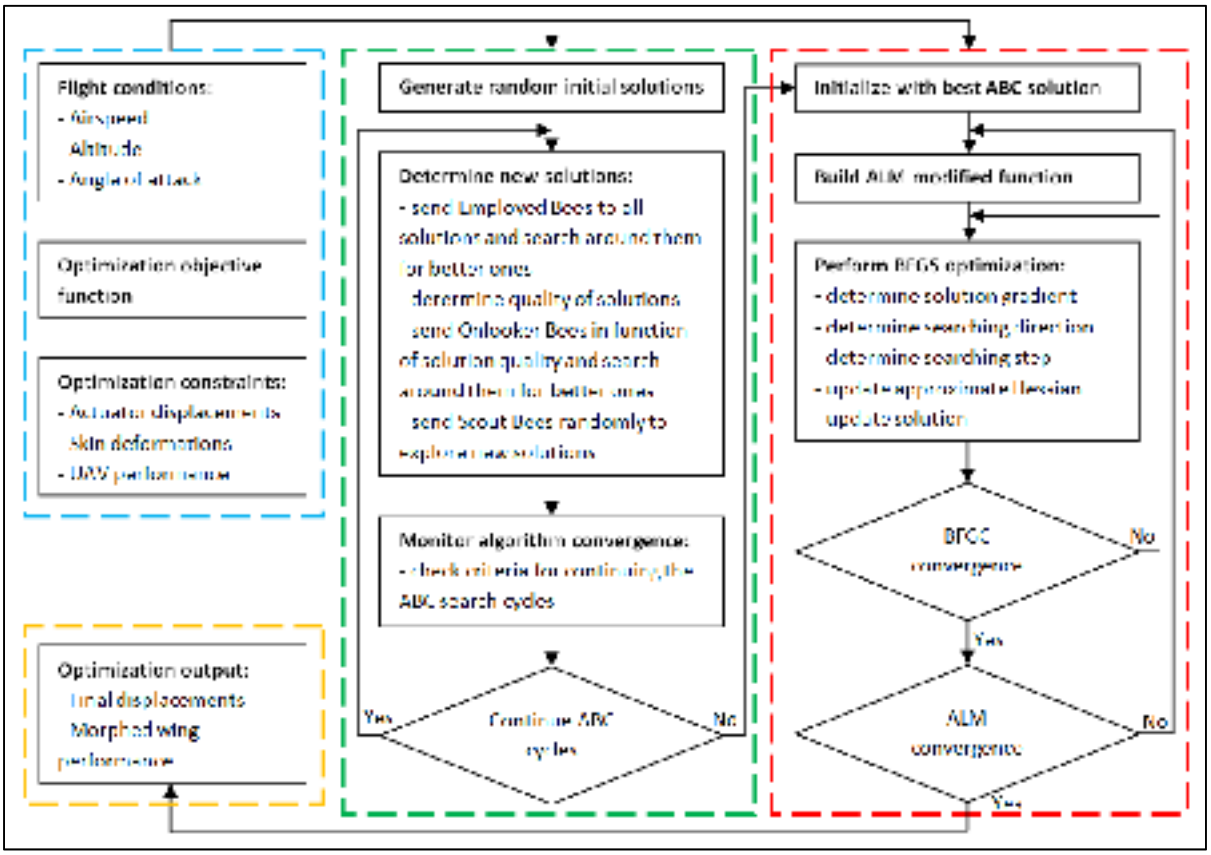

Figure 6.5 Details of the morphing wing optimization procedure

Once the region of the global optimum has been found, the algorithm's rate of convergence decreases, the local search routine of the ABC method is substituted by the Broyden-Fletcher-Goldfarb-Shanno (BFGS) algorithm (Bonnans et al., 2006), a type of quasi-Newton iterative method for nonlinear optimization problems. Since the BFGS method can only be applied to unconstrained optimization, it was coupled with the Augmented Lagrangian Method (ALM) (Powell, 1969) in order to introduce the desired optimization constraints. Using the ALM-BFGS approach allows for a significantly faster determination of the global optimum position, thus accelerating the convergence rate of the final steps of the

optimization procedure. The details of the ABC and BFGS algorithms are presented in Figure 6.5, as well as the general configuration of the morphing wing optimization procedure.

6.5 Validation of Results with High-Fidelity Data

In order to validate the morphing wing results obtained with the numerical lifting line model, the calculations were also performed using the state-of-the-art ANSYS FLUENT (ANSYS, 2015) flow solver, with advanced turbulent flow modelling and incorporating a laminar-to-turbulent transition criterion to provide accurate drag force estimations. The external flow around the wing is governed by the classical fluid dynamics equations for the conservation of mass and of momentum:

$$\frac{\partial \rho}{\partial t} + \nabla \cdot (\rho \mathbf{V}) = 0 \tag{6.12}$$

$$\frac{\partial}{\partial t}(\rho \mathbf{V}) + \nabla \cdot (\rho \mathbf{V}\mathbf{V}) = -\nabla p + \nabla \cdot \overline{\tau} \tag{6.13}$$

In Equations (6.12) and (6.13), ρ is the fluid density, $\mathbf{V}$ is the velocity vector, p is the static pressure and $\overline{\tau}$ is the stress tensor, given by the following expression:

$$\overline{\tau} = \mu \left[(\nabla \mathbf{V} + \nabla \mathbf{V}^T) - \frac{2}{3} \nabla \cdot \mathbf{V} \overline{I} \right] \tag{6.14}$$

Here, μ is the fluid dynamic viscosity and $\overline{I}$ is the unit tensor. The turbulent nature of the flow is modeled using the Reynolds-Averaged Navier-Stokes (RANS) approach and the Boussinesq hypothesis for modeling the Reynolds stresses.

The mathematical model closure and the calculation of the turbulent viscosity μ_t are done with the $k - \omega$ Shear-Stress Transport (SST) turbulence model (Menter, 2009). The $k - \omega$

SST model consists of two equations, one for the turbulent kinetic energy k and one for the specific dissipation rate ω:

$$\frac{\partial}{\partial t}(\rho k) + \frac{\partial}{\partial x_i}(\rho k u_i) = \frac{\partial}{\partial x_j}\left(\Gamma_k \frac{\partial k}{\partial x_j}\right) + G_k - Y_k \tag{6.15}$$

$$\frac{\partial}{\partial t}(\rho \omega) + \frac{\partial}{\partial x_i}(\rho \omega u_i) = \frac{\partial}{\partial x_j}\left(\Gamma_\omega \frac{\partial \omega}{\partial x_j}\right) + G_\omega - Y_\omega + D_\omega \tag{6.16}$$

In these equations, u_i are the components of the velocity vector, G_k represents the production of turbulent kinetic energy, G_ω represents the production of ω, Γ_k and Γ_ω are the effective diffusivities of k and ω, Y_k and Y_ω represent the dissipation of k and ω due to turbulence itself, while D_ω represents the cross-diffusion term.

In order to include the effects of laminar flow over the wing surface, and thus accurately determine the laminar-to-turbulent transition region, the $k-\omega$ SST turbulence model has been coupled with the $\gamma - Re_\theta$ transition model (Menter et al., 2006), (Langtry et al., 2006). The model uses two equations, one for the intermittency γ and one for the transition onset criteria in terms of the momentum thickness transition Reynolds number $Re_{\theta t}$:

$$\frac{\partial}{\partial t}(\rho \gamma) + \frac{\partial}{\partial x_i}(\rho \gamma u_i) = \frac{\partial}{\partial x_j}\left[\left(\mu + \frac{\mu_t}{\sigma_\gamma}\right)\frac{\partial \gamma}{\partial x_j}\right] + P_{\gamma 1} - E_{\gamma 1} + P_{\gamma 2} - E_{\gamma 2} \tag{6.17}$$

$$\frac{\partial}{\partial t}(\rho Re_{\theta t}) + \frac{\partial}{\partial x_i}(\rho Re_{\theta t} u_i) = \frac{\partial}{\partial x_j}\left[\sigma_{\theta t}(\mu + \mu_t)\frac{\partial Re_{\theta t}}{\partial x_j}\right] + P_{\theta t} \tag{6.18}$$

In Equations (6.17) and (6.18), $P_{\gamma 1}$ and $E_{\gamma 1}$ are the transition source terms, $P_{\gamma 2}$ and $E_{\gamma 2}$ are the destruction/relaminarization source terms, $P_{\theta t}$ is the transition momentum thickness Reynolds number source term, and σ_γ and $\sigma_{\theta t}$ are the model constants.

In the numerical simulation, the steady-state flow equations are solved using a projection method, achieving the constraint of mass conservation by solving a pressure equation. The

cell-face values of the velocity and of the turbulence variables are calculated with the third-order MUSCL (Monotone Upstream-Centered Scheme for Conservation Laws) scheme, while the cell-face values of the pressure are estimated using a second-order central-differencing interpolation scheme. The discrete equations are solved in a fully implicit coupled manner, using an Algebraic Multigrid (AMG) approach for providing significant convergence acceleration and the block-method Incomplete Lower-Upper (ILU) decomposition algorithm as the linear system smoother.

6.6 Results and Analysis

The morphing wing concept is used to improve the aerodynamic characteristics of the Hydra Technologies UAS-S4 Éhecatl. This UAS was designed and build in Mexico, and serves as a state-of-the-art aerial surveillance system, for both military and civilian missions. The geometrical characteristics of the UAS-S4 wing are presented in Table 6.1.

Table 6.1 Geometric characteristics of the UAS-S4 wing

Span [m]	Area [m^2]	Aspect ratio	Root chord [m]	Taper ratio	Sweep [deg]	MAC [m]
4.19	2.307	7.61	0.705	0.56	8.35	0.55

In the chordwise direction, the morphing skin stretches between $X/C = 0.01$ and $X/C = 0.55$, where C represents the local chord of the wing, while in the spanwise direction, the morphing skin extends between $Y/B = 0.19$ and $Y/B = 0.98$, where B represents the wing half-span, as measured from the fuselage centerline up to the wing tip. In order to analyse the influence of modifying the upper surface shape on the wing aerodynamic characteristics, four different configurations were proposed for the number and positions of the chordwise actuation lines. Table 6.2 presents the details of these four configurations. For convenience and to make reading the results easier, the configurations are named according to the number of actuation lines.

Table 6.2 Details of the four actuation lines' configurations

Configuration	Number of half-span actuation lines	Y/B spanwise positions of the actuation lines
Case 5	5	0.21, 0.37, 0.53, 0.68, 0.83
Case 4	4	0.37, 0.53, 0.68, 0.83
Case 3	3	0.40, 0.59, 0.79
Case 2	2	0.45, 0.72

For each configuration, only the wing cross-section airfoils corresponding to the actuation lines spanwise positions are parameterized using NURBS and are directly modified in the optimization procedure. Thus, the actuator displacements for any actuation line are simulated by changing the coordinates of the NURBS control points corresponding to that wing cross-section airfoil. The shape of the morphing wing surface between two consecutive actuation lines is determined by performing cubic splines interpolations in the spanwise direction. Figure 6.6 presents the Case 3 configuration of the morphing wing, where the spanwise positions of the three actuation lines and the limits of the morphing skin in the figure were not kept exact, for the purpose of better visualization. The blue outline represents the flexible upper skin, while the three wing cross-sections (A, B and C) represent the actuation lines where the local airfoil shapes can be directly optimized. The original airfoil is the same for all three cross-sections, but the morphed airfoil of each section can vary, as function of the optimization procedure results.

The optimization is focused on improving the wing lift-to-drag ratio L/D over a rage of angle of attack values. The analyses were performed at an airspeed of 50 m/s, with a Reynolds number of $Re = 2.133 \times 10^6$, as calculated with the mean aerodynamic chord. The reference values for air density, pressure and molecular viscosity are those of standard atmosphere at sea level ($\rho = 1.225\ kg/m^3,\ p_0 = 101000\,Pa,\ \mu = 1.79 \times 10^{-5}\,Pa \cdot s$). The turbulence intensity level was set to 0.07%, corresponding to calm atmospheric conditions. Detailed results showing the influence of the morphing upper skin on the performance of the UAS wing are presented for four angle of attack values.

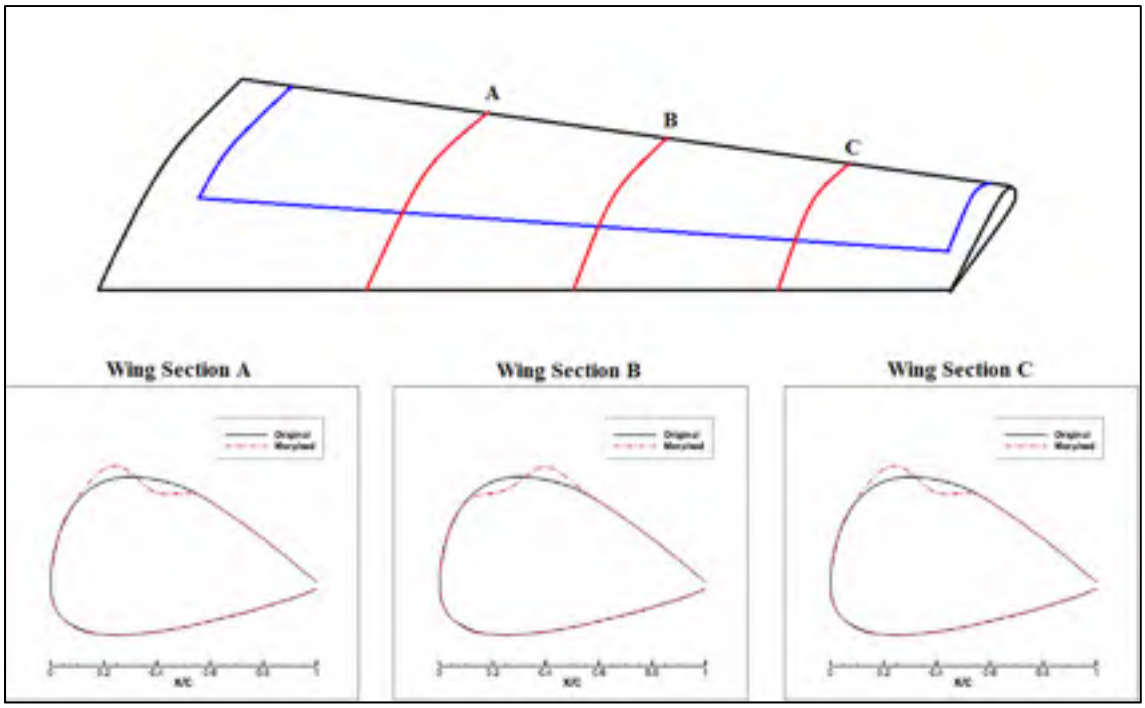

Figure 6.6 The modification of the upper surface morphing skin shape control using three spanwise actuation lines

Figure 6.7 presents a comparison of the spanwise variations of the local lift coefficient CL, the local induced drag coefficient CDI and the local profile drag coefficient $CD0$ for a wing angle of attack of -2 deg.

A comparison of the pressure coefficient distributions for two spanwise wing sections, $y = 1\,m$ (upper) and $y = 1.8\,m$ (lower), at a wing angle of attack of -2 deg, is presented in Figure 6.8.

Figure 6.9 presents a comparison of the spanwise variations of the local lift coefficient CL, the local induced drag coefficient CDI and the local profile drag coefficient $CD0$ for a wing angle of attack of 1 deg.

A comparison of the pressure coefficient distributions for two spanwise wing sections, $y = 1\,m$ (upper) and $y = 1.8\,m$ (lower), at a wing angle of attack of 1 deg, is presented in Figure 6.10.

Figure 6.11 presents a comparison of the spanwise variations of the local lift coefficient CL, the local induced drag coefficient CDI and the local profile drag coefficient $CD0$ for a wing angle of attack of 4 deg.

A comparison of the pressure coefficient distributions for two spanwise wing sections, $y = 1\,m$ (upper) and $y = 1.8\,m$ (lower), at a wing angle of attack of 4 deg, is presented in Figure 6.12.

Figure 6.13 presents a comparison of the spanwise variations of the local lift coefficient CL, the local induced drag coefficient CDI and the local profile drag coefficient $CD0$ for a wing angle of attack of 8 deg.

A comparison of the pressure coefficient distributions for two spanwise wing sections, $y = 1\,m$ (upper) and $y = 1.8\,m$ (lower), at a wing angle of attack of 8 deg, is presented in Figure 6.14.

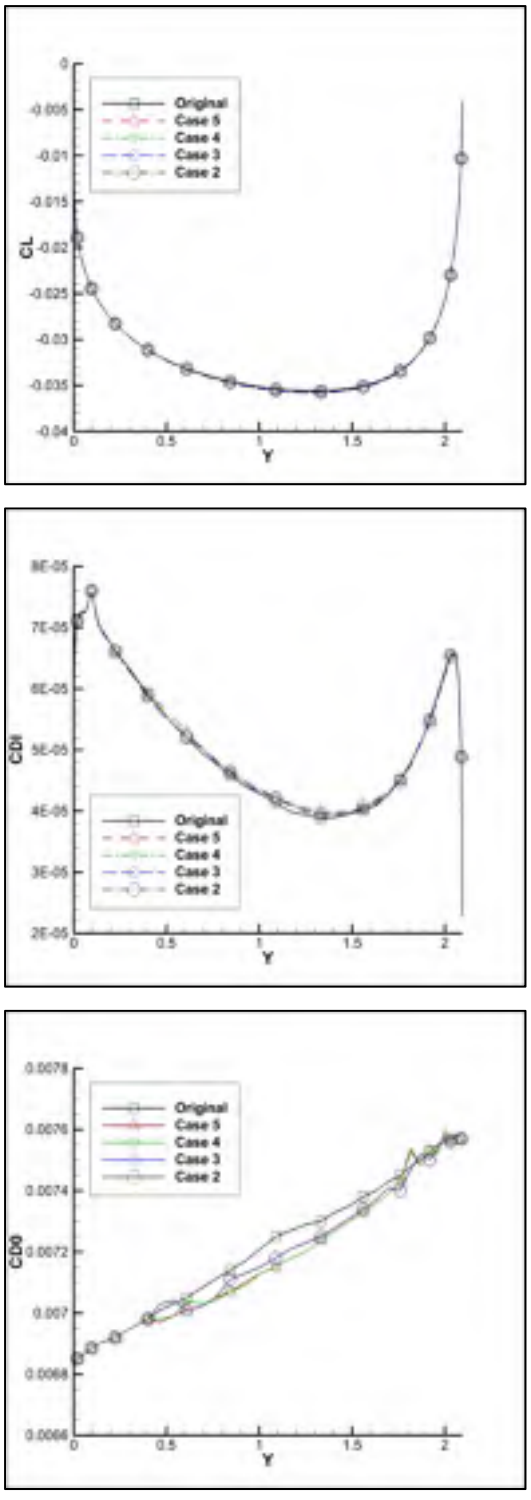

Figure 6.7 Spanwise variation of lift, induced drag and profile drag coefficients at a -2 deg angle of attack

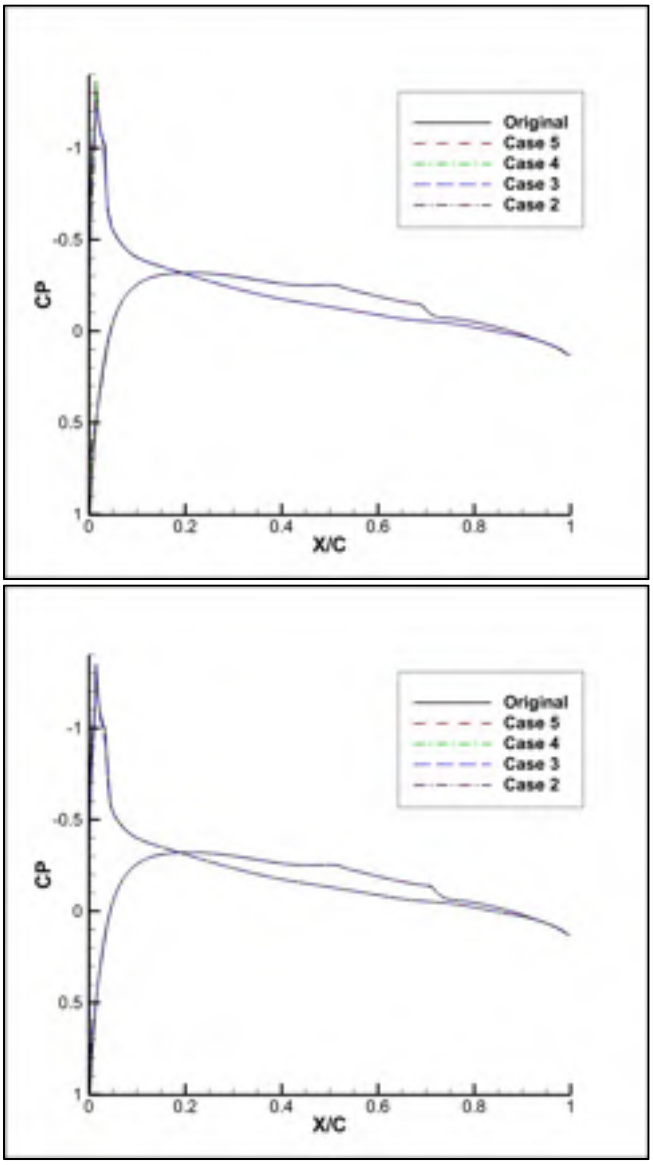

Figure 6.8 Pressure coefficient distributions for
y=1.0 (upper) and y=1.8 (lower) sections
at a -2 deg angle of attack

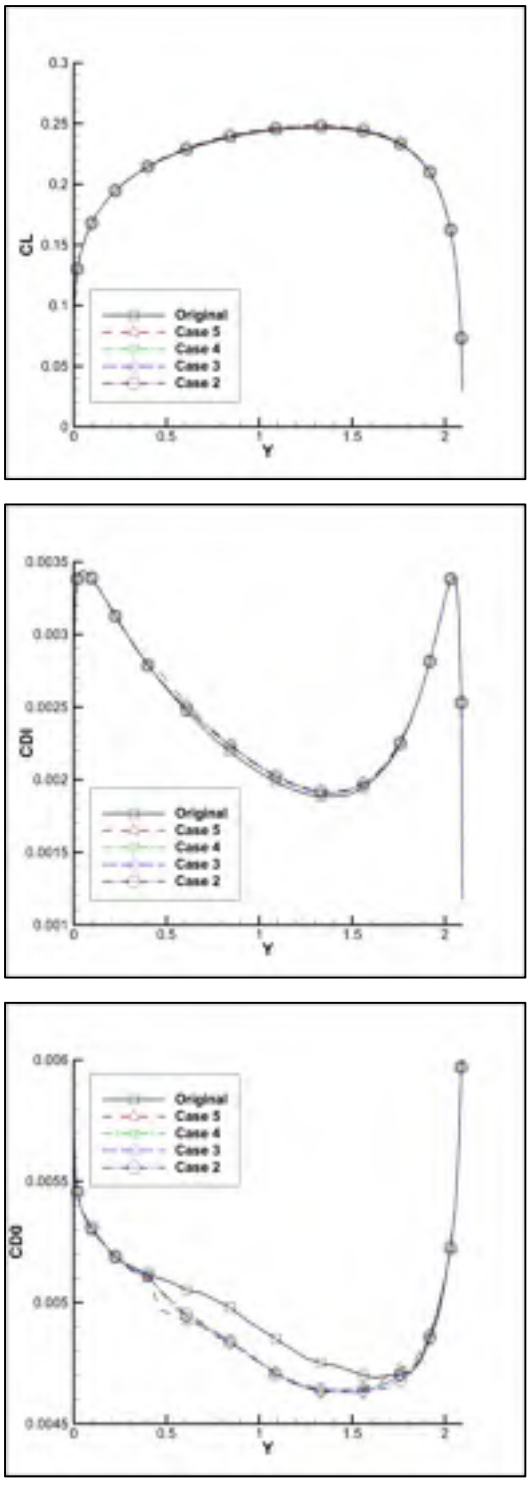

Figure 6.9 Spanwise variation of lift, induced drag and profile drag coefficients at a 1 deg angle of attack

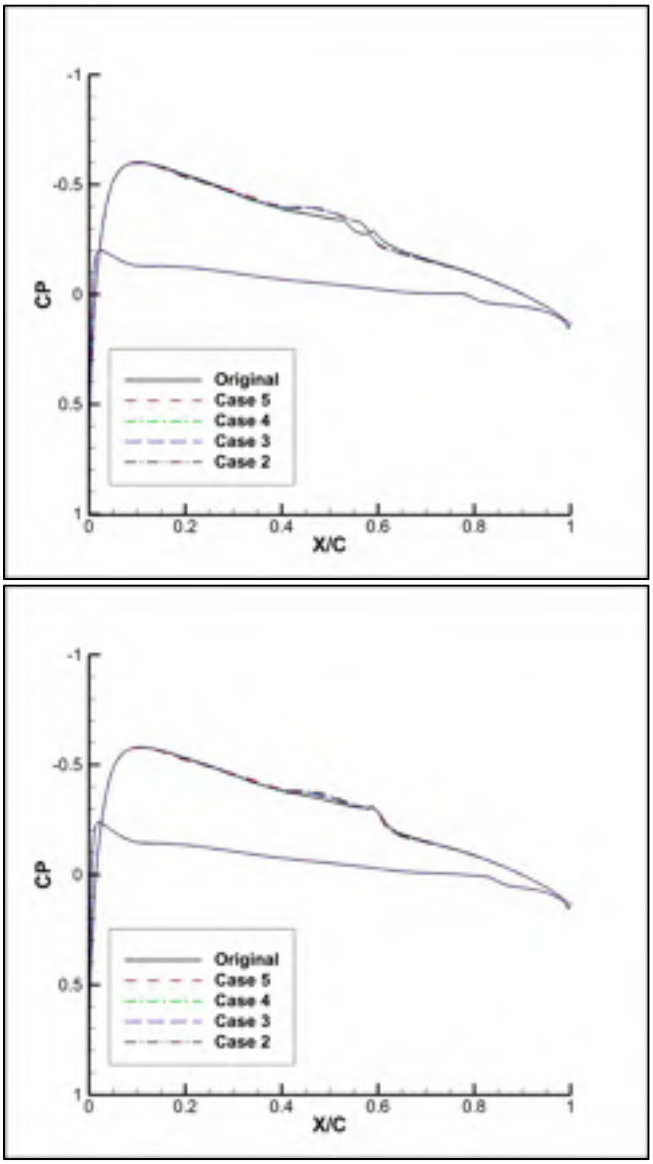

Figure 6.10 Pressure coefficient distributions for
y=1.0 (upper) and y=1.8 (lower) sections
at a 1 deg angle of attack

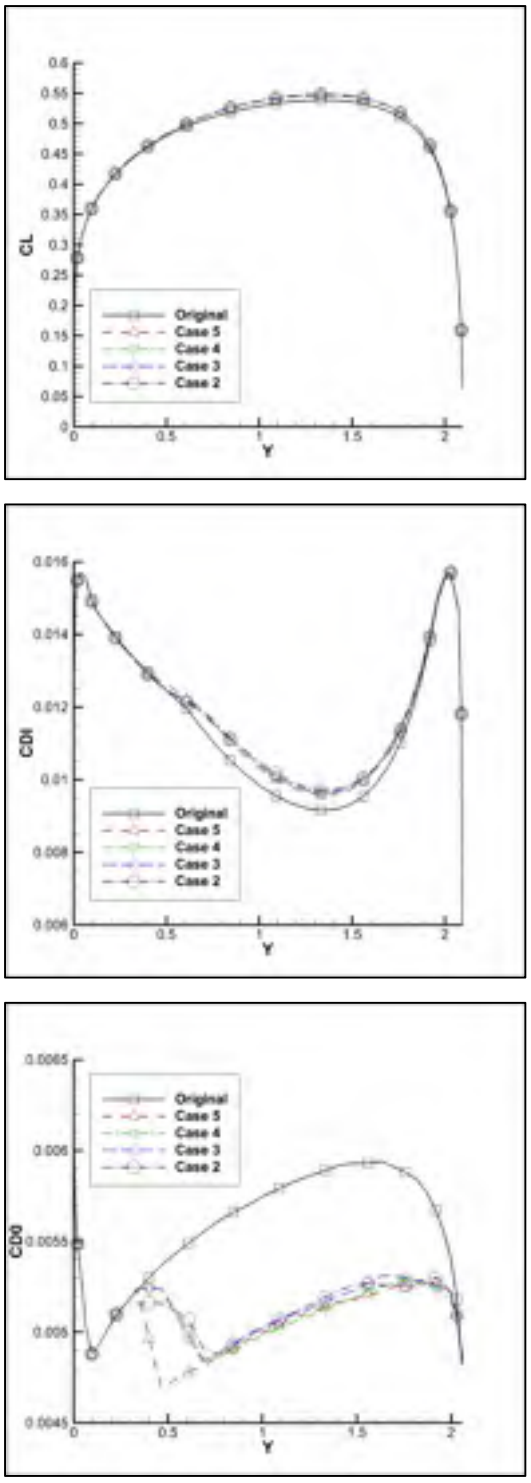

Figure 6.11 Spanwise variation of lift, induced drag and profile drag coefficients at a 4 deg angle of attack

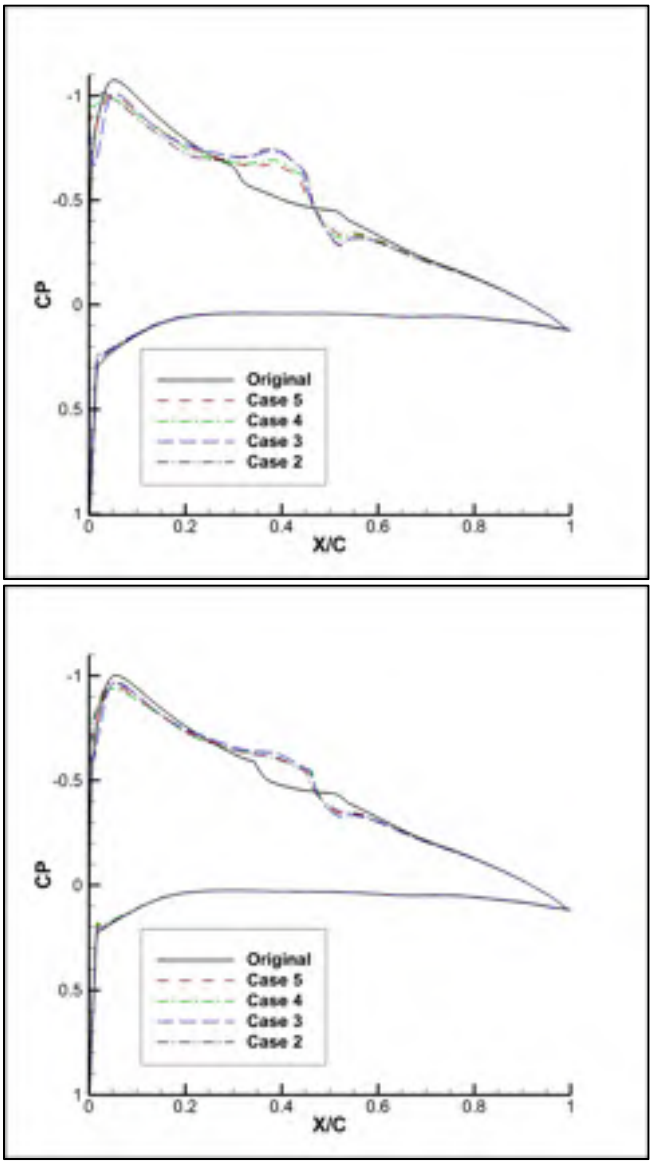

Figure 6.12 Pressure coefficient distributions for
y=1.0 (upper) and y=1.8 (lower) sections
at a 4 deg angle of attack

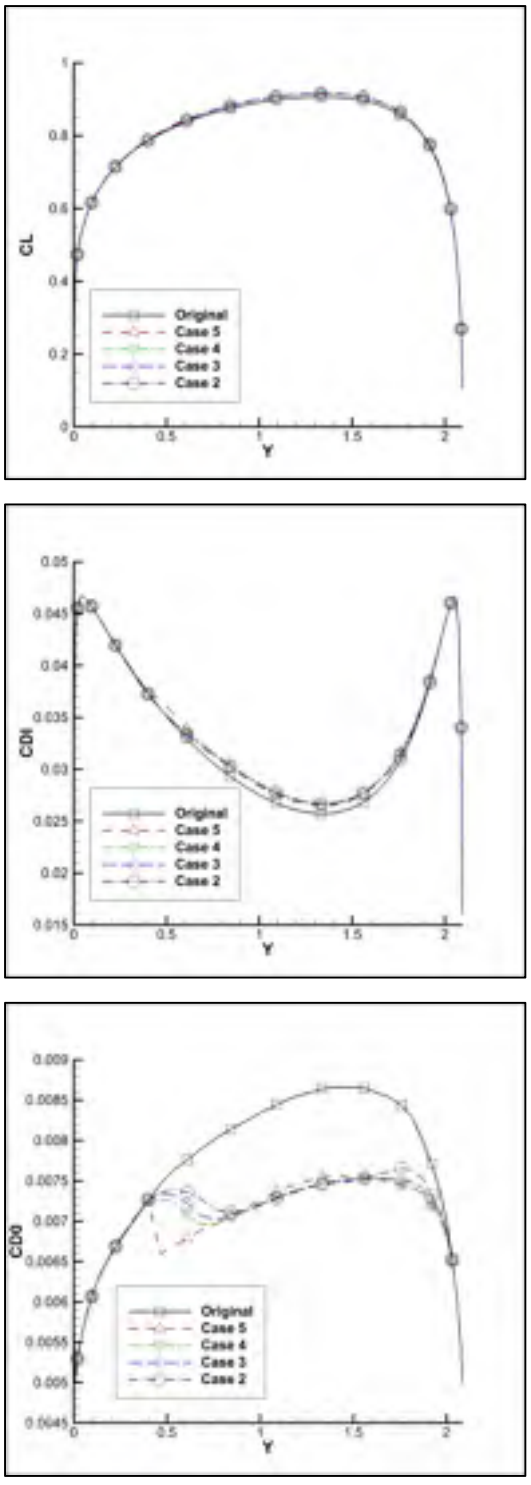

Figure 6.13 Spanwise variation of lift, induced drag and profile drag coefficients at a 8 deg angle of attack

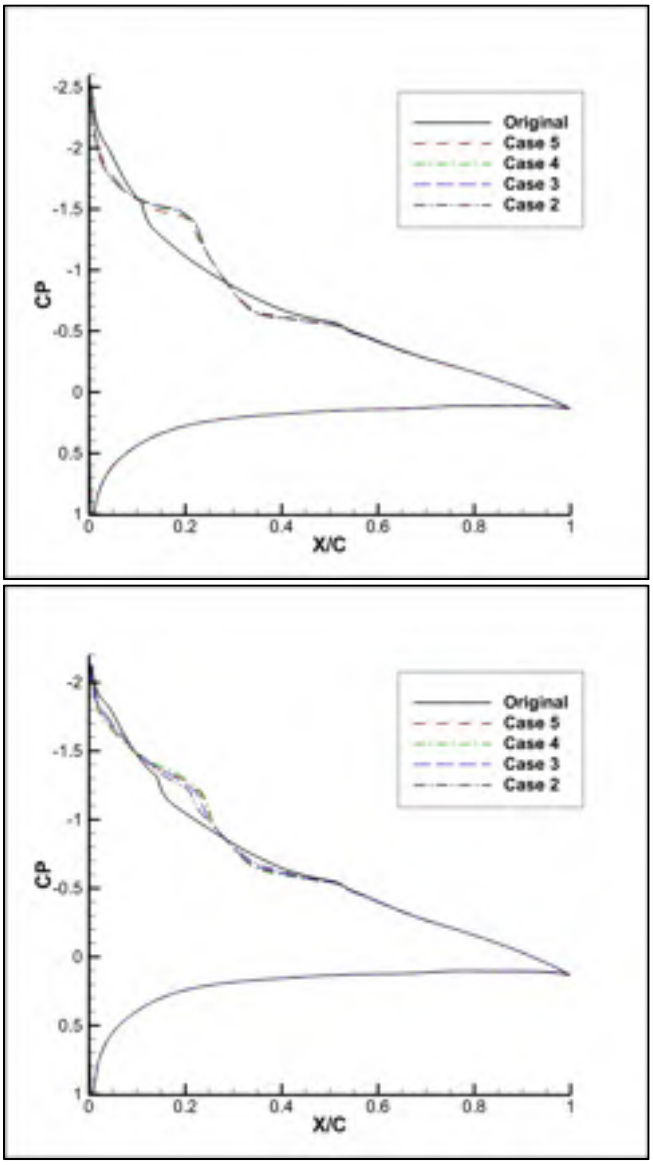

Figure 6.14 Pressure coefficient distributions for
y=1.0 (upper) and y=1.8 (lower) sections
at a 8 deg angle of attack

Concerning the impact on the spanwise distribution of lift and induced drag, it can be seen that all four proposed configurations give approximately the same results. From the angles of attack chosen for the detailed comparisons, the highest increase in spanwise lift is obtained for an angle of attack of 4 deg, as seen from Figure 6.11. The reduction of the spanwise profile drag coefficient is significant for all angles of attack, achieving increasingly higher performance as the angle of attack increases. The configuration with 5 actuator lines per wing semi-span obtains the most important reductions, but the gains over the other three configurations are not very large. The sudden drop in profile drag observed for Case 5 is attributed to the small distance between the flexible skin limit and the first actuation line. This drop cannot be observed for the other three configurations, as they present a smoother transition between the rigid and the flexible regions.

The analysis of the pressure coefficient distributions shows that the flexible skin reduced the adverse pressure gradient for the leading edge region of the wing, leading to a smoother pressure increase and thus increasing the lift. Again, the differences between the four proposed morphing wing configurations are relatively small, all of them successfully achieving the desired effects.

Table 6.3 presents a comparison between the CL/CD ratio for the original wing and for each of the four different configurations of the morphing wing. At each angle of attack value, the improvement percentage is indicated, in addition to the CL/CD numeric values.

An improvement of the lift-to-drag ratio of the morphing wing over the original wing was obtained for the entire range of angles of attack. All four configuration cases achieve the best improvements for the angle of attack interval between 2 and 4 deg, corresponding to the region of maximum lift-to-drag of the original wing. The five actuation lines per semi-span case consistently obtained the best performance increase.

Table 6.3 Results of CL/CD optimization at all considered angle of attack values

Angle of attack	Configuration								
	Original	Case 5		Case 4		Case 3		Case 2	
	CL/CD	CL/CD	[%] improve	CL/CD	[%] improve	CL/CD	[%] improve	CL/CD	[%] improve
-4	-20.4	-20.7	1.5	-20.6	1.0	-20.7	1.5	-20.6	1.0
-2	-4.4	-4.44	1.0	-4.43	0.7	-4.42	0.5	-4.44	1.0
0	18.6	18.7	0.5	18.7	0.5	18.6	0.0	18.6	0.0
1	29.4	29.8	1.4	29.7	1.2	29.7	1.2	29.7	1.2
2	30.6	31.3	2.3	31.2	2.0	31.2	2.0	31.2	2.0
3	30.0	31.2	4.0	31.0	3.3	31.0	3.3	31.0	3.3
4	27.6	28.3	2.5	28.2	2.2	28.2	2.2	28.2	2.2
6	23.2	23.6	1.8	23.6	1.8	23.5	1.4	23.5	1.4
8	19.6	19.9	1.5	19.8	1.1	19.8	1.1	19.8	1.1
10	16.8	17.0	1.2	16.9	1.1	16.9	1.1	16.9	1.1

The verification of the results obtained with the lifting-line method was performed with the ANSYS FLUENT solver. Two configurations were chosen for the comparison: the one with the highest number of spanwise actuation lines (Case 5) and the one with the lowest number of spanwise actuation lines (Case 2). The 3D single-block structured H-Type meshes around the original and morphed wing geometries were generated with the ANSYS ICEM-CFD grid generator. The normal distance for the wall cells was set to $2.0 \times 10^{-6}\ m$, while the far-field boundaries were placed 50 chords away from the wing. The calculations were performed at an airspeed of 50 m/s, with a Reynolds number of $Re = 2.133 \times 10^{6}$, as calculated with the mean aerodynamic chord, and at two angle of attack values: 1 deg and 4 deg. Figure 6.15 shows a cut out of the 3D mesh around the wing and Figure 6.16 presents an example of typical residual convergence curves. For all the calculations, the converged residuals were in the range of 10^{-5} to 10^{-10}, achieved within 500-550 AMG cycles.

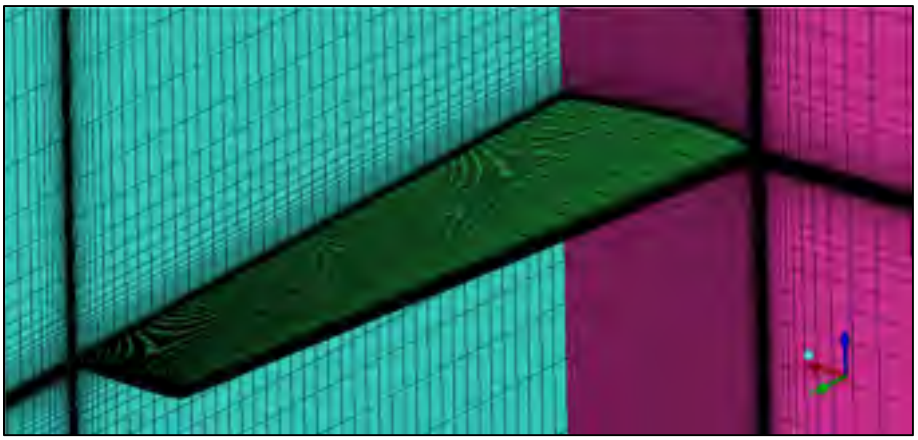

Figure 6.15 Cut of the UAS-S4 H-Type structured mesh

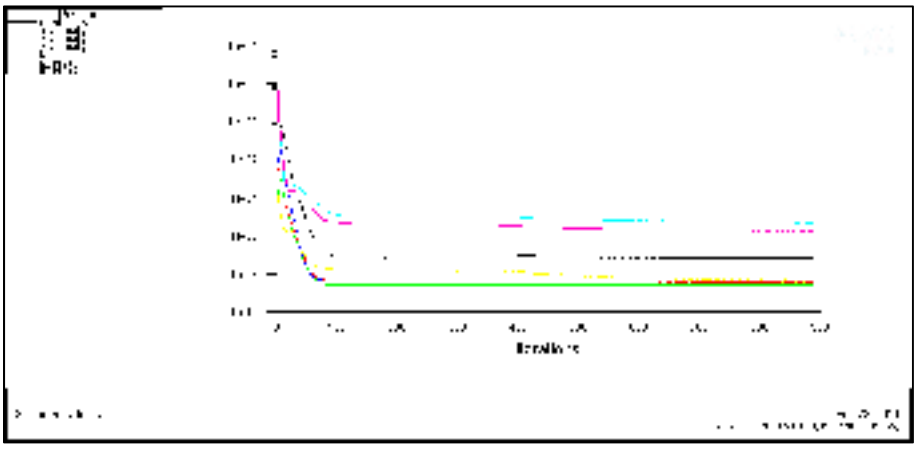

Figure 6.16 Typical residual convergence curves

A comparison between the lift coefficient, the drag coefficient, the pitching moment coefficient and the lift-to-drag ratio for the original wing and the two configurations chosen (Case 2 and Case 5) for the validation is presented in Table 6.4.

The 3D results obtained with FLUENT are compared to those obtained with the nonlinear lifting line method coupled with the 2D section viscous data. It can be observed, for the comparisons between the original and morphed wings, that the performance improvements obtained with the optimization procedure and the rapid, lifting line code are also present in the results obtained using the high-fidelity CFD solver. These results show that the lifting

line code can be used for wing optimization procedures, as it provides sufficiently accurate wing performance information, and it can predict whether the modified geometry outperforms the original geometry with respect to the desired optimization goal.

Table 6.4 Comparison of aerodynamic coefficients obtained with the in-house code and FLUENT

Angle of Attack	**5 actuator lines per semi-span – Case 5**							
	FLUENT results				**Nonlinear Lifting Line results**			
	Original		**Morphed**		**Original**		**Morphed**	
1 deg	CL	2.10e-1	CL	2.11e-1	CL	2.19e-1	CL	2.21e-1
	CD	7.85e-3	CD	7.73e-3	CD	7.45e-3	CD	7.40e-3
	Cm	-1.18e-1	Cm	-1.18e-1	Cm	-1.24e-1	Cm	-1.25e-1
	CL/CD	26.8	CL/CD	27.3	CL/CD	29.4	CL/CD	29.8
4 deg	CL	4.69e-1	CL	4.79e-1	CL	4.76e-1	CL	4.84e-1
	CD	1.77e-2	CD	1.63e-2	CD	1.72e-2	CD	1.70e-2
	Cm	-2.31e-1	Cm	-2.40e-1	Cm	-2.40e-1	Cm	-2.44e-1
	CL/CD	26.5	CL/CD	29.3	CL/CD	27.6	CL/CD	28.3
Angle of Attack	**2 actuator lines per semi-span – Case 2**							
	FLUENT results				**Nonlinear Lifting Line results**			
	Original		**Morphed**		**Original**		**Morphed**	
1 deg	CL	2.10e-1	CL	2.15e-1	CL	2.19e-1	CL	2.21e-1
	CD	7.85e-3	CD	7.63e-3	CD	7.45e-3	CD	7.38e-3
	Cm	-1.18e-1	Cm	-1.20e-1	Cm	-1.24e-1	Cm	-1.25e-1
	CL/CD	26.8	CL/CD	28.2	CL/CD	29.4	CL/CD	29.7
4 deg	CL	4.69e-1	CL	4.79e-1	CL	4.76e-1	CL	4.83e-1
	CD	1.77e-2	CD	1.65e-2	CD	1.72e-2	CD	1.70e-2
	Cm	-2.31e-1	Cm	-2.40e-1	Cm	-2.40e-1	Cm	-2.44e-1
	CL/CD	26.5	CL/CD	29.0	CL/CD	27.6	CL/CD	28.2

The detailed RANS results show that the drag reductions observed in Table 6.4 can be attributed to the larger extent of laminar flow on the upper surface of the morphed geometries. Figures 6.17 and 6.18 present the surface plot of the turbulent kinetic energy, for the original wing and the Case 5 morphed wing. It can be seen that for the morphed geometries, the onset of turbulent flow is significantly delayed towards the trailing edge.

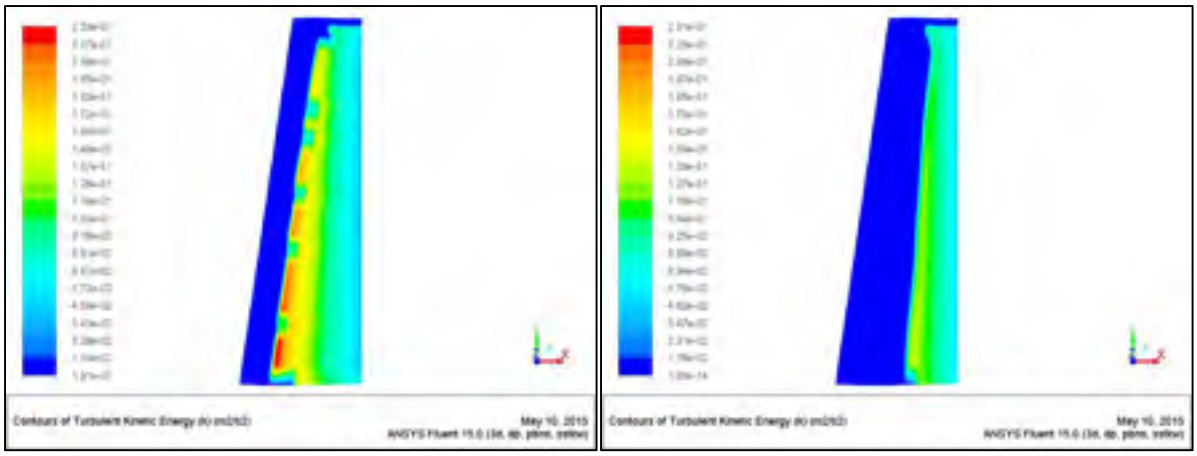

Figure 6.17 Plot of turbulent kinetic energy on the upper surface on the original wing (left) and the Case 5 morphed wing (right) at a 1 deg angle of attack

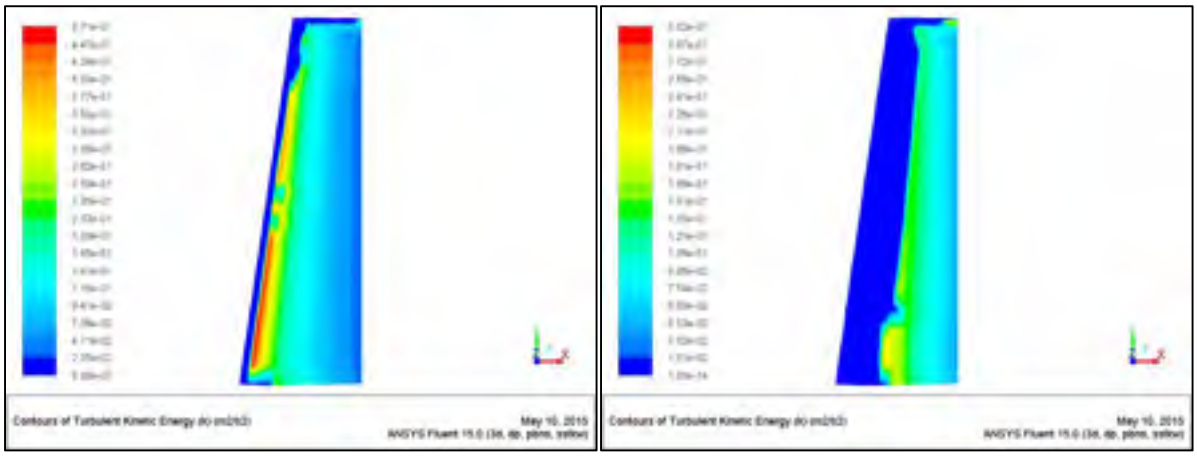

Figure 6.18 Plot of turbulent kinetic energy on the upper surface on the original wing (left) and the Case 5 morphed wing (right) at a 4 deg angle of attack

A comparison between the pressure coefficient distributions obtained with the in-house nonlinear lifting line code (NLL) and those obtained with FLUENT is presented next. Figure 6.19 shows the comparison at 1 deg angle of attack for the $y = 1\,m$ section, while Figure 6.20 presents the comparison, at the same angle of attack, for the $y = 1.8\,m$ section. In Figure 6.21 and Figure 6.22, the pressure coefficient comparisons are made for the same spanwise stations, but for an angle of attack of 4 deg.

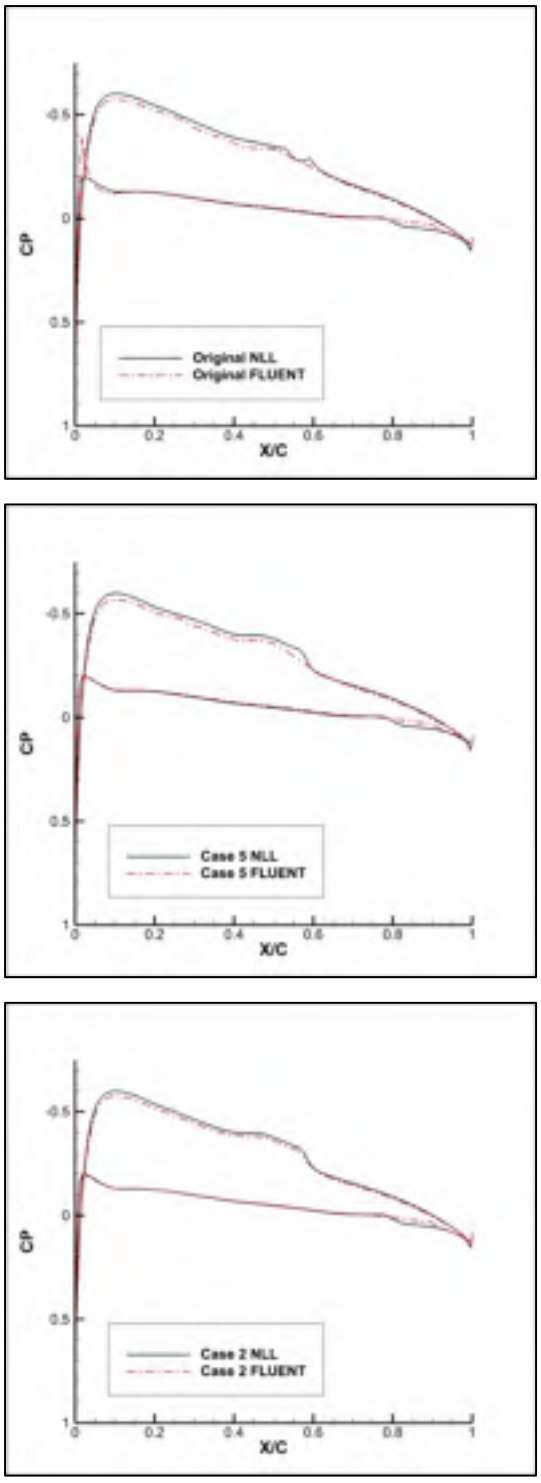

Figure 6.19 Pressure coefficient distributions
for y=1.0 sections at a 1 deg angle of attack

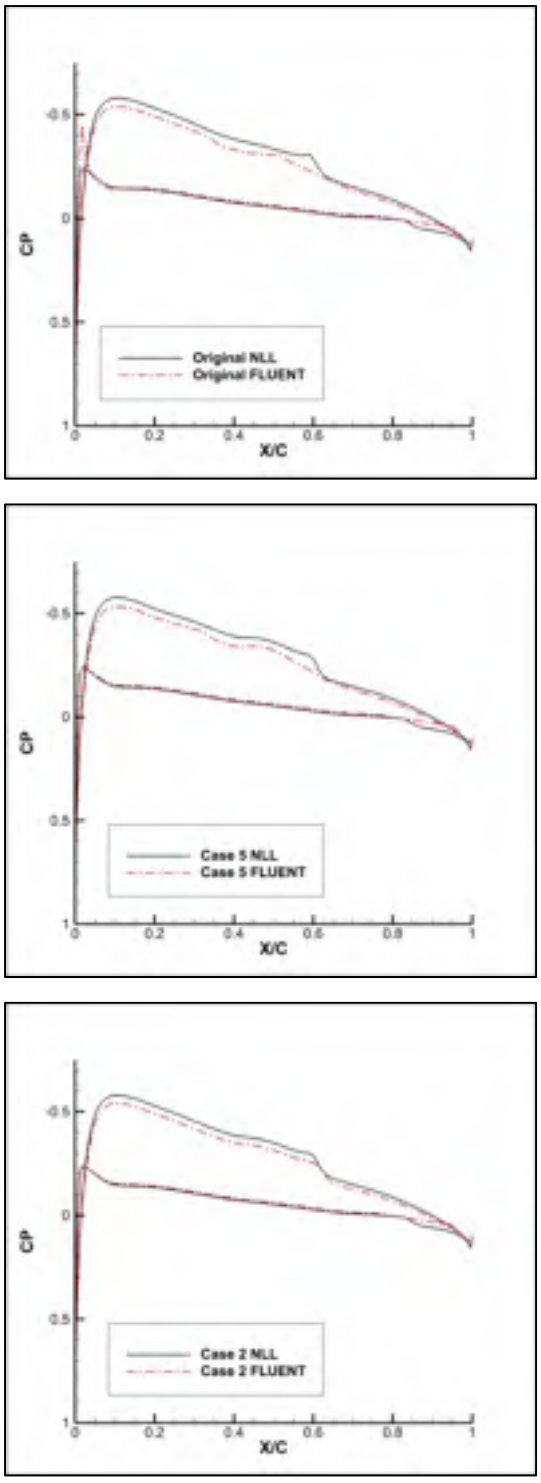

Figure 6.20 Pressure coefficient distributions
for y=1.8 sections at a 1 deg angle of attack

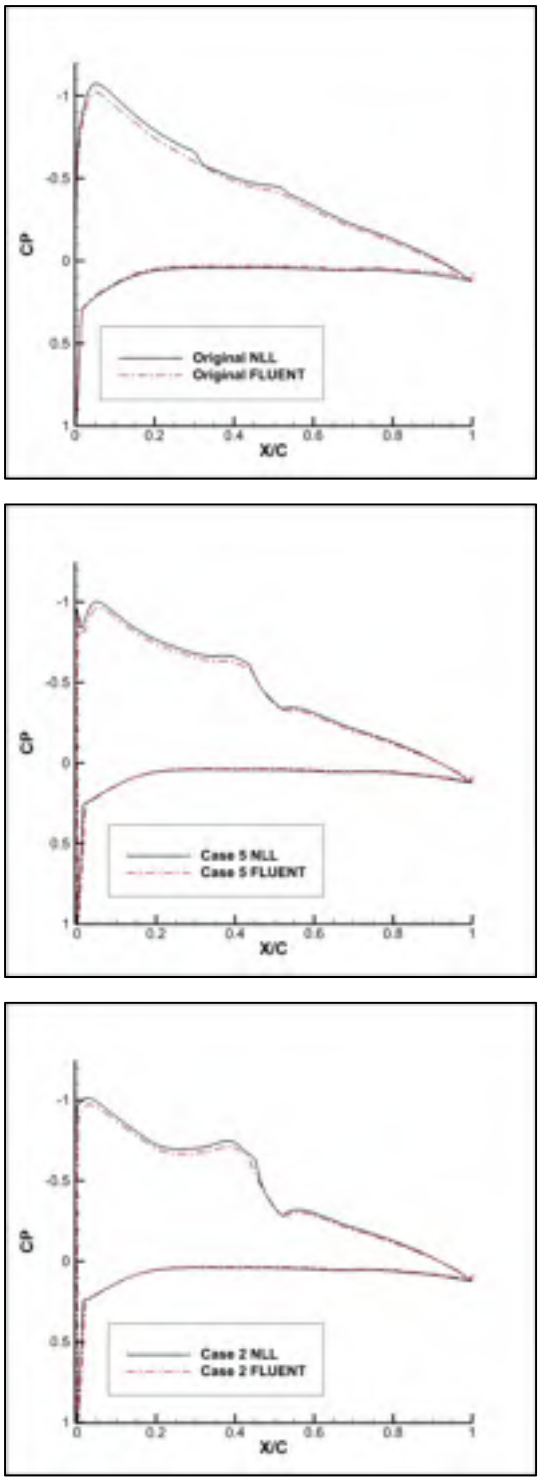

Figure 6.21 Pressure coefficient distributions
for y=1.0 sections at a 4 deg angle of attack

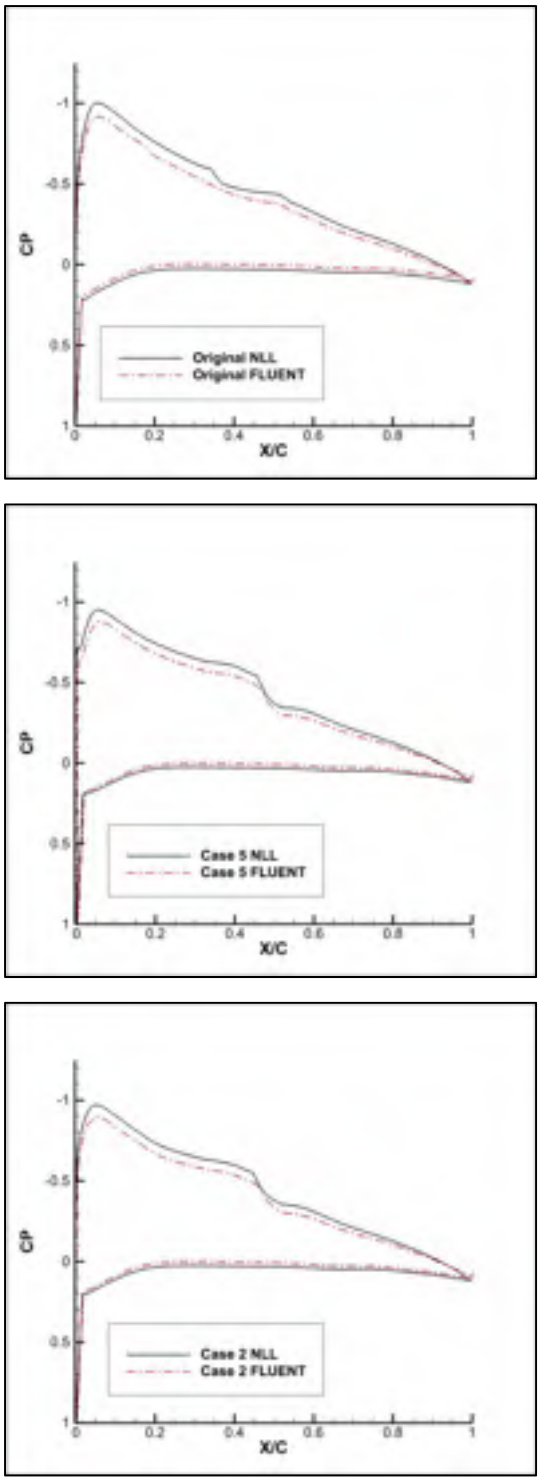

Figure 6.22 Pressure coefficient distributions
for y=1.8 sections at a 4 deg angle of attack

6.7 Conclusions

The aerodynamic performance of the Hydra Technologies UAS-S4 wing was improved using a numerical morphing wing optimization approach. The shape of the wing upper surface was modified as function of the flight condition with the goal of increasing the lift-to-drag ratio compared to the baseline design. In the numerical optimizations, the wing cross-sections were parameterized using Non-Uniform Rational B-Splines, and the upper surface displacements were achieved by moving the spline curves control points along predetermined directions. Four possible configurations were proposed, as function of different number of actuation lines placed on each half-span of the wing.

For each different flight condition, defined by a given Reynolds number, airspeed and angle of attack, the optimal displacements were determined with an optimization code based on a coupling of the Artificial Bee Colony and the Broyden-Fletcher-Goldfarb-Shanno algorithms. The aerodynamic qualities of each morphed wing geometry were calculated using a rapid, nonlinear lifting line method, coupled with a two-dimensional viscous flow solver. For validation purposes, several selected wing geometries were also calculated using a high fidelity Navier-Stokes solver. The results proved that the lifting line code could successfully be used for the optimization routine, as this code provides accurate wing performance information.

The wing optimizations were performed at a fixed airspeed within the UAS-S4 flight envelope, for an angle of attack range between -4 and 8 deg, with the objective function of increasing the lift-to-drag ratio. All four proposed actuator configurations significantly reduced the profile drag over the entire span of the flexible skin, for the complete range of angles of attack. The configuration using the highest number of spanwise actuator lines achieved the best results, allowing morphing wing lift-to-drag ratio to increase up to 4% compared to the original geometry.

6.8 Future work

In order to reproduce the numerically calculated optimized shapes, a part of the UAS-S4 upper surface will be replaced by a flexible, composite material skin whose shape can be modified using internally placed actuators. A material suitable for achieving the desired skin displacements must be chosen. Based on the errors between the aerodynamic target shapes and the finite element model calculated shapes, several configurations will be analysed: keeping the morphing skin an active structural component of the UAS wing or redesigning the spars and ribs so that the skin can be freed from the loads induced by wing bending and torsion. An internal actuation system must be designed, capable of providing the desired displacements while constrained by the available internal space and position of spars and ribs. Once the skin material and the final wing structure are established, an energy consumption analysis of the morphing system under combined aerodynamic and structural forces will be performed, thus quantifying the overall power consumption gains of the concept.

Acknowledgements

We would like to thank the Hydra Technologies Team in Mexico for their continuous support, and especially Mr. Carlos Ruiz, Mr. Eduardo Yakin and Mr. Alvaro Gutierrez Prado. We would also like to thank to the Natural Sciences and Engineering Research Council of Canada (NSERC) for the funding of the Canada Research Chair in Aircraft Modeling and Simulation Technologies. In addition we would like to thank to the Canada Foundation of Innovation (CFI), to the Ministère du Développement économique, de l'Innovation et de l'Exportation (MDEIE) and to Hydra Technologies for the acquisition of the UAS-S4 using the Leaders Opportunity Funds.

CHAPTER 7

A NEW NONLINEAR VORTEX LATTICE METHOD: APPLICATIONS TO WING AERODYNAMIC OPTIMIZATIONS

Oliviu Şugar Gabor, Andreea Koreanschi and Ruxandra Mihaela Botez
LARCASE Laboratory of Applied Reasearch in Active Controls,
Avionics and Aeroservoelasticity
École de Technologie Supérieure, 1100 rue Notre Dame Ouest,
Montréal, H3C1K3, Québec, Canada

This article was submitted to *Chinese Journal of Aeronautics*

Résumé

L'article présente une nouvelle formulation non-linéaire de la méthode classique Vortex Lattice, qui est utilisée pour calculer les propriétés aérodynamiques de surfaces portantes. Le modèle mathématique est construit à l'aide des analyses bidimensionnelles visqueuses des sections de l'aile en long de son envergure, après la théorie des bandes, et ensuite par le couplage des forces visqueuses de bande avec les forces générées par les anneaux tourbillonnaires répartis sur la surface de la cambrure de l'aile, et calculées avec une loi entièrement en trois dimensions. Les résultats numériques obtenus avec la méthode proposée sont très bien validés avec les données expérimentales et montrent un bon accord en termes des coefficients de la portance et du moment de tangage, mais aussi pour la prédiction de la traînée de l'aile. Les coûts de calcul faibles transforment cette méthode en un bon outil pour les procédures de conception des ailes ou les procédures d'optimisation. La méthode est appliquée pour modifier l'aile d'un système autonome de vol afin d'augmenter son efficacité aérodynamique, et pour calculer les réductions de traînée obtenues par une technique de déformation de la surface supérieure pour une aile d'avion de transport.

Abstract

This paper presents a new non-linear formulation of the classical Vortex Lattice Method approach for calculating the aerodynamic properties of lifting surfaces. The mathematical model is constructed by using two-dimensional viscous analyses of the wing span-wise sections, according to strip theory, and then coupling the strip viscous forces with the forces generated by the vortex rings distributed on the wing camber surface, calculated with a fully three-dimensional vortex lifting law. The numerical results obtained with the proposed method are validated with experimental data and show good agreement in predicting both the lift and pitching moment, as well as predicting the wing drag. The low computational costs make it a good tool for rapid wing design or wing optimization. The method is applied on modifying the wing of an Unmanned Aerial System to increase its aerodynamic efficiency, and to calculate the drag reductions obtained by an upper surface morphing technique for an adaptable regional aircraft wing.

7.1 Introduction

The air transportation industry is a commercial and economical sector with a very fast growth rate. The International Civil Aviation Organization (ICAO) estimates that the number of flights will triple by 2040 (ICAO, 2010). This growth rate, together with growing global concern for environmental protection and the reduction of greenhouse gas emissions obliges the aerospace industry to search for solutions to improve aircraft efficiency.

One possibility for achieving this desired efficiency is wing morphing, through its active and controlled modification of one or several wing geometrical characteristics during flight. Researchers have proposed different technological solutions for obtaining the desired wing adaptability, with some concepts achieving significant performance improvements with respect to the baseline design. Sofla et al. (2010), Stanewsky (2001) or Barbarino et al. (2011) presented exhaustive reviews on the research performed on various morphing wing technologies, both by academia and by the aerospace industry. Morphing wings were used to

adapt the wing span and airfoil camber (Gamboa et al., 2007), (do Vale et al., 2011), the winglet cant and toe angles (Falcao, 2011), to replace conventional high-lift devices (Pecora et al., 2011), (Diodati et al., 2013), (Pecora et al., 2014), or the conventional control surfaces (Pecora, 2012).

In Canada, the CRIAQ 7.1 project, a collaboration between Ecole de Technologie Superieure, Ecole Polytechnique de Montreal, Bombardier Aeronautique, Thales Canada and the Institute for Aerospace Research – Canada National Research Council took place between 2006-2009. The objective of this project was to improve and control the laminarity over a morphing wing wind tunnel model, in order to obtain significant drag reductions (Botez, 2007). The wing was equipped with a flexible composite material upper surface whose shape could be changed using internally-placed Shape Memory Alloy (SMA) actuators (Brailovski et al., 2008). The numerical study revealed very promising results: the morphing system was able to delay the transition location downstream by up to 30% of the chord and reduce the airfoil drag by up to 22% (Pages, 2007). The actuator optimal displacements for each flight condition were provided by using both a direct open loop approach (Grigorie, 2009), (Popov et al., 2010) and a closed loop configuration based on real time pressure readings from the wing upper surface (Popov et al., 2010). In addition, a new controller based on an optimal combination of the bi-positional and PI laws was developed (Grigorie et al., 2012). The wind tunnel tests were performed in the 2 m by 3 m atmospheric closed circuit subsonic wind tunnel at IAR-CNRC, and validated the numerical wing optimisations (Sainmont et al., 2009) and designed control techniques (Grigorie, 2012).

Recently, research on the capabilities of morphing wings equipped with flexible upper surfaces included the optimization performed by Sugar Gabor et al., of the ATR42 regional aircraft airfoil (Sugar Gabor and Koreanschi, 2012) and of the Hydra Technologies S4 Unmanned Aerial System (UAS) airfoil (Sugar Gabor et al., 2014). Both cases obtained notable transition delays of up to 20% of the chord and significant drag reductions of up to 15%. The morphing system designed for improving and controlling the laminarity of the flow could also provide performance improvements at high angles of attack. For the UAS-S4

airfoil, a 2 degree increase of the stall angle, with a corresponding increase of the maximum lift coefficient by 6% have been obtained, using the morphing upper skin to delay the boundary layer separation (Sugar Gabor et al., 2014).

In order to obtain three-dimensional wing performance improvements with upper surface morphing, a fast and efficient aerodynamic solver was required. A three dimensional, non-linear numerical extension of the classic lifting line theory, coupled with a two-dimensional viscous flow solver, gave sufficiently accurate estimations of the aerodynamic characteristics of the UAS-S4 wing (Sugar Gabor, 2013). A study of the UAS-S4 wing revealed that for typical cruise and surveillance flight conditions, the morphing wing could provide drag reductions of up to 5% (Sugar Gabor, 2013). Further research was performed to determine the influence of the number of internally-placed actuators and their positions along the wing span on the aerodynamic gains. The aerodynamic calculations were done using the numerical non-linear lifting line code, while the optimized upper skin shapes were determined by a novel technique based on a hybrid Artificial Bee Colony (ABC) and the Broyden-Fletcher-Goldfarb-Shanno (BFGS) algorithm (Sugar Gabor, 2014).

The CRIAQ MDO 505 project is a continuation of the CRIAQ 7.1 project and is centered on the implementation of the adaptive upper surface morphing concept on a real regional aircraft wing tip. The wing box, including all the spars, ribs and stringers present on the wing, was manufactured from aluminum, while its flexible upper surface, localized between 20% and 65% of the wing chord, was specifically designed and optimized from carbon composite materials. Four in-house manufactured electrical actuators were fixed to the ribs and to the flexible upper skin, inside the wing box. The actuators are located on two parallel ribs, at 37% and 75% of the model span, while on each of the two ribs the actuators are placed at 32% and 48% of the local wing chord.

Unlike the UAS-S4 wing, that has a high aspect ratio of 7.61, the MDO 505 wing tip model has a low aspect ratio of 2.33. The lifting line model can be corrected for low aspect ratio wings by using semi-empirical correction factors (Lingard, 1995), but a lifting surface model

such as the Vortex Lattice Method (VLM) could provide the results without requiring further corrections. In addition, the surface modelling of both span-wise and chord-wise aerodynamic force distributions provides better and more detailed results even for higher aspect ratio wings, such as that of the UAS-S4.

The VLM represents a powerful tool for preliminary wing design and optimization. Initially, the method used a distribution of horseshoe vortices over the wing surface, with only one segment bound to the surface (Hedman, 1966), but researchers presented alternative, more accurate formulations using ring vortices (Katz and Plotkin, 1991). The unsteady VLM was extensively used to calculate the aerodynamic loads for aeroelasticity and flight dynamics simulations (Murua, 2012). Recently, the steady VLM was used for multi-objective optimization studies for existing commercial aircraft (Leifsson, 2014), for the development of morphing wings (Smith et al., 2012), for Unmanned Aerial Vehicles aerodynamic performance optimizations (Tianyuan and Xiongqing, 2009) and for the design of non-conventional Blended Wing Body aircraft geometries (Peifeng et al., 2012).

7.2 Nonlinear VLM Methodology

7.2.1 Linear non-planar VLM formulation

Before developing the new non-linear method, a presentation of the classic VLM is performed, to establish the basic equation from which the new method was constructed. Within the framework of the VLM approach (Katz and Plotkin, 1991), the singularity element is the vortex line solution of the incompressible potential flow equation, while the imposed boundary condition is that of zero flow in the direction normal to the wing's solid surface:

$$\nabla(\Phi_\infty + \varphi) \cdot \mathbf{n} = 0 \tag{7.1}$$

where ϕ_∞ represents the potential of the freestream flow, φ is the perturbation potential and **n** represents the vector normal to the wing surface.

The boundary condition is imposed on the wing's mean camber surface, constructed from the camber lines of several span-wise airfoil sections (Xie et al., 2013). The solid surface is divided into rectangular panels, and the vortex ring singularity elements are placed on these panels. The leading edge segment of a vortex ring is placed on the quarter chord line of the corresponding panel, while the collocation point is placed at the center of the panel's three-quarter chord line. Figure 7.1 presents an example of wing geometry divided into panels, with the vortex rings placed on the panels and the surface normal vectors defined at the panel collocation points.

The wake vortices are aligned with the incoming flow velocity, and the circulation of each wake vortex is equal to the circulation of the trailing edge vortex placed directly upstream of it. Thus, the three-dimensional Kutta condition of null trailing edge circulation, presented in the next equation, is satisfied:

$$\gamma_{TE} = 0 \tag{7.2}$$

Each vortex ring is composed of six vortex lines, the leading edge line placed on the quarter chord line of the corresponding panel and the trailing edge line placed on the quarter chord line of the panel directly downstream. The direction of positive circulation is defined according to the right hand rule. Figure 7.2 presents the geometry of a typical vortex ring, where C is the chord of the surface panel over which the vortex ring is placed, B is the panel span and n is the collocation point normal vector.

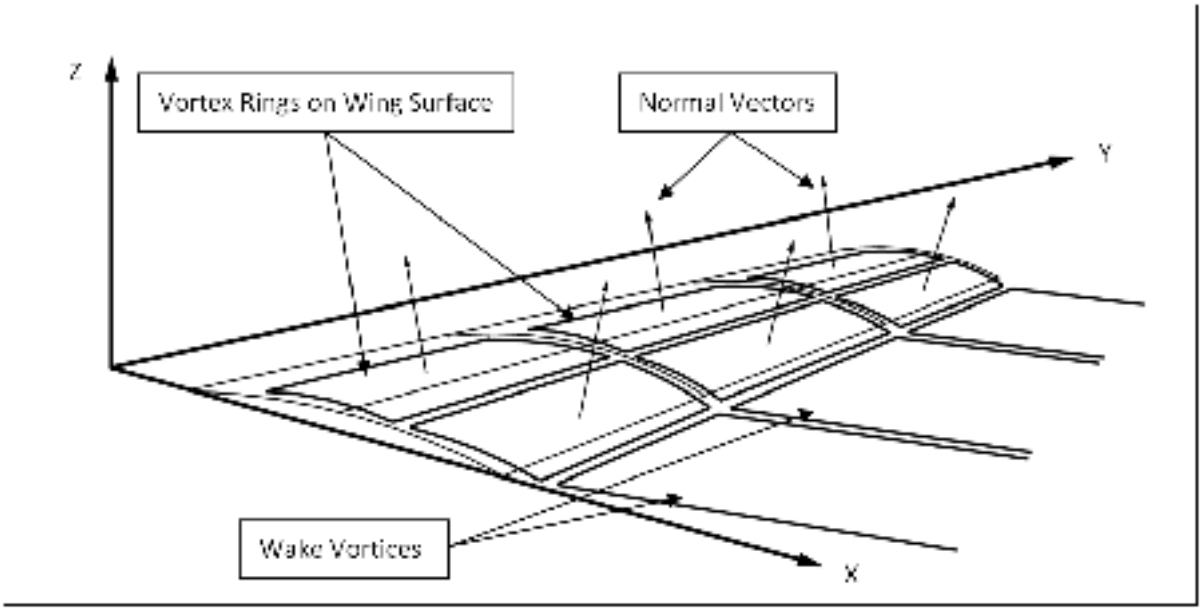

Figure 7.1 Vortex rings over the mean camber surface of a typical wing

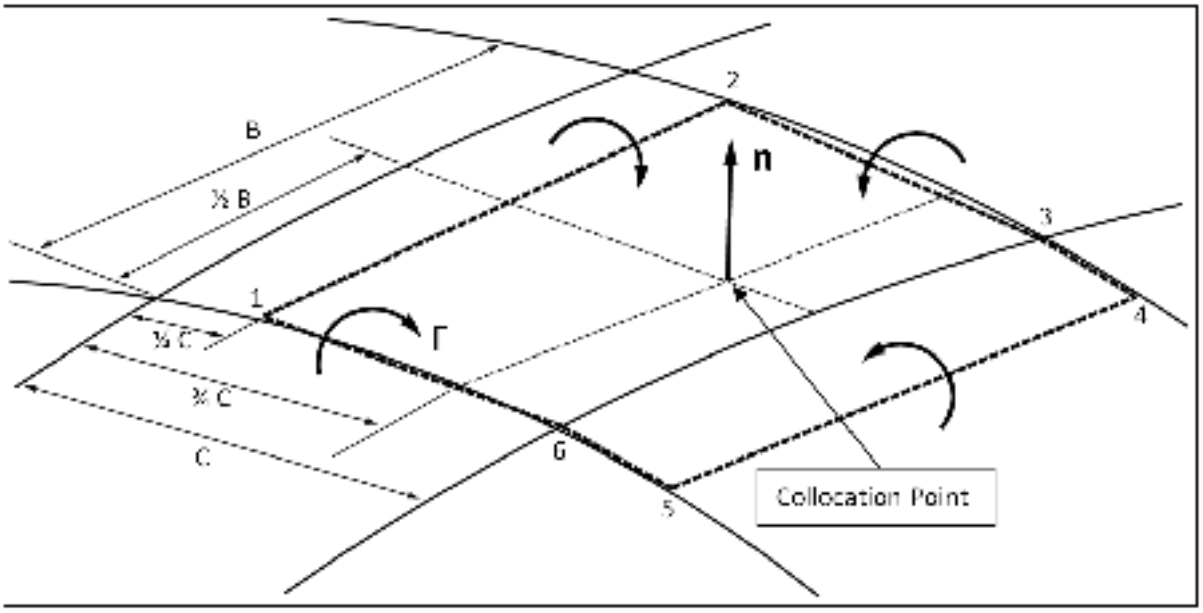

Figure 7.2 Details of a six-edged vortex ring placed over a wing panel

The velocity induced by each of the six vortex lines of a vortex ring at an arbitrary point in space is given by the Biot-Savart law (Katz and Plotkin, 1991):

$$\mathbf{V} = \frac{\Gamma}{4\pi} \frac{\mathbf{r}_1 \times \mathbf{r}_2}{|\mathbf{r}_1 \times \mathbf{r}_2|^2} \mathbf{r}_0 \cdot \left(\frac{\mathbf{r}_1}{r_2} - \frac{\mathbf{r}_2}{r_1} \right) \tag{7.3}$$

In Equation (7.3), $\mathbf{V}$ is the induced velocity, Γ is the vortex intensity, $\mathbf{r}_1$ is the position vector from the beginning of the vortex line to an arbitrary point in space, $\mathbf{r}_2$ is the position vector from the end of the vortex line to an arbitrary point in space, $\mathbf{r}_0$ is the vector from the beginning to the end of the vortex line and r_1 and r_2 are the magnitudes of the vectors. Equation (7.3) can be rewritten in a more suitable form for numerical calculations (Phillips and Snyder, 2000):

$$\mathbf{V} = \frac{\Gamma}{4\pi} \frac{(r_1 + r_2)(\mathbf{r}_1 \times \mathbf{r}_2)}{r_1 r_2 (r_1 r_2 + \mathbf{r}_1 \cdot \mathbf{r}_2)} \tag{7.4}$$

The induced velocity given in Equation (7.4) can be also written as a product between the vortex intensity Γ and the velocity induced by the unit strength vortex line, which is effectively a geometric vector that depends only on the positions of the vortex line and the point where the induced velocity is calculated:

$$\mathbf{V} = \Gamma \mathbf{v}_{12} \tag{7.5}$$

The velocity induced by a complete vortex ring at an arbitrary point in space is the sum of the velocities induced by each of the six vortex lines:

$$\mathbf{V} = \Gamma(\mathbf{v}_{12} + \mathbf{v}_{23} + \mathbf{v}_{34} + \mathbf{v}_{45} + \mathbf{v}_{56} + \mathbf{v}_{61}) = \Gamma \mathbf{v} \tag{7.6}$$

In the classical VLM approach, the unknown intensities of all the vortex rings distributed over the wing surface are determined by requiring that the zero normal flow boundary condition expressed in Equation (7.1) would be satisfied for all collocation points (Katz and

Plotkin, 1991). Knowing that for each collocation point the local velocity is equal to the sum of the freestream velocity and the velocities induced by all the vortex rings over the wing surface and the wake, the boundary condition is written as:

$$\left(\mathbf{V}_\infty + \sum_{j=1}^{N} \Gamma_j \mathbf{v}_{ij}\right) \cdot \mathbf{n}_i = 0 \tag{7.7}$$

In Equation (7.7), $\mathbf{V}_\infty$ is the freestream velocity, N is the total number of vortex rings over the wing surface, $\mathbf{v}_{ij}$ is the velocity induced by the unit strength vortex ring j at the i^{th} panel collocation point and $\mathbf{n}_i$ is the surface normal vector calculated at the i^{th} panel collocation point. The velocities induced by the wake vortices have been added to the velocities induced by the wing trailing edge vortices, since the wake vortices' intensities are determined with the condition of null trailing edge circulation.

Writing Equation (7.7) for all collocation points, a linear system that allows the calculation of all unknown vortex rings intensities is obtained:

$$\begin{gathered}\sum_{j=1}^{N} \mathbf{v}_{ij} \cdot \mathbf{n}_i \Gamma_j = -\mathbf{V}_\infty \cdot \mathbf{n}_i \quad i = 1, 2, \ldots, N \\ \sum_{j=1}^{N} a_{ij} \Gamma_j = b_i \quad i = 1,2, \ldots, N\end{gathered} \tag{7.8}$$

where $a_{ij} = \mathbf{v}_{ij} \cdot \mathbf{n}_i$ are the aerodynamic influence coefficients and $b_i = -\mathbf{V}_\infty \cdot \mathbf{n}_i$ are the right hand side terms.

7.2.2 Ring vortex intensities' correction

In the new nonlinear VLM approach, the intensities of the vortex rings obtained by solving the linear system presented in Equation (7.8) are adjusted using nonlinear viscous data. For each vortex ring, a correction $\Delta\Gamma$ is defined, so that the final values of the vortex intensities become:

$$\Gamma_j \rightarrow \Gamma_j + \Delta\Gamma_j \quad j = 1,2,\dots,N \tag{7.9}$$

The corrected vortex rings' intensities cannot satisfy the same boundary conditions as the uncorrected intensities, since Equation (7.7) leads to the uniquely determined solution of the linear system (7.8). By considering that a variation in the intensity of a vortex ring determines a variation in the velocities induced by that vortex ring, the introduction of the $\Delta\Gamma_j$ corrections is followed by the introduction of a secondary induced velocity field over the wing surface. Thus, for the nonlinear VLM approach, Equation (7.7) becomes:

$$\left(\mathbf{V}_\infty + \sum_{j=1}^{N}\left(\Gamma_j + \Delta\Gamma_j\right)\mathbf{v}_{ij} + \mathbf{V}_i^T\right)\cdot\mathbf{n}_i = 0 \tag{7.10}$$

In Equation (7.10), the unknown added velocity $\mathbf{V}_i^T$ determined by the introduction of the vortex rings' intensity corrections can be considered as a type of surface transpiration velocity, being a direct measure of the alteration of the classic VLM boundary condition. For simplification, it is useful to orient this surface transpiration velocity in the direction of the panel collocation point normal:

$$\mathbf{V}_i^T = V_i^T\mathbf{n}_i \tag{7.11}$$

where V_i^T represents the modulus of the surface transpiration velocity.

By combining Equations (7.7), (7.10) and (7.11), an expression that links the vortex rings' intensity corrections with the surface transpiration velocities at the panel collocation points is obtained:

$$\sum_{j=1}^{N} \mathbf{v}_{ij} \cdot \mathbf{n}_i \Delta\Gamma_j = -V_i^T \quad i = 1,2,\dots,N \tag{7.12}$$

7.2.3 Strip analysis of the wing

In order to obtain the second set of equations needed for the problem resolution, a nonlinear viscous pressure coefficient distribution is required. This data is obtained by performing a two-dimensional strip analysis of the wing. Let N_X be the number of chord-wise panels and N_Y the number of spanwise panels into which the wing mean camber surface is divided, with the total number of panels being $N = N_X N_Y$. Each chord-wise line of panels is also considered a wing strip. Figure 7.3 presents the division of an example half wing geometry into surface panels and span-wise strips.

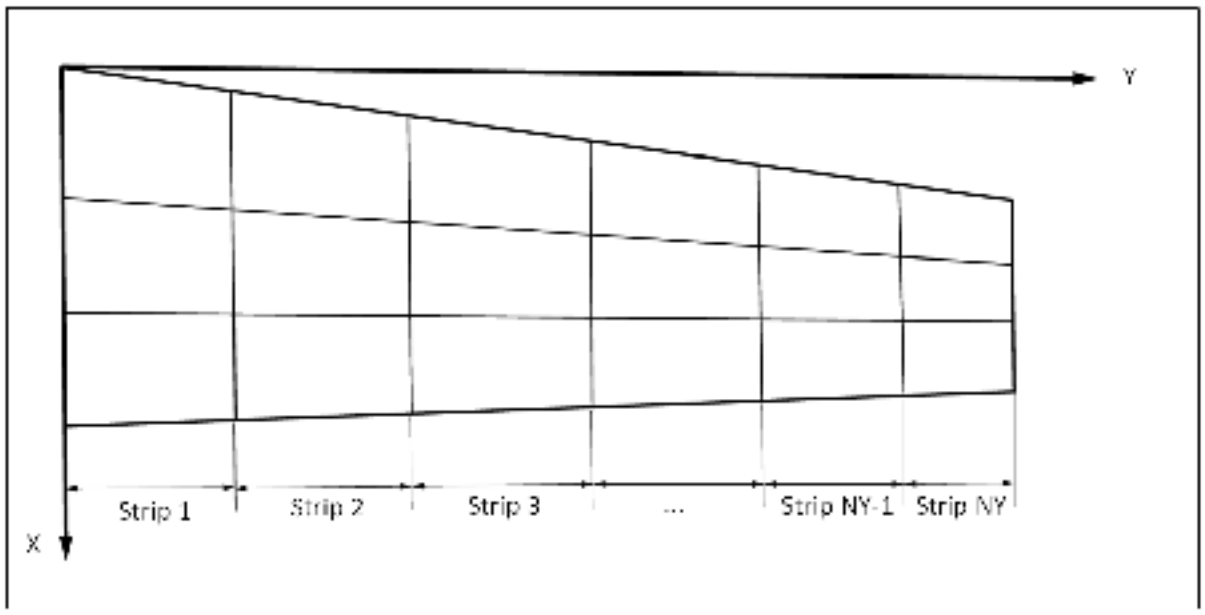

Figure 7.3 Span-wise strips and surface panels division of example half wing geometry

To obtain the nonlinear viscous pressure coefficient distribution, the span-wise strips are analysed under the local flow conditions, using a two-dimensional viscous flow solver. For each strip, a control point is defined, placed at the middle of the three-quarter chord line of the strip and projected on the camber line of the local strip airfoil. The local velocity at the control point is then calculated with the following equation:

$$\mathbf{V}_i = \mathbf{V}_\infty + \sum_{j=1}^{N} (\Gamma_j + \Delta\Gamma_j)\mathbf{v}_{ij} \tag{7.13}$$

In Equation (7.13), $\mathbf{V}_\infty$ is the freestream velocity, N is the total number of vortex rings over the wing surface and $\mathbf{v}_{ij}$ is the velocity induced by the unit strength vortex ring j at the i^{th} strip control point. The strip's local effective angle of attack is:

$$\alpha_i = \tan^{-1}\left(\frac{\mathbf{V}_i \cdot \mathbf{ns}_i}{\mathbf{V}_i \cdot \mathbf{cs}_i}\right) = \tan^{-1}\left[\frac{\left(\mathbf{V}_\infty + \sum_{j=1}^{N}(\Gamma_j + \Delta\Gamma_j)\mathbf{v}_{ij}\right) \cdot \mathbf{ns}_i}{\left(\mathbf{V}_\infty + \sum_{j=1}^{N}(\Gamma_j + \Delta\Gamma_j)\mathbf{v}_{ij}\right) \cdot \mathbf{cs}_i}\right] \tag{7.14}$$

Here, $\mathbf{cs}_i$ is the unit vector in the direction of the chord, $\mathbf{ns}_i$ is the unit vector in the direction normal to the chord, both vectors being in the plane of the local airfoil corresponding to the i^{th} wing strip, and $\mathbf{v}_{ij}$ is the velocity induced by the unit strength vortex ring j at the i^{th} strip collocation point.

After the determination of the local flow conditions with Equations (7.13) and (7.14), the viscous pressure coefficient distribution is determined using the two-dimensional flow solver:

$$CP_i^{visc} = f(airfoil_i, Re_i, \|\mathbf{V}_i\|, \alpha_i) \quad i = 1,2,\dots,N_Y \tag{7.15}$$

where CP_i^{visc} represents the viscous pressure coefficient distribution, Re_i is the Reynolds number, $\|\mathbf{V}_i\|$ is the modulus of the total velocity at the control point and α_i represents the effective angle of attack, all variables being calculated for the i^{th} wing strip.

From the pressure coefficient distribution over the local strip airfoil, the pressure coefficient difference between the lower and upper surfaces can be determined for the collocation points of the wing panels that are placed on each specific wing strip. For the results presented here, the two-dimensional strip airfoil characteristics are determined using the XFOIL solver (Drela, 1989). In the case where the wing has a large sweep angle, the strip theory analysis is extended using sweep theory, and the local values of the effective angle of attack and of the strip airfoil aerodynamic characteristics are corrected using the iterative methodology presented in (Mariens, 2014), (Elham, 2015).

7.2.4 Nonlinear non-planar VLM formulation

The equations needed to calculate the vortex rings' intensity corrections are constructed from the assumption that for all N panels on the wing surface, the pressure coefficient variation obtained from the vortex rings' intensities is equal to the nonlinear viscous pressure coefficient variation obtained from the wing strip analysis. For all panels, the following equality is written:

$$\Delta CP_i = \Delta CP_i^{visc} \quad i = 1,2,\dots,N \tag{7.16}$$

The pressure coefficient variation for all panels on the wing surface can be written as:

$$\Delta CP_i = -\frac{\mathbf{F}_i \cdot \mathbf{n}_i}{A_i Q_\infty} \tag{7.17}$$

In Equation (7.17), $\mathbf{F}_i$ is the aerodynamic force generated by all the vortex lines placed on the panel, $\mathbf{n}_i$ is the surface normal vector calculated at the panel collocation point, A_i is the panel area and Q_∞ is the freestream dynamic pressure. By combining Equations (7.16) and (7.17):

$$-\mathbf{F}_i \cdot \mathbf{n}_i + A_i Q_\infty \Delta CP_i^{visc} = 0 \quad i = 1,2,\dots,N \tag{7.18}$$

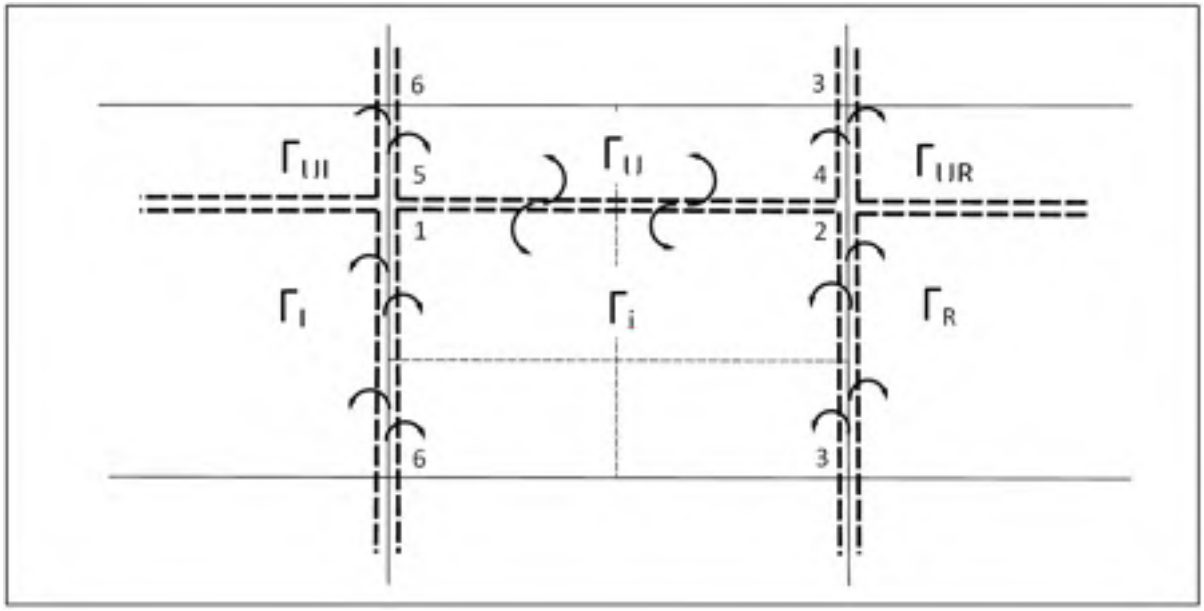

Figure 7.4 Neighbouring rings for a general, arbitrary vortex ring of the wing model

In order to determine the aerodynamic force acting on a panel of the wing surface, Figure 7.4 presents an arbitrary panel, its neighbours and all the vortex rings that must be included in the analysis. For certain panels, such as those situated at the wing leading edge or at the wing tips, one or several of the neighbouring panels do not exist, and thus are not included in the calculation of the force.

Following the notations indicated in Figure 7.4, the force can be calculated as (using the three-dimensional vortex lifting law (Saffman, 1992)):

$$\mathbf{F}_i = \rho(\Gamma_i - \Gamma_U)\mathbf{V}_i \times \boldsymbol{\gamma}_{12} + \rho(\Gamma_i - \Gamma_R)\mathbf{V}_i \times \boldsymbol{\gamma}_{23} + \rho(\Gamma_i - \Gamma_L)\mathbf{V}_i \times \boldsymbol{\gamma}_{61} + \\ + \rho(\Gamma_U - \Gamma_{UR})\mathbf{V}_i \times \boldsymbol{\gamma}_{34} + \rho(\Gamma_U - \Gamma_{UL})\mathbf{V}_i \times \boldsymbol{\gamma}_{56} \tag{7.19}$$

where ρ is the air density, Γ is the intensity of a vortex ring, $\mathbf{V}_i$ is the local velocity at the panel collocation point and $\boldsymbol{\gamma}$ is the supporting geometric segment of a vortex line. The force given in Equation (7.19) is projected onto the direction of the local normal vector:

$$\mathbf{F}_i \cdot \mathbf{n}_i = \rho(\Gamma_i - \Gamma_U)(\mathbf{V}_i \times \boldsymbol{\gamma}_{12}) \cdot \mathbf{n}_i + \rho(\Gamma_i - \Gamma_R)(\mathbf{V}_i \times \boldsymbol{\gamma}_{23}) \cdot \mathbf{n}_i \\ + \rho(\Gamma_i - \Gamma_L)(\mathbf{V}_i \times \boldsymbol{\gamma}_{61}) \cdot \mathbf{n}_i + \rho(\Gamma_U - \Gamma_{UR})(\mathbf{V}_i \times \boldsymbol{\gamma}_{34}) \cdot \mathbf{n}_i \\ + \rho(\Gamma_U - \Gamma_{UL})(\mathbf{V}_i \times \boldsymbol{\gamma}_{56}) \cdot \mathbf{n}_i \tag{7.20}$$

Using the scalar triple product and the linear properties of the dot product, Equation (7.20) can be rearranged as follows:

$$\mathbf{F}_i \cdot \mathbf{n}_i = \rho(\mathbf{n}_i \times \mathbf{V}_i) \\ \cdot [(\Gamma_i - \Gamma_U)\boldsymbol{\gamma}_{12} + (\Gamma_i - \Gamma_R)\boldsymbol{\gamma}_{23} + (\Gamma_i - \Gamma_L)\boldsymbol{\gamma}_{61} \\ + (\Gamma_U - \Gamma_{UR})\boldsymbol{\gamma}_{34} + (\Gamma_U - \Gamma_{UL})\boldsymbol{\gamma}_{56}] \tag{7.21}$$

Each of the vortex rings' intensities included in Equation (7.21) can be written as the sum between the classic inviscid intensity and the correction factor, as presented in Equation (7.9). In addition, the local velocity at the panel collocation point will be:

$$\mathbf{V}_i = \mathbf{V}_\infty + \sum_{j=1}^{N} (\Gamma_j + \Delta\Gamma_j)\mathbf{v}_{ij} \tag{7.22}$$

By combining Equations (7.20), (7.9) and (7.22), the following expression is obtained for the normal force acting on each of the wing surface panels:

$$\begin{aligned}\mathbf{F}_i \cdot \mathbf{n}_i = \rho \Bigg[\mathbf{n}_i \times \Bigg(\mathbf{V}_\infty + \sum_{j=1}^{N} (\Gamma_j + \Delta\Gamma_j)\mathbf{v}_{ij} \Bigg) \Bigg] \\ \cdot [(\Gamma_i - \Gamma_U)\boldsymbol{\gamma}_{12} + (\Gamma_i - \Gamma_R)\boldsymbol{\gamma}_{23} + (\Gamma_i - \Gamma_L)\boldsymbol{\gamma}_{61} \\ + (\Gamma_U - \Gamma_{UR})\boldsymbol{\gamma}_{34} + (\Gamma_U - \Gamma_{UL})\boldsymbol{\gamma}_{56} + (\Delta\Gamma_i - \Delta\Gamma_U)\boldsymbol{\gamma}_{12} \\ + (\Delta\Gamma_i - \Delta\Gamma_R)\boldsymbol{\gamma}_{23} + (\Delta\Gamma_i - \Delta\Gamma_L)\boldsymbol{\gamma}_{61} + (\Delta\Gamma_U - \Delta\Gamma_{UR})\boldsymbol{\gamma}_{34} \\ + (\Delta\Gamma_U - \Delta\Gamma_{UL})\boldsymbol{\gamma}_{56}] \quad i = 1,2,\dots,N\end{aligned} \tag{7.23}$$

By introducing the normal force $\mathbf{F}_i$ given by Equation (7.23) into the equality presented in Equation (7.18), and by coupling the resulting equations with Equation (7.12), a nonlinear system of $2N$ equations is obtained:

$$\mathbf{R} = \begin{Bmatrix} \vdots \\ -\mathbf{F}_i \cdot \mathbf{n}_i + A_i Q_\infty \Delta C P_i^{visc} \\ \vdots \\ \sum_{j=1}^{N} \mathbf{v}_{ij} \cdot \mathbf{n}_i \Delta\Gamma_j + V_i^T \\ \vdots \end{Bmatrix} = \mathbf{0} \tag{7.24}$$

The unknown variables of the system are the N values of the vortex rings' intensity corrections and the N values of the surface transpiration velocities:

$$\mathbf{X} = \{\cdots \quad \Delta\Gamma_i \quad \cdots \quad \cdots \quad V_i^T \quad \cdots\}^{\mathbf{T}} \tag{7.25}$$

7.2.5 Nonlinear system analysis and solution

The nonlinear system of equations can be solved using Newton's method (Deuflhard, 2004). Starting with an initial guess of the solution vector $\mathbf{X}^0$, the quality of this estimate can be improved using the following iterative procedure:

$$\mathbf{J}(\mathbf{X}^k)\Delta\mathbf{X} = -\mathbf{R}(\mathbf{X}^k)$$
$$\mathbf{X}^{k+1} = \mathbf{X}^k + \Omega\Delta\mathbf{X} \tag{7.26}$$

In Equation (7.26), $\mathbf{J}(\mathbf{X}^k)$ is the Jacobian matrix of first-order partial derivatives, calculated with the current estimate of the solution vector, $-\mathbf{R}(\mathbf{X}^k)$ is the system residual, calculated with the current estimate of the solution vector, $\Delta\mathbf{X}$ is the solution increment and Ω is an under-relaxation factor. The iterative solution procedure continues until the magnitude of the largest residual becomes smaller than the desired convergence criteria.

Starting from the expression of the nonlinear system in Equation (7.24), the Jacobian matrix can be computed in four partitions as follows:

$$\mathbf{J} = \frac{\partial R_i}{\partial X_k} = \begin{bmatrix} \dfrac{\partial\left(-\mathbf{F}_i \cdot \mathbf{n}_i + A_i Q_\infty \Delta CP_i^{visc}\right)}{\partial \Delta\Gamma_k} & \Big| & \dfrac{\partial\left(-\mathbf{F}_i \cdot \mathbf{n}_i + A_i Q_\infty \Delta CP_i^{visc}\right)}{\partial V_k^T} \\ - - - - - - - - - - - - - - - & \Big| & - - - - - - - - - - - - - - - \\ \dfrac{\partial\left(\sum_{j=1}^{N} \mathbf{v}_{ij} \cdot \mathbf{n}_i \Delta\Gamma_j + V_i^T\right)}{\partial \Delta\Gamma_k} & \Big| & \dfrac{\partial\left(\sum_{j=1}^{N} \mathbf{v}_{ij} \cdot \mathbf{n}_i \Delta\Gamma_j + V_i^T\right)}{\partial V_k^T} \end{bmatrix} \tag{7.27}$$

The derivatives of the normal force determined by Equation (7.23) with respect to the vortex rings' intensity corrections can be obtained through mathematical operations. More attention will be given to the derivative of the viscous pressure coefficient difference. These values were obtained following a two-dimensional strip analysis of the wing, where each strip airfoil was calculated at the corresponding local flow conditions. Assuming incompressible flow, the strip pressure coefficient distribution depends only on the local angle of attack given by Equation (7.14). It must be observed that the local value of the pressure coefficient difference between the lower and upper surfaces also depends on the chord-wise position where it is calculated. Thus, the derivative of the pressure coefficient difference can be written as:

$$\left(\frac{\partial \Delta CP^{visc}}{\partial \Delta \Gamma_k}\right)_{for\ panel\ (i)} = \left(\frac{\partial \Delta CP^{visc}}{\partial \alpha_l}\right)_{for\ strip\ (l) and\ \left(\frac{X}{C}\right) chordwise\ position} \frac{\partial \alpha_l}{\partial \Delta \Gamma_k} \tag{7.28}$$

where α_l represents the l^{th}strip effective angle of attack.

The first right hand side term of Equation (7.28) can be estimated for each wing strip while performing the two-dimensional strip analysis, and then the values can be interpolated for the current panel i, as a function of the strip l on which the panel is placed and the relative chord-wise position of the panel collocation point on the local airfoil chord. The derivative of the strip angle of attack can be determined based on Equation (7.14) and is equal to:

$$\frac{\partial \alpha_l}{\partial \Delta \Gamma_k} = \frac{(\mathbf{v}_{lk} \cdot \mathbf{ns}_l)V_c - (\mathbf{v}_{lk} \cdot \mathbf{cs}_l)V_n}{V_c^2 + V_n^2} \tag{7.29}$$

Here $\mathbf{cs}_l$ is the unit vector in the direction of the chord, $\mathbf{ns}_l$ is the unit vector in the direction normal to the chord, both vectors being in the plane of the local airfoil of the l^{th} strip, and $\mathbf{v}_{lk}$ is the velocity induced by the unit strength vortex ring k at the l^{th} strip collocation point.

The following notations have been introduced:

$$V_n = \left(\mathbf{V}_\infty + \sum_{j=1}^{N} (\Gamma_j + \Delta \Gamma_j)\mathbf{v}_{lj}\right) \cdot \mathbf{ns}_l \tag{7.30}$$

$$V_c = \left(\mathbf{V}_\infty + \sum_{j=1}^{N} (\Gamma_j + \Delta \Gamma_j)\mathbf{v}_{lj}\right) \cdot \mathbf{cs}_l \tag{7.31}$$

The other three partitions of the Jacobian can be determined much faster than the first partition. The second partition is the $N \times N$ null matrix, the third partition is simply the

matrix given by the linear VLM method, as determined in Equation (7.8), while the last partition is the $N \times N$ identity matrix, giving the Jacobian matrix the form presented in Equation (7.32):

$$\mathbf{J} = \frac{\partial R_i}{\partial X_k} = \\ = \begin{bmatrix} \dfrac{\partial(-\mathbf{F}_i \cdot \mathbf{n}_i)}{\partial \Delta\Gamma_k} + A_i Q_\infty \dfrac{\partial\left(\Delta CP_i^{visc}\right)}{\partial \Delta\Gamma_k} & | & \mathbf{0} \\ - - - - - - - - - - - - - - - & | & - - - - - - - - - - - - - - - \\ \mathbf{v}_{ik} \cdot \mathbf{n}_i & | & \mathbf{I} \end{bmatrix} \tag{7.32}$$

7.2.6 Aerodynamic forces and moments

After the determination of the values of the vortex rings' corrections with the iterative Newton procedure described in Equation (7.26), the aerodynamic forces for each panel on the wing surface can be computed with Equation (7.19), in which the circulation values are updated to their final values according to Equation (7.9). The total aerodynamic force is equal to the sum of the forces acting on each of the wing surface panels:

$$\mathbf{F} = \sum_{i=1}^{N} \mathbf{F}_i \tag{7.33}$$

The total aerodynamic moment generated about a desired wing reference point, such as the quarter chord point of the wing root section, is given by the following expression, in which $\mathbf{r}_i$ is the position vector from the chosen wing reference point to the collocation point of the i wing panel:

$$\mathbf{M} = \sum_{i=1}^{N} \mathbf{r}_i \times \mathbf{F}_i \tag{7.34}$$

The aerodynamic force given by Equation (7.33) is calculated with respect to the wing-fixed reference system. To determine the wing lift C_L and induced drag C_{DI}, the obtained force is projected onto the wind-oriented reference system:

$$\begin{aligned} C_L &= F(z)\cos(\alpha_g) - F(x)\sin(\alpha_g) \\ C_{DI} &= F(x)\cos(\alpha_g) + F(z)\sin(\alpha_g) \end{aligned} \tag{7.35}$$

where α_g is the global (geometric) angle of attack of the wing, while $F(x)$ and $F(z)$ are the components of the aerodynamic force on the respective axes of the wing-fixed system. Following the wing strip analysis performed as part of the solution procedure, the total wing profile drag C_{D0} (also known as parasite drag) can be calculated based on the two-dimensional airfoil drag by direct integration:

$$C_{D0} = \frac{1}{S}\int_{-B/2}^{B/2} C_d(y)c(y)dy \tag{7.36}$$

In Equation (7.36), S is the wing area, B is the wingspan, $C_d(y)$ is the two-dimensional drag coefficient of the local airfoil section and $c(y)$ is the local chord of the wing. Finally, the total drag coefficient is given by the sum of the induced drag coefficient and the profile drag coefficient:

$$C_D = C_{DI} + C_{D0} \tag{7.37}$$

7.3 Nonlinear VLM Validation for Different Test Cases

7.3.1 Grid resolution convergence study

To verify the influence of the wing surface grid resolution on the converged values of the aerodynamic coefficients, a study was performed using four test wing geometries. The wings

were generated using the NACA0012 airfoil and cover four different scenarios: low aspect ratio – low sweep angle, low aspect ratio – high sweep angle, high aspect ratio – low sweep angle and high aspect ratio – high sweep angle. Details on the geometries of the four test wings are presented in Table 7.1.

Table 7.1 Details of test wings used for grid convergence study

Detail	Wing 1	Wing 2	Wing 3	Wing 4
Aspect Ratio	4	4	12	10
Sweep Angle	0 deg.	60 deg.	0 deg.	45 deg.
Span	1.00	1.00	4.50	3.20
MAC	0.26	0.26	0.42	0.42
Taper Ratio	0.60	0.60	0.285	0.45

All four tests were performed using the same Newton iteration convergence criterion of 10^{-3} imposed for the maximum residual value. Eight different surface grids of increasing mesh density were generated for each of the geometries, each grid having a constant spacing in both chord-wise and span-wise directions. The total number of cells for the wing semi-span generated for each of the eight grids, as well as the chord-wise number N_X and span-wise number N_Y are presented in Table 7.2.

Table 7.2 Number of cells included in each grid level used for convergence study

Cells	Grid 1	Grid 2	Grid 3	Grid 4	Grid 5	Grid 6	Grid 7	Grid 8
N_X	2	4	8	10	12	15	18	20
N_Y	4	8	16	20	25	30	35	40
Total	8	32	128	200	300	450	630	800

In Figure 7.5, the variations of the lift coefficient, drag coefficient and pitching moment coefficient about the quarter chord point of the root chord are presented, for the four test wings, as a function of the grid refinement level. For a better visualisation, and in order to provide direct information on the aerodynamic coefficients variation with the refinement level, all the coefficient values have been normalized using the value obtained for the finest grid, which is Grid 8. It can be observed that the nonlinear VLM approach requires a

sufficiently refined grid to achieve results that are grid-independent, as only for the level seven grid refinement are the results for all three aerodynamic coefficients values and for all four wing geometries within 1% of the values obtained with the most refined grid.

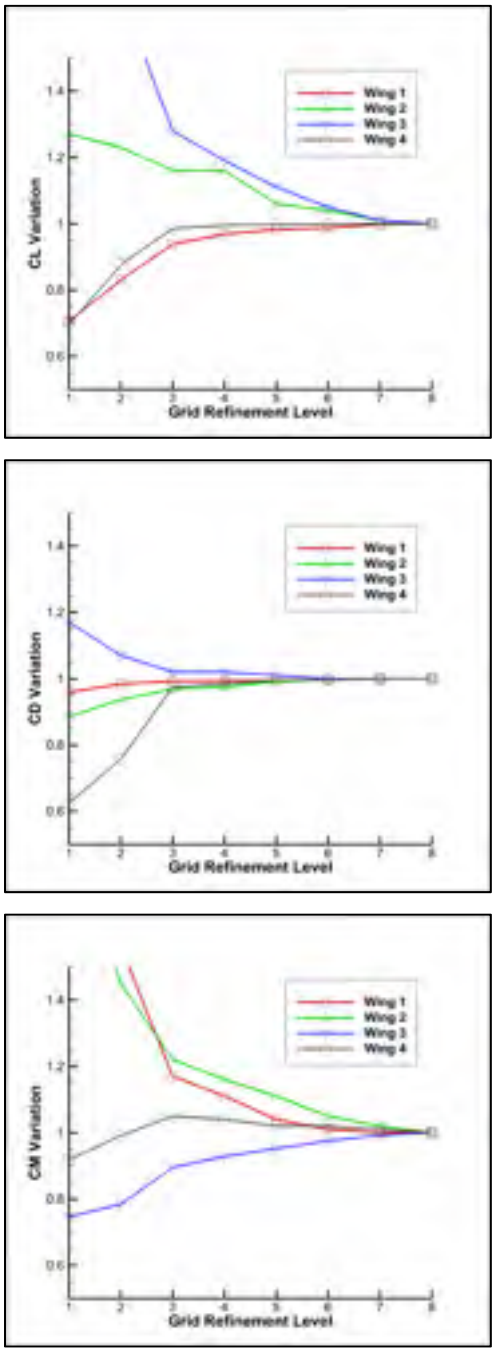

Figure 7.5 Convergence of the aerodynamic coefficients with grid refinement level

Figure 7.6 presents the convergence curves for different mesh refinement levels that were presented in Table 7.2. The first two grid levels did not achieve the desired convergence error of 10^{-3}, and thus only Grid 2 was presented, because it obtained better results. For Grids 7 and 8, the convergence curves are almost superposed, and only Grid 7 was chosen for display, to provide better visualisation. The nonlinear algorithm reaches convergence in five or six iterations, and the minimum residual value varies with the refinement level, achieving lower values on the finer meshes.

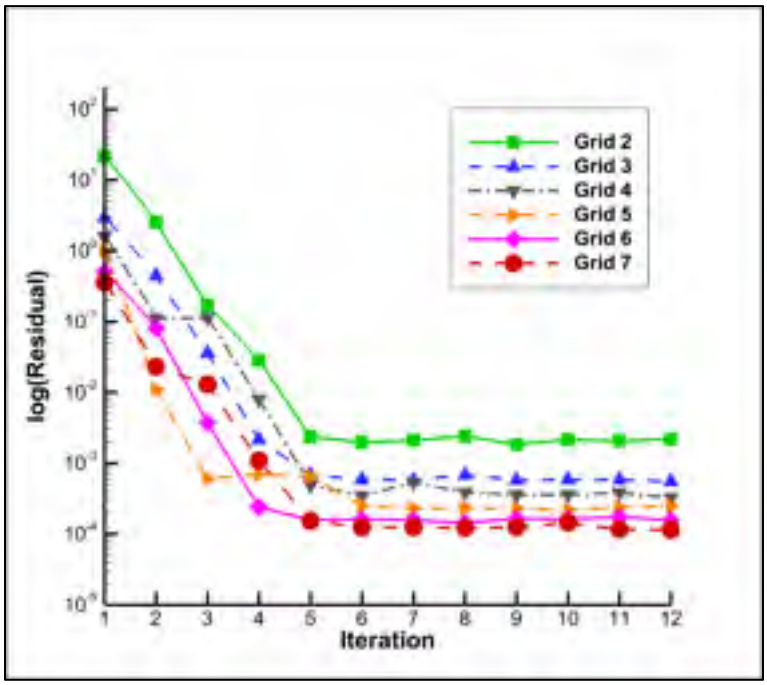

Figure 7.6 Residual convergence curves with grid refinement level

7.3.2 Verification of linear results with theoretical data

For the first verification case, the inviscid numerical results obtained with the new code are compared with the theoretical results for a two-dimensional flat plate section (McCormick, 1995). To achieve the desired two-dimensional flow conditions, a wing model of very high aspect ratio was constructed, with no taper, sweep, dihedral or twisting, and the results were plotted for its symmetry section. The model has a wing span of 20 meters and a chord of

1 meter, and it was analysed at an angle of attack of 10 degrees and an airspeed of 10 meters/second. Figure 7.7 presents a comparison between the numerically-obtained pressure coefficient difference ΔCP values for the model symmetry section and the values predicted by two-dimensional linear potential theory for the given flow conditions. It can be seen that a very good agreement exists between the two sets of results.

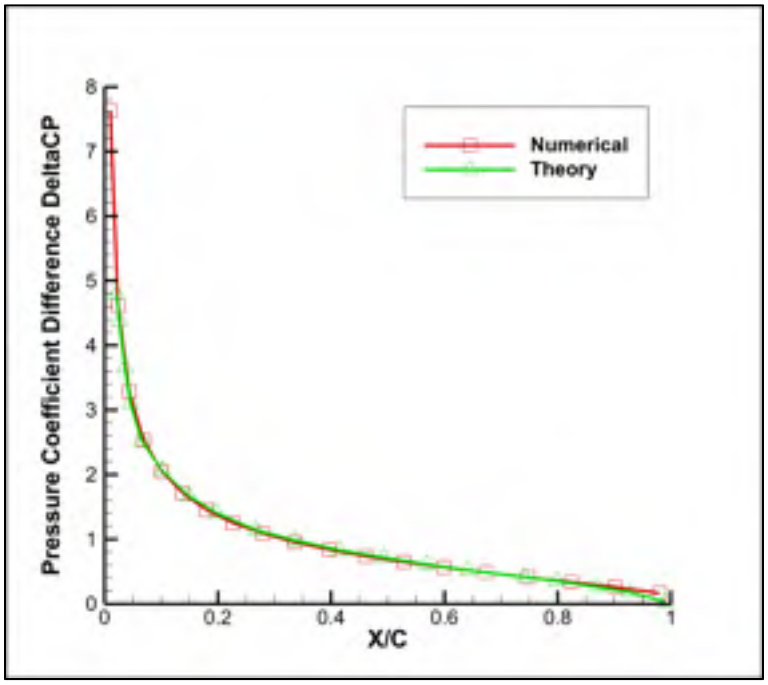

Figure 7.7 Pressure coefficient variation for a flat plate, compared to exact linear potential theory

The second validation test is performed on the Warren 12 wing, a geometry that is classically used to verify the accuracy of vortex lattice codes (SURFACES, 2009). The Warren 12 wing has a low aspect ratio, high sweep angle, flat surface geometry, and its characteristics are presented in Table 7.3.

Table 7.3 Geometry details for the Warren 12 test wing

Aspect Ratio	Span	Root Chord	Taper Ratio	Sweep angle	Area
2.83	2.83 m	1.50 m	0.3333	53.54 deg.	2.83 m^2

The theoretical and numerical lift and pitching moment coefficients derivatives with the angle of attack are shown in Table 7.4. For the reference results presented, the lift and pitching moment coefficients were calculated using the average geometrical chord (instead of the mean aerodynamic chord that is often used), and the pitching moment coefficient was calculated about the root chord leading edge point. The VLM results were obtained using a wing surface mesh of 10 chord-wise panels and 15 span-wise panels per semi-span. The results are very good, with an error of 0.51% for the lift coefficient derivative with α and 0.32% for the pitching moment coefficient derivative with α.

Table 7.4 Comparison of lift and pitching moment coefficients slopes

Results	$C_{L\alpha}$	$C_{M\alpha}$
Theoretical	2.743/rad	-3.10/rad
Numerical	2.757/rad	-3.09/rad

7.3.3 Validation of nonlinear results with experimental data

The first viscous flow validation test performed using the nonlinear VLM was done using geometrical and experimental data taken from the NACA Technical Note 1270 (Neely et al., 1947). The wing geometry chosen is a high aspect ratio shape with no sweep and a relatively high taper ratio. This wing is constructed using airfoils from the NACA 44-series, with the root section airfoil being a NACA 4422 and the tip section airfoil a NACA 4412. Table 7.5 presents details about the geometry of the test wing model.

Table 7.5 Geometric characteristics of the NACA TN 1270 test wing

Aspect Ratio	Span	Root Chord	Taper Ratio	Sweep Angle	Area	Tip Twist	MAC
12	4.56 m	0.5915 m	0.285	0 deg.	1.733 m^2	-3 deg.	0.421 m

The experimental results were obtained in the NACA variable density subsonic wind tunnel, for an airspeed of 65 m/s and a Reynolds number equal to 4×10^6, as calculated with the

mean aerodynamic chord value. For the numerical calculations, a mesh of 18 chordwise panels and 35 spanwise panels per wing semi-span was used. The solution of the nonlinear system was obtained with a convergence criterion of 10^{-3} imposed for the maximum residual value. For low values of the angle of attack, the solution procedure required no under-relaxation, but for the flight conditions close to stall, an under-relaxation factor of 0.75 was used to assure the convergence of the solution.

In Figures 7.8 to 7.10, the results expressed in terms of wing lift coefficient, drag coefficient and quarter chord pitching moment coefficient are compared with the experimental data. The calculations are performed with both the well-known XFLR5 code and the new proposed non-linear coupled algorithm.

The nonlinear VLM code produces an accurate estimation of the viscous lift coefficient slope, and it slightly overestimates the stall angle (16 degrees in the numerical results versus 14.8 degrees in the experiment) and the maximum lift coefficient value (1.425 in the numerical results versus 1.340 in the experiment). With XFLR5's viscous lifting line model, a very good estimation of the lift curve slope is obtained, but the maximum C_L value and the stall angle are significantly over-estimated.

The drag coefficient estimation is very accurate for the lift coefficient range below 0.6, after which the numerical code tends to underestimate the drag coefficient values, but it still captures the steep increase associated with stall progression over the wing surface. XFLR5's drag prediction accuracy is equally good, except for the very high lift conditions, where the over-predicted stall angle results in under-predicted drag coefficient values.

Concerning the pitching moment coefficient, the numerical nonlinear VLM results are in closer agreement with the experimental ones, capturing both the linear variation and predicting the nonlinear behaviour characteristic of the higher angles of attack cases. An underestimation of the pitching moment value can be observed for the higher lift coefficient conditions, but the quality of the results is good.

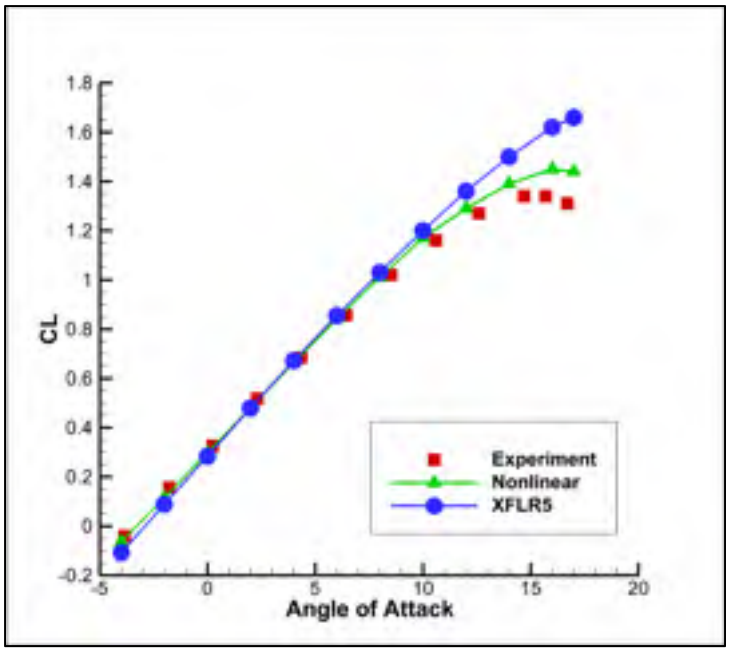

Figure 7.8 Numerical versus experimental lift coefficient variation with the angle of attack for the NACA TN 1270 wing

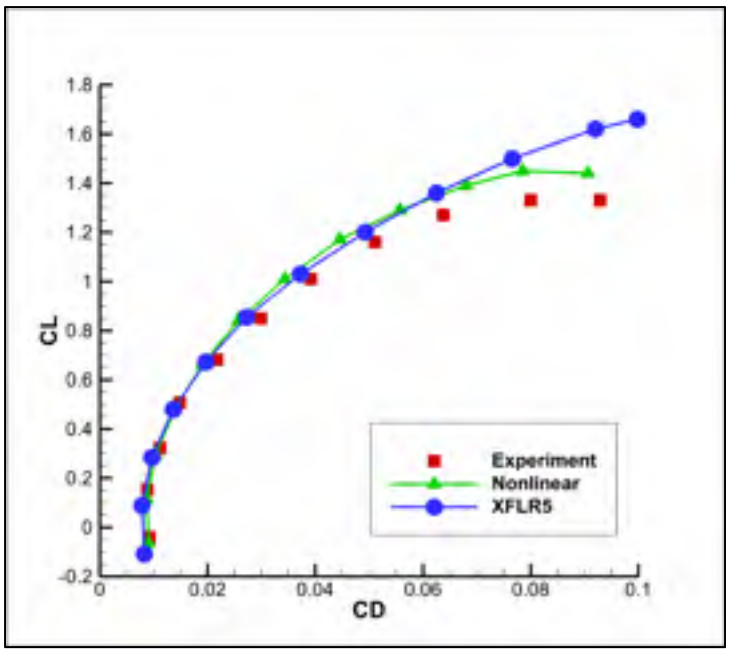

Figure 7.9 Numerical versus experimental drag coefficient variation with the lift coefficient for the NACA TN 1270 wing

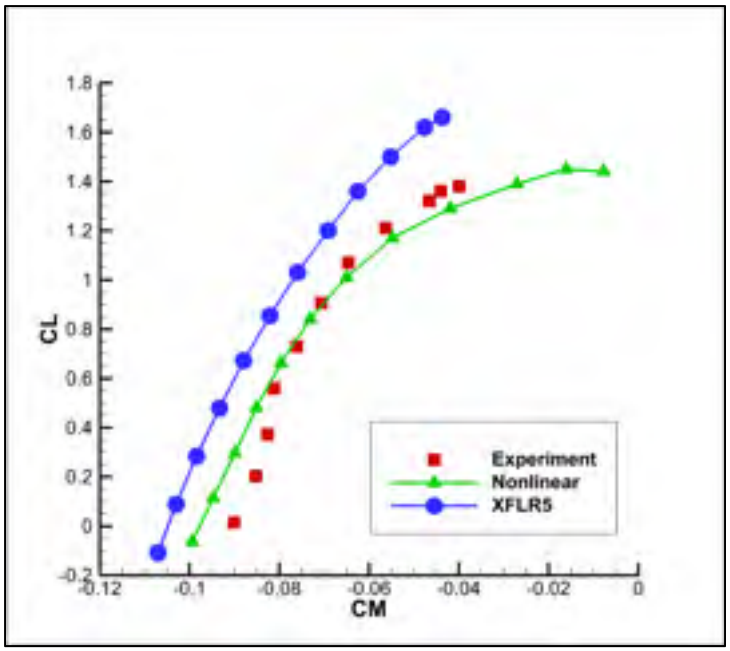

Figure 7.10 Numerical versus experimental pitching moment coefficient variation with the lift coefficient for the NACA TN 1270 wing

The second validation test performed using the nonlinear VLM was done using geometrical and experimental data taken from the NACA Technical Note 1208 (Schneider, 1951). The wing geometry features a high aspect ratio and a high sweep back angle. The model is constructed using a NACA 6-series airfoil section constant along the wingspan. The geometrical characteristics of the test wing are presented in Table 7.6.

Table 7.6 Geometric characteristics of the NACA TN 1208 test wing

Aspect Ratio	Span	Root Chord	Taper Ratio	Sweep angle	Area	MAC
8	3.23 m	0.5573 m	0.45	45 deg.	1.305 m^2	0.421 m

As for the previous validation case, the experimental results were obtained in the NACA variable density subsonic wind tunnel, for an airspeed of 65 m/s and a Reynolds number of 4×10^6. The numerical results were obtained using a mesh of 18 chordwise panels and 35

spanwise panels per wing semi-span and the convergence criterion of 10^{-3} imposed for the maximum residual value.

In Figures 7.11 and 7.12, the results for the wing lift coefficient and quarter chord pitching moment coefficient are compared with the experimental data. Drag coefficient data was not provided in the reference to allow for a comparison.

The viscous lift coefficient slope predicted by the nonlinear VLM is slightly higher than the experimental value, with a lift overestimation for angles of attack higher than 10 degrees. There is an underestimation of the stall angle (21 degrees for the experiment, versus 19.5 degrees in the numerical results), but a very good agreement exists for the maximum lift coefficient (1.01 for the experiment, versus 1.04 in the numerical results). XFLR5 accurately predicts the lift curve slope, but it slightly overestimates the lift values for the entire analysis range. Results could not be obtained for angles of attack higher than 18 degrees due to convergence problems, but again the maximum C_L value is not accurately predicted.

The linear variation of the pitching moment coefficient is very well captured, but there are some differences for the nonlinear higher lift conditions, where the swept back wing experiences an early tip stall phenomenon. As this behaviour is difficult to accurately capture, it is responsible for the numerical over-prediction of both pitching moment and lift coefficients. However, there is an important quality improvement over the XFLR5 code, especially concerning the high angle of attack characteristics of the high-sweep wing.

In addition to the lift and pitching moment coefficients' variations and their numerical versus experimental comparisons, the span-wise wing loading is validated with the wind tunnel experimental data (Schneider, 1951). The comparison is performed at an angle of attack of 4.7 degrees and is presented in Figure 7.13.

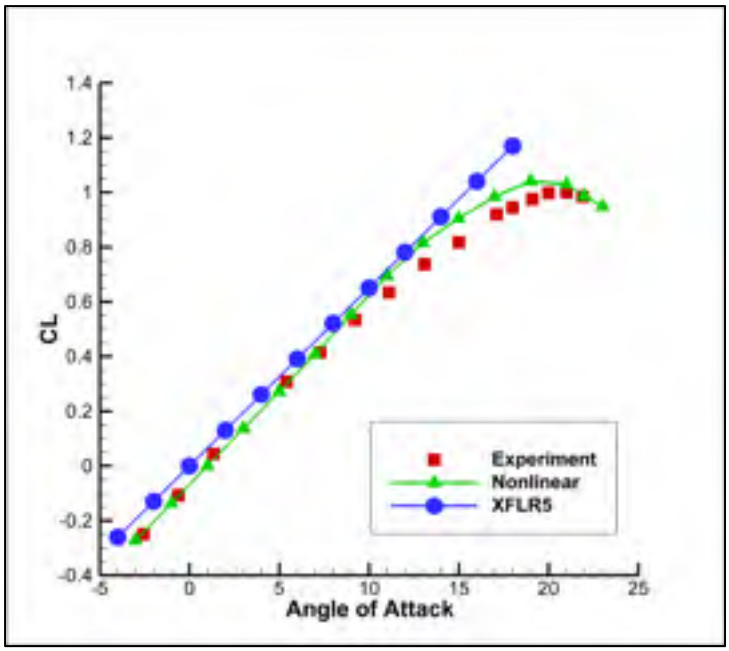

Figure 7.11 Numerical versus experimental lift coefficient variation with the angle of attack for the NACA TN 1208 wing

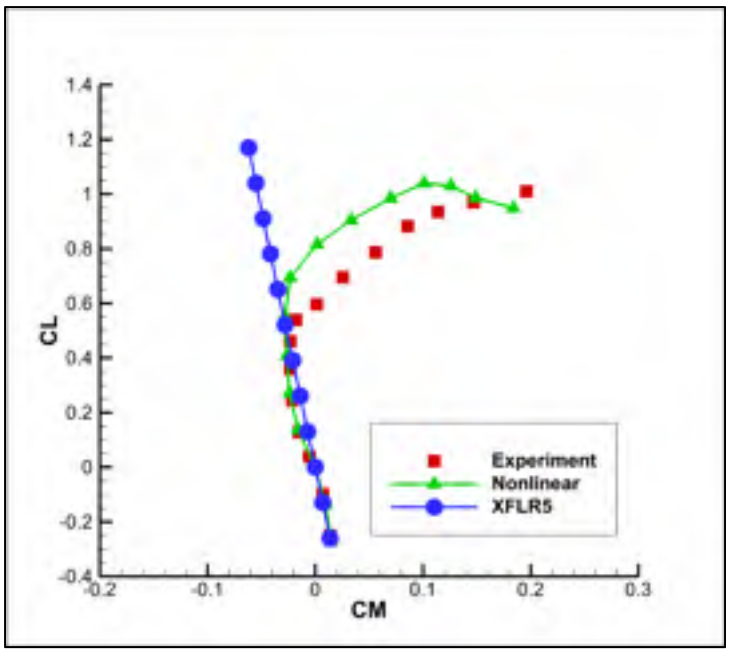

Figure 7.12 Numerical versus experimental pitching moment coefficient variation with the lift coefficient for the NACA TN 1208 wing

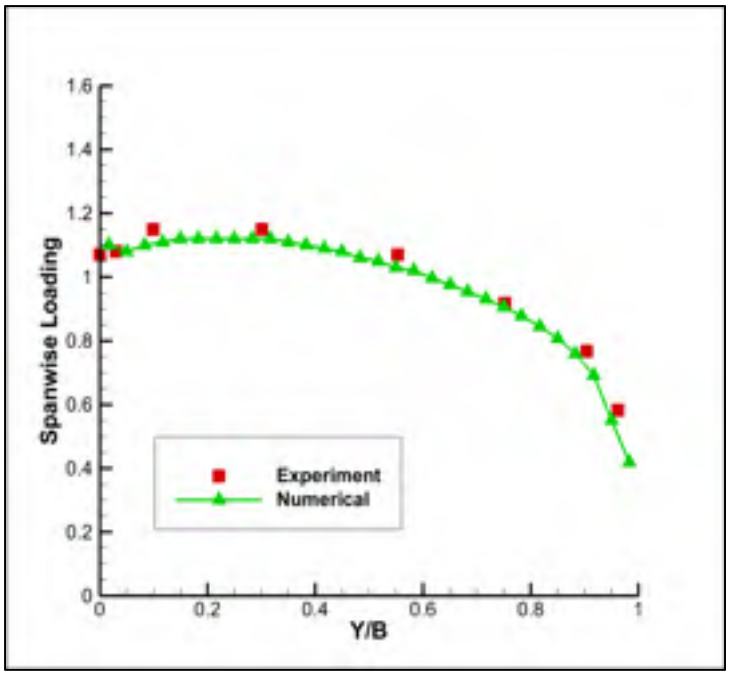

Figure 7.13 Comparison of span-wise loading for the NACA TN 1208 wing at 4.7 degrees angle of attack

The third viscous flow validation test performed using the nonlinear VLM is done using geometrical and experimental data taken from the NACA Research Memorandum L50F16 (Cahill and Gottlieb, 1950). The wing geometry chosen is a very low aspect ratio shape with high sweep angle. This wing is constructed using the NACA 65A006 airfoil. Table 7.7 presents details on the geometry of the test wing model.

Table 7.7 Geometric characteristics of the NACA RM L50F16 test wing

Aspect Ratio	Span	Root Chord	Taper Ratio	Sweep angle	Area	MAC
2	0.65 m	0.4066 m	0.60	45 deg.	0.211 m^2	0.332 m

The experimental results were obtained in the NACA variable density subsonic wind tunnel, for an airspeed of 35 m/s and a Reynolds number equal to 6×10^6, as calculated with the mean aerodynamic chord value. For the numerical calculations, a mesh of 18 chordwise panels and 35 spanwise panels per wing semi-span was used. The solution of the nonlinear

system was obtained with a convergence criterion of 10^{-2} imposed for the maximum residual value. For low values of the angle of attack, the solution procedure required no under-relaxation, but for the flight conditions close to stall, an under-relaxation factor of 0.75 was used to assure the convergence of the solution.

In Figures 7.14 to 7.16, the wing lift coefficient, drag coefficient and quarter chord pitching moment coefficient obtained numerically with the new proposed non-linear VLM and the XFLR5 code are compared with the experimental data.

A very good prediction of the lift coefficient exists for angles of attack smaller than 10 degrees. When the angle of attack increases above this value, the lift values predicted by the nonlinear code are smaller than the experimental ones. XFLR5 obtains a slightly better estimation of the lift coefficient for angles of attack higher than 10 degrees, but an under-prediction still exists. Both numerical codes cannot obtain converged results for angles of attack higher than 20 degrees, and thus the maximum lift coefficient and the stall angle are not captured in these numerical results.

Concerning the drag coefficient estimation, there is a very good match between the nonlinear VLM results and the experimental data, especially for lift coefficient values smaller than 0.4, but the overall quality of the numerical results remains good for the entire analysis range. XFLR5's drag prediction accuracy is equally good for the lower lift range, and an under-estimation is observed for lift coefficient values higher than 0.4.

For the rest of the analysis range, the non-linear moment variation is captured by the numerical results, but the predicted values are much smaller than the experimental measurements. The XFLR5 results are also good for C_L smaller than 0.3, but the moment variation remains linear for the entire range, a behaviour characteristic to the classic VLM models.

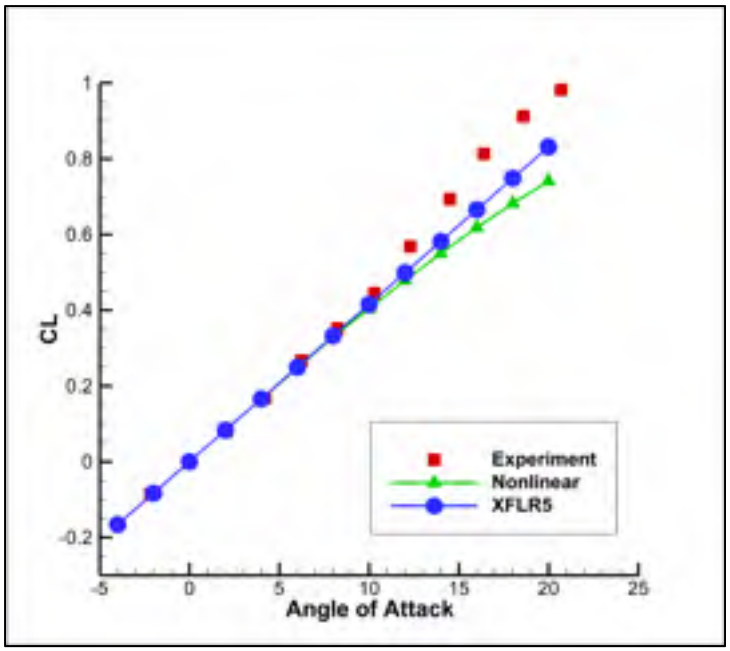

Figure 7.14 Numerical versus experimental lift coefficient variation with the angle of attack for the NACA RM L50F16 wing

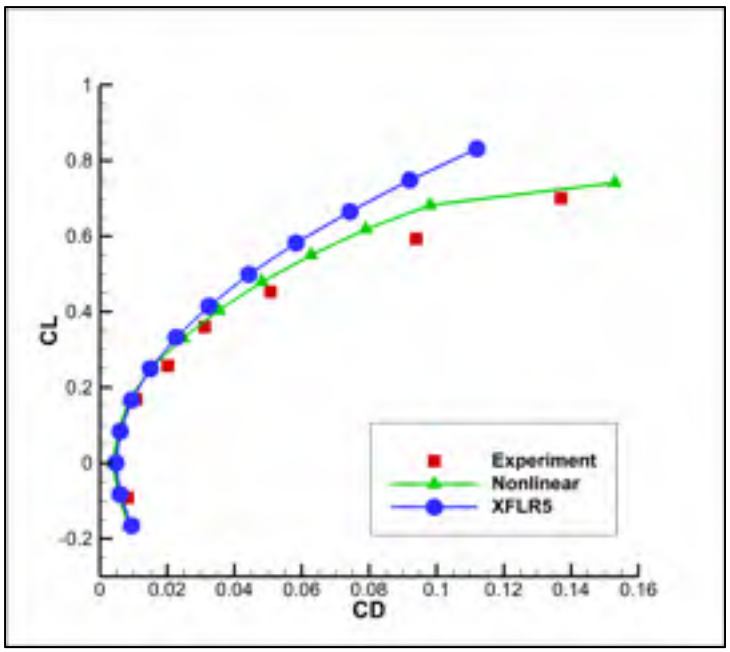

Figure 7.15 Numerical versus experimental drag coefficient variation with the lift coefficient for the NACA RM L50F16 wing

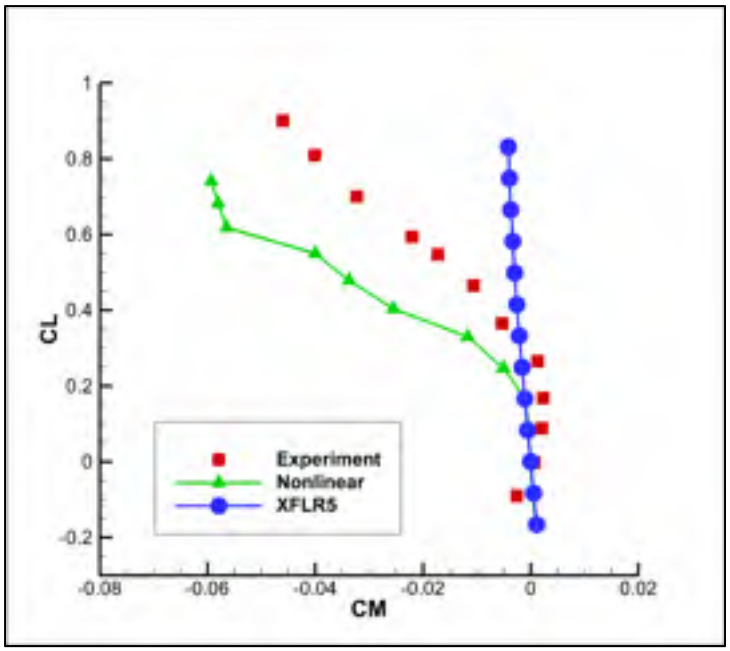

Figure 7.16 Numerical versus experimental pitching moment coefficient variation with the lift coefficient for the NACA RM L50F16 wing

For all the validation results presented, the strip airfoil aerodynamic characteristics were calculated during the program execution with the XFOIL solver. It must be noted that the quality of the three-dimensional results is significantly influenced by the quality of the two-dimensional airfoil calculations, due to the very strong coupling between them, coupling that constitutes the base for constructing the non-linear mathematical model. This observation is especially true for the higher angles of attack, where the XFOIL solver precision is significantly influenced by the airfoil characteristics (camber distribution, thickness values) and by the Reynolds number value.

The use of a two-dimensional flow solver was preferred to the use of experimentally determined airfoil performance databases because of the plan to utilize the code to perform wing optimizations and morphing wing analysis that would also include modifications of the airfoil shape.

7.4 Application to Wing Design and Optimization

7.4.1 Redesign of the Hydra Technologies S4 UAS wing

The nonlinear Vortex Lattice Method described above could be used in the early design phases of subsonic aircraft lifting surfaces, as it provides sufficiently accurate estimations of viscous aerodynamic characteristics for only a fraction of the computational requirements needed to perform a three-dimensional CFD calculation. On a typical desktop workstation, the execution time of the code is only around 1% of the equivalent CFD solution time. When the strip airfoil analyses are performed during execution, then a much greater amount of time is devoted to that task than the amount of time needed to calculate the Jacobian matrix and solve the linear system. Thus, the calculation times can be significantly further reduced by performing the strip calculations in parallel mode, or by using airfoil experimental performance databases instead of running the two-dimensional solver.

In addition to its application to wing design, the method could also be integrated in optimization routines aimed at improving one or several of a wing's geometrical characteristics and aerodynamic coefficients, since the rapid execution time compensates for the high number of evaluations usually associated with optimization procedures.

A redesign of the Hydra Technologies S4 Unmanned Aerial System (UAS) wing was performed using the nonlinear VLM solver coupled with an optimization routine based on the Artificial Bee Colony algorithm. This UAS was designed and build in Mexico, and serves as an aerial surveillance system, for both military and civilian missions. The geometrical characteristics of the UAS-S4 wing are presented in Table 7.8.

Table 7.8 Geometrical characteristics of the UAS-S4 wing

Aspect Ratio	Span	Root Chord	Taper Ratio	Sweep angle	Area	MAC
7.61	4.20 m	0.705 m	0.56	8.35 deg.	2.307 m^2	0.55 m

The wing redesign was performed by means of an optimization aimed at improving the wing lift-to-drag ratio L/D over a rage of angle of attack values. The optimization procedure was focused only on aerodynamic performance, and so no structural or weight aspects were considered. The analyses were performed at an airspeed of 50 m/s, with a Reynolds number of 2.13×10^6, as calculated with the mean aerodynamic chord.

The wing shape modification was performed by specifying the wing span, taper ratio and sweep angle as optimization variables. In addition to a redesign focused only on the geometrical parameters changes, a modification of the wing airfoil was also performed in a second optimization procedure. The airfoil curve was parameterized using Non-Uniform Rational B-Splines (NURBS), and the coordinates of four NURBS control points situated on the airfoil upper surface were added to the optimization variables. Other possible techniques are the CIRCLE method (Korakianitis et al., 2012) or the radial basis function method (Fincham and Friswell, 2015). The airfoil shape change could be achieved by the upper skin morphing concept detailed in (Sugar Gabor et al., 2014), (Sugar Gabor, 2013), (Sugar Gabor, 2014).

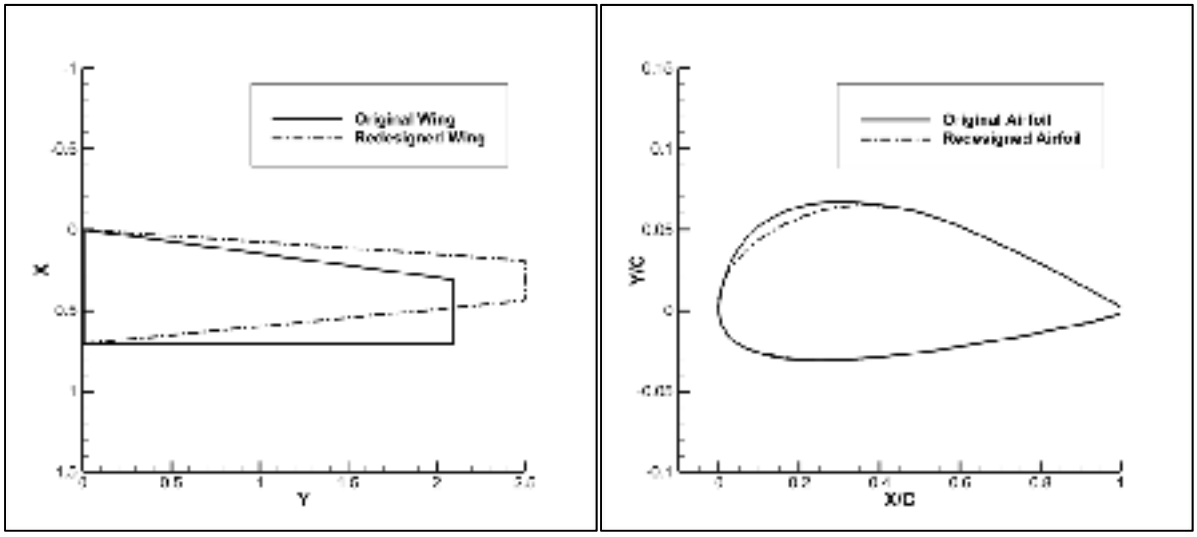

Figure 7.17 Comparison between the original and the redesigned wing and airfoil shapes

Figure 7.17 presents a comparison between the original and redesigned wing shapes, as well as between the original and redesigned airfoil. In Table 7.9, the detailed values of the aerodynamic coefficients for the original wing, the redesigned wing with shape modification and the redesigned wing with both shape and airfoil modifications are presented.

In Figure 7.18, a comparison is presented between the lift coefficient C_L variations with the angle of attack, the drag coefficients variations with the lift coefficient (the total drag coefficient C_D, the induced drag coefficient C_{DI} and the profile drag coefficient C_{D0}) for the original wing, the optimized wing with redesigned geometrical shape and the optimized wing with redesigned geometrical shape and airfoil.

As expected, the higher aspect ratio, lower sweep redesigned wing provides a higher lift coefficient than the original design at any given angle of attack value in the chosen design range. Concerning the induced drag, significant reductions were obtained, with an average reduction value of 20%. The wing with the redesigned geometry develops higher profile drag coefficient values compared to the baseline wing, the increase being as high as 6% for the 4 deg. angle of attack flight condition. However, this performance loss observed in the profile drag variation does not cancel out the improvements gained in induced drag. Thus, the redesigned wing generates a smaller total drag coefficient for the entire design range, with drag reductions of up to 10%, allowing to obtain a higher lift-to-drag ratio and therefore a higher aerodynamic efficiency for the UAS-S4 during surveillance flights.

The second optimization procedure, in which the baseline airfoil was also modified in addition to the wing plan-form shape, was performed with the goal of eliminating the profile drag increase that was observed in the first redesign procedure. Because of the fact that the wing profile drag represents the spanwise integration of the 2D drag generated by the wing cross-sections, its value could be modified by changing the wing airfoil shape.

Table 7.9 Comparison of aerodynamic coefficients generated by the UAS-S4 original and two redesigned wings, for all of the analysed flight conditions

Angle of Attack	Coefficient	Original	Redesigned (wing shape change)	Variation (wing shape change) [%]	Redesigned (wing and airfoil shape change)	Variation (wing and airfoil shape change) [%]
-2	C_L	-5.48E-03	-5.53E-03	0.91	-6.97E-04	-87.30
	C_D	6.71E-03	6.78E-03	1.16	6.69E-03	-0.25
	C_{DI}	2.00E-06	1.45E-06	-27.62	5.88E-07	-70.59
	C_{D0}	6.71E-03	6.78E-03	1.17	6.69E-03	-0.23
-1	C_L	7.58E-02	8.03E-02	5.94	8.32E-02	9.75
	C_D	6.23E-03	6.18E-03	-0.78	5.96E-03	-4.44
	C_{DI}	2.34E-04	1.88E-04	-19.76	2.03E-04	-13.38
	C_{D0}	6.00E-03	6.00E-03	-0.04	5.75E-03	-4.09
0	C_L	1.56E-01	1.65E-01	5.56	1.68E-01	7.28
	C_D	6.42E-03	6.12E-03	-4.67	5.82E-03	-9.27
	C_{DI}	1.01E-03	8.01E-04	-20.66	8.28E-04	-18.05
	C_{D0}	5.41E-03	5.32E-03	-1.68	5.00E-03	-7.62
1	C_L	2.36E-01	2.49E-01	5.79	2.53E-01	7.42
	C_D	7.08E-03	6.67E-03	-5.80	6.47E-03	-8.58
	C_{DI}	2.29E-03	1.83E-03	-19.99	1.89E-03	-17.55
	C_{D0}	4.78E-03	4.83E-03	1.01	4.58E-03	-4.28
2	C_L	3.14E-01	3.43E-01	9.31	3.48E-01	10.93
	C_D	8.97E-03	8.65E-03	-3.67	8.29E-03	-7.63
	C_{DI}	4.06E-03	3.47E-03	-14.43	3.57E-03	-11.97
	C_{D0}	4.92E-03	5.17E-03	5.21	4.72E-03	-4.05
3	C_L	4.10E-01	4.35E-01	6.23	4.38E-01	6.98
	C_D	1.23E-02	1.12E-02	-8.54	1.09E-02	-11.28
	C_{DI}	6.90E-03	5.57E-03	-19.34	5.66E-03	-18.00
	C_{D0}	5.37E-03	5.66E-03	5.35	5.23E-03	-2.65
4	C_L	4.96E-01	5.24E-01	5.74	5.30E-01	6.89
	C_D	1.60E-02	1.43E-02	-10.62	1.41E-02	-11.68
	C_{DI}	1.01E-02	8.06E-03	-20.27	8.26E-03	-18.35
	C_{D0}	5.89E-03	6.24E-03	5.95	5.88E-03	-0.21

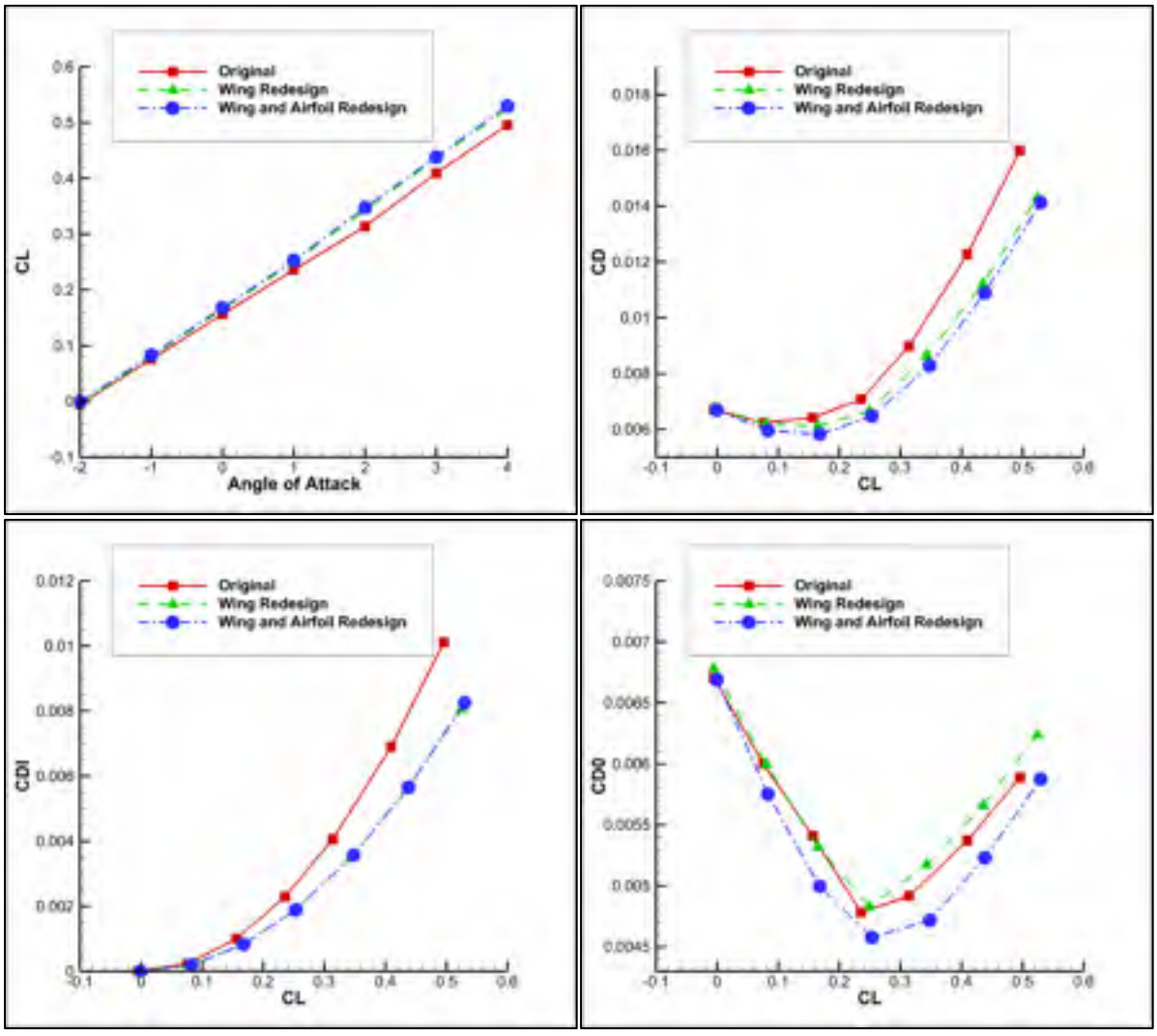

Figure 7.18 Comparison between the lift and drag coefficients for the original and redesigned wings

The obtained results show that the optimized wing airfoil shape provides a better performance in terms of profile drag, with the maximum reduction of 7.62% over the baseline design being obtained for an angle of attack of 0 deg. This reduction becomes smaller as the angle of attack increases or decreases. However, after the comparison of the profile drag coefficient values calculated for the two redesigned wings (the wing with only geometrical change and the wing with both geometrical change and airfoil optimization), it can be observed that profile drag increase mentioned above was effectively eliminated. Thus, by modifying the wing airfoil in addition to its plan-form shape, further drag coefficient reductions between 1% and 4.5% were obtained.

7.4.2 Analysis of the CRIAQ MDO 505 project morphing wing

The wing model used in the MDO 505 project has been designed to be representative of a real regional aircraft wing tip, and thus all its dimensions were designed according to this objective. The geometrical characteristics of the wing model are presented in Table 7.9. The wing model was equipped with a flexible upper surface whose shape can be modified, as function of the flight condition, using four electrical actuators placed inside the wing box and arranged in two spanwise actuation lines. The flexible skin extends between 20% and 65% of the wing chord, over the entire span of the model.

Table 7.10 Geometric characteristics of the CRIAQ MDO 505 wing

Aspect Ratio	Span	Root Chord	Taper Ratio	Sweep angle	Area	MAC
2.62	1.5 m	1.5 m	0.72	8 deg.	1.935 m^2	1.33 m

Aerodynamic optimizations were performed to determine the displacements of the electrical actuators required to improve the performance of the morphing wing with reference to the original wing. The optimizations were performed with the objective of delaying the laminar-to-turbulent transition location on the upper surface, and thus to achieve drag coefficient reductions through the reduction of the wall friction stress.

In order to reduce the execution computing times as much as possible, the aerodynamic optimizations were performed under the two-dimensional flow assumption using XFOIL and a genetic algorithm optimizer, but for the local flow conditions (Reynolds number, effective angle of attack) corresponding to the mean aerodynamic chord of the model (Koreanschi, 2014).

The two-dimensional optimization provided good results, because of the fact that upper surface transition location delay of up to 4% of the chord and airfoil drag coefficient reductions of up to 4% were obtained. It must be noted that the aerodynamic optimization procedure was performed under all constraints imposed by the actual behaviour of the model structure and by the technical limitations of the flexible composite-material upper skin.

To verify the impact of the two-dimensional optimizations on the overall three-dimensional wing model performance, the morphing wing geometry was analysed in 3D using the non-linear VLM model. A total of nine flight conditions were considered, all of them at a Mach number of 0.15 and a flow Reynolds number of 4.57×10^6. For each case, the geometry of the wing was constructed using the original airfoil for the root and tip sections, and the corresponding morphed airfoil shapes for the two spanwise sections where the electrical actuators were placed.

Table 7.11 presents the values of the aerodynamic coefficients for the original wing and for the morphed wing. Reductions of the profile drag coefficient of up to 3% were obtained by morphing the wing upper surface, thus verifying the accuracy of the two-dimensional optimizations. Compared to the baseline design, the optimized wing generates lift coefficient values smaller with 0.10%-0.30%, but it also achieves a reduction of the induced drag coefficient, the reduction percentage being between 0.60% and 3%. The total drag coefficient reductions obtained by the morphing wing compared to the original design are between 0.70% and 3%.

Table 7.11 Comparison of aerodynamic coefficients generated by the MDO 505 project original and morphed wings, for all of the analysed flight conditions

Angle of Attack	Coefficient	Original	Morphing	Variation [%]
-0.50	C_L	1.34E-01	1.33E-01	-0.34
	C_D	9.66E-03	9.37E-03	-2.98
	C_{DI}	3.83E-03	3.71E-03	-3.07
	C_{D0}	5.83E-03	5.66E-03	-2.92
-0.25	C_L	1.48E-01	1.48E-01	-0.14
	C_D	9.45E-03	9.20E-03	-2.60
	C_{DI}	3.66E-03	3.58E-03	-2.15
	C_{D0}	5.79E-03	5.63E-03	-2.88
0	C_L	1.62E-01	1.61E-01	-0.33
	C_D	9.42E-03	9.14E-03	-2.98
	C_{DI}	3.64E-03	3.54E-03	-2.98
	C_{D0}	5.77E-03	5.60E-03	-2.98
0.25	C_L	1.75E-01	1.75E-01	-0.16
	C_D	9.52E-03	9.26E-03	-2.73
	C_{DI}	3.76E-03	3.67E-03	-2.48
	C_{D0}	5.76E-03	5.59E-03	-2.89
0.50	C_L	1.88E-01	1.88E-01	-0.08
	C_D	9.71E-03	9.46E-03	-2.59
	C_{DI}	3.97E-03	3.88E-03	-2.30
	C_{D0}	5.73E-03	5.57E-03	-2.80
0.75	C_L	2.02E-01	2.02E-01	-0.01
	C_D	9.97E-03	9.75E-03	-2.18
	C_{DI}	4.29E-03	4.22E-03	-1.71
	C_{D0}	5.68E-03	5.53E-03	-2.55
1	C_L	2.16E-01	2.16E-01	-0.09
	C_D	1.04E-02	1.02E-02	-2.00
	C_{DI}	4.75E-03	4.67E-03	-1.59
	C_{D0}	5.61E-03	5.48E-03	-2.35

Angle of Attack	Coefficient	Original	Morphing	Variation [%]
1.25	C_L	2.30E-01	2.30E-01	-0.10
	C_D	1.08E-02	1.07E-02	-1.53
	C_{DI}	5.32E-03	5.26E-03	-1.17
	C_{D0}	5.53E-03	5.42E-03	-1.88
1.50	C_L	2.44E-01	2.44E-01	-0.15
	C_D	1.15E-02	1.14E-02	-0.71
	C_{DI}	6.02E-03	5.98E-03	-0.63
	C_{D0}	5.46E-03	5.41E-03	-0.79

Due to its very low aspect ratio, the wing model gives a poor performance concerning the induced drag, whose contribution to the total drag is higher than for a regular, high aspect ratio transport aircraft wing. Because of the fact that the upper skin morphing concept was designed to reduce the friction drag coefficient by delaying the laminar-to-turbulent transition location, its efficiency is reduced when applied to a low aspect ratio wing. However, for a typical wing of high aspect ratio, such as the UAS-S4 wing analysed in the previous section, the flexible upper skin could prove to be effective in providing significant total drag reductions.

In Figure 7.19, a comparison is presented between the lift coefficient C_L variations with the angle of attack, the drag coefficients variations with the lift coefficient (the total drag coefficient C_D, the induced drag coefficient C_{DI} and the profile drag coefficient C_{D0}) for the original and morphed wings.

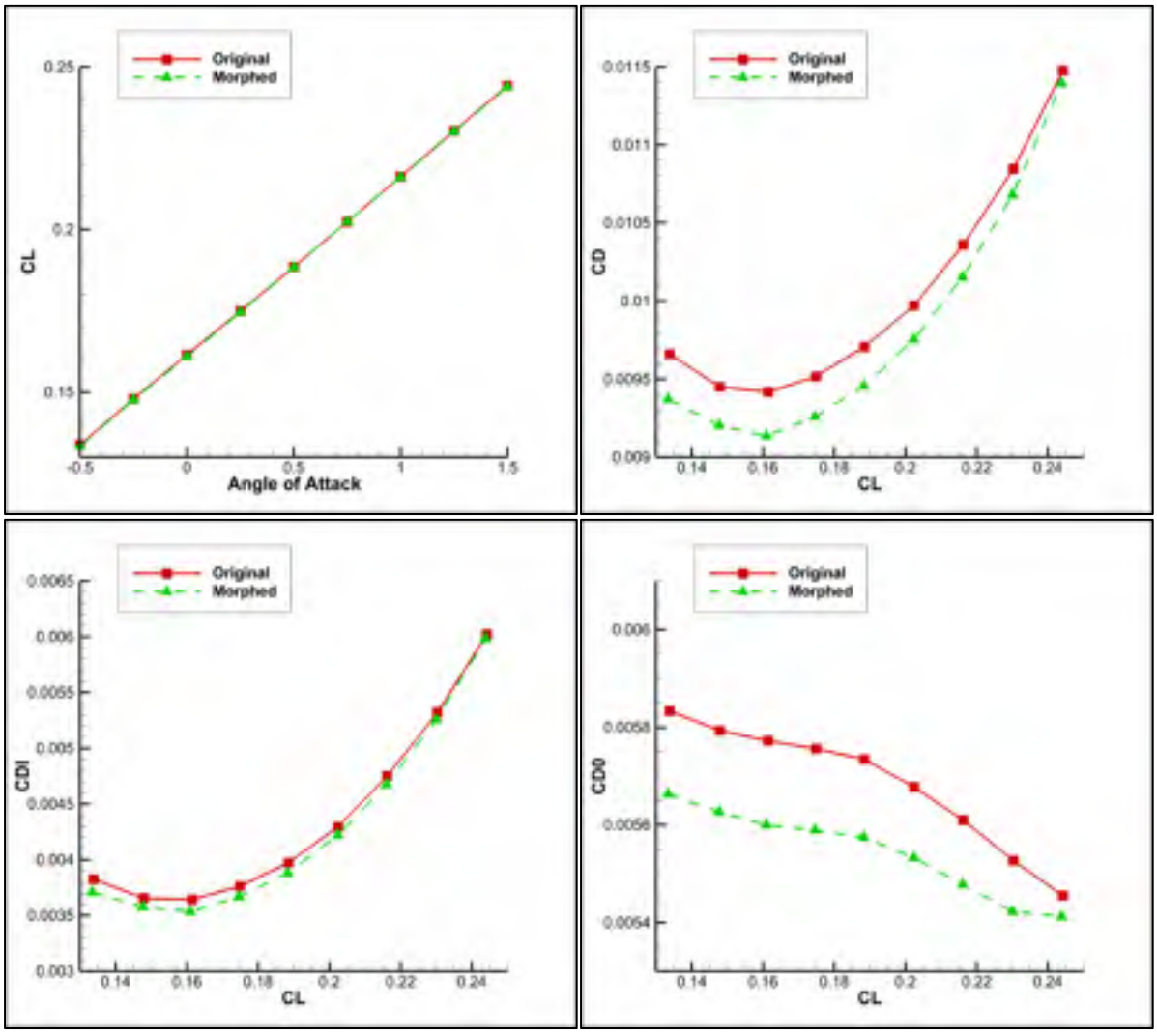

Figure 7.19 Comparison between the lift and drag coefficients for the original and morphed wings

7.5 Conclusions

The starting point for the non-linear VLM equations was the inviscid non-planar formulation of the classical VLM. The intensities of the vortex rings were modified by the introduction of a correction term. Viscous aerodynamic forces were calculated by analysing the wing strips with a two-dimensional flow solver and by interpolating the results on the wing surface mesh. The non-linear equations allowing the calculation of the correction terms were constructed by making the inviscid pressure coefficient difference equal to the determined viscous pressure coefficient difference, and then the non-linear system was solved using Newton's classic method.

Convergence studies were performed on several different test wings and have shown that the non-linear VLM method required a sufficiently refined mesh in order to achieve mesh-independent results. Validations of the obtained results were performed using wing performance experimental data available in the literature. Good results were obtained in the estimation of the aerodynamic coefficients for both low and high sweep wings. Lift coefficient and pitching moment coefficient curve derivatives were very well predicted, as well as an accurate estimation of the drag coefficient. The results could be improved further by using experimental performance databases for the strip airfoil calculations, as there is a strong coupling with the quality of the two-dimensional calculations.

The non-linear VLM method was applied for a classic wing redesign problem on the Hydra Technologies S4 UAS. For flight conditions typical of cruise and surveillance flights, the lower sweep and higher aspect ratio wing obtained following the optimization provided better lift to drag ratios, as expected. A second optimization was performed, in which the wing airfoil shape was added to the optimization variables. Very good results were obtained, with further drag reductions of up to 5% obtained over the simple redesigned wing.

Another application of the code was the calculation of the aerodynamic performance gains obtained through upper surface morphing for a low aspect ratio wing model based on the

wing tip of a real regional aircraft. The optimizations were performed in two-dimensions and took into consideration all the constraints imposed by the structure. The morphing wing has the potential to reduce the viscous drag coefficient by up to 3% over the baseline design.

Acknowledgments

We would like to thank the Hydra Technologies Team in Mexico for their continuous support, and especially Mr. Carlos Ruiz, Mr. Eduardo Yakin and Mr. Alvaro Gutierrez Prado. We would also like to thank to the Natural Sciences and Engineering Research Council of Canada (NSERC) for the funding of the Canada Research Chair in Aircraft Modeling and Simulation Technologies. In addition we would like to thank to the Canada Foundation of Innovation (CFI), to the Ministère du Développement économique, de l'Innovation et de l'Exportation (MDEIE) and to Hydra Technologies for the acquisition of the UAS-S4 using the Leaders Opportunity Funds.

We would like to indicate our appreciation for the financial support obtained in the framework of the CRIAQ MDO-505 project and for the implication of our industrial partners Bombardier Aerospace and Thales Canada. We also wish to thank NSERC for their support. Special thanks are dues to our collaborators and leaders in this project: Mr. Patrick Germain and Mr. Fassi Kafyeke from Bombardier Aerospace, Mr. Philippe Molaret from Thalès Canada and Mr. Eric Laurendeau from École Polytechnique.

CHAPTER 8

NUMERICAL SIMULATION AND WIND TUNNEL TESTS INVESTIGATION AND VALIDATION OF A MORPHING WING-TIP DEMONSTRATOR AERODYNAMIC PERFORMANCE

Oliviu Şugar Gabor, Andreea Koreanschi and Ruxandra Mihaela Botez
LARCASE Laboratory of Applied Reasearch in Active Controls,
Avionics and Aeroservoelasticity
École de Technologie Supérieure, 1100 rue Notre Dame Ouest,
Montréal, H3C1K3, Québec, Canada

Mahmoud Mamou and Youssef Mebarki
Aerodynamics Laboratory, NRC Aerospace
National Research Council Canada, Ottawa, K1A0R6, Ontario, Canada

This article was submitted to the *Aerospace Science and Technology*

Résumé

Cet article présente les résultats obtenus en utilisant des simulations numériques et des essais en soufflerie pour une aile déformable, équipée avec une surface supérieure flexible et un aileron contrôlable. Le démonstrateur technologique représente l'extrémité de l'aile d'un avion, et il a été conçu avec une peau supérieure réalisée en matériaux composites, dont la forme peut être modifiée en fonction de la condition de vol, par quatre actionneurs électriques placés à l'intérieur de la structure de l'aile. Les optimisations ont été effectuées pour contrôler la longueur de la zone d'écoulement laminaire, et les formes résultantes ont été analysées à l'aide de photogrammétrie haute précision. Les simulations numériques ont été réalisées à l'aide de la Dynamique Computationnelle des Fluides et ont inclus un modèle de prévision de la transition laminaire-turbulent sur la surface de l'aile. Les analyses portaient sur des cas avec des angles d'attaque situés dans un intervalle de cinq degrés et trois angles

de déflection pour l'aileron. Les résultats obtenus ont été comparés à la thermographie en infrarouge pour capturer la transition, des mesures de la pression et des mesures des forces prises lors des essais subsoniques en soufflerie effectués au Conseil National de Recherches du Canada.

Abstract

This paper presents the results obtained using numerical simulation and experimental wind tunnel testing for a morphing wing equipped with a flexible upper surface and controllable actuated aileron. The technology demonstrator was modeled after an aircraft wing tip section, and was fitted with a composite material upper skin whose shape can be modified, as function of the flight condition, by four electrical actuators placed inside the wing structure. The optimizations were performed with the aim of controlling the extent of the laminar flow region, and the resulting shapes were scanned using high-precision photogrammetry. The numerical simulations were performed using Computational Fluid Dynamics and included a model for predicting the laminar-to-turbulent transition over the entire wing surface. The analyses included cases with three aileron deflection angles and angles of attack situated within five degrees range. The obtained results were compared with Infra-Red thermography for transition prediction, pressure sensors measurements and force balance measurements taken during subsonic wind tunnel tests performed at the National Research Council Canada.

8.1 Introduction

The air transportation industry is one of the key areas that contribute to economic development around the world. Since the beginning of civil aviation, there has been a steady increase in the number of passengers using airplanes as a fast and safe transportation method, with airlines carried almost 3 billion passengers worldwide in 2014 alone. This high level of development that has been achieved has also transformed the air transport industry into a non-negligible source of pollution. It is estimated that in 2014, over 2% of the worldwide carbon dioxide emissions were caused by the commercial airline companies (ATAG, 2014).

The high growth rate experienced up to present day will accelerate over the next several decades. The International Civil Aviation Organization (ICAO) estimates that the number of flights will triple by the year 2050 (ICAO, 2010). This high growth rate, together with growing global concern for the preservation of the environment and the reduction of greenhouse gas emissions is forcing the aerospace industry to search for solutions to improve aircraft fuel burn efficiency.

One possibility of achieving this desired efficiency is through the new-generation technologies of morphing various aircraft lifting components, that can be activated and deformed according to the flight conditions, thus allowing a multi-point design of the aircraft and improving aerodynamics performance. A morphing wing could allow the aircraft to fly at optimal lift to drag ratios for any condition encountered during a flight, by changing some of the wing's characteristics according to the flow conditions. Researchers have proposed different technological solutions for obtaining the desired wing adaptability, and some concepts achieved important theoretical performance improvements compared to the baseline design. However, the technology is still in the early stages of development, its technological readiness level is still very low, and only a few concepts have sufficiently progressed to reach wind tunnel testing, and even fewer have actually been flight tested (Barbarino et al., 2011).

Wing morphing techniques can be classified into three major types: plan-form transformations (sweep angle, span and chord), out-of-plane transformations (twisting, dihedral and spanwise bending) and airfoil transformations (camber and thickness) (Barbarino et al., 2011). Morphing wings were used to adapt the wing span and airfoil camber (Gamboa et al., 2007), (do Vale et al., 2011) and the winglet's cant and toe angles (Falcao, 2011), to replace conventional high-lift devices, (Diodati et al., 2013), (Pecora et al., 2012), or even the conventional control surfaces (Pecora, 2012).

Lockheed Martin developed the Agile Hunter Unmanned Aerial Vehicle (UAV) (Bye and McClure, 2007), (Ivanco et al., 2007), (Love et al., 2007), capable of folding the inner region of the wing over the fuselage, in order to achieve drag reductions during transonic cruise at

lower altitudes. A morphing wind tunnel prototype was built and tested up to a Mach number of 0.60. The model demonstrated a successful and accurate actuation under aerodynamic loads, achieving the desired wing shape change in approximately one minute. An important project for the development of morphing wings was the NexGen Aeronautics MFX1 UAV, showing wing sweep and chord changes (Andersen, 2007), (Flanagan et al., 2007). The wing was based on a morphing truss structure that could be controlled using electrical actuators. A prototype of the UAV was built and successfully flight tested. The morphing wing sustained sweep angle variations of 20 degrees and area changes of 40% under aerodynamic loading, for flight speeds up to 100 knots.

A detailed computational and experimental analysis was performed by Smith et al. (2014) on the wing of a conventional aircraft equipped with two outboard morphing partitions capable of varying the twist and dihedral angles. The morphing system was capable of providing twist variations of up to 3 degrees, and dihedral variations of up to 90 degrees. Researchers from NASA Dryden Flight Research Center conducted several flight tests with a UAV equipped with inflatable wings whose span could be modified by adjusting the pressure input (Murray et al., 2002). The wings were made from several spanwise inflatable tubes, surrounded by sponge and a flexible nylon skin in order to maintain the airfoil shape during flight. A variable wing plan-form UAV was designed and tested by Neal et al. (2004). The system used pneumatic actuators to drive the telescopic and rotating wing, capable of achieving significant wing span and sweep angle changes. Wind tunnel tests were performed and showed that only three morphing wing configurations were needed to increase the significantly lift-to-drag ratio for the entire flight envelope of the UAV.

Pecora et al. (2011) demonstrated the effectiveness of replacing the conventional segmented flap with a morphing compliant high-lift device, in the case of a regional transport aircraft. Bilgen et al. (2007), (2009) also presented a concept of replacing the wing trailing edge devices with a morphing surface, capable of achieving continuous camber variations instead of rigid deflections. The morphing system was designed to replace the ailerons of a UAV, and thus used rapid, electrical actuation mechanisms. Both wind tunnel experiments and

preliminary flight test were performed, and demonstrated the effectiveness of the concept at providing accurate roll control. Pankonien and Inman (2015) presented a concept for morphing ailerons designed to replace the conventional wing control surfaces of a UAV. The aerodynamic performance of the system was evaluated using wing tunnel testing, with measurements focused on the drag coefficient penalty associated with classic control surface deflections at off-design flight conditions. The morphing trailing edge achieved drag reductions up to 20% compared to the original design, thus justifying its increased mass and complexity.

The CRIAQ 7.1 project, which took place between 2006 and 2009, was realized following a collaborative effort between teams from École de Technologie Supérieure, École Polytechnique de Montréal, Bombardier Aerospace, Thales Canada and the National Research Center Canada. The objective of the project was to improve and control the laminarity of the flow past a morphing wing in order to obtain substantial drag reductions (Botez, 2007).

In this project, the active structure of the morphing wing consisted of three main subsystems: a flexible, a composite material upper surface spanning between 3% and 70% of the airfoil chord, a rigid inner surface and a Shape Memory Alloy (SMA) actuator group located inside the wing box, which could morph the flexible skin in two actuation points, located respectively at 25.3% and 47.6% of the chord (Brailovski et al., 2008). The reference airfoil chosen for the project was the WTEA laminar airfoil and the morphing system was designed for low subsonic flow conditions. A theoretical study of the morphing wing system was performed (Pages, 2007), and very promising results were obtained: the morphing system was able to delay the transition location downstream by up to 30% of the chord, and to reduce the airfoil drag by up to 22%.

Two control approaches were used for providing the optimal SMA actuator displacements for each different flight condition. In the open loop configuration, the desired displacements were directly imposed on the system (Popov et al., 2010), while a novel, adaptive, neuro-

fuzzy approach was used to predict and control the morphing wing performance (Grigorie et al., 2009). In the closed loop configuration, the displacements were automatically determined as a function of the pressure readings from the wing upper surface (Popov et al., 2010). In addition, two new controllers were developed, the first based on an optimal combination of the bi-positional and Proportional-Integral (PI) laws (Grigorie et al., 2012), while the second was a hybrid fuzzy logic-PID controller (Grigorie et al., 2012). The wind tunnel tests were performed in the 2 m by 3 m atmospheric closed circuit subsonic wind tunnel at NRC and validated the numerical wing optimizations (Sainmonet et al., 2009) and the designed control techniques (Grigorie, 2012).

8.2 Description of the CRIAQ MDO 505 Project

8.2.1 Project information

The CRIAQ MDO 505 project is performed as a continuation of the CRIAQ 7.1 project adaptive upper-surface wing concept. In this project a real wing structure was considered and designed following structural and materials optimizations based on new aerodynamic optimization constraints and new morphing skin control challenges, using an electrical actuation system along with classical and adaptive ailerons.

The research presented in this paper was performed within the framework of the MDO 505 project, a multiple partners project involving an international collaboration between Canadian and Italian industries, universities and research centres (Bombardier Aerospace, Thales Canada and Alenia Aeronautica on the industry side, École de Technologie Supérieure, École Polytechnique de Montreal and the University of Naples on the academic side and the National Research Council Canada and the Italian Institute for Aerospace Research CIRA on the research centres side).

The purpose of the CRIAQ MDO 505 project is to demonstrate the structural, aerodynamic and control abilities of a wind tunnel wing model equipped with an adaptive upper surface

and both a rigid and an adaptive aileron, designed for low speed (subsonic) wind tunnel tests. The novelty of this project consists in the design, analysis and manufacturing of a wind tunnel model having the structural and aerodynamic properties of a real aircraft wing-tip. Figure 8.1 presents the position of the morphing upper skin on a typical aircraft wing, while Figure 8.2 presents the structural elements of the morphing wing model.

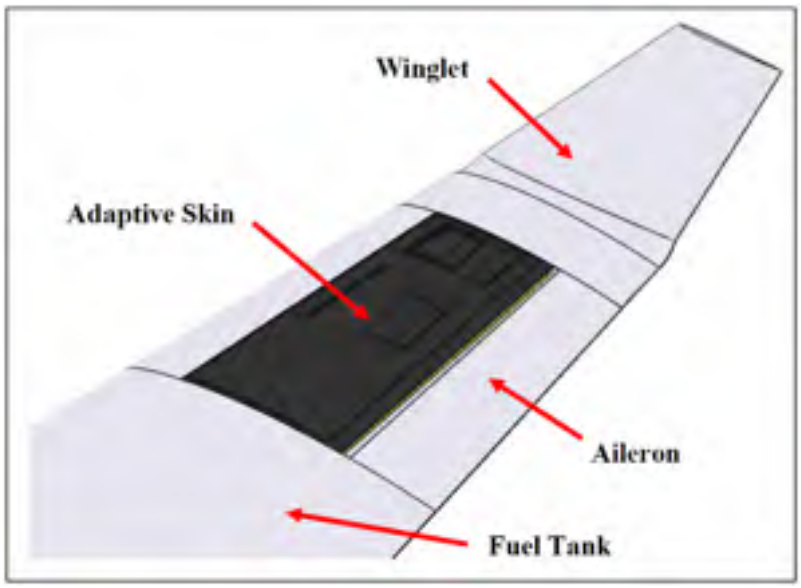

Figure 8.1 The position of the morphing skin on the aircraft wing

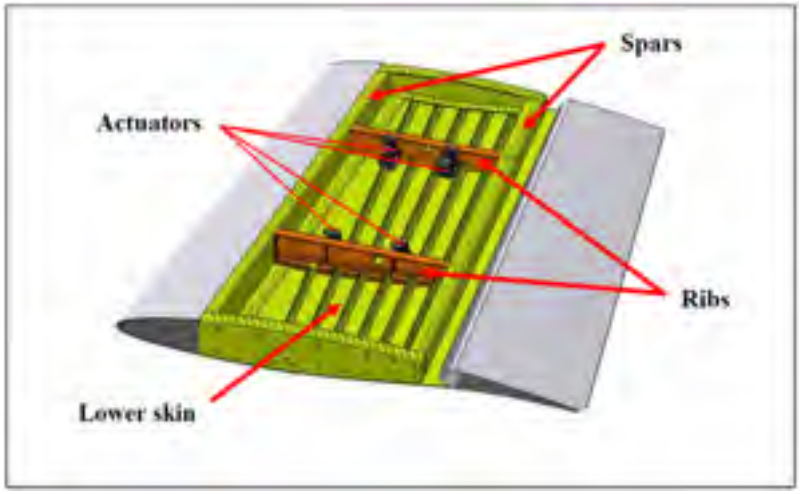

Figure 8.2 The structural elements of the CRIAQ MDO 505 morphing wing concept (the morphing skin is not shown in the figure)

8.2.2 General details about the morphing wing model

The full-scale morphing wing model is an optimized structure with a 1.5 m span and a 1.5 m root chord, a taper ratio of 0.72 and a leading and trailing edges sweep angle of 8°. The wing box and internal structure (spars, ribs, and lower skin) was manufactured from aluminum alloys, while the composite material adaptive upper surface was positioned between 20% and 65% of the wing chord. The adaptive upper surface skin was specifically designed and optimised for the project, using carbon fibre composite materials (Michaud, 2014).

The deformation of skin shape is a function of the flight condition (defined in terms of Mach number, Reynolds number and angle of attack) and is driven by actuators placed inside the wing box structure. These actuators were specifically designed and manufactured to meet the project requirements. Four electric actuators were installed on two actuation lines, two actuators each, placed at 37% and 75% of the wing span, fixed to the ribs and to the composite skin, and each actuator has the ability to operate independently from the others. On each line, the actuators were positioned at 32% and 48% of the local wing chord.

The aileron's articulation was located at 72% of the chord. Two ailerons were designed and manufactured. One aileron is structurally rigid, while the other one represents a new morphing aileron concept. Both ailerons were designed to be attached to the same hinge axis of the wing box (one at a time), and both are able to undergo a controlled deflection between -7 and +7 deg. Figure 8.3 presents a sketch of the morphing wing model concept as it would be mounted and tested in the NRC subsonic wind tunnel test section. Up to present day, only the classical, rigid aileron was installed and used during wind tunnel testing.

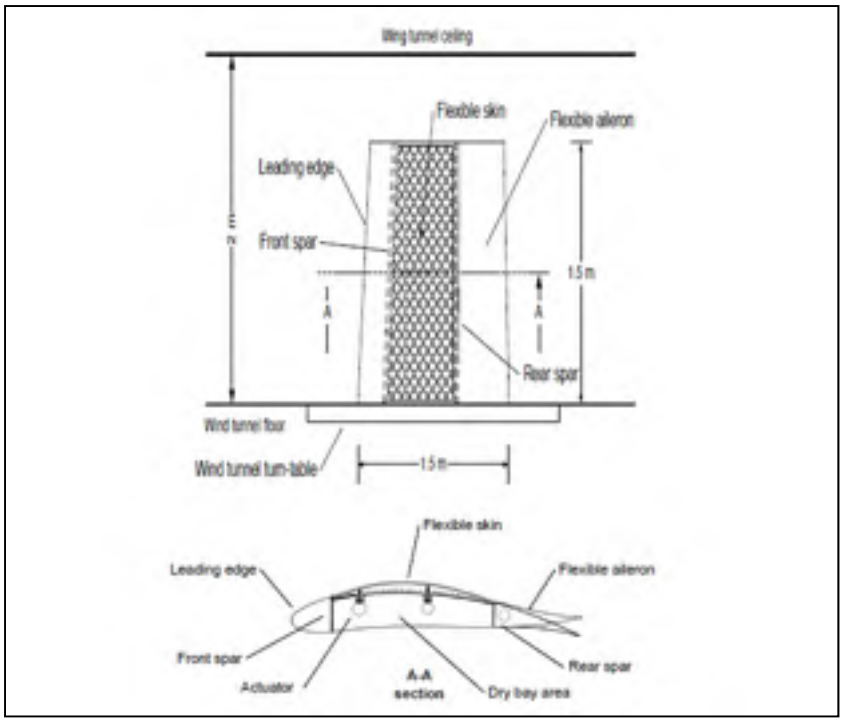

Figure 8.3 CRIAQ MDO 505 morphing wing concept

8.2.3 The structural design of the morphing wing model

Unlike the wing model developed for the previous CRIAQ 7.1 project, the MDO 505 morphing wing was designed to have a structural rigidity similar to a real aircraft wing, while the upper surface morphing skin was created not only to be an active structural element, rigidly fixed around its perimeter and able to withstand real flight loads, but in addition to permit the required aerodynamic shape changes and actuator displacements while remaining structurally loaded.

Two finite element models (FEM) were created for the design process: a simplified, general model (GFEM) that was used to numerically create and optimize the carbon fibre upper surface skin, and a detailed model (DFEM) that was used for the design and numerical analysis of the rigid structure (lower skin, spars, ribs, internal actuators). The aerodynamic loads used for dimensioning and calculating the structural elements of the morphing wing

model correspond to the limit load factors of +2.5g and -1g typical of civil transport aviation, multiplied by the ultimate security coefficient of 1.5.

The flexible skin design and optimization were performed while trying to match as close as possible the aerodynamically optimized upper surface shapes (Michaud, 2014). An error analysis performed for a number of optimized cases showed that the average shape error between the skin FEM and the spline target shapes was 0.25 mm, or 7% of the maximum actuator displacement. Given the multidisciplinary nature of the MDO 505 project and the high number of structural requirements on the carbon fibre skin, a good reproduction of the desired optimized shapes was numerically obtained using the FEM analysis.

8.2.4 The wing model control system

The core of the wing control system was the embedded real time controller PXI-e 8135 of National Instruments. This controller ran on a real time operating system, and was connected to all the system hardware peripherals through several input and output modules. All four upper skin actuators (BLDC motors), the rigid aileron actuator, the LVDT sensors for providing the actuators positions feedback, as well as the upper skin Kulite pressure sensors were connected to the PXI-e 8135 system. The controller was monitored by the host PC via an Ethernet network using the TCP/IP communication protocol, which had a static IP address that was personalized and fixed by the system operator. The Windows OS machine (the host PC) served for the control program deployment, system state control, and data monitoring in real time. All communication tasks, control and data logging were entirely operated by the PXI-e 8135, which ran independently of the host PC. Figure 8.4 Overview of the morphing wing control system presents an overview of the integrated controller and data monitoring system of the morphing wing model.

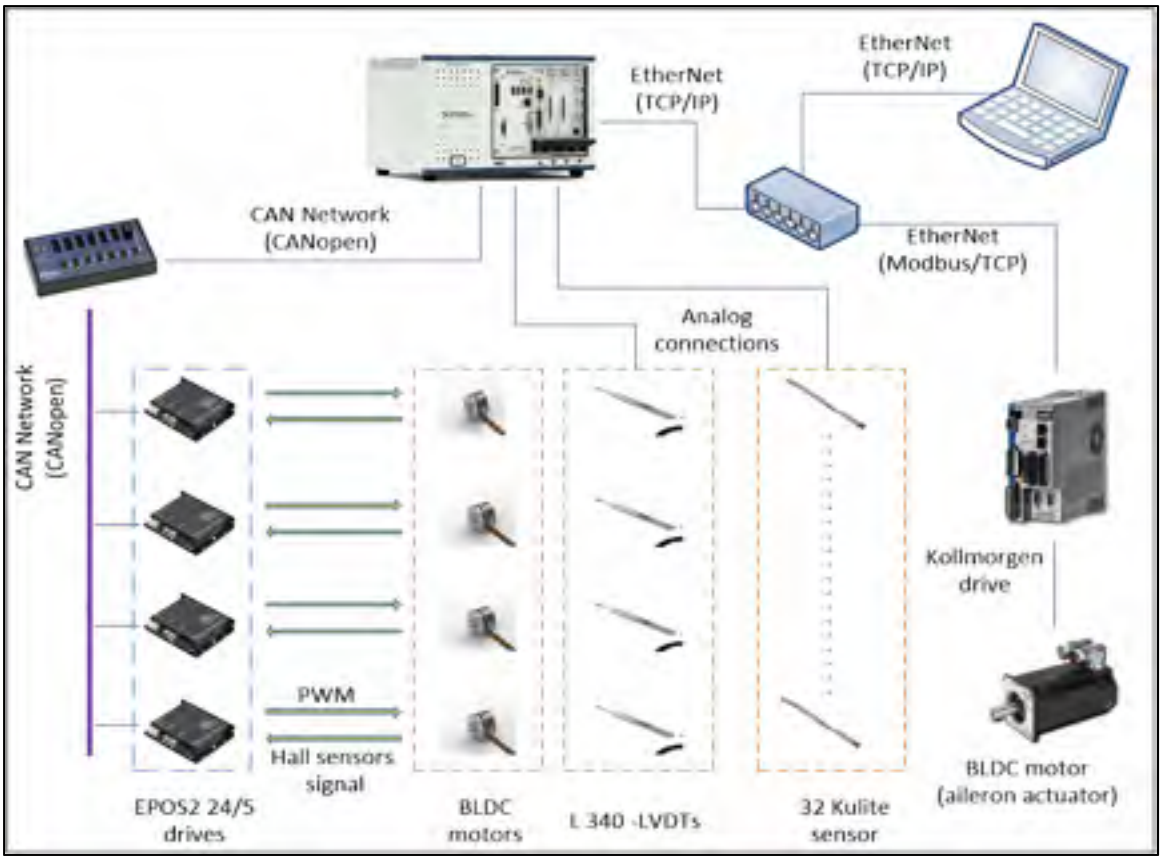

Figure 8.4 Overview of the morphing wing control system

8.3 Flow Equations, Turbulence and Transition Models

CFD simulations were performed to simulate the flow past the wing under the wind tunnel test conditions and experimental setup. The dynamics of fluid flow is governed by the Navier-Stokes equations, which represent the fundamental principles of mass, momentum and energy conservation. For turbulent flows, the Reynolds Averaging technique is used to decompose the instantaneous flow variables into their average values and turbulent fluctuations, while the Boussinesq eddy-viscosity hypothesis is used to relate the Reynolds stress tensor and turbulent heat flux terms to the average flow variables. With these assumptions, the Reynolds Averaged Navier-Stokes (RANS) equations can be written as follows:

$$\frac{\partial \rho}{\partial t} + \frac{\partial}{\partial x_j}\left(\rho U_j\right) = 0 \tag{8.1}$$

$$\begin{gathered} \frac{\partial}{\partial t}(\rho U_i) + \frac{\partial}{\partial x_j}\left(\rho U_j U_i\right) = \\ = -\frac{\partial P}{\partial x_i} + \frac{\partial}{\partial x_j}\left[\mu_{eff}\left(\frac{\partial U_i}{\partial x_j} + \frac{\partial U_j}{\partial x_i}\right) - \frac{2}{3}\mu_{eff}\frac{\partial U_k}{\partial x_k}\delta_{ij}\right] \end{gathered} \tag{8.2}$$

$$\begin{gathered} \frac{\partial}{\partial t}(\rho H) - \frac{\partial P}{\partial t} + \frac{\partial}{\partial x_j}\left(\rho U_j H\right) = \frac{\partial}{\partial x_j}\left[\lambda\frac{\partial T}{\partial x_j} + \frac{\mu_t}{Pr_t}\frac{\partial h}{\partial x_j}\right] + \\ + \frac{\partial}{\partial x_j}\left\{U_i\left[\mu_{eff}\left(\frac{\partial U_i}{\partial x_j} + \frac{\partial U_j}{\partial x_i}\right) - \frac{2}{3}\mu_{eff}\frac{\partial U_k}{\partial x_k}\delta_{ij}\right] + \mu\frac{\partial k}{\partial x_j}\right\} \end{gathered} \tag{8.3}$$

where ρ is the fluid density, U_i are the components of the velocity field, P is the sum of the static pressure and the $(2\rho\delta_{ij}k)/3$ term resulting from the Boussinesq assumption, μ_{eff} is the effective viscosity, given by the sum of the molecular viscosity μ and the turbulent viscosity μ_t, δ_{ij} is the Kronecker delta function, H is the total enthalpy, T is the fluid temperature, λ is the thermal conductivity, Pr_t is the turbulent Prandtl number, h is the static enthalpy and k is the turbulent kinetic energy.

The turbulent viscosity and the kinetic energy are determined using the $k-\omega$ Shear Stress Transport (SST) model (Menter, 1994). The SST model represents a blend of the $k-\omega$ model, used in the near wall region, and the $k-\varepsilon$ model, used for the rest of the flow. Thus, it achieves both accurate boundary layer representation up to the viscous sub-layer and insensitivity to boundary conditions and free-stream flow. The SST turbulence model equations are presented below :

$$\frac{\partial}{\partial t}(\rho k) + \frac{\partial}{\partial x_j}\left(\rho U_j k\right) = P_k - D_k + \frac{\partial}{\partial x_j}\left[(\mu + \sigma_k\mu_t)\frac{\partial k}{\partial x_j}\right] \tag{8.4}$$

$$\frac{\partial}{\partial t}(\rho\omega) + \frac{\partial}{\partial x_j}\left(\rho U_j \omega\right) = \frac{\gamma}{\mu} P_k - \beta\rho\omega^2 + \frac{\partial}{\partial x_j}\left[(\mu + \sigma_\omega \mu_t)\frac{\partial \omega}{\partial x_j}\right] + \\ +2(1 - F_1)\rho\sigma_{\omega 2}\frac{1}{\omega}\frac{\partial k}{\partial x_j}\frac{\partial \omega}{\partial x_j} \tag{8.5}$$

where k is the turbulent kinetic energy, P_k is the turbulent kinetic energy production term, D_k is the turbulent kinetic energy destruction term, ω is the specific turbulence dissipation rate, F_1 is a blending function specific to the SST model, and γ, β, σ_k, σ_ω and $\sigma_{\omega 2}$ are the constants of the model. The turbulent viscosity is calculated as:

$$\mu_t = min\left(\frac{\rho k}{\omega}, \frac{a_1 \rho k}{S F_2}\right) \tag{8.6}$$

where $a_1$is a damping coefficient, S is the strain rate magnitude and F_2 is a second blending function specific to the SST model.

In order to include the effects of laminar flow and model the laminar-to-turbulent transition process, the $\gamma - Re_{\theta t}$ model is used (Langtry and Menter, 2009). This model includes two additional equations, one for the intermittency and one for the transition momentum thickness Reynolds number:

$$\frac{\partial}{\partial t}(\rho\gamma) + \frac{\partial}{\partial x_j}\left(\rho U_j \gamma\right) = P_\gamma - E_\gamma + \frac{\partial}{\partial x_j}\left[(\mu + \frac{\mu_t}{\sigma_f})\frac{\partial \gamma}{\partial x_j}\right] \tag{8.7}$$

$$\frac{\partial}{\partial t}(\rho\overline{Re_{\theta t}}) + \frac{\partial}{\partial x_j}\left(\rho U_j \overline{Re_{\theta t}}\right) = P_{\theta t} + \frac{\partial}{\partial x_j}\left[\sigma_{\theta t}(\mu + \mu_t)\frac{\partial \overline{Re_{\theta t}}}{\partial x_j}\right] \tag{8.8}$$

where γ is the intermittency, P_γ is the intermittency production term, E_γ is the intermittency destruction/relaminarization term, $\overline{Re_{\theta t}}$ is the transition momentum thickness Reynolds number, $P_{\theta t}$ is the transition momentum thickness Reynolds number production term and σ_f and $\sigma_{\theta t}$ are model constants.

The transition onset is controlled by an empirical correlation between $Re_{\theta c}$, the critical Reynolds number where the intermittency starts to increase in the boundary layer, and $\overline{Re_{\theta t}}$ (Langtry and Menter, 2009). The model contains correction terms to account for laminar separation-induced transition and strong pressure-gradient flows. Coupling of the $\gamma - Re_{\theta t}$ transition model with the $k - \omega$ SST turbulence model is done by modifying P_k and D_k, the turbulent kinetic energy production and destruction terms, and thus deactivating the turbulence model for the laminar boundary layer region.

The numerical computations were performed with the ANSYS FLUENT solver. The steady-state flow equations were solved using a projection method, achieving the constraint of mass conservation by solving the pressure equation, with the pressure-velocity coupling being accomplished using a high order Rhie-Chow scheme. The cell-face values of the pressure were interpolated using a second order central differencing scheme, while for all other variables, including the turbulence and transition model equations, a second order upwind scheme was used. The discrete linear equations were solved in a fully implicit, coupled manner. Convergence acceleration was achieved with a coupled algebraic multi-grid (AMG) approach, using a block-method Incomplete Lower-Upper (ILU) factorization scheme as the linear system smoother.

8.4 Morphed Geometries and Mesh Generation

8.4.1 The theoretical optimized upper surface shapes

The core concept of an active morphing of the wing upper surface is to provide an optimized airfoil shape for each flight condition. A single point optimization must be performed for each combination of Mach number, Reynolds number and angle of attack. This procedure increases the aerodynamic performance of the shape-changing airfoil (with respect to the desired optimization objective) compared to the multi-point designed baseline airfoil.

Aerodynamic optimizations were performed to determine the displacements of the electrical actuators required to improve the performance of the morphing wing with respect to the original wing. In order to greatly reduce calculation times, the aerodynamic optimizations were performed under the two-dimensional flow assumption using the XFOIL solver (Drela, 1989) and an in-house genetic algorithm optimizer (Koreanschi, 2014), for the local flow conditions (local Reynolds number and angle of attack) corresponding to the mean aerodynamic chord of the wing model (Koreanschi, 2015).

For the numerical optimizations, the upper skin shapes between 20% and 65% of the chord were approximated using cubic splines, as function of the actuator displacements. This mathematical model was chosen because it enforces the tangency condition with the rigid part of the airfoil (up to the curvature continuity given by the second derivative), it provides an iso-arc-length condition and it shares mathematical properties with a beam bending under an applied load. Due to constraints related to the structural rigidity of the composite skin, the actuator displacements were limited to +/- 3.5 mm, while the maximum difference between the two displacements was limited to 6 mm.

8.4.2 Measurement of the real upper surface shapes

Due to the high degree of multidisciplinary involved in the development of the MDO 505 morphing wing project, the contradictory requirements that the morphing upper surface had to satisfy (rigid in order to withstand flight loads, but at the same time flexible enough to allow proper controlled deformations) and the very high precision required for the aerodynamic optimization, it was decided to scan the shapes obtained after the completion of the manufacturing process. This way, the simulations would be performed on geometries that were practically achieved, and not on surfaces reconstructed using mathematical modeling.

To construct the geometries required for the 3D calculations, the real shapes of the morphing skin surface for all flight cases were scanned using a high precision photogrammetry procedure, using three 3D-tracking cameras (Mebarki and Kameya, 2014). Circular retro-

reflective markers were applied on the wing upper surface, and their positions were recorded for each skin shape. Figure 8.5 presents the marker positions for the un-deformed skin, as measured with the scanning procedure. The estimated maximum position error with this procedure is 0.07 mm, using the known positions of the four actuators.

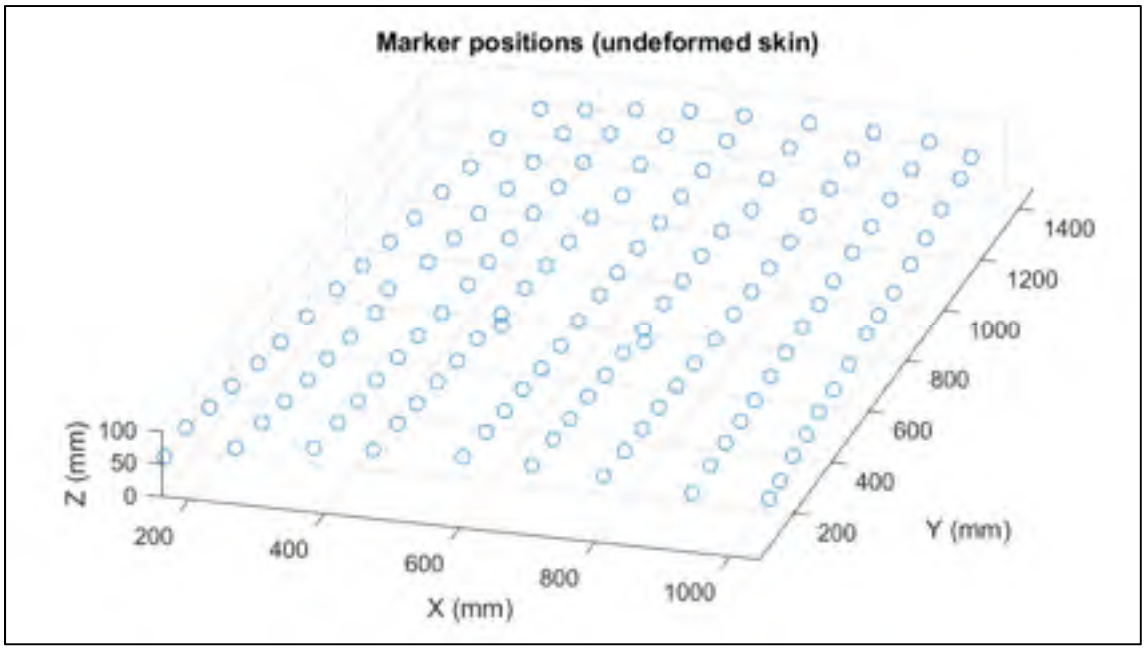

Figure 8.5 Marker positions for the un-deformed upper skin

To increase the resolution of the scanned data, a bi-harmonic spline interpolation procedure was performed between the marker positions, and the number of points was increased to 100, in both chord-wise and span-wise directions. Figure 8.6 presents the 100x100 grid of points obtained by interpolation for the un-deformed skin (upper image), and the deformed shape of the flexible skin for the C41 configuration (lower image).

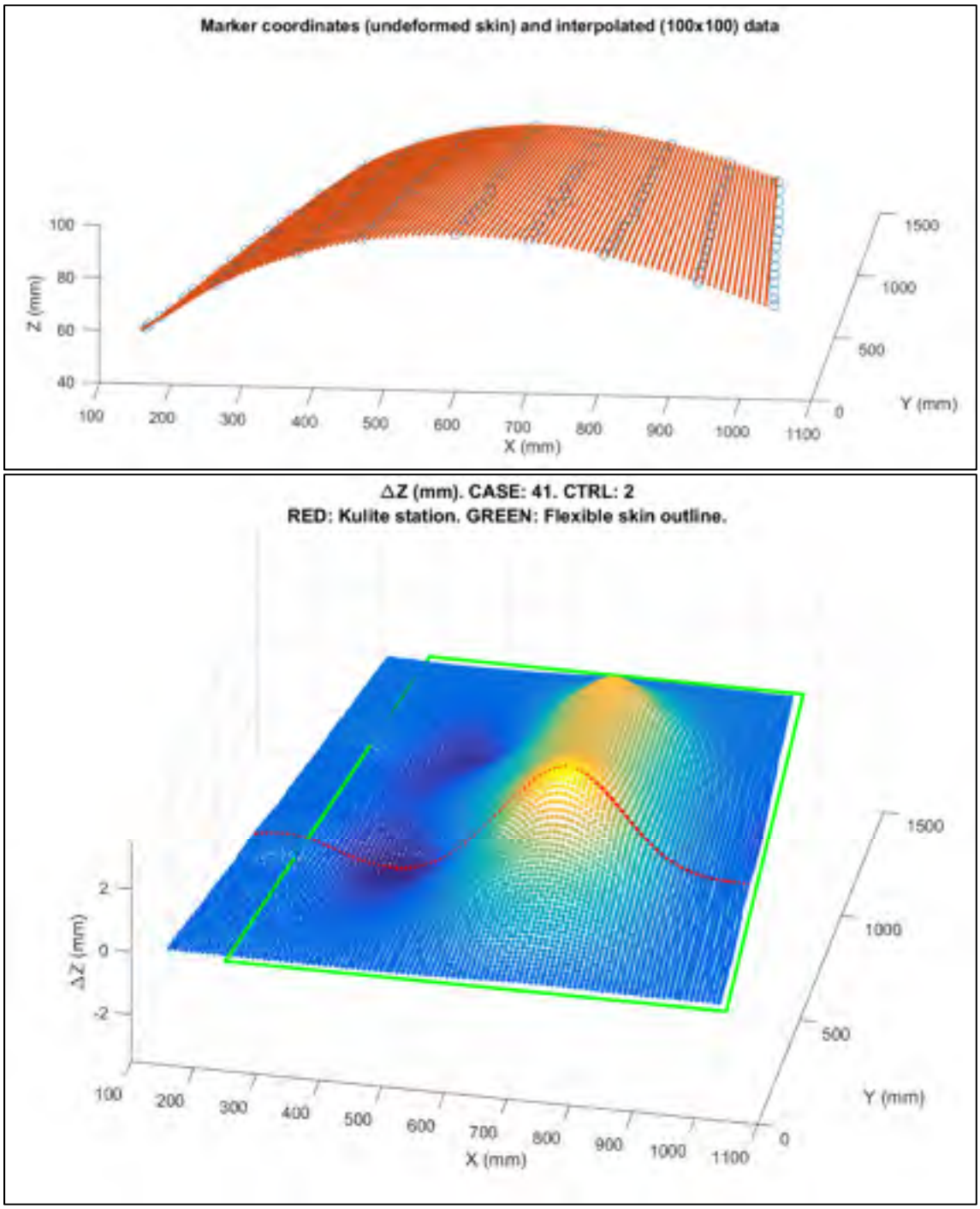

Figure 8.6 Interpolated point grid constructed from the scanned marker positions for the un-deformed upper skin

The procedure of determining the marker positions through the photogrammetry technique and interpolating using splines to increase the density of surface points was repeated for all the morphing cases. The data was further used to construct the geometries required for the 3D calculations, by patching the upper surface skin shapes on the rigid geometry representing the rest of the wing model. Thus, an accurate representation of the real skin shapes was available for performing the numerical simulations.

8.4.3 Grid convergence study

The structured meshes used for the numerical simulation were generated using the ICEM-CFD software. A grid convergence study was performed in order to evaluate the mesh density required for grid-independent aerodynamic coefficients values. Four meshes of increasing cell density were generated, and each one was analysed at a Mach number of 0.15, a Reynolds number of 4.53E+06 (as calculated with the wing mean aerodynamic chord) and an angle of attack of 0 deg. Details regarding the wall cell density for the generated meshes are presented in Table 8.1.

Table 8.1 Details about the four generated meshes

Mesh type	Chord-wise cells on wall	Span-wise cells on wall	Maximum y+
Coarse	100	40	2.66
Medium	200	80	1.33
Fine	400	160	0.66
Extra Fine	800	320	0.33

The wing aerodynamic coefficients values (lift, drag and pitching moment coefficient about the root section quarter chord point) and the transition point locations on the upper surface, at the 37% and 75% of the span stations are presented in Table 8.2. The transition point locations were determined using the intermittency variable γ distribution. The table shows that the difference in aerodynamic coefficient values between the Fine mesh level and the Richardson extrapolation of the convergence study is lower than 1%, and thus the Fine mesh

provides sufficiently accurate results. It can be observed that the $\gamma - Re_{\theta t}$ model requires a good stream-wise mesh refinement level before the grid convergence of the transition point location is achieved (thus also affecting the grid convergence of the drag coefficient, through the variation of the laminar flow region length).

Table 8.2 Results obtained for the grid convergence study

Mesh type	**CL**	**CD**	**Cm**	**Transition at 37% of span (% of local chord)**	**Transition at 75% of span (% of local chord)**
Coarse	1.531E-01	1.308E-02	-9.235E-02	13.4%	3.4%
Medium	1.587E-01	9.855E-03	-9.264E-02	48.2%	32.8%
Fine	1.593E-01	9.621E-03	-9.273E-02	57.5%	36.9%
Extra Fine	1.596E-01	9.609E-03	-9.274E-02	58.0%	37.1%
Richardson Extrapolation	1.597E-01	9.605E-03	-9.276E-02	58.2%	37.1%

The characteristics of the meshes used to perform the simulations were determined based on the above results of the grid convergence study. In order to ensure that the same meshing parameters were used for all the morphed wing cases, an automatic mesh generation procedure was implemented by creating a script to be used for the ICEM-CFD code. The automatic procedure can also handle rigid aileron deflections between +/- 7 deg. The meshes were constructed based on the Fine mesh level created for the convergence study, and include 400 cells around the wing section (200 cells on both the lower and upper surfaces), and 160 cells in the direction of the span (80 cells on both the lower and upper surfaces). The wall normal spacing was set to 3.0E-06 m, refined enough to provide the required $y+< 1$ condition. Figures 8.7 and 8.8 present two cross-section views of the mesh constructed around the original, non-morphed wing.

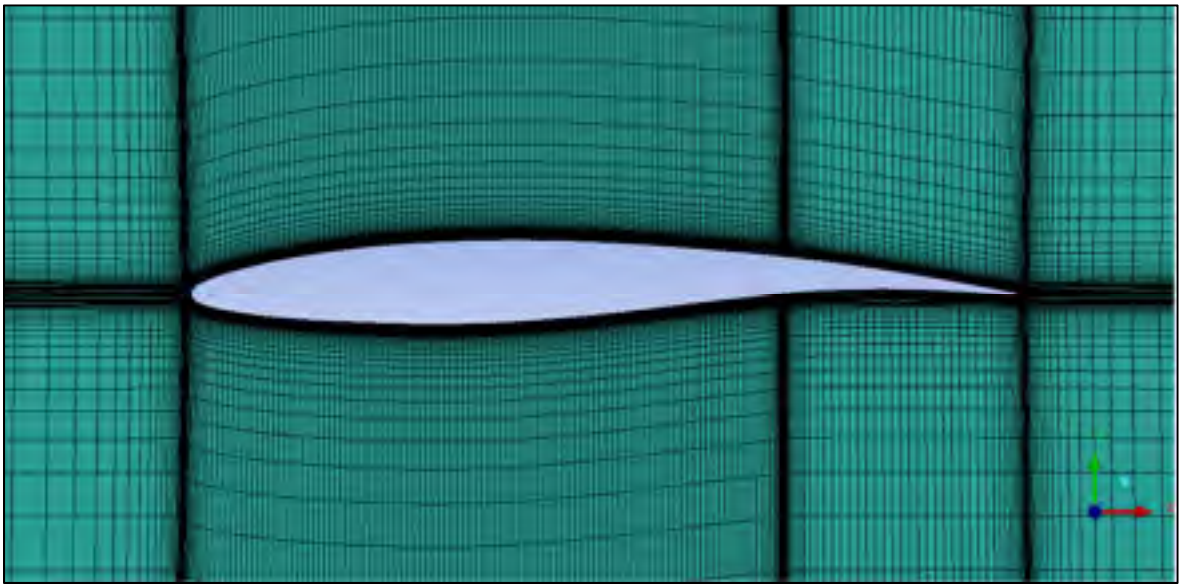

Figure 8.7 Chord-wise cross-section view of the mesh

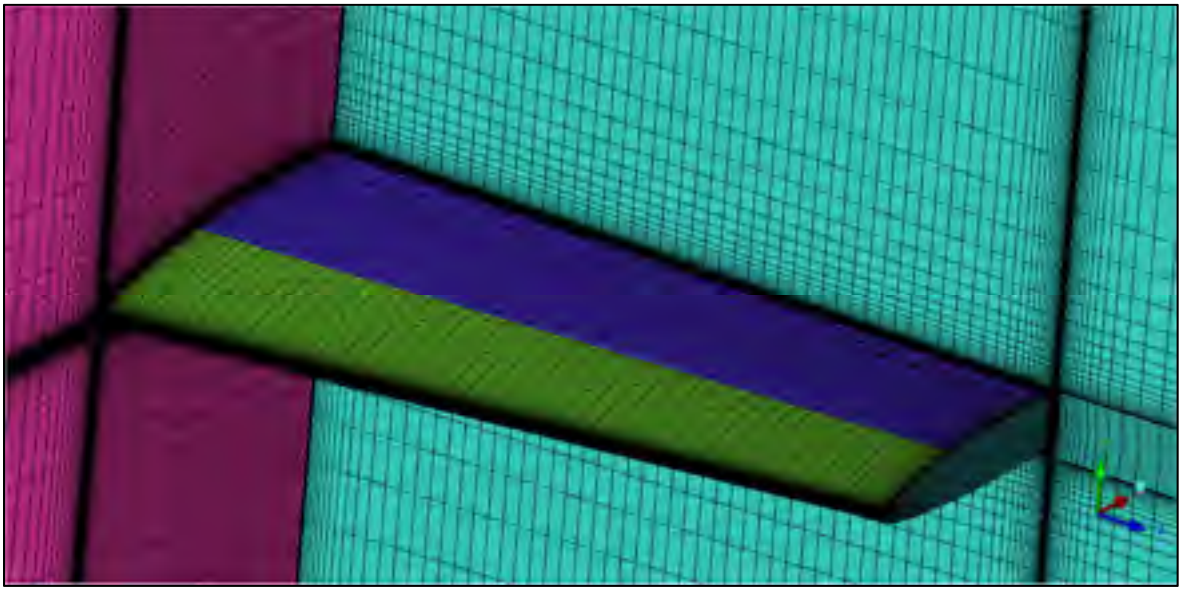

Figure 8.8 Span-wise cross-section view of the mesh

8.5 Experimental Testing and Data Acquisition

The wind tunnel tests were performed at the 2 x 3 m atmospheric closed circuit subsonic wind tunnel of the National Research Council. The tunnel allows blowing speeds up to a Mach number of 0.33, at atmospheric pressure and constant temperature.

The upper surface flexible skin was equipped with 32 high precision Kulite piezoelectric-type transducers that were for pressure measurement and then processed to determine the laminar-to-turbulent transition location. These sensors were installed in two staggered lines (with 16 Kulite sensors on each line), situated at 0.600 m and 0.625 m from the wing root section. In addition to the Kulite piezoelectric sensors, at the same two span-wise stations, 60 static pressure taps were installed (30 on each line) on the wing leading edge, lower surface and aileron, thus providing complete experimental pressure distribution around the wing cross section at 40% of the wing span.

The experimental measurements also included the use of a wake rake pressure acquisition system, to measure the wing profile drag at different span-wise positions, and the use of a wind tunnel balance for measuring the aerodynamic forces and moments. Figure 8.9 presents the MDO 505 morphing wing model installed in the tunnel test section, viewed from both the leading edge (left figure) and the trailing edge (right figure).

Infra-red (IR) thermography camera visualisations were performed for capturing the transition region on the entire wing model surface. The wing leading edge, its upper surface flexible skin and the aileron interface were coated with high emissivity black paint to improve the quality of the IR photographs. The span-wise stations where the two pressure sensors lines were installed were not painted, in order not to influence the pressure reading quality. A Jenoptik Variocam camera, with a resolution of 640 by 480 pixels, was used to measure the surface temperatures (Mebarki, 2009). This camera was equipped with a 60 degrees lens in order to capture the flow transition on the entire upper surface of the wing. A

custom wooden window was installed on the tunnel test section wall, through which the IR camera operated.

Figure 8.9 MDO 505 wing model setup in the wind tunnel test section

The IR thermography visualisation allows the identification of the laminar-to-turbulent transition region based on the temperature gradient between the two flow regimes, which is determined by the different convective heat transfer coefficient and heat flux dissipation existing in the two regimes when the surface is heated to a fixed temperature. Figure 8.10 presents an example of the IR visualisation of the wing model upper surface transition, for one flight condition (Mach number of 0.15, 1 deg. angle of attack and no aileron deflection) and for both un-morphed (left figure) and morphed (right figure) skin shapes.

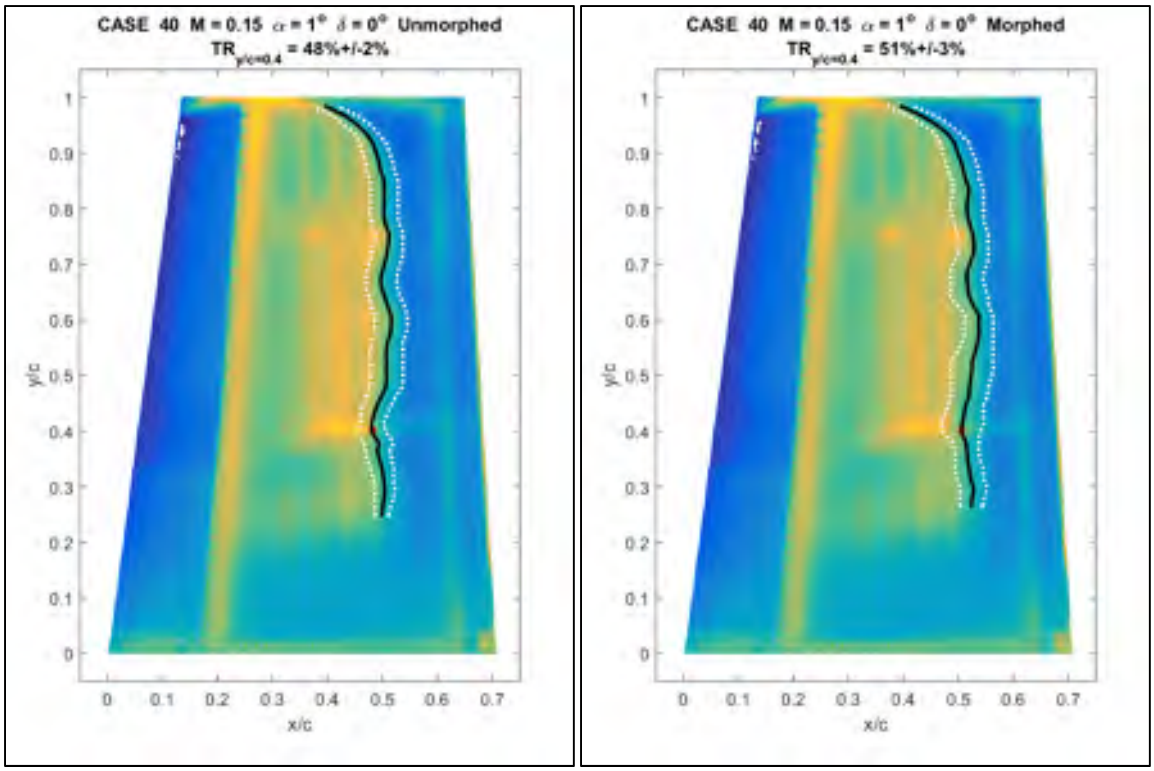

Figure 8.10 IR visualisation of the laminar-to-turbulent transition region on the upper surface for both un-morphed (left) and morphed (right) skin shapes

The black line represents the average transition line on the upper surface, and its variation as function of the span-wise position can clearly be observed. The two dashed white lines represent the estimated extent of the transition region, determined as function of the chord-wise temperature gradient existing between laminar and turbulent regimes. The transition region detection was fully automated for the entire IR image of the wing upper surface (Mebarki, 2009). The red dot corresponds to the estimated transition in the span-wise section situated at 0.612 m from the root section (40% of the model span), that is half-way between the two Kulite piezoelectric pressure sensors lines. The accuracy of the transition detection for this section was estimated to +/- 2% of the local chord, based on the known Kulite positions and their thermal signatures in the images.

8.6 Results and Discussion

8.6.1 The test cases

The two-dimensional aerodynamic optimizations that determined the electrical actuators displacements were performed with the objective of controlling the extent of laminar flow on the upper surface of the wing model.

These optimizations were performed for several flight conditions (expressed in terms of Mach number, Reynolds number and angle of attack) and several rigid aileron deflection angles. The cases that were optimized, analysed and experimentally tested for laminar flow increase are presented in Table 8.3. The Reynolds numbers that correspond to the two Mach numbers are 4.28×10^6 and 5.27×10^6 (and were calculated using the wing mean aerodynamic chord). A downwards aileron deflection was considered positive, while an upwards aileron deflection was considered negative.

Table 8.3 Test cases optimized for laminar flow improvement

Mach	**Delta [deg.]**	**Angle of Attack [deg.]**										
		0	0.50	0.75	1.00	1.25	1.50	2.00	2.50	3.00	4.00	5.00
0.15	0	-	-	C39	C40	C41	C42	C43	C44	C45	-	-
0.20	4	C68	C69	-	C70	-	C71	C72	C73	-	-	-
0.20	-4	C74	C75	-	C76	-	C77	C78	C79	C80	C81	C82

8.6.2 Upper surface transition location

For each case, the transition point location on the pressure sensors line was determined from the numerical simulation and was compared to the experimentally measured transition location, determined using the IR thermography. The transition point location in the numerical results was determined by plotting the turbulence intermittency γ versus the local chord, for the upper and lower wing surfaces. In order to consistently extract the transition

location, the first derivative of the intermittency plot was used. Since the intermittency is approximately constant for the laminar boundary layer and its value significantly increases in the transition region, the first derivative can be used to identify this region of very high gradient. The transition point was considered to be the most upstream point where the derivative becomes non-zero. As an example, Figure 8.11 shows the intermittency distribution at 0.612 m span-wise section, for case C39 un-morphed. The laminar-to-turbulent transition corresponds to the region of high gradient.

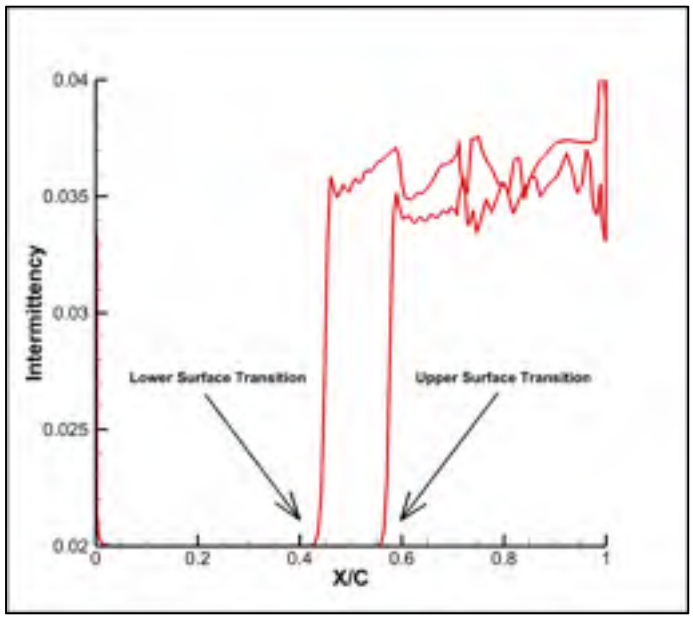

Figure 8.11 Transition for Case 39 un-morphed
using the turbulence intermittency

Figure 8.12 presents a comparison between the predicted and the measured transition location for the un-morphed and morphed wing upper surface skin, at a spanwise station corresponding to 40% of the wing span, the station where the pressure sensors lines were installed. The comparison shows both numerical and IR experimental results for cases C39 to C45 (Mach number of 0.15, no aileron deflection and angles of attack between 0.75 and 3 deg.).

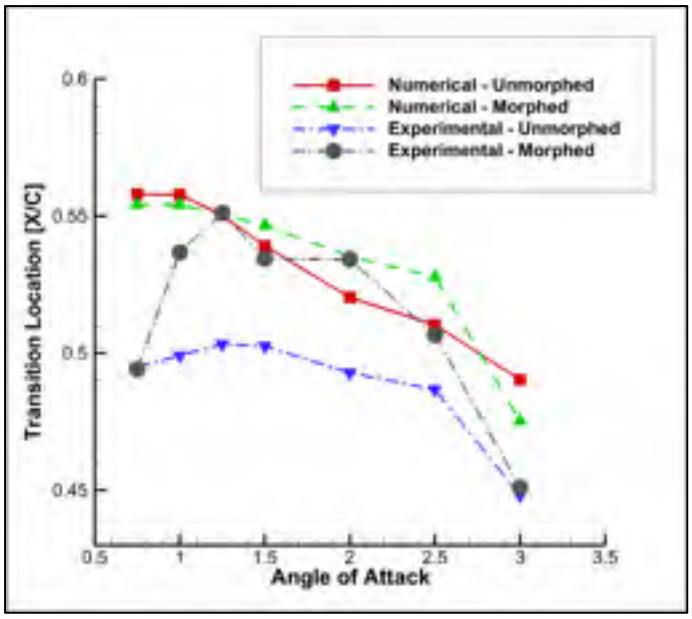

Figure 8.12 Comparison between numerical and IR experimental transition detection for the station located at 40% of the span, for the cases C39 – C45 un-morphed and morphed wings

Figure 8.13 displays the experimental transition location measurement compared to the numerical predictions for cases C68 to C73 (Mach number of 0.20, 4 deg. downwards aileron deflection and angles of attack between 0 and 2.5 deg.). No IR experimental data was available for case C68 (0 deg. angle of attack).

In Figure 8.14, the experimental and numerical transition location detection for cases C74 to C82 (Mach number of 0.20, 4 deg. upwards aileron deflection and angles of attack between 0 and 5 deg.) is presented for both un-morphed and morphed wing geometries. No IR experimental data was available for cases C74 (0 deg. angle of attack) and C80 (3 deg. angle of attack).

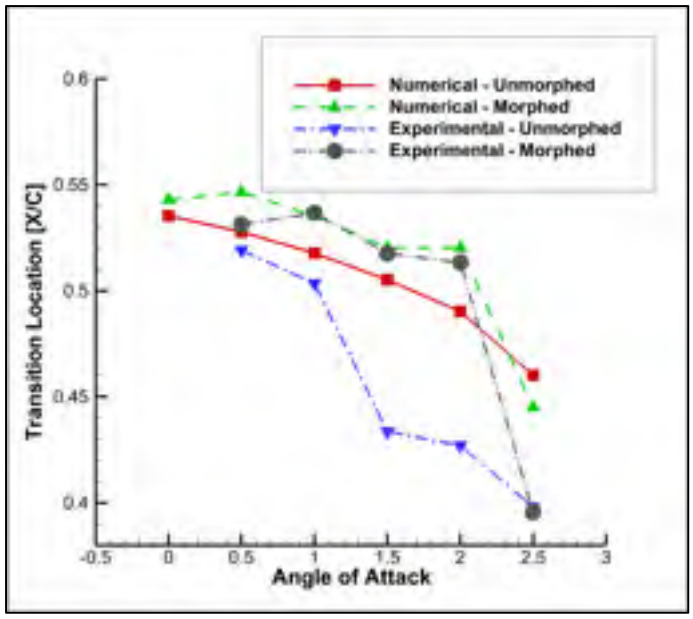

Figure 8.13 Comparison between numerical and IR experimental transition detection for the station located at 40% of the span, for the cases C68 – C73 un-morphed and morphed wings

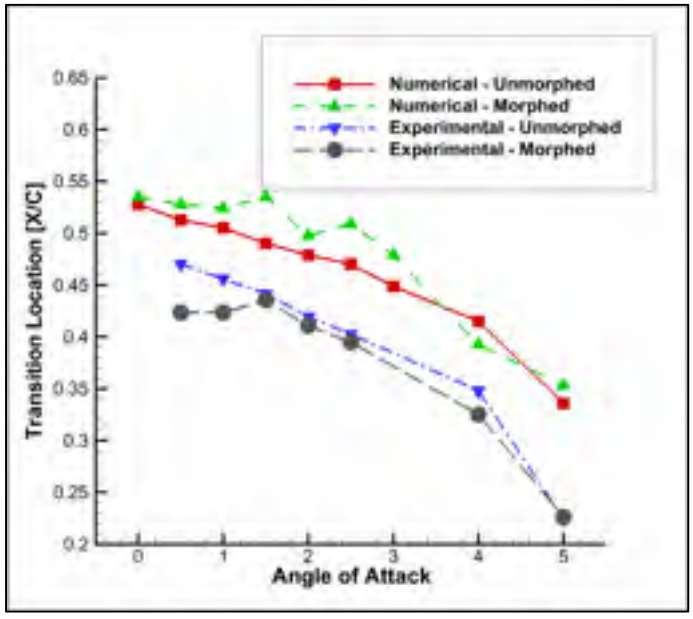

Figure 8.14 Comparison between numerical and IR experimental transition detection for the station located at 40% of the span, for the cases C74 – C82 un-morphed and morphed wings

It can be seen that a reasonable agreement exists between the experimental and the numerically determined transition point location at the pressure sensors section, for the un-morphed wing. For cases C39 to C45 (Figure 8.12) and C74 to C82 (Figure 8.14), the error is around 5% of the local chord (corresponding to 0.05C in the figure) In Figure 8.13, at 0.5 and 1 deg. angle of attack, there is excellent agreement between the results obtained for the un-morphed wing, but the discrepancy is seen to increase for angles of attack higher than 1.5 deg., the experimental measurements showing an early transition occurrence escalating towards the wing leading edge.

The IR experimental results in Figures 8.11 and 8.12 show a successful improvement of laminar flow for the section of interest. For the cases with no aileron deflection (C39 to C45), the transition was delayed towards the trailing edge by 3-5% of the chord (equivalent to 0.03-0.05C in the figures), while for the cases with 4 deg. deflection (C68 to C73), delays of 9% of the chord were obtained for two angles of attack (1.5 and 2 deg.). There is a very good agreement between the numerical and IR transition positions for the morphed geometries, with average errors smaller that 5%. The laminar flow increase predicted by the numerical simulations was smaller than what was observed in the IR data.

For cases C74 to C82 (-4 deg. aileron deflection), there is a good agreement between the IR data and the numerical results for the un-morphed wing (transition position errors of 5% of the chord), but the differences are higher for the morphed wing geometries. For the angles of attack between 1 and 3 deg. the laminar flow delay predicted by the numerical results was not observed in the IR measurements.

Since all of the above presented results were obtained for the section located at 40% of the span, they only offer local information about the performance of the morphing upper skin. To provide a qualitative assessment of the skin's influence on the transition region for entire upper surface of the, surface plots are presented in Figures 8.15 to 8.17, for cases C40 (Figure 8.15), C72 (Figure 8.16) and C77 (Figure 8.17). These cases were chosen among those for which important transition location delays were observed on the pressure sensors

span-wise section (as shown in Figures 8.12 to 8.14), and they cover all three aileron deflection angles. This choice makes it possible to verify if the extension of laminar flow was a phenomenon present on the entire upper surface, or if it was limited to a certain span-wise interval.

In the numerical results, the disturbances in transition position appearing near the wing root section were given by the 6.5 mm gap between the wing root rib and the symmetry plane. This gap was present in the experimental setup and included in the simulations. Its effect was not captured with the IR measurements due to the decrease in data quality in the region close to the wing root section.

For the wing tip region, the precision of the numerical simulations breaks down and an unrealistic laminar flow appears in all the results. This can be explained by the fact that the $\gamma - Re_{\theta t}$ model contains one empirical correlation for the transition onset that was calibrated especially for natural transition (stream-wise Tollmien-Schlichting instabilities) and laminar separation bubbles, while the wing tip region is strongly contaminated by complex, cross-flow instabilities induced by the presence of the wing tip vortex.

An analysis of Figures 8.15 to 8.17 shows that the behaviour of the laminar flow region (under the actuation of the upper skin) that was observed from the pressure sensors line (indicated by the red dot in the experimental IR data and by the black line in the numerical results) can also be observed for other span-wise sections. Thus, when a successful transition delay was obtained for the pressure sensors line, this delay can be seen occurring not only locally but for a high percentage of the wing's span, indicating the effectiveness of the upper surface morphing skin.

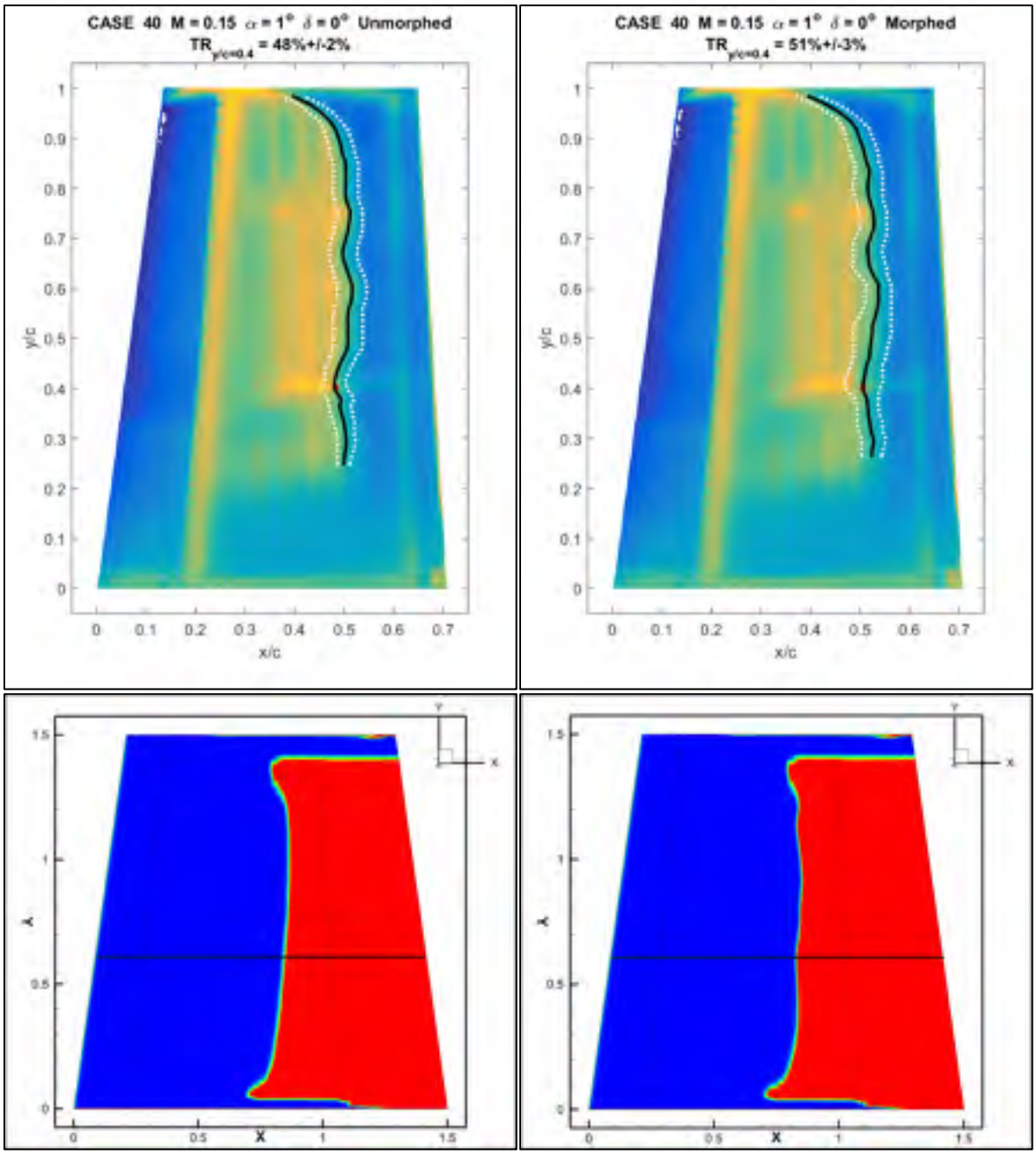

Figure 8.15 Comparison between experimental and numerical transition location on the wing upper surface for case C40, for both un-morphed (left) and morphed (right) geometries

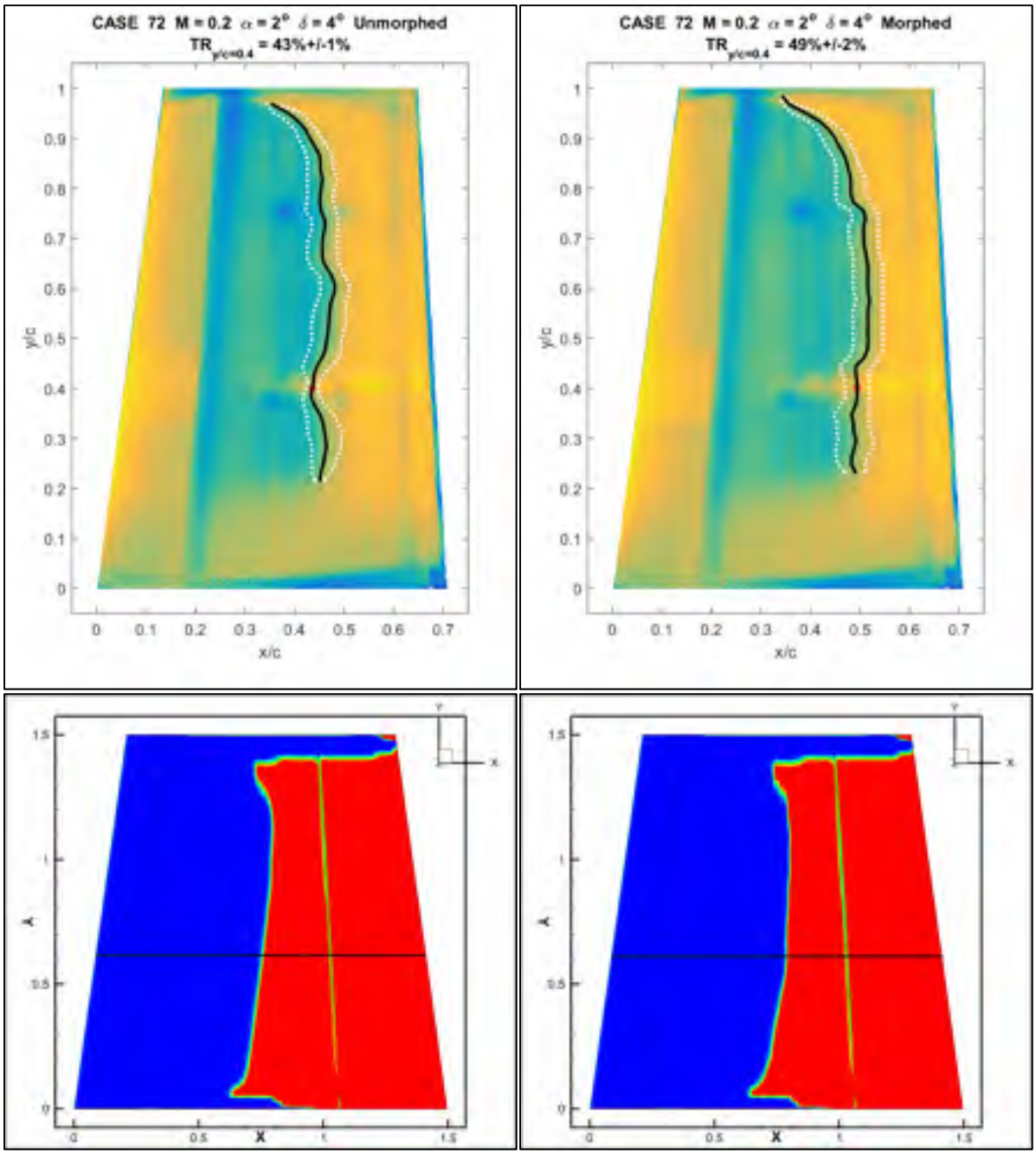

Figure 8.16 Comparison between experimental and numerical transition location on the wing upper surface for case C72, for both un-morphed (left) and morphed (right) geometries

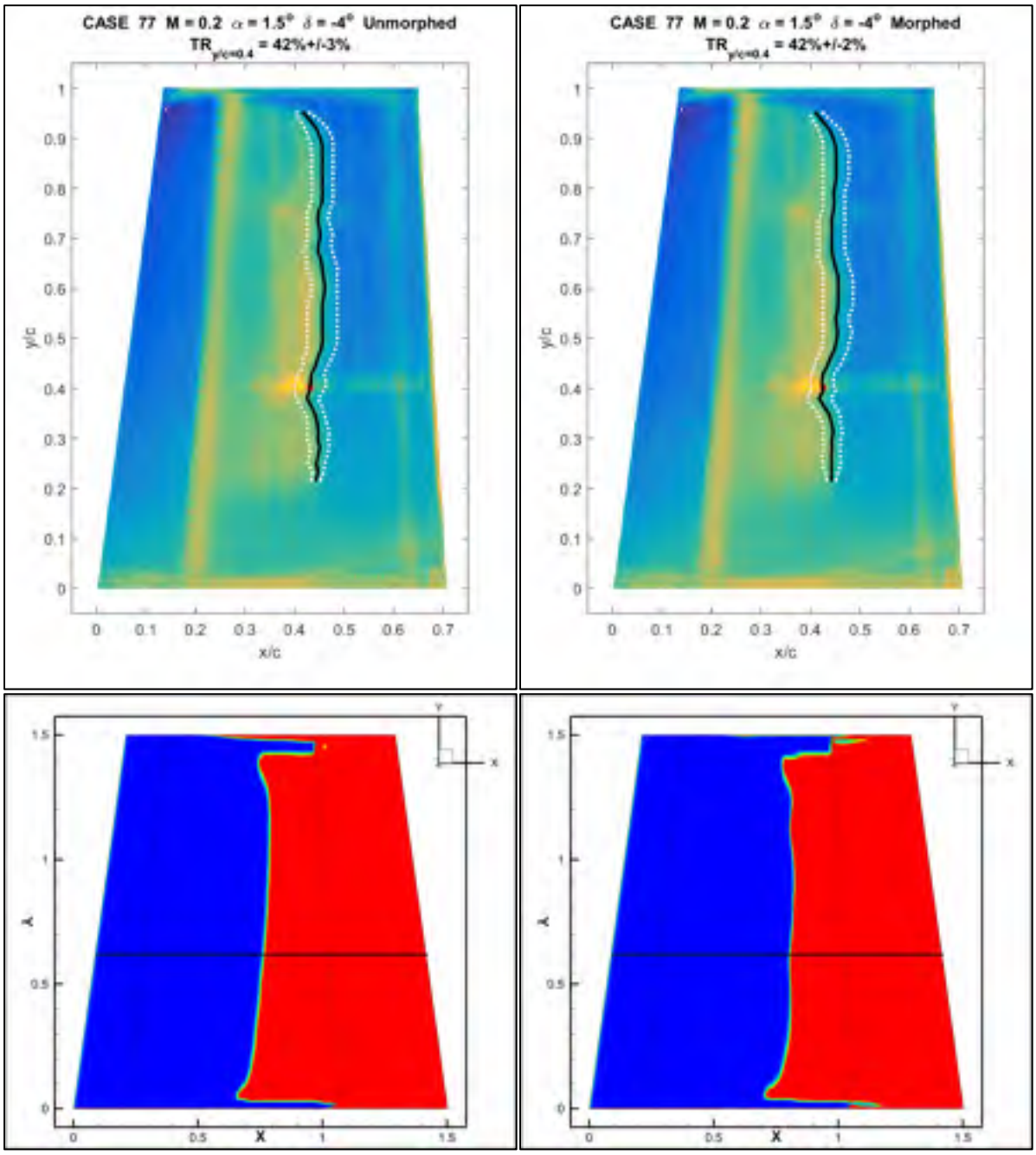

Figure 8.17 Comparison between experimental and numerical transition location on the wing upper surface for case C77, for both un-morphed (left) and morphed (right) geometries

8.6.3 Pressure coefficient distribution comparison

A comparison between the experimental and numerical pressure coefficient distributions for the section located at 40% of the wing span is presented in Figures 8.18 to 8.21, for the following 4 cases: C40 (Mach 0.15, 1 deg. angle of attack and no aileron deflection), C68 (Mach 0.20, 0 deg. angle of attack and 4 deg. aileron deflection) and for C79 and C82 (Mach 0.20, 2.5 and 5 deg. angle of attack and -4 deg. aileron deflection). This choice of cases allows comparisons for angles of attack for the entire analysis range.

Good agreement exits between numerical predictions and the wind tunnel measurements for the two sets of results given by case C40 and C 68 (Figures 8.18 and 8.19). The influence of the upper skin shape change can be observed from the differences between the un-morphed (left) and morphed (right) pressure coefficient distributions, for the chordwise interval between 25% and 60% of the chord. The skin morphing extends the region where the air accelerates over the upper surface, thus creating more favourable conditions for laminar flow, this effect being clearly visible in the two Figures.

For cases C79 and C82 (shown in Figures 8.19 and 8.20), a small difference in the exists in the upper surface pressure coefficient up to 50% of the chord, and very good agreement exists between the numerical and experimental results for the aileron, rigid lower skin and the upper surface downstream of 50% of the chord. Again, the influence of the morphing skin is clearly observable by comparing the left (un-morphed) and right (morphed) pressure distributions for the two Figures.

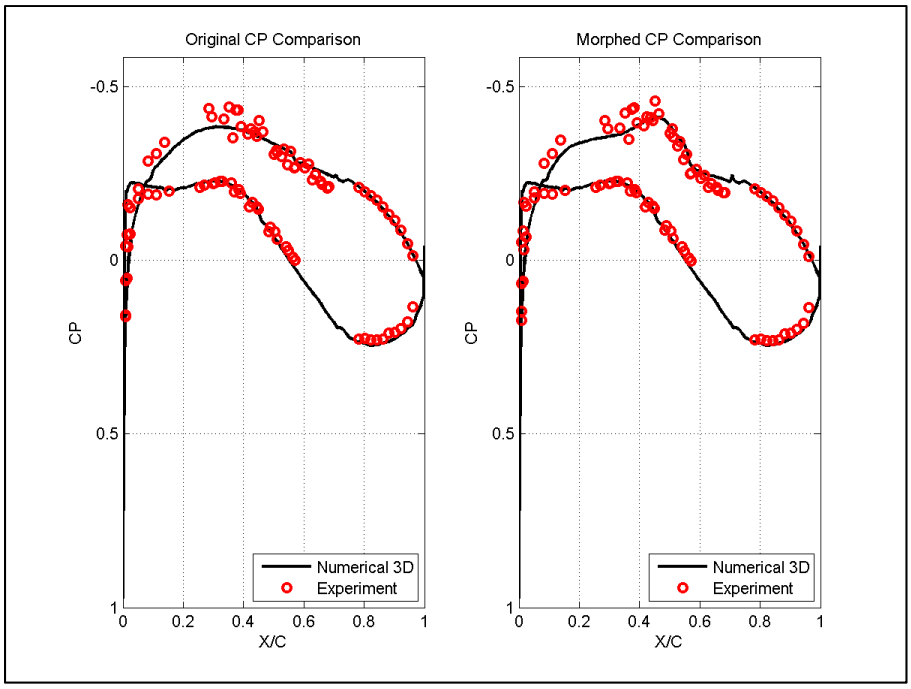

Figure 8.18 Comparison of experimental versus numerical pressure coefficient distribution for case C40 un-morphed (left) and morphed (right)

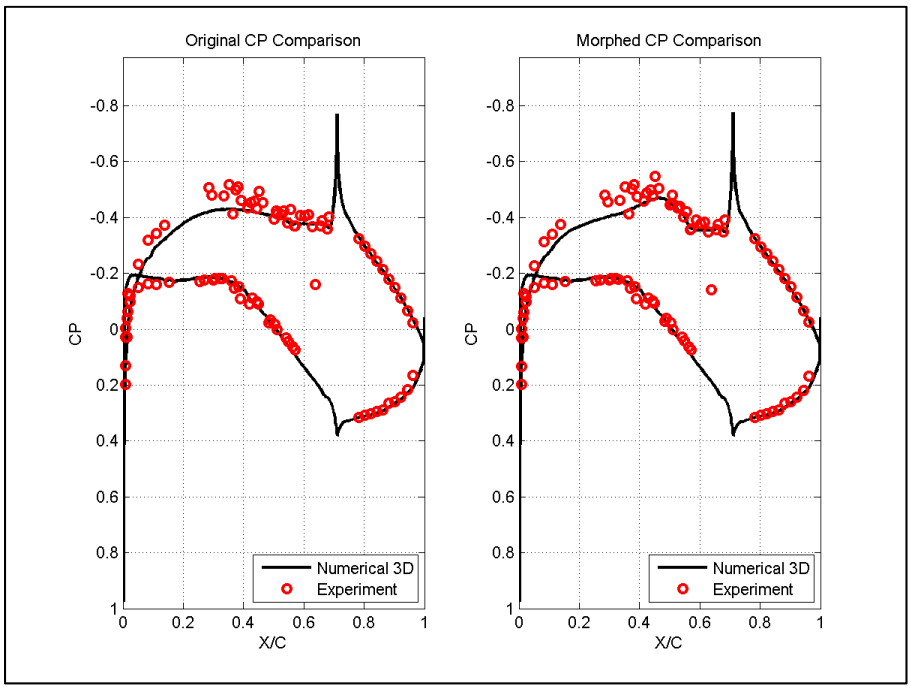

Figure 8.19 Comparison of experimental versus numerical pressure coefficient distribution for case C68 un-morphed (left) and morphed (right)

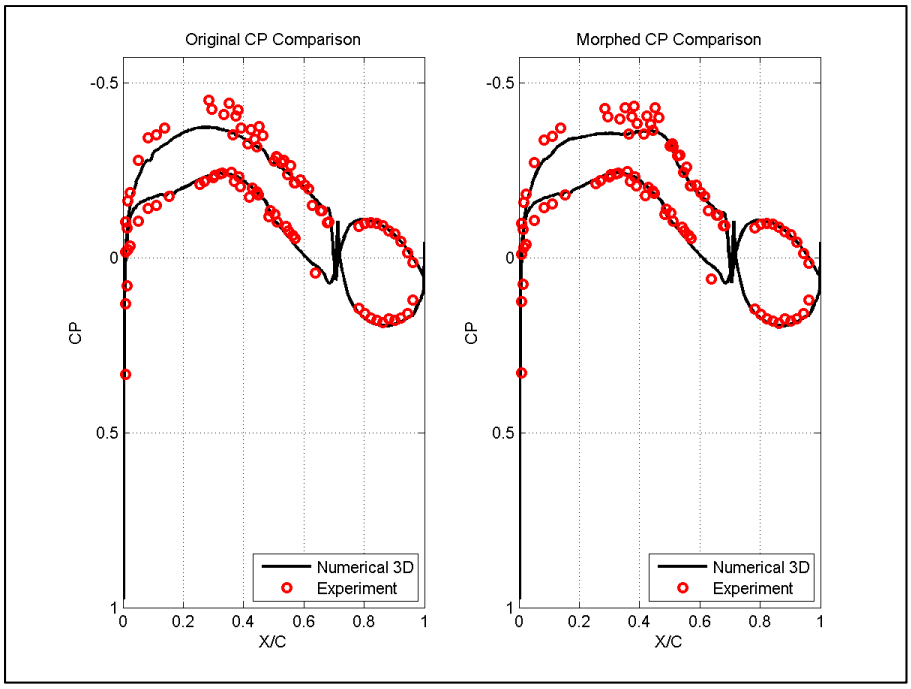

Figure 8.20 Comparison of experimental versus numerical pressure coefficient distribution for case C79 un-morphed (left) and morphed (right)

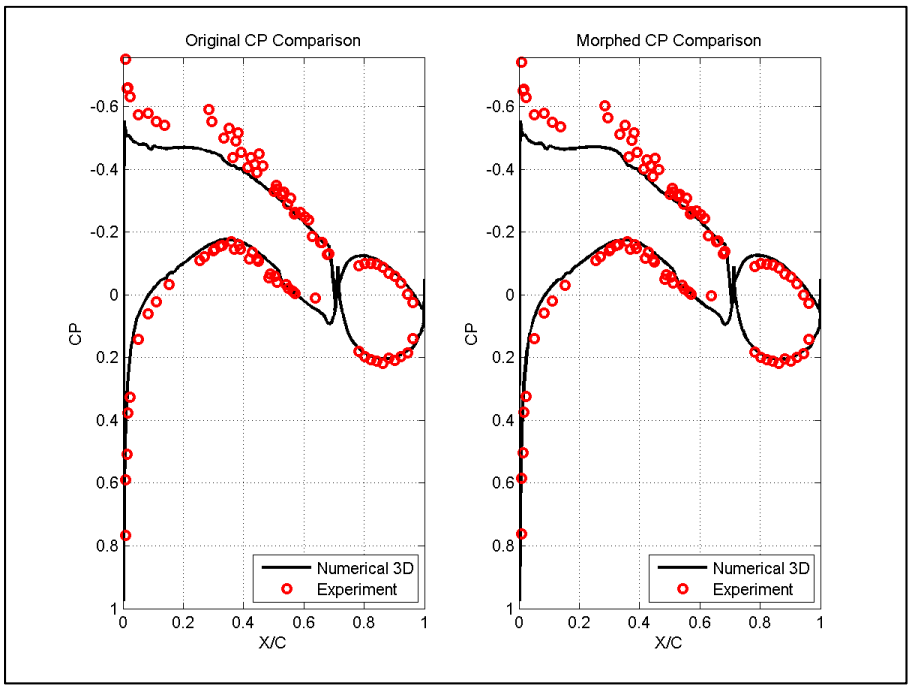

Figure 8.21 Comparison of experimental versus numerical pressure coefficient distribution for case C82 un-morphed (left) and morphed (right)

8.6.4 Aerodynamic coefficients comparison

In Tables 8.4 and 8.5, a comparison is made between the lift and drag coefficients for the un-morphed and morphed geometries, obtained through the numerical simulations and the experimental test. The comparison is presented for cases C38 to C45, which were analysed at a Mach number of 0.15 and had no aileron deflection.

Table 8.4 Comparison between the numerical un-morphed and morphed wing lift and drag coefficients for cases C39 to C45

Numerical Results						
Case	**Angle of Attack [deg.]**	**Un-morphed Wing**		**Morphed Wing**		**Drag Variation [%]**
		CL	CD	CL	CD	
C39	0.75	0.2058	0.0118	0.2059	0.0118	-0.01%
C40	1	0.2191	0.0126	0.2196	0.0126	0.24%
C41	1.25	0.2325	0.0134	0.2330	0.0134	0.18%
C42	1.50	0.2460	0.0142	0.2464	0.0142	0.10%
C43	2	0.2729	0.0161	0.2736	0.0161	0.19%
C44	2.50	0.3002	0.0183	0.3009	0.0183	0.13%
C45	3	0.3276	0.0206	0.3278	0.0206	0.18%

Table 8.5 Comparison between the experimental un-morphed and morphed wing lift and drag coefficients for cases C39 to C45

Experimental Results (loads balance measurements)						
Case	**Angle of Attack [deg.]**	**Un-morphed Wing**		**Morphed Wing**		**Drag Variation [%]**
		CL	CD	CL	CD	
C39	0.75	NA	NA	NA	NA	NA
C40	1	0.2150	0.0156	0.2165	0.0156	-0.20%
C41	1.25	0.2324	0.0168	0.2329	0.0167	-0.47%
C42	1.50	0.2483	0.0180	0.2490	0.0178	-0.51%
C43	2	0.2794	0.0206	0.2788	0.0204	-0.60%
C44	2.50	0.3102	0.0235	0.3109	0.0234	-0.40%
C45	3	0.3434	0.0267	0.3424	0.0266	-0.23%

The numerical lift coefficient values in Table 8.4 were found to be in good agreement with the experimental values included in Table 8.5, a small underestimation being observed for the 2.5 and 3 deg. angles of attack. Concerning the drag coefficient, the numerical values are always under-predicted compared to the experimental ones, the average error being around 25%. The experimental drag coefficient data shows that the morphing of the upper surface skin caused a reduction of the wing model drag coefficient, with values between 0.20% and 0.60%, for all analysed cases, while the numerical simulations did not capture this reduction. Table 8.6 shows the detailed errors obtained between the numerical and experimental coefficients.

Table 8.6 Errors between the numerical and experimental wing lift and drag coefficients for cases C39 to C45

Case	**Angle of Attack [deg.]**	**Un-morphed Wing**		**Morphed Wing**	
		CL Error $[\cdot 10^{-2}]$	CD Error $[\cdot 10^{-3}]$	CL Error $[\cdot 10^{-2}]$	CD Error $[\cdot 10^{-3}]$
C39	0.75	NA	NA	NA	NA
C40	1	-0.409	3.030	-0.305	2.968
C41	1.25	-0.015	3.412	-0.007	3.308
C42	1.50	0.228	3.753	0.257	3.648
C43	2	0.652	4.444	0.524	4.291
C44	2.50	0.999	5.220	1.001	5.101
C45	3	1.578	6.110	1.457	6.013

Another comparison was done between the lift and drag coefficients obtained for the un-morphed and morphed geometries, through the numerical simulations and the experimental tests, and is presented in Tables 8.7 and 8.8. Cases C68 to C73, analysed at a Mach number of 0.20 and having a 4 deg. aileron deflection were included in the comparison. Details about the errors obtained between the numerical and experimental results are shown in Table 8.9.

Table 8.7 Comparison between the numerical un-morphed and morphed wing lift and drag coefficients for cases C68 to C73

Numerical Results						
Case	**Angle of Attack [deg.]**	**Un-morphed Wing**		**Morphed Wing**		**Drag Variation [%]**
		CL	CD	CL	CD	
C68	0	0.2990	0.0191	0.2994	0.0191	0.03%
C69	0.5	0.3254	0.0212	0.3260	0.0212	0.07%
C70	1	0.3519	0.0236	0.3527	0.0237	0.19%
C71	1.5	0.3783	0.0263	0.3780	0.0263	0.13%
C72	2	0.4047	0.0292	0.4057	0.0292	0.15%
C73	2.5	0.4318	0.0323	0.4300	0.0322	-0.09%

Table 8.8 Comparison between the experimental un-morphed and morphed wing lift and drag coefficients for cases C68 to C73

Experimental Results (loads balance measurements)						
Case	**Angle of Attack [deg.]**	**Un-morphed Wing**		**Morphed Wing**		**Drag Variation [%]**
		CL	CD	CL	CD	
C68	0	0.3023	0.0231	0.3034	0.0230	-0.15%
C69	0.5	0.3350	0.0261	0.3358	0.0260	-0.36%
C70	1	0.3671	0.0295	0.3671	0.0294	-0.41%
C71	1.5	0.3996	0.0333	0.3999	0.0332	-0.15%
C72	2	0.4318	0.0373	0.4329	0.0372	-0.26%
C73	2.5	0.4660	0.0417	0.4634	0.0416	-0.25%

The qualitative behaviour of the results remains the same as for cases C39 to C45. A good agreement between the experimental and numerical lift coefficients, and a 20-25% under-estimation of the numerically calculated drag, compared to the experimental values. The upper skin morphing determines 0.15-0.40% reduction of the wing drag coefficient, as confirmed by the results shown in Table 8.7. The numerically calculated drag coefficient for the morphed wing was higher than the value calculated for the un-morphed wing, thus not predicting the reduction effect observed experimentally.

Table 8.9 Errors between the numerical and experimental wing lift and drag coefficients for cases C68 to C73

Case	Angle of Attack [deg.]	Un-morphed Wing		Morphed Wing	
		CL Error $[\cdot 10^{-2}]$	CD Error $[\cdot 10^{-3}]$	CL Error $[\cdot 10^{-2}]$	CD Error $[\cdot 10^{-3}]$
C68	0	0.329	3.954	0.397	3.914
C69	0.5	0.963	4.922	0.980	4.813
C70	1	1.516	5.892	1.437	5.726
C71	1.5	2.132	6.960	2.093	6.878
C72	2	2.708	8.117	2.718	7.979
C73	2.5	3.412	9.447	3.335	9.373

Tables 8.10 and 8.11 show the comparison between the lift and drag coefficients for the un-morphed and morphed wing geometries, using the results that were obtained through the numerical simulations and the experimental test. This comparison is presented for cases C74 to C82, analysed at a Mach number of 0.15 and an aileron deflection angle of -4 deg.

Concerning the comparison between the numerical and experimental results, the remarks made in the paragraphs above apply as well for cases C74 to C82. There is an under-estimation of the calculated drag coefficient, and there is a better agreement in the case of the lift. The impact of the upper surface skin morphing on the drag coefficient was not uniform. In some cases reductions up to 0.67% were obtained, while in others, an increase was obtained. These drag variations were present in both experimental and numerical results. Table 8.12 shows the detailed errors obtained between the numerical and experimental results.

The upper skin morphing reduces the friction drag coefficient through the extension of the laminar flow region. Due to its very low aspect ratio, the wing gives a poor performance in terms of the lift-induced drag, which has a much higher contribution to the total drag than in the case of a typical high aspect ratio wing (the complete wing of an aircraft). Thus, when the friction drags' percentage contribution in the total drag is higher (as, for example, during cruise flight), the drag reduction obtained could be higher.

Table 8.10 Comparison between the numerical un-morphed and morphed wing lift and drag coefficients for cases C74 to C82

Numerical Results						
Case	**Angle of Attack [deg.]**	**Un-morphed Wing**		**Morphed Wing**		**Drag Variation [%]**
		CL	CD	CL	CD	
C74	0	0.0206	0.0061	0.0208	0.0061	-0.13%
C75	0.5	0.0461	0.0063	0.0461	0.0062	-0.28%
C76	1	0.0716	0.0064	0.0718	0.0065	0.67%
C77	1.5	0.0967	0.0069	0.0963	0.0070	0.20%
C78	2	0.1222	0.0077	0.1227	0.0076	-0.51%
C79	2.5	0.1477	0.0086	0.1470	0.0085	-0.34%
C80	3	0.1733	0.0098	0.1738	0.0097	-0.44%
C81	4	0.2250	0.0128	0.2243	0.0128	0.01%
C82	5	0.2765	0.0168	0.2766	0.0168	-0.05%

Table 8.11 Comparison between the experimental un-morphed and morphed wing lift and drag coefficients for cases C74 to C82

Experimental Results (loads balance measurements)						
Case	**Angle of Attack [deg.]**	**Un-morphed Wing**		**Morphed Wing**		**Drag Variation [%]**
		CL	CD	CL	CD	
C74	0	0.0082	0.0083	0.0082	0.0083	0.04%
C75	0.5	0.0383	0.0084	0.0382	0.0084	-0.09%
C76	1	0.0679	0.0088	0.0680	0.0088	0.33%
C77	1.5	0.0983	0.0094	0.0992	0.0095	0.76%
C78	2	0.1294	0.0105	0.1230	0.0105	0.09%
C79	2.5	0.1602	0.0119	0.1560	0.0119	-0.14%
C80	3	0.1917	0.0137	0.1912	0.0136	-0.67%
C81	4	0.2531	0.0182	0.2541	0.0183	0.59%
C82	5	0.3175	0.0241	0.3171	0.02401	-0.03%

Table 8.12 Errors between the numerical and experimental wing lift and drag coefficients for cases C74 to C82

Case	Angle of Attack [deg.]	Un-morphed Wing		Morphed Wing	
		CL Error $[\cdot 10^{-2}]$	CD Error $[\cdot 10^{-3}]$	CL Error $[\cdot 10^{-2}]$	CD Error $[\cdot 10^{-3}]$
C74	0	-1.241	2.078	-1.252	2.089
C75	0.5	-0.774	2.132	-0.788	2.142
C76	1	-0.369	2.349	-0.381	2.334
C77	1.5	0.158	2.452	0.284	2.510
C78	2	0.726	2.784	0.730	2.832
C79	2.5	1.252	3.267	1.274	3.279
C80	3	1.845	3.876	1.737	3.828
C81	4	2.813	5.362	2.981	5.467
C82	5	4.102	7.307	4.047	7.308

In the present CRIAQ MDO 505 project, an industrial wing-tip was morphed, and for this reason, structural limitations existed. In order to continue performing other types of research studies in morphing wing and airplane aero-structural areas, it will be interesting to study other multidisciplinary approaches defined in (Martins and Lambe, 2013) by other authors.

8.7 Conclusions

The results obtained using CFD numerical simulation and experimental wind tunnel testing for a morphing wing equipped with a flexible upper surface and controllable rigid aileron were presented in this paper. The morphing wing tip was manufactured and fitted with a composite material upper skin. Two-dimensional optimizations were performed with the aim of controlling the extent of the laminar flow region, and the resulting skin shapes were scanned using high-precision photogrammetry. A grid convergence study was performed to determine the optimal mesh refinement required by the numerical transition model. Subsonic wind tunnel tests were performed at the NRC wind tunnel, and the experimental measurements included Infra-Red thermography, pressure sensors measurements and balance loads measurements.

Three series of cases were analyzed, each consisting of a sweep over a range of angles of attack, at a constant Mach number and aileron deflection angle. Comparisons were made between the un-morphed and morphed upper skin shapes, for the transition point location at the station situated at 40% of the wing span, corresponding to the pressure sensors station. Good agreement was obtained between the numerical and IR results, with an average prediction error of around 5% of the chord. Both the IR measurements and the numerical results have shown that an increase in the laminar flow region was obtained after the optimization. The experimental transition delay was between 3 and 9% of the chord, while the numerical improvements were smaller. The laminar flow extension was obtained for an important percentage of the upper skin span. Pressure coefficient comparisons were performed for the 40% of the span section, and a very good match was obtained. The lift and drag coefficients were determined for all 22 cases analysed, for both un-morphed and morphed geometries. The force balance results show reductions in the drag coefficient up to 0.67%. The numerical results prediction obtained with the chosen turbulence and transition models does not appear to be accurate enough to capture this drag variation.

Acknowledgments

We would like to express our appreciation for the financial support and contribution obtained from our industrial partners Bombardier Aerospace and Thales Canada, in the framework of the CRIAQ MDO 505 project. We also wish to thank NSERC for their financial support. Special thanks are dues to our collaborators and leaders in this project: Mr. Patrick Germain and Mr. Fassi Kafyeke from Bombardier Aerospace, Mr. Philippe Molaret from Thales Canada, Mr. Eric Laurendeau from Ecole Polytechnique, and Mr. Erik Sherwood and his team from DFS-NRC for the design and fabrication of the wind tunnel model.

DISCUSSION OF RESULTS

The research performed and included in Chapters 3 to 8 established a general framework for the performance analysis of a morphing wing, presented the development of the tools needed to perform the study (optimization algorithms, geometry parameterization and modification, aerodynamic calculations) and presented improvements obtained from the application of the morphing concept in both two and three dimensions. The results obtained have been independently presented in the aforementioned chapters, while the present section presents a summary and analysis of these results from global and integrated perspective.

Chapters 3 to 7 presented numerical results obtained for the UAS-S4 morphing wing, while Chapter 8 presented the comparison between the numerical and the experimental results for the CRIAQ MDO 505 morphing wing.

Discussion of Chapter 3 Results

The first research paper concentrated on the development of the tools needed for determining the shapes of the morphed geometries for the UAS-S4, and thus it included only a limited number of results. An important part of the wing surface was considered for morphing. On the chordwise section of the wing, the flexible skin started at 20% of the chord on the lower surface, went around the leading edge and extended up to 65% of the chord on the upper surface. From a spanwise perspective, the morphing skin extended over the entire available space, from the wingtip up to the station that corresponds to the junction with the fuselage. Although the airfoil sections of the wing were parameterized with NURBS, no control existed over the distribution of control points, their number and positions resulted from the curve fitting process performed on the original airfoil.

The optimizations were performed with the objective of reducing the wing drag coefficient over a range of angles of attack between 0 and 5 degrees, at three Mach numbers (0.10, 0.15 and 0.20) and three Reynolds numbers (1.33E+06, 1.99E+06 and 2.61E+06, as calculated

using the mean aerodynamic chord). The optimizations were performed without taking into account any constraints on the lift and pitching moment coefficients, only the limitations on the maximum allowed motion for the NURBS control points were considered. The results showed drag reductions of 5-8% for angles of attack of 0 and 1 degrees and reduction of 1-1.5% for angles of attack higher than 3 degrees. The lift and pitching moment coefficients also presented average variations of around 1% because of the lack of constraints. Although preliminary, these results demonstrated the potential of the morphing skin for obtaining the desired performance increase.

Discussion of Chapter 4 Results

In the second paper, several modifications were implemented in order to obtain a morphing skin that would be feasible from a structural point of view. It was assumed that the skin started at 5% of the chord on the lower surface and extended only to 55% of the chord on the upper surface. These new limits allowed for a good control of the leading edge shape and did not interfere with the control surfaces (ailerons) and high-lift devices (flaps) installed on the wing. In addition, the positions of the NURBS control points were redistributed over the skin in order to provide a better suited distribution. These displacements were limited to a maximum of 2.5 mm and were better restricted to the direction normal to the airfoil curve. The aerodynamic calculations were performed in two-dimensions using the XFOIL solver.

The optimizations were performed at high angles of attack values, between 10 and 19 degrees with the objective of increasing the maximum lift coefficient and delaying boundary layer separation. A constraint was included to limit the length variation of the skin to a maximum of 0.75% with respect to its original length. Calculations were performed at three Mach number values (0.10, 0.15 and 0.20) and three corresponding Reynolds number values (1.41E+06, 2.17E+06 and 2.82E+06). The results showed that the morphing skin successfully achieved the goal of delaying boundary layer separation even when the separation point is downstream of the skin limit. For the maximum lift condition that occurs at approximately 15 degrees angle of attack, the original airfoil presented trailing edge

separation at 72% of the chord and a lift coefficient value of 1.54. The morphing skin delayed the separation point to 81% of the chord and increases the maximum lift coefficient value by 5.8%, to a value of 1.63.

In the case when the separation occurred closer to the leading edge, thus over the length of the flexible skin, its effectiveness was increased, as our numerical results showed separation point delays of up to 15%. However, it must be noted that the degree of uncertainty regarding the post-stall results is greatly increased for angles of attack higher than 17 degrees, due to the difficulty of numerically predicting the behaviour of massively separated flow, as is the case when leading edge separation occurs. Only two high-fidelity CFD models (the Direct Numerical Simulation and the Large Eddy Simulation) are capable of accurately simulating such flows, and they require extremely high computational time and resources.

Discussion of Chapter 5 Results

The third research paper investigated laminar-to-turbulent transition point delay and drag reductions obtained for the two-dimensional airfoil of the UAs-S4 equipped with the morphing skin. The limits of the skin, the distribution of NURBS control points, the maximum allowed displacements and the constraints regarding its length variation were the same as the ones considered for the second paper. It must be noted that this setup also remains valid for the results presented in the fourth article. The flight conditions investigated included three Mach number values (0.10, 0.15 and 0.20), three corresponding Reynolds number values (1.41E+06, 2.17E+06 and 2.82E+06) and an angle of attack range between -2 and 10 degrees.

Two approaches were used for performing the aerodynamic optimizations, using two different objective functions in order to achieve the desired results. In the first approach, the drag coefficient of the airfoil was used as the objective function, while the second approach used the position of the upper surface transition point. In both cases, the constraint of not allowing the lift coefficient to become smaller than the lift coefficient of the original airfoil

was imposed. Important drag coefficient reductions were obtained for almost the entire range of lift coefficients, but variations exist depending on the Reynolds number and Mach number. For Mach 0.10, drag reductions of 9-10% were obtained, but only for lift coefficient values higher than 0.40. At Mach 0.15 and 0.20, the drag reduction range was extended to lift values smaller than 0.40, but higher than 0.20, achieving 10-12% improvement with respect to the original airfoil. An analysis of the skin friction coefficient distribution plots for different flight cases showed that a significant increase in laminar flow was responsible for the obtained drag reduction, with transition point delays as important as 15% of the chord for the small angles of attack. Even at 10 degrees angle of attack a delay could be observed, the flexible skin effectively modified the transition point position even if it is located in the leading edge region of the airfoil.

Concerning the mechanism through which the laminarity increase was obtained, the pressure coefficient distribution plots showed a delayed recompression after the initial leading edge pressure peak, and thus a smaller adverse pressure gradient. For many of the morphed airfoils, a pressure plateau followed by a large and sudden pressure increase could be observed in the transition region, possibly indicating a laminar separation bubble. The ability of the morphing skin to influence the laminar-to-turbulent transition vanished when the transition was situated downstream of the 55% of the chord skin limit. This phenomenon explained the lack of improvements that was observed for lift coefficients smaller than 0.20 (angles of attack smaller than 0 degrees). An interesting observation that can be made is that for most of the flight conditions considered, the optimized airfoil shape obtained by the two different objective functions was almost identical.

Discussion of Chapter 6 Results

The fourth research paper presented the aerodynamic improvements that were obtained by applying the morphing skin concept on the wing the UAS-S4. The change from two-dimensional to three-dimensional analysis added extra parameters to the flexible skin geometry, which were the proportion of the wingspan over which the skin stretches and the

number of actuation stations placed on each half-wing. Concerning the spanwise extent of the skin, its limits were chosen so that the morphing surface was as large as possible. Thus, the skin started close to the wing/fuselage junction and extended up to the wing tip. The choice of the number of spanwise actuation stations was not so straightforward, and thus 4 configurations were considered and compared, where the number of actuation stations varied between 2 and 5. The stations were distributed so that the shape changes of the skin were as uniform as possible over the entire span of each half-wing.

For the analysis of three-dimensional wings, the drag determined by viscous effects represents only one component of the total drag, the other component being the lift-induced drag. Because of the extra component, all performance gains obtained in two-dimensional optimizations cannot be reproduced to the same order of magnitude in three-dimensions. In this 3D analysis, the morphing skin increased the lift-to-drag ratio of the UAS-S4 wing with an average of around 1.8% over the entire considered range of angles of attack that were analysed, with a maximum increase of 4% obtained for the maximum lift-to-drag flight condition. The improvements could be explained by the friction drag reduction associated with a delayed laminar-to-turbulent transition. High fidelity CFD simulations were performed with the ANSYS Fluent solver and clearly identified this effect.

The behaviour observed in the two-dimensional optimizations, where very good results were obtained for lift coefficient values greater than 0.20 could also be observed in the three-dimensional optimizations. For negative angles of attack the improvements were only marginal, but as the angle of attack increased, so were the gains achieved through morphing. At 3 degrees angle of attack, the maximum lift-to-drag improvements of 4% were obtained. Even if the highest profile drag reductions were obtained for the highest angle of attack values, the overall impact on the UAS performance was the smallest for these cases. This fact was explained by the fact that the induced drag became much more important than the profile drag (the induced drag is proportional with the square of the lift coefficient), and thus even an important reduction of profile drag resulted only in a minor reduction of total drag. The conclusion is that the morphing skin concept is most efficient for those baseline wing designs

that develop a low induced drag, so that the improvements achieved through morphing would not be lost (designs with a high aspect ratio, low sweep angles and moderate taper ratio).

Discussion of Chapter 7 Results

In the fifth paper, the mathematical development of the nonlinear vortex lattice method was presented. Convergence studies showed that the algorithm requires a sufficiently refined mesh on the wing surface in order to achieve grid-independent values for the aerodynamic coefficients. Validation of the proposed algorithm was performed using experimental data available in the literature. Results were obtained for both a low-sweep high aspect ratio wing and for a high-sweep high aspect ratio wing. Very good agreement between the numerical results and the experimental data was obtained, not only of the lift, but also of the drag and pitching moment coefficients.

Following the conclusions of the fourth paper, a redesign of the baseline shape of the UAS-S4 wing was performed, with the objective of reducing the induced drag. The calculations were done at an airspeed of 50 m/s and a Reynolds number of 2.13E+06 as calculated with the mean aerodynamic chord. The shape change was achieved by using the wing span, taper ratio and sweep angle as design variables. The redesign was performed as a multi-point optimization process over an angle of attack range between -2 and 4 degrees. Results showed important reductions of the induced drag coefficient, with an average decrease of 19% over the initial wing shape. Then, the upper surface skin morphing was applied to the new wing geometry, and an optimization of the airfoil shape was performed with the objective of increasing the lift-to-drag ratio. Due to the lower contribution that the induced drag had in the total drag coefficient, the performance of the morphing skin became more significant. For the considered range of angles of attack, the morphing wing provided an average lift-to-drag ratio increase of 5.2%, with a maximum increase of 7% over the performance of the new baseline wing design. The gains were again explained by the profile drag reductions determined by the optimized airfoil shapes, reductions that were between 2.5E-04 (2.5 drag counts) and 4.5E-04 (4.5 drag counts).

The nonlinear vortex lattice method can be used for the aerodynamic analysis of low aspect ratio wings, thus having a greater application range than the nonlinear lifting line method. Results were presented for the morphing wing model developed in the frame of the MDO 505 project. The airfoil optimizations were performed in two-dimensions, at a Mach number of 0.15 and a Reynolds number of 4.5E+06, with the objective of reducing the drag coefficient, and the complete wing geometry was reconstructed using the optimized shapes. In three-dimensions, for angles of attack between -0.5 and 1.5 degrees, profile drag reductions of 3% were obtained, but the very high induced drag reduces most of the improvements gained due to morphing. For a typical aircraft high aspect ratio wing however, the flexible upper skin would be more effective in providing significant drag reductions.

Discussion of Chapter 8 Results

The sixth research paper presented the aerodynamic improvements that were obtained by applying the morphing skin concept on the MDO 505 project technology demonstrator. Due to the complex, non-linear shapes of the composite materials flexible skin, a high precision photogrammetry procedure was used to scan the morphed shapes. A spline interpolation procedure was used to increase the point density of the scanned data, and the resulting skin geometries were patched on the rigid geometry representing the rest of the wing model. A grid convergence study was performed at a Mach number of 0.15, a Reynolds number of 4.53E+06 and an angle of attack of 0 deg. The study results showed the refined meshing requirements of the $\gamma - Re_{\theta t}$ transition model, as 400 cells around the wing section and 160 cells in the span direction, together with a strict $y+< 1$ condition had to be used in order to obtain grid-independent results.

Two-dimensional optimizations were performed in order to increase the extent of laminar flow on the wing upper surface and determine the actuator displacements. The flight conditions chosen were at two Mach numbers (0.15 and 0.20), two Reynolds numbers (4.28E+06 and 5.27E+06) and angles of attack between 0 and 5 degrees. The three-dimensional analyses were able to confirm that the two-dimensionally obtained

improvements were valid. IR thermography visualisations were performed during the wind tunnel testing and allow the identification of the laminar-to-turbulent transition region on the wing upper surface. Detailed comparisons between the numerically predicted and experimentally measured transition locations were presented for the spanwise station corresponding to the pressure sensors lines (approximately 40% of the wingspan, as measured from the root section). A good agreement was observed between the two sets of results, with average errors of around 5%-7% of the local wing chord. The morphing upper skin achieved the improvement of laminar flow, as the transition location was delayed towards the trailing edge by 3% to 9% of the chord. The laminar flow increase predicted by the numerical simulations was smaller than what was observed in the IR measurements.

The pressure coefficient distributions showed that the skin morphing delays the start of the recompression on the upper surface by shifting the point of lowest pressure towards the trailing edge, thus creating more favourable conditions for laminar flow. The comparison between the numerical and experimental pressure distributions, performed for 4 chosen cases, showed a very good agreement. Concerning the aerodynamic loads, the experimental measurements indicated a slight reduction in drag coefficient between the un-morphed and morphed geometries, with values between 0.25% and 0.67%. The numerical prediction was not sensitive enough to capture this variation. The simulation always under-predicted the values of the drag coefficient, and the average errors were around 25%. The comparison between the predicted and measured lift coefficients showed a good agreement. The experimental loads measurements showed a reduction in the friction drag coefficient through the extension of the laminar flow region. Due to its very low aspect ratio, the wing gave poor performance in terms of the lift-induced drag, which has a much higher contribution to the total drag than in the case of a typical high aspect ratio wing (the complete wing of an aircraft). Thus, when the friction drags' percentage contribution in the total drag is higher (as, for example, during cruise flight) the drag reduction obtained through the upper surface morphing concept could be higher.

CONCLUSION

In this thesis, several novel methods and algorithms were developed and applied for the study of the aerodynamic improvements obtained through the application of a morphing wing concept on the UAS-S4 and the MDO 505 project technical demonstrator. The morphing system consisted of a flexible surface whose shape could be deformed using an actuation system placed inside the wing structure.

A wing geometry deformation algorithm was implemented in order to simulate the flexible skin, by coupling a NURBS parameterization of the wing sections equipped with actuators and a cubic splines interpolation technique for the reconstruction all other sections required to obtain an accurate geometry. The NURBS control points allowed a good simulation of actuator displacements, while the modifications implemented during least-squares curve fitting process allowed a local modification of the airfoil shape, between the desired skin limits.

The ABC algorithm represents a powerful global optimization tool, suitable for constrained, highly non-linear problems, such as aerodynamic optimizations. Coupling of the algorithm with the BFGS gradient-based local method allowed an acceleration of the convergence rate in the final iterations. This hybrid method, that used finite-difference approximations for calculating the objective function gradient, was suitable for problems with a low to moderate number of design parameters due to the computational cost associated with the gradient evaluation. For the two-dimensional optimizations and for the three-dimensional optimizations with 2 or 3 actuations sections on each wing half the method proved to be effective, while for the cases with 4 or 5 actuation sections, the computational cost associated with calculating the gradient one time became greater than the cost on running and entire additional ABC cycle, and so the optimizations were performed only with the ABC method. For these cases, other methods of estimating the gradient should be implemented, such as the adjoint method.

Two original methods were developed for the calculation of the aerodynamic characteristics of the morphing wings: a nonlinear lifting line method and a nonlinear vortex lattice method. Both methods provide fast and accurate results for the forces and moments, including the calculation of the total wing drag coefficient. The validations performed using experimental data available in literature demonstrated the accuracy of the proposed algorithms. Because of the fact that the methods include strip analysis of the span-wise wing sections, they can account for the airfoil shape modifications induced by the morphing upper surface skin, and thus were capable of analysing the morphing skin concept. The main advantages of these methods are the ease of implementing geometry modifications, the very good accuracy and the fast computational times, which are orders of magnitude smaller than the time required to perform three-dimensional CFD simulations. These methods do not provide the same level of detail regarding the flow behaviour around the wing as classic three-dimensional CFD, but they were conceived and are very well suited for the initial wing design and optimization phases.

Two-dimensional optimizations of the UAS-S4 airfoil equipped with the morphing skin were performed for several Mach numbers, Reynolds numbers and for an extended range of angles of attack. The morphing skin proved to be very efficient at delaying the laminar-to-turbulent transition point and thus decreasing the airfoil drag coefficient. Good results were obtained for all angles of attack where the transition point of the original airfoil was situated on the flexible skin. In addition, it can provide an increase in the maximum lift coefficient and a delay in boundary layer separation for angles of attack immediately after stall.

For the three-dimensional optimization of the morphing skin on the UAS-S4 wing, good results were also obtained. The skin's ability of reducing the profile drag over its entire span determined a significant increase in the lift-to-drag ratio. It was found that the improvement percentages are influenced by the wing's efficiency in terms of the induced drag, and thus a good wing plan-form is required in order to fully take advantage of the morphing skin. A multi-point redesign of the baseline wing shape demonstrated the increased effectiveness of

the morphing concept. Thus, the aircraft that could gain the most from implementing the system would be surveillance aircraft with high aspect ratio, low sweep wing designs.

High-fidelity simulations of the CRIAQ MDO 505 wing equipped with the upper surface morphing skin were performed. The geometry was constructed based on the results of a high-resolution scanning procedure, in order to accurately capture the skin shapes. An automated mesh generation procedure was created in order to provide identical mesh quality for all geometries. Simulations were performed for several flight conditions, and the numerical results were validated using experimental wing tunnel data. Very good numerical versus experimental agreement was obtained for the upper surface pressure distribution and for the laminar-to-turbulent transition region as function of the morphing skin shapes and different flight cases.

RECOMMENDATIONS

The research presented in the thesis could further be improved using the following comments and recommendations:

- Because the nonlinear lifting line and vortex lattice methods are strongly coupled with the wing strip analysis, the precision of these two-dimensional calculations is crucial. Thus, instead of XFOIL, a high-fidelity CFD code could be used;
- If the airfoil analysis tool could perform compressible flow simulations, the application range of the codes themselves could be extended to transonic or supersonic flow, with the aid of analytical compressibility corrections;
- Another choice of development is the introduction of unsteady effects and unsteady wake models. By using airfoil performance databases instead of real-time airfoil calculations, on a high-performance workstation the methods could be integrated within a flight simulation environment, where they could provide more accurate aerodynamic results;
- Refinements of the geometric modelling of the wing could be proposed, by using complete three-dimensional NURBS parameterizations instead of the coupled NURBS/cubic splines approach currently implemented;
- Research could also be extended by analysing the effects of the morphing wing on the flight performance during manoeuvres (deflected ailerons) and during take-off/landing (deflected flaps). Analysis could be further performed to verify if the flexible skin can counter the loss of control surface effectiveness for certain flight conditions.

An aspect of great importance for the design and study of upper surface morphing wings is the quality of the flexible skin shapes. As the results obtained for the MDO 505 project show, numerical predictions were not accurately validated due to unwanted spanwise non-uniformities in the skin deformation. When performing numerical aerodynamic optimizations, mathematical geometry parameterization techniques (such as NURBS) are not able to reproduce the behaviour and real deformed shapes of composite materials. One possibility of minimizing the impact of this problem is to perform aero-structural optimizations, and thus use a finite element model (instead of mathematical model) to

recreate the skin shapes during the aerodynamic optimization procedure. This technique would also be subjected to limitations (such as the accuracy of the finite element model), but it would provide direct information regarding the feasibility of the aerodynamically required shapes.

LIST OF REFERENCES

Ajaj, R.M., E.S. Flores, M.I. Friswell, G. Allegri, B.K.S. Woods, A.T. Isikveren and W.G. Dettmer. 2013. « The Zigzag wingbox for a span morphing wing ». Aerospace Science and Technology, vol. 28, no 1, p. 364-375.

Akay, Bahriye, and Dervis Karaboga. 2012. « A modified artificial bee colony algorithm for real-parameter optimization ». Information Sciences, vol. 192, p. 120-142.

Andersen, Gerald R., David L. Cowan and David J. Piatak. 2007. « Aeroelastic modeling, analysis and testing of a morphing wing structure ». In Proceedings 48th AIAA/ASME/ASCE/AHS/ASC Structures, Structural Dynamics, and Materials Conference. Vol. 1734.

Anderson, John D., and Stephen Corda. 1980. « Numerical lifting line theory applied to drooped leading-edge wings below and above stall ». Journal of Aircraft, vol. 17, no 12, p. 898-904.

ANSYS. FLUENT. < www.ansys.com >.

ATAG. 2014. Aviation: Benefits Without Borders.

Attinello, John S. 1961. « Design and engineering features of flap blowing installations ». In Boundary Layer and Flow Control. Its Principles and Application, sous la dir. de Lachmann, Gustav Victor. Vol. 1, p. 463-515. New York: Pergamon Press.

Barbarino, Silvestro. 2009. « Smart Morphing Concepts and Applications for Advanced Lifting Surfaces ». Università degli Studi di Napoli Federico II.

Barbarino, Silvestro, Onur Bilgen, Rafic M. Ajaj, Michael I. Friswell and Daniel J. Inman. 2011. « A review of morphing aircraft ». Journal of Intelligent Material Systems and Structures, vol. 22, no 9, p. 823-877.

Barbarino, Silvestro, Rosario Pecora, Leonardo Lecce, Salvatore Ameduri and Luigi De Rosa. 2011. « Airfoil structural morphing based on SMA actuator series: numerical and experimental studies ». Journal of Intelligent Material Systems and Structures, vol. 22, no 10, p. 987-1003.

Bartley-Cho, Jonathan D., Donny P. Wang, Christopher A. Martin, Jayanth N. Kudva and Mark N. West. 2004. « Development of high-rate, adaptive trailing edge control surface for the smart wing phase 2 wind tunnel model ». Journal of Intelligent Material Systems and Structures, vol. 15, no 4, p. 279-291.

Berbente, C., S. Mitran and S. Zancu. 1998. Numerical Methods. Bucharest: Editura Tehnica.

Bilgen, Onur, Kevin Kochersberger, Edward C. Diggs, Andrew J. Kurdila and Daniel J. Inman. 2007. « Morphing wing micro-air-vehicles via macro-fiber-composite actuators ». In Proceedings of the 48th AIAA/ASME/ASCE/AHS/ASC Structures, Structural Dynamics, and Materials Conference. (Honolulu, Hawaii, USA), p. 23-26.

Bilgen, O., K.B. Kochersberger and D. J. Inman. 2009. « Macro-fiber composite actuators for a swept wing unmanned aircraft ». Aeronautical Journal, vol. 113, no 1144, p. 385-395.

Bonnans, Joseph-Frédéric, Jean Charles Gilbert, Claude Lemaréchal and Claudia Sagastizábal. 2006. Numerical optimization: theoretical and practical aspects. Springer Science & Business Media.

Botez, Ruxandra Mihaela, Philippe Molaret and Eric Laurendeau. 2007. « Laminar flow control on a research wing project presentation covering a three year period ». In 2007 AERO Conference and 54th Annual General Meeting, 2007 CASI Annual General Meeting. (Toronto, Ontario, Canada), p. 25-26.

Boyd, Stephen, and Lieven Vandenberghe. 2004. Convex optimization. Cambridge University Press.

Brailovski, Vladimir, Patrick Terriault, Daniel Coutu, Thomas Georges, Emeric Morellon, Charles Fischer and Sébastien Bérubé. 2008. « Morphing laminar wing with flexible extrados powered by shape memory alloy actuators ». In ASME 2008 Conference on Smart Materials, Adaptive Structures and Intelligent Systems. (Ellicott City, Maryland, USA), p. 615-623. American Society of Mechanical Engineers.

Braslow, A.L. 1999. « History of Suction-Type Laminar-Flow Control with Emphasis on Flight Resrearch ». In. Vol. 13. Coll. « Monographs in Aerospace History ».

Broyden, Charles G. 1965. « A class of methods for solving nonlinear simultaneous equations ». Mathematics of Computation, vol. 19, p. 577-593.

Bunge, Roberto A., and Ilan M. Kroo. 2012. « Compact formulation of nonlinear inviscid aerodynamics for fixed-wing aircraft ». AIAA Paper, vol. 2771.

Bye, Derek R., and Paul D. McClure. 2007. « Design of a morphing vehicle ». In 48th AIAA Structures, Structural Dynamics, and Materials Conference. Vol. 23.

Cahill, J.F., and S.M. Gottlieb. 1950. Low-Speed Aerodynamic Characteristics of a Series of Swept Wings Having NACA 65A006 Airfoil Sections. L50F16: NACA.

Coley, David A. 1999. An introduction to genetic algorithms for scientists and engineers, 1655. World Scientific Singapore.

Daynes, Stephen, Xavier Lachenal and Paul M. Weaver. 2015. « Concept for morphing airfoil with zero torsional stiffness ». Thin-Walled Structures, vol. 94, p. 129-134.

De Boor, Carl. 1978. « A practical guide to splines ». Mathematics of Computation.

Deb, K., and D.E. Goldberg. 1991. « A comparison of selection schemes used in genetic algorithms ». In Foundations of Genetic Algorithms. p. 69-93. Morgan Kaufmann.

Deuflhard, Peter. 2011. Newton methods for nonlinear problems: affine invariance and adaptive algorithms, 35. Coll. « Springer Series in Computational Mathematics ». Springer Science & Business Media.

Diodati, Gianluca, Sergio Ricci, Alessandro De Gaspari, Fabien Huvelin, Antoine Dumont and Jean-Luc Godard. 2013. « Estimated performance of an adaptive trailing-edge device aimed at reducing fuel consumption on a medium-size aircraft ». In SPIE Smart Structures and Materials+ Nondestructive Evaluation and Health Monitoring. (San Diego, California, USA) Vol. 8690-14. International Society for Optics and Photonics.

do Vale, Jose Lobo, Andre Leite, Fernando Lau and Afzal Suleman. 2011. « Aero-structural optimization and performance evaluation of a morphing wing with variable span and camber ». Journal of Intelligent Material Systems and Structures, vol. 22, no 10, p. 1057-1073.

Drela, Mark. 1989. « Integral boundary layer formulation for blunt trailing edges ». AIAA paper, vol. 89, p. 2200.

Drela, Mark. 1989. « XFOIL: An analysis and design system for low Reynolds number airfoils ». In Low Reynolds number aerodynamics. p. 1-12. Springer.

Drela, Mark. 1990. « Elements of airfoil design methodology ». In Applied Computational Aerodynamics, sous la dir. de Henne, P. A. Vol. 125, p. 167-189. Coll. « Progress in Astronautica and Aeronautics ».

Drela, Mark. 1998. « Pros and cons of airfoil optimization ». In Frontiers of computational fluid dynamics, sous la dir. de Caughey, D. A., et M. M. Hafez. World Scientific.

Drela, Mark. 2003. « Implicit Implementation of the Full en Transition Criterion ». In 21st AIAA Applied Aerodynamics Conference. (Orlando, Florida, USA).

Drela, Mark, and David Youngren. 2001. XFOIL.(Version 6.96). < http://web.mit.edu/drela/Public/web/xfoil/ >.

Elham, Ali. 2015. « Adjoint quasi-three-dimensional aerodynamic solver for multi-fidelity wing aerodynamic shape optimization ». Aerospace Science and Technology, vol. 41, p. 241-249.

ESTECO. modeFrontier. < http://www.esteco.com/modefrontier/ >.

Falcão, Luís, Alexandra Gomes and Afzal Suleman. 2011. « Aero-structural design optimization of a morphing wingtip ». Journal of Intelligent Material Systems and Structures, vol. 22, no 10, p. 1113-1124.

Farin, Gerald E. 1999. NURBS: from projective geometry to practical use, 2nd Edition. AK Peters, Ltd.

Filippone, Antonio. 2014. « Range performance improvement with morphing wing configurations ». In Royal Aeronautical Society Structural Design Conference. (Belfast, UK).

Fincham, J.H.S., and M.I. Friswell. 2015. « Aerodynamic optimisation of a camber morphing aerofoil ». Aerospace Science and Technology, vol. 43, p. 245-255.

Flanagan, John S., Rolf C. Strutzenberg, Robert B. Myers and Jeffrey E. Rodrian. 2007. « Development and flight testing of a morphing aircraft, the NextGen MFX-1 ». In 48th AIAA/ASME/ASCE/AHS/ASC Structures, Structural Dynamics and Materials Conference. Vol. 1707.

Friedmann, Peretz P., and Thomas A. Millott. 1995. « Vibration reduction in rotorcraft using active control-a comparison of various approaches ». Journal of Guidance, Control, and Dynamics, vol. 18, no 4, p. 664-673.

Gallay, S., and E. Laurendeau. 2015. « Nonlinear Generalized Lifting-Line Coupling Algorithms for Pre/Poststall Flows ». AIAA Journal, p. 1-9.

Gamboa, P., P. Aleixo, J. Vale, F. Lau and A. Suleman. 2007. Design and Testing of a Morphing Wing for an Experimental UAV. DTIC Document.

Gamboa, P., J. Vale, F. Lau and A. Suleman. 2009. « Optimization of a morphing wing based on coupled aerodynamic and structural constraints ». AIAA journal, vol. 47, no 9, p. 2087-2104.

Gano, Shawn E., and John E. Renaud. 2002. « Optimized unmanned aerial vehicle with wing morphing for extended range and endurance ». In 9th AIAA/ISSMO Symposium and Exhibit on Multidisciplinary Analysis and Optimization. (Atlanta, Georgia, USA).

Ghommem, M., N. Collier, A.H. Niemi and V.M. Calo. 2012. « Shape optimization and performance analysis of flapping wings ». In Proceedings of The Eighth International Conference on Engineering Computational Technology. (Stirlingshire, UK).

Glauert, Hermann. 1983. The elements of aerofoil and airscrew theory. Cambridge University Press.

Greenblatt, David, and Israel J. Wygnanski. 2000. « The control of flow separation by periodic excitation ». Progress in Aerospace Sciences, vol. 36, no 7, p. 487-545.

Grigorie, Teodor Lucian, and Ruxandra Mihaela Botez. 2010. « New adaptive controller method for SMA hysteresis modelling of a morphing wing ». Aeronautical Journal, vol. 114, no 1151, p. 1-13.

Grigorie, Teodor Lucian, Ruxandra Mihaela Botez and Andrei Vladimir Popov. 2009. « Adaptive neuro-fuzzy controllers for an open-loop morphing wing system ». Proceedings of the Institution of Mechanical Engineers, Part G: Journal of Aerospace Engineering, vol. 223, no 7, p. 965-975.

Grigorie, Teodor Lucian, Ruxandra Mihaela Botez and Andrei Vladimir Popov. 2012. « Design and experimental validation of a control system for a morphing wing" ». In AIAA Atmospheric Flight Mechanics conference.

Grigorie, Teodor Lucian, Ruxandra Mihaela Botez, Andrei Vladimir Popov, Mahmoud Mamou and Youssef Mébarki. 2012. « A hybrid fuzzy logic proportional-integral-derivative and conventional on-off controller for morphing wing actuation using shape memory alloy, Part 2: Controller implementation and validation ». The Aeronautical Journal, vol. 116, no 1179, p. 451-465.

Grigorie, Teodor Lucian, Ruxandra Mihaela Botez, Andrei Vladimir Popov, Mahmoud Mamou and Youssef Mébarki. 2012. « A hybrid fuzzy logic proportional-integral-derivative and conventional on-off controller for morphing wing actuation using shape memory alloy-Part 1: Morphing system mechanisms and controller architecture design ». Aeronautical Journal, vol. 116, no 1179, p. 433.

Grigorie, Teodor Lucian, Ruxandra Mihaela Botez, Andrei Vladimir Popov, Mahmoud Mamou and Youssef Mébarki. 2012. « On–off and proportional–integral controller for a morphing wing. Part 1: Actuation mechanism and control design ». Proceedings of the Institution of Mechanical Engineers, Part G: Journal of Aerospace Engineering, vol. 226, no 2, p. 131-145.

Grigorie, Teodor Lucian, Ruxandra Mihaela Botez, Andrei Vladimir Popov, Mahmoud Mamou and Youssef Mébarki. 2012. « On–off and proportional–integral controller for a morphing wing. Part 2: Control validation–numerical simulations and

experimental tests ». Proceedings of the Institution of Mechanical Engineers, Part G: Journal of Aerospace Engineering, vol. 226, no 2, p. 146-162.

Gross, Andreas, and Hermann Fasel. 2010. « Numerical Investigation of Separation for Airfoils at Low Reynolds Numbers ». AIAA Paper, vol. 4736.

Hedman, Sven G. 1966. Vortex lattice method for calculation of quasi steady state loadings on thin elastic wings in subsonic flow. Aeronautical Research Institute of Sweden: DTIC Document.

Herrera, Francisco, Manuel Lozano and Jose L. Verdegay. 1998. « Tackling real-coded genetic algorithms: Operators and tools for behavioural analysis ». Artificial intelligence review, vol. 12, no 4, p. 265-319.

Iannotta, B. 2002. « Vortex Draws Flight Research Forward ». Aerospace America. no March.

ICAO. 2010. Aviation's Contribution to Climate Change. Coll. « Environmental Report ».

Ivanco, Thomas G., Robert C. Scott, Michael H. Love, Scott Zink and Terrence A. Weisshaar. 2007. « Validation of the Lockheed Martin morphing concept with wind tunnel testing ». AIAA Paper, vol. 2235.

Jones, Robert T. 1941. Correction of the lifting line theory for the effect of the chord. 817: NACA.

Joshi, Shiv P., Zeb Tidwell, William A. Crossley and Sekaripuram Ramakrishnan. 2004. « Comparison of morphing wing strategies based upon aircraft performance impacts ». In 45th AIAA/ASME/ASCE/AHS/ASC Structures, Structural Dynamics and Materials Conference. (Palm Springs, California, USA) Vol. 2.

Karaboga, Dervis, and Bahriye Akay. 2009. « A comparative study of artificial bee colony algorithm ». Applied Mathematics and Computation, vol. 214, no 1, p. 108-132.

Karaboga, Dervis, and Bahriye Basturk. 2007. « Artificial bee colony (ABC) optimization algorithm for solving constrained optimization problems ». In Foundations of Fuzzy Logic and Soft Computing. p. 789-798. Springer.

Karaboga, Dervis, and Bahriye Basturk. 2007. « A powerful and efficient algorithm for numerical function optimization: artificial bee colony (ABC) algorithm ». Journal of global optimization, vol. 39, no 3, p. 459-471.

Katz, Joseph, and Allen Plotkin. 1991. Low-speed aerodynamics: from wing theory to panel methods. McGraw-Hill, Incorporated.

Kim, J., S.J. Kline and J.P. Johnston. 1980. « Investigation of a reattaching turbulent shear layer: flow over a backward-facing step ». Journal of Fluids Engineering, vol. 102, no 3, p. 302-308.

Korakianitis, T., M.A. Rezaienia, I.A. Hamakhan, E.J. Avital and J.J.R. Williams. 2012. « Aerodynamic Improvements of Wind-Turbine Airfoil Geometries With the Prescribed Surface Curvature Distribution Blade Design (CIRCLE) Method ». Journal of Engineering for Gas Turbines and Power, vol. 134, no 8, p. 082601.

Koreanschi, Andreea, Oliviu Sugar Gabor and Ruxandra Mihaela Botez. 2014. « New Numerical Study of the Boundary Layer Behavior on Morphing Wing-with-Aileron System ». In 32nd AIAA Applied Aerodynamics Conference. (Atlanta, Georgia, USA).

Koreanschi, Andreea, Oliviu Sugar Gabor and Ruxandra Mihaela Botez. 2015. « Drag Optimization of a Wing Equipped with a Morphing Upper Surface ». The Aeronautical Journal, vol. accepted for publication.

Lachmann, Gustav Victor. 2014. Boundary layer and flow control: its principles and application. Elsevier.

Langtry, Robin B., and Florian R. Menter. 2009. « Correlation-based transition modeling for unstructured parallelized computational fluid dynamics codes ». AIAA journal, vol. 47, no 12, p. 2894-2906.

Langtry, R.B., F.R. Menter, S.R. Likki, Y.B. Suzen, P.G. Huang and S. Völker. 2006. « A correlation-based transition model using local variables—Part II: Test cases and industrial applications ». Journal of Turbomachinery, vol. 128, no 3, p. 423-434.

Leifsson, Leifur, Slawomir Koziel and Adrian Bekasiewicz. 2014. « Fast Low-fidelity Wing Aerodynamics Model for Surrogate-based Shape Optimization ». Procedia Computer Science, vol. 29, p. 811-820.

Levin, Daniel, and Joseph Katz. 1981. « Vortex-lattice method for the calculation of the nonsteady separated flow over delta wings ». Journal of Aircraft, vol. 18, no 12, p. 1032-1037.

Lingard, J.S. 1995. « Ram-air parachute design ». In 13th AIAA Aerodynamic Decelerator Systems Technology Conference, Clearwater Beach. p. 1-51.

Liu, Yun, Bo Cheng, Sanjay P. Sane and Xinyan Deng. 2015. « Aerodynamics of dynamic wing flexion in translating wings ». Experiments in Fluids, vol. 56, no 6, p. 1-15.

Love, M.H., P.S. Zink, R.L. Stroud, D.R. Bye, S. Rizk and D. White. 2007. « Demonstration of morphing technology through ground and wind tunnel tests ». In 48thAIAA/ASME/ASCE/AHS/ASC structures, structural dynamics, and materials conference, AIAA. Vol. 1729, p. 1-12.

Lyu, Z., and J.R.R.A. Martins. 2014. « Aerodynamic Shape Optimization of an Adaptive Morphing Trailing Edge Wing ». In Proceedings of the 15th AIAA/ISSMO Multidisciplinary Analysis and Optimization Conference. (Atlanta, Georgia, USA).

Mack, S., C. Brehm, B. Heine, A. Kurz and H.F. Fasel. 2008. « Experimental investigation of separation and separation control on a laminar airfoil ». In 4th AIAA Flow Control Conference. p. 23-26.

Majji, Manoranjan, Othon K. Rediniotis and John L. Junkins. 2007. « Design of a morphing wing: modeling and experiments ». In Proceedings of the AIAA Atmospheric Flight Mechanics Conference and Exhibit. (Hilton Head, South Carolina, USA), p. 20-23.

Mariens, J., A. Elham and M.J.L. van Tooren. 2014. « Quasi-Three-Dimensional Aerodynamic Solver for Multidisciplinary Design Optimization of Lifting Surfaces ». Journal of Aircraft, vol. 51, no 2, p. 547-558.

Martins, Joaquim R.R.A., and Andrew B. Lambe. 2013. « Multidisciplinary design optimization: a survey of architectures ». AIAA journal, vol. 51, no 9, p. 2049-2075.

MathWorks. MATLAB.(Version R2013). < http://www.mathworks.com/products/matlab/ >.

McAvoy, Christopher W., and Ashok Gopalarathnam. 2002. « Automated cruise flap for airfoil drag reduction over a large lift range ». Journal of aircraft, vol. 39, no 6, p. 981-988.

McCormick, Barnes W. 1989. « An iterative non-linear lifting line model for wings with unsymmetrical stall ». SAE, vol. Technical Paper 891020.

McCormick, Barnes W. 1995. Aerodynamics, aeronautics, and flight mechanics, 2. Wiley New York.

McMichael, James M. 1996. Progress and prospects for active flow control using microfabricated electromechanical system (MEMS). American Institute of Aeronautics and Astronautics.

Mebarki, Y., and T. Kameya. 2014. Optical Real-Time Tracking using Passive Markers in the NRC 1.5 m Wind Tunnel: Application to the Wind Tunnel Testing of Stores Release from an Internal Weapons Bat. LTR AL-2014-0042: National Research Council Canada.

Mebarki, Y., M. Mamou and M. Genest. 2009. Infra-red Measurements of the Transition Detection on the CRIAQ project Morphing Wing Model. LTR AL-2009-0075: National Research Council Canada.

Melin, Tomas. 2000. « A vortex lattice MATLAB implementation for linear aerodynamic wing applications ». Royal Institute of Technology (KTH), Stockholm, Sweden.

Menter, Florian R. 1994. « Two-equation eddy-viscosity turbulence models for engineering applications ». AIAA journal, vol. 32, no 8, p. 1598-1605.

Menter, Florian R. 2009. « Review of the shear-stress transport turbulence model experience from an industrial perspective ». International Journal of Computational Fluid Dynamics, vol. 23, no 4, p. 305-316.

Menter, F.R., R.B. Langtry, S.R. Likki, Y.B. Suzen, P.G. Huang and S. Völker. 2006. « A correlation-based transition model using local variables—Part I: model formulation ». Journal of turbomachinery, vol. 128, no 3, p. 413-422.

Michaud, Francois. 2014. « Design and Optimization of a Composite Skin for an Adaptive Wing ». Montreal, Canada, Ecole de Technologie Superieure.

Monner, H.P., E. Breitbach, T. Bein and H. Hanselka. 2000. « Design aspects of the adaptive wing-the elastic trailing edge and the local spoiler bump ». Aeronautical Journal, vol. 104, no 1032, p. 89-95.

Multhopp, H., and M. Schwabe. 1938. « Die Berechnung der Auftriebsverteilung von Tragflügeln ». Luftfahrtforschung, vol. 4, p. 153-169.

Murray, James E., Joseph W. Pahle, Stephen Thornton, Shannon Vogus, Tony Frackowiak, Joe Mello and Brook Norton. 2002. Ground and flight evaluation of a small-scale inflatable-winged aircraft. NASA Dryden Flight Research Center.

Murua, Joseba, Rafael Palacios and Michael R. Graham. 2012. « Applications of the unsteady vortex-lattice method in aircraft aeroelasticity and flight dynamics ». Progress in Aerospace Sciences, vol. 55, p. 46-72.

Neal, David A., Matthew G. Good, Christopher O. Johnston, Harry H. Robertshaw, William H. Mason and Daniel J. Inman. 2004. « Design and wind-tunnel analysis of a fully adaptive aircraft configuration ». In Proceedings of AIAA/ASME/ASCE/AHS/ASC SDM. (Palm Springs, California, USA).

Neely, Robert H., Thomas V. Bollech, Gertrude C. Westrick and Robert R. Graham. 1947. Experimental and calculated characteristics of several NACA 44-series wings with aspect ratios of 8, 10, and 12 and taper ratios of 2.5 and 3.5. Coll. « Technical Report », 1270: NACA.

Neto, Antônio B. Guimarães, Roberto G.A. da Silva and Pedro Paglione. 2014. « Control-point-placement method for the aerodynamic correction of the vortex-and the doublet-lattice methods ». Aerospace Science and Technology, vol. 37, p. 117-129.

Okamoto, Nicole DeJong, Jinny Rhee and Nikos J. Mourtos. 2005. « Educating students to understand the impact of engineering solutions in a global/societal context ». In 8th UICEE Annual Conference on Engineering Education. (Kingston, Jamaica).

OWL, Great. 2009. SURFACES. Great OWL Publishing.

Pages, L., O. Trifu and I. Paraschivoiu. 2007. « Optimized laminar flow control on an airfoil using the adaptable wall technique ». In Proceedings of the CASI Aero 2007 Symposium. Vol. 56, p. 1346-1354.

Pankonien, Alexander M., and Daniel J. Inman. 2015. « Spanwise morphing trailing edge on a finite wing ». In SPIE Smart Structures and Materials and Nondestructive Evaluation and Health Monitoring. (San Diego, California, USA), p. 94310T-94310T-15. International Society for Optics and Photonics.

Pecora, Rosario, Francesco Amoroso, Gianluca Amendola and Antonio Concilio. 2014. « Validation of a smart structural concept for wing-flap camber morphing ». SMART STRUCTURES AND SYSTEMS, vol. 14, no 4, p. 659-678.

Pecora, Rosario, Francesco Amoroso and Leonardo Lecce. 2012. « Effectiveness of wing twist morphing in roll control ». Journal of aircraft, vol. 49, no 6, p. 1666-1674.

Pecora, Rosario, Silvestro Barbarino, Leonardo Lecce and Salvatore Russo. 2011. « Design and functional test of a morphing high-lift device for a regional aircraft ». Journal of Intelligent Material Systems and Structures, vol. 22, no 10, p. 1005-1023.

Pecora, R., M. Magnifico, F. Amoroso and E. Monaco. 2014. « Multi-parametric flutter analysis of a morphing wing trailing edge ». AERONAUTICAL JOURNAL, vol. 118, no 1207, p. 1063-1078.

Peifeng, Li, Binqian Zhang, Chen Yingchun, Yuan Changsheng and Lin Yu. 2012. « Aerodynamic design methodology for blended wing body transport ». Chinese Journal of Aeronautics, vol. 25, no 4, p. 508-516.

Phillips, W.F. 2004. « Lifting-line analysis for twisted wings and washout-optimized wings ». Journal of aircraft, vol. 41, no 1, p. 128-136.

Phillips, Warren F., and Nicholas R. Alley. 2007. « Predicting maximum lift coefficient for twisted wings using lifting-line theory ». Journal of aircraft, vol. 44, no 3, p. 898-910.

Phillips, W.F., and D.O. Snyder. 2000. « Modern adaptation of Prandtl's classic lifting-line theory ». Journal of Aircraft, vol. 37, no 4, p. 662-670.

Phlips, P.J., R.A. East and N.H. Pratt. 1981. « An unsteady lifting line theory of flapping wings with application to the forward flight of birds ». Journal of Fluid Mechanics, vol. 112, p. 97-125.

Piegl, Les, and Wayne Tiller. 1997. The NURBS book. 1997. Coll. « Monographs in Visual Communication ». Springer Berlin.

Poles, Silvia. 2003. MOGA-II an improved multi-objective genetic algorithm. Coll. « ESTECO Technical Report », 006.

Popov, Andrei Vladimir, Teodor Lucian Grigorie, Ruxandra Mihaela Botez, Youssef Mébarki and Mahmood Mamou. 2010. « Closed-loop control validation of a morphing wing using wind tunnel tests ». Journal of Aircraft, vol. 47, no 4, p. 1309-1317.

Popov, Andrei Vladimir, Teodor Lucian Grigorie, Ruxandra Mihaela Botez, Youssef Mébarki and Mahmood Mamou. 2010. « Modeling and testing of a morphing wing in open-loop architecture ». Journal of Aircraft, vol. 47, no 3, p. 917-923.

Popov, Andrei Vladimir, Teodor Lucian Grigorie, Ruxandra Mihaela Botez, Youssef Mébarki and Mahmood Mamou. 2010. « Real time airfoil optimisation of a morphing wing in a wind tunnel" ». AIAA Journal of Aircraft, vol. 47, no 4, p. 1346-1354.

Powell, Michael J.D. 1967. « " A method for non-linear constraints in minimization problems" ». In Optimization. p. 283-298. New York: Academic Press.

Prabhakar, Nirmit, Richard J. Prazenica and Snorri Gudmundsson. 2015. « Dynamic analysis of a variable-span, variable-sweep morphing UAV ». In Aerospace Conference, 2015 IEEE. p. 1-12. IEEE.

Prandtl, L. 1918. « Tragflügel-Theorie, 1. u. 2 ». Mitteilung. Nachr. von der Kgl. Gesellschaft der Wissenschaften. Math. Phys. Klasse, vol. 151, p. 451-477.

Previtali, Francesco, Andres F. Arrieta and Paolo Ermanni. 2014. « Performance of a Three-Dimensional Morphing Wing and Comparison with a Conventional Wing ». AIAA Journal, vol. 52, no 10, p. 2101-2113.

Rasmussen, M.L., and D.E. Smith. 1999. « Lifting-line theory for arbitrarily shaped wings ». Journal of Aircraft, vol. 36, no 2, p. 340-348.

Rodriguez, Armando R. 2007. « Morphing aircraft technology survey ». In 45th AIAA Aerospace Sciences Meeting and Exhibit. (Reston, Virginia, USA).

Rom, J., B. Melamed and D. Almosnino. 1993. « Experimental and nonlinear vortex lattice method results for variouswing-canard configurations ». Journal of aircraft, vol. 30, no 2, p. 207-212.

Rusak, Z., E. Wasserstrom and A. Seginer. 1985. « Convergence characteristics of a vortex-lattice method for nonlinearconfiguration aerodynamics ». Journal of aircraft, vol. 22, no 9, p. 743-749.

Saffman, Philip G. 1992. Vortex dynamics. Cambridge university press.

Sainmont, C., I. Paraschivoiu, D. Coutu, V. Brailovski, E. Laurendeau, M. Mamou, Y. Mebarki and M. Khalid. 2009. « Boundary layer behaviour on an morphing wing: simulation and wind tunnel tests ». In Proceedings of the CASI Aero 2009 Symposium. (Toronto, Ontario, Canada).

Schneider, Willaim C. 1954. A comparison of the spanwise loading calculated by various methods with experimental loadings obtained on a 45 degree sweptback wing of aspect ratio 8.02 at a Reynolds number of 4.0 x 10 (6). Coll. « Technical Report », 1208: NACA.

Shyy, W., D. Jenkins and R. Smith. 1997. « Study of adaptive shape airfoils at low Reynolds number in oscillatory flows ». AIAA journal, vol. 35, no 9, p. 1545-1548.

Simpson, Roger L. 1996. « Aspects of turbulent boundary-layer separation ». Progress in Aerospace Sciences, vol. 32, no 5, p. 457-521.

Sivells, James C., and Robert H. Neely. 1947. Method for calculating wing characteristics by lifting-line theory using nonlinear section lift data. 1269: NACA.

Sleesongsom, S., S. Bureerat and K. Tai. 2013. « Aircraft morphing wing design by using partial topology optimization ». Structural and Multidisciplinary Optimization, vol. 48, no 6, p. 1109-1128.

Smith, D.D., R.M. Ajaj, A.T. Isikveren and M.I. Friswell. 2012. « Multi-objective optimization for the multiphase design of active polymorphing wings ». Journal of Aircraft, vol. 49, no 4, p. 1153-1160.

Smith, D.D., M.H. Lowenberg, D.P. Jones and M.I. Friswell. 2014. « Computational and Experimental Validation of the Active Morphing Wing ». Journal of Aircraft, vol. 51, no 3, p. 925-937.

Sodja, Jurij, Marcias J. Martinez, John C. Simpson and Roeland De Breuker. 2015. « Experimental Evaluation of the Morphing Leading Edge Concept ». In AIAA SciTech 2015. (Kissimmee, Florida, USA).

Sofla, A.Y.N., S.A. Meguid, K.T. Tan and W.K. Yeo. 2010. « Shape morphing of aircraft wing: Status and challenges ». Materials & Design, vol. 31, no 3, p. 1284-1292.

Spalart, Philippe R. 2014. « Prediction of Lift Cells for Stalling Wings by Lifting-Line Theory ». AIAA journal, vol. 52, no 8, p. 1817-1821.

Stanewsky, E. 2001. « Adaptive wing and flow control technology ». Progress in Aerospace Sciences, vol. 37, no 7, p. 583-667.

Sugar Gabor, Oliviu, Andreea Koreanschi and Ruxandra Mihaela Botez. 2012. « Low-speed aerodynamic characteristics improvement of ATR 42 airfoil using a morphing wing approach ». In IECON 2012-38th Annual Conference on IEEE Industrial Electronics Society. (Montreal, Quebec, Canada), p. 5451-5456. IEEE.

Sugar Gabor, Oliviu, Andreea Koreanschi and Ruxandra Mihaela Botez. 2013. « An efficient numerical lifting line method for practical wing optimization through morphing ». In Canadian Aeronautics and Space Institute AERO13 Conference. (Toronto, Ontario, Canada).

Sugar Gabor, Oliviu, Andreea Koreanschi and Ruxandra Mihaela Botez. 2013. « Optimization of an Unmanned Aerial System'wing using a flexible skin morphing wing ». SAE International Journal of Aerospace, vol. 6, no 1, p. 115-121.

Sugar Gabor, Oliviu, Andreea Koreanschi and Ruxandra Mihaela Botez. 2014. « Numerical Study of UAS-S4 Ehecatl Aerodynamic Performance Improvement Using a Morphing Wing Technology ». In Unmanned Systems Canada Annual Conference. (Montreal, Quebec, Canada).

Sugar Gabor, Oliviu, Antoine Simon, Andreea Koreanschi and Ruxandra Botez. 2014. « Numerical Optimization of the S4 Éhecatl UAS Airfoil using a Morphing Wing Approach ». In AIAA 32nd Applied Aerodynamics Conference. (Atlanta, Georgia, USA).

Sugar Gabor, Oliviu, Antoine Simon, Andreea Koreanschi and Ruxandra Botez. 2014. « Application of a Morphing Wing Technology on Hydra Technologies Unmanned Aerial System UAS-S4 ». In ASME 2014 International Mechanical Engineering Congress and Exposition. (Montreal, Quebec, Canada). American Society of Mechanical Engineers.

Supekar, Abhijit Hiraman. 2007. Design, analysis and development of a morphable wing structure for unmanned aerial vehicle performance augmentation. ProQuest.

Tani, Itiro. 1934. A simple method of calculating the induced velocity of a monoplane wing. 111: Tokyo Imperial University.

Tianyuan, Hu, and Yu Xiongqing. 2009. « Aerodynamic/stealthy/structural multidisciplinary design optimization of unmanned combat air vehicle ». Chinese Journal of Aeronautics, vol. 22, no 4, p. 380-386.

Vest, Michael S., and Joseph Katz. 1996. « Unsteady aerodynamic model of flapping wings ». AIAA journal, vol. 34, no 7, p. 1435-1440.

Weissinger, J. 1947. The lift distribution of swept-back wings. 1120: NACA.

Wickenheiser, Adam, and Ephrahim Garcia. 2007. « Aerodynamic modeling of morphing wings using an extended lifting-line analysis ». Journal of Aircraft, vol. 44, no 1, p. 10-16.

Woods, Benjamin K.S., and Michael I. Friswell. 2015. « The Adaptive Aspect Ratio morphing wing: Design concept and low fidelity skin optimization ». Aerospace Science and Technology, vol. 42, p. 209-217.

Xie, Changchuan, Libo Wang, Chao Yang and Yi Liu. 2013. « Static aeroelastic analysis of very flexible wings based on non-planar vortex lattice method ». Chinese Journal of Aeronautics, vol. 26, no 3, p. 514-521.

Xu, Chunfang, Haibin Duan and Fang Liu. 2010. « Chaotic artificial bee colony approach to Uninhabited Combat Air Vehicle (UCAV) path planning ». Aerospace Science and Technology, vol. 14, no 8, p. 535-541.

Zhu, Guopu, and Sam Kwong. 2010. « Best-guided artificial bee colony algorithm for numerical function optimization ». Applied Mathematics and Computation, vol. 217, no 7, p. 3166-3173.

Zingg, David W., Laslo Diosady and Laura Billing. 2006. « Adaptive airfoils for drag reduction at transonic speeds ». AIAA paper, vol. 3656.